CFD SIMULATION OF PRESSURISED METERED-DOSE INHALER (pMDI)

By:

BARZIN GAVTASH

A DOCTORAL THESIS

SUBMITTED IN PARTIAL FULFILMENT OF THE REQUIREMENTS FOR THE AWARD OF DOCTOR OF PHILOSOPHY OF LOUGHBOROUGH UNIVERSITY

WOLFSON SCHOOL OF MECHANICAL, ELECTRICAL & MANUFACTURING ENGINEERING

May 2016

Abstract

Pressurised metered dose inhalers (pMDI) are the most widely used aerosol delivery devices to treat asthma and COPD due to its unique ability to produce numerous inhalable droplets. However the mechanism leading to droplet generation is elusive, mainly due to small length scales and short time scale, causing experimental difficulties to obtain flow information. Such lack of insight has - to date - limited predictive capability of theoretical approaches and impeded device optimisation. The main aim of this research is to improve understanding of the thermo-fluid dynamic processes leading to droplet generation by constructing validated numerical models to predict pMDI aerosol characteristics as a function of device geometry and formulation composition.

The thesis presents a systematic study of existing two-phase flow models to predict the flow conditions and the rate of propellant flow through a pMDI actuator: the homogeneous equilibrium model (HEM), the slip equilibrium model (SEM) and the homogeneous frozen model (HFM). It was established that pMDIs mainly operate under choked flow condition. The velocity predictions of the HFM were found to be in better agreement with PDA measurements than the others. A new model – the hybrid HFM or H-HFM model - was proposed to include an account of mass transfer in the spray orifice due to propellant bubble nucleation and growth. Outcomes of our novel H-HFM model in combination with nuclei population empirical correlation (Senda et al., 1994), indicates that evaporation of propellant inside spray orifice is minimal and hence model predictions are close to those obtained by HFM.

Two atomisation models were proposed to determine the aerosol droplet size. The two models describe aerodynamic atomisation and flashing atomisation, which were previously proposed as the main candidate mechanisms by Clark (1991) and Finley (2001). The aerodynamic model was based on the widely-used LISA model for the breakup of liquid films (Senecal et al., 1999). The flashing model was based on the H-HFM account of nuclei population and bubble growth in conjunction with the geometric theory of droplet formation by Sher & Elata (1977). The aerodynamic model showed good agreement with PDA measurement over 95% of mass emission. The results of the flashing model showed how it may be possible to account for a shift of the dominant atomisation mechanism from aerodynamic dominant to multimode, to flashing dominant if the nuclei population varies as a function of available superheat.

The effect of the presence of less volatile ethanol in the formulation was accounted for within the models by incorporating an empirical correlation to represent mixture vapour pressure based on experimental measurements. Large departures from Raoult's law were measured. The predicted aerosol plume velocity was almost independent of ethanol fraction within the range of practical solution formulations (5-20 w/w%), whereas the predicted droplet size showed a moderate increase with increasing ethanol concentration. Both findings were confirmed by PDA measurements.

The implementation of the above-mentioned models within a CFD methodology of pMDI aerosol generation and plume development was demonstrated. The predicted instantaneous flow rate and velocity of vapour and liquid phase as well as the droplet size were supplied as injector sources. Such representation of source enables us to define spray properties based on key physics, governing the upstream flow in pMDI actuator, rather than using assumed values or case specific experimental data. This, in turn, led to improved predictions of post-injection spray characteristics, when compared with available PDA measurements. Axial trend and magnitude of velocity and droplet size showed a good match with the measured values in the vicinity of the spray orifice.

Acknowledgement

First and foremost, I would like to express my deepest appreciation for my amazing supervisors, Mr. Henk Versteeg and Professor Graham Hargrave, for providing me this invaluable opportunity to pursue a PhD degree. Their patience allowed me not to be fearful of making mistakes, yet their guidance helped ensure I never made the same mistake twice. Since the very first moments of this work, I have been privileged to have Henk and Graham's limitless moral and scientific support, enabling me to grow as a research scientist. One could not wish for more exceptional or kind supervisors.

I am also thankful to my great friend and colleague, Mr. Ben Myatt who provided the experimental data for model validation. The enthusiasm and the fresh spirit he brought into the group, made my working environment a lot more pleasurable. Special thanks are due to my good friend and colleague, Dr. Peng Zhao, for his great input in atomisation group meetings and also the advice he gave me during the CFD phase of the research. I would also like to acknowledge Dr. Hanieh Yazdanfar's genuine and much appreciated effort during the stage of producing the final text to a standard quality.

I would also like to cease this opportunity and gratefully acknowledge the industrial partner of this project, Chiesi Farmaceutici SpA, for providing the necessary funding. Specifically my sincerest gratitude is offered to Dr. David Lewis, Mrs. Tanya Church, Mr. Gaetano Brambilla and Professor Brian Meakin for their regular discussions and scientific input. They provided me the freedom to peruse my scientific ideas and gave me guidance and self-belief to gain the necessary pharmaceutical related skills. I am highly grateful to my awesome friends Ms. Helen O'Shea, Ms. Francesca Mason and Ms. Magdalena Melerska, for their kindness and technical support during different stages of the work. They are truly amazing people to work with.

Special thanks are due to Professor Eran Sher for his invaluable advice regarding the fundamentals of flash atomization and speed of sound in multiphase medium. I also am grateful to Dr. Eric Lemmon (NIST) for his assistance and prompt responses to my questions regarding metastability and REFPROP scripting. I would also like to acknowledge the efforts and cooperation of Dr. Konstantinos Karantonis (CD-adapco), for providing me the necessary licensing for CFD code.

Beyond the world of science, I wish to thank my wonderful family and my dearest friends in Iran, the UK and the US, for their dependability and devotion as well as the emotional and moral support they have offered me during difficult moments I have encountered. It is a true blessing to have them around me.

Lastly (and undoubtedly most importantly), I would like to give my heartfelt thanks to my beloved parents, Mrs. Jaleh Behzadi and Mr. Alireza Gavtash, whose love, compassion and sacrifice has made this journey possible for me. I cannot put into words how grateful I am for their support or how proud I am to be their son. I love them from the depths of my heart and am forever indebted to them.

Dedicated to my mother,
the most precious gift that life has offered me,

and to my farther,
who has been and will always be my best and closest friend

“If I had a world of my own, everything would be nonsense.
Nothing would be what it is, because everything would be what it isn’t.
And contrary wise, what is, it wouldn’t be.
And what it wouldn’t be, it would. You see?”

Lewis Carroll, Alice in Wonderland

Contents

List of Figures

List of Tables

Nomenclature

Roman letters	Definition	Unit
$2P$	Perimeter	m
A	Surface area	m^2
a	Speed of sound	$\mathrm{m/s}$
B	Spalding mass transfer number	(-)
C_c	Single phase contraction coefficient	(-)
C_d	Discharge coefficient	(-)
c_p	Specific heat at constant pressure	$\mathrm{J/kg.K}$
D	Diameter	m
D_{10}	Arithmetic diameter	m
D_{30}	Volume mean diameter	m
D_{32}	Sauter mean diameter	m
D_g	Mass diffusion coefficient	m^2/s
d_{jet}	Jet diameter	m
E	Specific total energy	$\mathrm{J/kg}$
F	Force	N
G	Mass flux	$\mathrm{kg/s.m}^2$

g^*	Mass transfer conductance	$\mathrm{kg/m^2.s}$
H	Enthalpy	J
h	Specific enthalpy	$\mathrm{J/kg}$
h	Sheet thickness in atomisation-related formula	m
h'	Half sheet thickness	m
$\bar{h}$	Heat transfer coefficient	$\mathrm{W/m^2.K}$
i, j	Cartesian coordinates in suffix notation of flow equations	
Ja	Jacob number	(-)
k	Thermal conductivity	$\mathrm{W/m.K}$
k	Wave number in atomisation related formula	$1/\mathrm{m}$
K_s	Wave number of maximum growth rate	$1/\mathrm{m}$
L	Characteristic length	m
l_{ave}	Average distance between adjacent bubbles	m
l_t	Turbulence length scale	m
m	Mass	kg
M	Molecular weight	$\mathrm{kg/mol}$
$\dot{m}$	Mass flow rate	$\mathrm{kg/s}$
N_b	Number of bubble per liquid unit volume	$1/\mathrm{m^3}$

n_b	Number of bubbles	(-)
n_π	Number of parcels per unit volume	$1/\mathrm{m}^3$
Oh	Ohnesorge number	(-)
p	Pressure	Pa
Pr	Prandtl number	(-)
R	Radius	m
Re	Reynolds number	(-)
s	Specific entropy	$\mathrm{J/kg.K}$
S	Slip ratio	(-)
S_E	Enrgy equation source term	$\mathrm{J/m^3.s}$
S_{ij}	Mean strain rate	$1/\mathrm{s}$
S_m	Continuity equation source term	$\mathrm{kg/m^3.s}$
S_M	Momentum equation source term	$\mathrm{kg/m^2.s^2}$
Sc	Schmidt number	(-)
t	Time	s
T	Temperature	K
Ta	Taylor number	(-)
v	Specific volume	$\mathrm{m^3/kg}$

V	Velocity	$\mathrm{m/s}$
$\bar{V}$	Mean velocity	$\mathrm{m/s}$
V'	Fluctuating velocity	$\mathrm{m/s}$
Vol	Volume	$\mathrm{m^3}$
We	Weber number	(-)
x	Flow quality	(-)
x_E	Equilibrium quality/ethanol mole fraction	(-)
x_H	HFA mole fraction	(-)
x_s	Effective plume source location	m
y	Vaporisation index	(-)
y'	Droplet distortion parameter	(-)
y^+	Non-dimensional wall distance	(-)
Y_E	Ethanol mass fraction	(-)
Y_H	HFA mass fraction	(-)
z	Axial distance	m

Greek letters	Definition	Unit
α	Void fraction	(-)
α	Thermal diffusivity in chapter two	m^2/s
$\Delta\theta$	Superheat degree	K
γ	Isentropic index	(-)
δ	PIF algorithm tuning factor	(-)
δ_{ij}	Kronecker delta function	(-)
δt_d	Droplet residence time in control volume	s
ε	Turbulent dissipation rate	$\mathrm{m}^2/\mathrm{s}^3$
ϵ	Convergence parameter	(-)
η	Pressure ratio	(-)
λ	Wavelength	m
Λ	Wave length in 4-21	m
μ	Dynamic viscosity	$\mathrm{Pa.\,s}$
ν	Kinematic viscosity	m^2/s
ρ	Density	kg/m^3
σ	Surface tension	N/m
σ_ε	Turbulent Prandtl number for dissipation rate	(-)

σ_k	Turbulent Prandtl number for kinetic energy	(-)
τ	Intermediate time	s
τ_c	Droplet/eddy crossing time	s
τ_e	Eddy life time	s
τ_M	Momentum relaxation time	s
Φ	Two-phase multiplier	(-)
Ω	Disturbance growth rate in 4-22	$1/s$
ω_r	Disturbance growth rate	$1/s$

Subscripts	Definition
0	Stagnation condition in supply reservoir
∞	Far-field condition
b	Bubble
C	Chamber
c	Critical
cl	Centreline
$core$	Core of spray orifice
D	Drag

ds	Downstream
e	Exit
E	Equilibrium conditions/Ethanol
ec	Expansion chamber
eff	Effective
f	Flash
g	Gas
imp	Impossible
in	Inlet
$init$	Initial
jet	Jet related property
l	Liquid
lay	Liquid layer inside spray orifice
lig	Ligament
ls	Liquid solution
M	Metastable
max	Maximum
min	Minimum

mix	Mixture
NO	Near-orifice
NV	Non volatile
opt	Optimum
p	Parent (primary) droplet
pos	Possible
ref	Reference
rel	Relative
Res	Residual
RP	Rayleigh-Plesset
sat	Saturated
set	Settling
SO	Spray orifice
sp	Single phase
t	Throat
us	Upstream
wb	Wet bulb

Superscripts	Definition
∞	Far-field
$-$	Average value
.	First derivative with respect to time d/dt
..	Second derivative with respect to time d^2/dt^2
$*$	Non-dimensional quantity
s	Droplet surface

Acronyms	Definition
API	Aerodynamic Particle Sizer
CFC	Chlorofluorocarbon
CFD	Computational Fluid Dynamics
CMD	Count Median Diameter
DEM	Delayed Equilibrium Model
DPM	Discrete Phase Model
EIM	Eddy Interaction Model
ETAB	Enhanced-Taylor Analogy Break-up
FDA	Food and Drug Administration
GSD	Geometric Size Distribution

HEM	Homogeneous Equilibrium Model
HFA	Hydrofluoroalkane
HFM	Homogeneous Frozen Model
H-HFM	Hybrid-Homogeneous Frozen Model
HSI	High Speed Imaging
IDEM	Improved-Delayed Equilibrium Model
IFM	Internal Flow Model
IHE	Isentropic Homogeneous Equilibrium
KH	Kelvin Helmholtz
LHM	Locally Homogeneous Model
LISA	Linear Instability Sheet Atomisation
MMAD	Mass Median Aerodynamic Diameter
MMD	Mass Median Diameter
MRI	Magnetic Resonance Imaging
NHS	National Health Service
PCS	Primitive Cubic System
PDA	Phase Doppler Anemometry
PIF	Possible Impossible Flow

PIV	Particle Image Velocimetry
pMDI	Pressurised Metered Dose Inhaler
PSD	Particle Size Distribution
PSS	Pseudo Spray Source
RANS	Reynolds-Averaged Navier Stokes
RT	Rayleigh Taylor
SEM	Slip Equilibrium Model
SFM	Separate Flow Model
SST	Shear Stress Transport
SVP	Saturated Vapour Pressure
TAB	Taylor Analogy Break-up
TDR	Turbulence Dissipation Rate
TKE	Turbulence Kinetic Energy
USP-IP	United State Pharmacopoeia – Induction Port
UV	Ultra Violet
VMD	Volume Mean Diameter

Chapter One

Introduction

Chapter One: Introduction

1.1 Asthma: symptom overview

The word “asthma” has the Greek root of “aazein” meaning “to exhale with an open mouth”. It is claimed that the very first appearance of the term was in Iliad (epic and heroic Greek poem by Homerus). However the first use of asthma as medical term dates back to the documented works called “Corpus Hippocraticum” by Hippocrates (460-360 BC). Asthma is a chronic condition of human respiratory tract which can be managed but not cured.

Asthma is classified as a type of chronic obstructive pulmonary disease (COPD) occurring due to inflammation and subsequent shrinkage of the airway cross sectional area which restricts the flow of air to the alveolar sacs where O_2 and CO_2 are exchanged with the blood stream. Along with the mentioned inflammation, airways are usually blocked with excessive amount of sticky mucus (phlegm) which further confines the air flow path. This process is schematically shown in Figure 1.1. The inadequacy of inhalation air results in symptoms such as hissing and breathing difficulties, coughing (sometimes with blood) and permanent damage to the airways and lung.

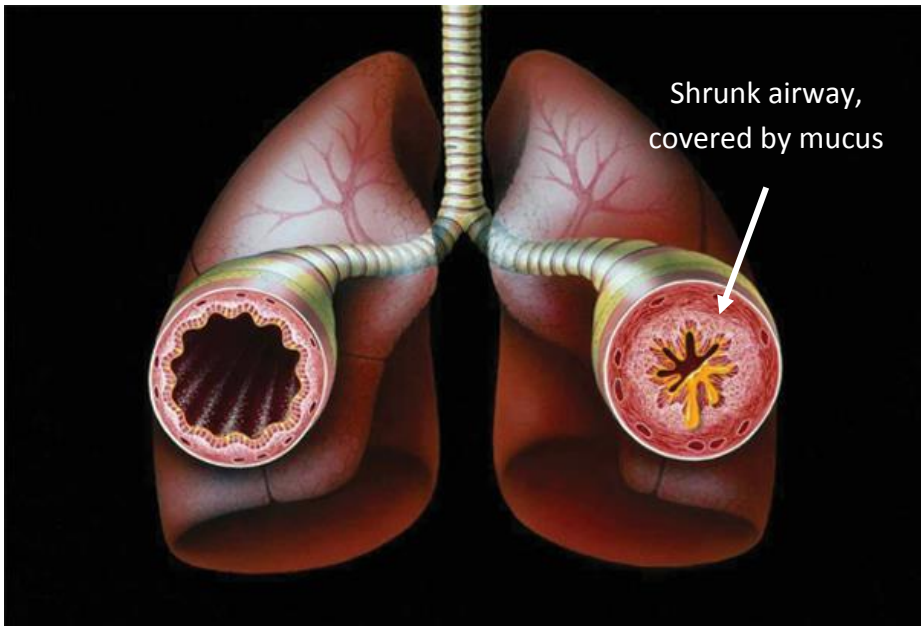

Figure 1.1 Schematic representation of (left) healthy air way in contrast with (right) asthmatic air way (Jeffery & Haahtela, 2006)

If the condition is not controlled by taking appropriate medication, severe complications may occur that require emergency hospitalisation and, in extreme cases, the condition may be lethal. During asthma, the human respiratory system is highly sensitive to and easily irritated by external triggers namely asthmatic triggers. The common triggers could be environmental dust or pollutant, cold or warm air, animal fur, moisture, chest infections or even emotional stresses. In children the main triggers of asthma are contagious and viral diseases, mainly those which cause the common cold.

Although asthma cannot be cured, there are efficient treatment methods to control the condition based upon two fundamental targets: (i) to eliminate the symptoms; (ii) to avoid the occurrence of future symptoms. This healing and prevention process requires combination of a well-adapted lifestyle, reasonable knowledge to identify and avoid possible triggers and undoubtedly effective medications.

1.2 Pressurised metered dose inhaler (pMDI)

1.2.1 Historical background

From pharmacological perspective, asthma medications are divided into two broad classes namely relievers and preventers. Relievers are those which are designed to quickly reduce the acute symptoms during an asthma attack. Preventers repair injury and reduce inflammation after the attack has happened (Clark, 1995). The delivery of both categories of compound requires a medical inhaler to generate respirable drug particles (typically below 5 μm).

Pressurised metered dose inhalers (pMDI) are known as the most efficient and widely used aerosol delivery devices in the world to treat asthma (Dolovich & Fink, 2001). Portability, light weight, pocket size in combination with device robustness, ease of operation and high dose numbers are the most notable characteristics which made pMDIs to be an attractive choice from the patients' perspective. These advantages are somewhat offset by patient-device coordination difficulties. Since the device operates in a press and fire manner, a deep (and relatively slow) inhalation must take place at the same time as the device is actuated. Accurate coordination increases the level of drug deposition in the lung and significantly reduces unwanted oropharyngeal deposition.

The initial concept of the pMDI, traces back to 1955 when a thirteen year old asthmatic girl complained about the leakage of a bulb atomiser and the complexities associated with device operation. She believed that the apparatus should be as easy to operate as a hair spray. Based up on this statement, the girl's father, Dr. George Maison (who was the scientific director of the Riker laboratories which now is part of the 3M cooperation) and his development team founded the basis of today's pMDI technology. The components of their initial prototype were a 50 µl metering device, 10 ml propellant and a mouthpiece made of plastic with a nozzle to direct the epinephrine and isoproterenol salts (Thiel, 1996). After the therapeutic level of the prototype device was assessed, eventually in March 1956 the new device application was approved by the Food and Drug Administration (FDA). This approval is seen as the starting point for a rapid technological and medical progress in the field of pMDIs. 1957 was the birth year of the first commercially available formulation with added pulmonary surfactants to the propellant to prevent alveolar collapse by surface tension reduction at alveoli interface (Freedman, 1957).

The adoption of Chlorofluorocarbons (CFCs) as pMDI propellant had a drastic impact on patients' everyday life in 1960s and 1970s. However, the widespread use of CFCs in other applications has resulted in detrimental effects associated with the potential of chlorine delivery to stratosphere and interference with the cycle of natural ozone layer creation or destruction, which protects the earth from hazardous UV radiation. A sequence of international discussions eventually led to CFCs phase out in 1987 described in the Montreal Protocol (Montreal Protocol, 1987).

CFC was widely used in pMDI formulations and the Montreal Protocol provided for a gradual reduction of its use with a dead end no later than 2010. Consequently, much work had to be done to bridge the transition stage from CFC phase out to an appropriate replacement. After comprehensive programmes of safety and efficacy testing the pharmaceutical industry settled on hydrofluroalkanes HFA134 and HFA227 (Noakes, 2002).

1.2.2 Hardware overview

A pMDI consists of the container, actuator, metering valve and formulation. Figure 1.2 shows pMDI components schematically. The container is a metal canister filled with a mixture of propellant, preservatives, surfactants and active pharmaceutical ingredient (API) or drug. Typical pMDI devices contain approximately 20 - 5000 µg of drug. The medicine is dispersed or dissolved in 10 - 100 µl metered volume. This arrangement allows the release of more than 200 actuations.

Since the propellant is under high pressure (around 6 - 8 bars), the container has to be robustly designed to withstand the generated internal stresses. Inert material must be utilised to fabricate the canister ensuring formulation chemical stability (Smyth, 2003). Lightweight materials are preferred for portability. Aluminium is the preferred choice for canister fabrication since it provides the afore-mentioned requirements (Gad, 2008). However, depending on the characteristics of formulation, coating and anodizing of the internal container surfaces might be required for two main reasons. Firstly, to avoid possible drug agglomeration on canister internal walls and, secondly, to reduce the risk of canister material degradation if ethanol is present in the propellant formulation (Klang et al., 1994).

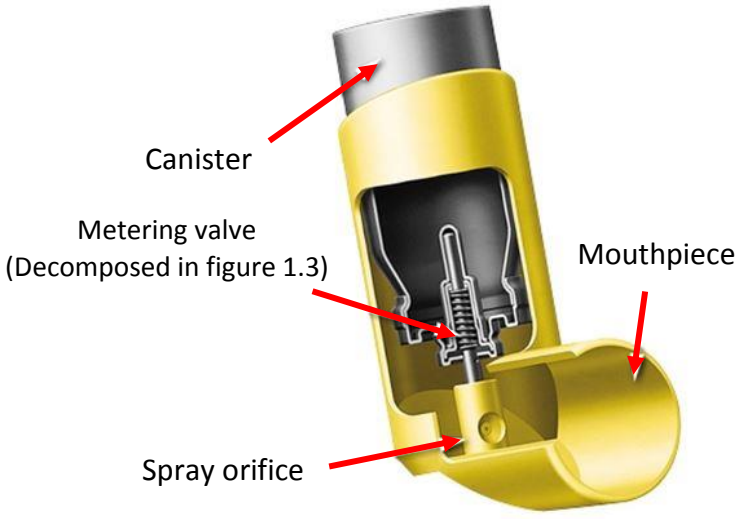

Figure 1.2 Principal components of a pMDI (Shaik, 2010)

The combination of the device body, mouthpiece and the spray nozzle, is termed as "actuator". It is a pocket size plastic envelope to hold the canister. The actuator is usually manufactured as a single piece injection moulding.

The actuator body is designed in a way to allow the metering valve stem to be depressed and emit the drug aerosol through the mouthpiece. The mouthpiece functions as the interface between the device and the patient who inhales air flow along with the drug aerosol (Dunbar, 1997). The spray nozzle diameter is a significant design parameter which mainly influences the emitted plume characteristics.

The "metering valve" isolates and delivers a specific amount of drug dose during each actuation/inhalation event. Another important function of the metering valve is to seal the high pressure propellant in the canister when the system is at rest. Although there are several available designs for a metering valve, typical components are as shown in Figure 1.3.

A mixture of API, propellant, surfactant and excipients is called the formulation. Formulations are categorised into two main classes. Solution formulations contain drug which is dissolved in the mixture of excipients and propellant, whereas suspension formulations contain the drug as suspended micro-size particles in the mixture.

The main driving force of a pMDI spray event is provided by liquefied HFA propellant, which has a low boiling point. The propellant is compressed into the liquid state and placed in the canister by either pressure filling or cold filling techniques. Compatibility with drug formulation, non-toxicity, non-flammability as well as having desirable physical properties such as density, boiling point and vapour pressure are the main requirements for a pMDI propellant (Noakes, 2002).

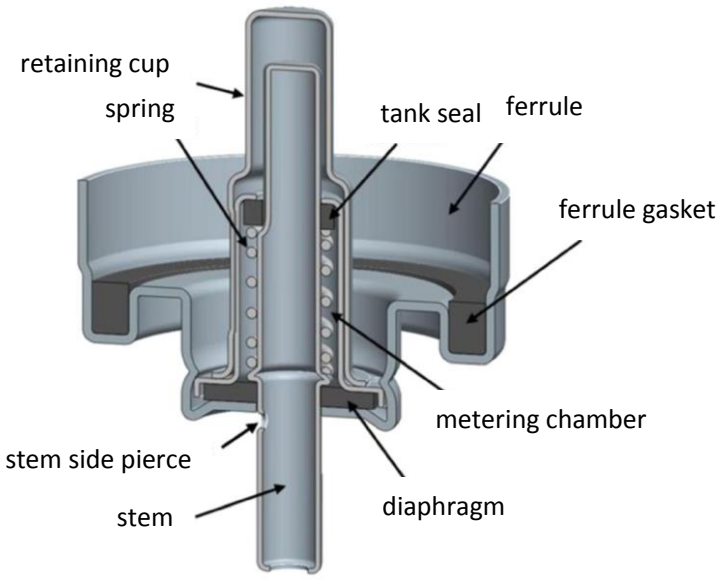

Figure 1.3 Typical components of metering valve adopted from (Stein et al., 2014)

Maintaining constant vapour pressure is one of the most significant characteristics of propellant so that consistent dosing in each actuation is guaranteed. Combinations of CFC11, CFC12 and CFC114 were the preferred choices of propellant systems due to suitable vapour pressure, appropriate chemical stability and low level of toxicity. After the banning of CFCs following the adoption of the Montreal Protocol (1987) (Mario et al., 1974) HFA134 and HFA227 were used as the substitute device propellants.

1.2.3 Operating principle

The metering valve isolates the prescribed amount of propellant and drug dose in readiness for each actuation event. As illustrated in Figure 1.4 the metering valve is connected to the canister on one side and to the spray nozzle at the other side. The connection is routed via one-way inlet and outlet valves. According to Figure 1.4, the inlet valve is open when the system is at rest and the formulation is allowed to freely flow into the metering chamber. At the end of this filling stage, the metering chamber is full (stage 1). At the start of the actuation, the valve stem moves, causing inlet valve closure which isolates the metering chamber contents (stage 2).

Subsequently, the outlet valve opens and the formulation discharges through the spray nozzle (stage 3). After the actuation is completed, the valve stem is released and returns back to its initial position by means of the valve stem spring.

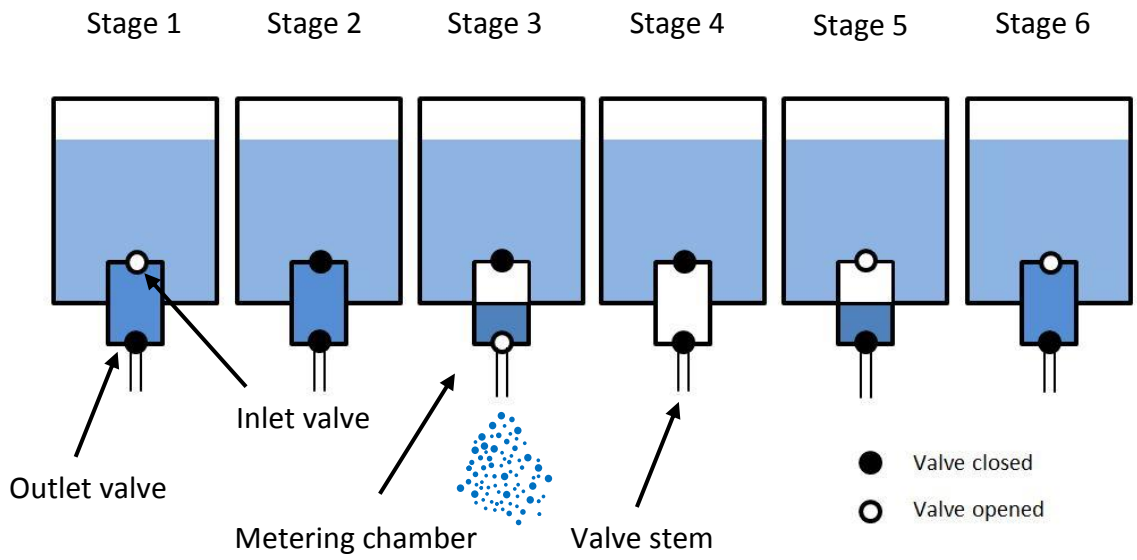

Figure 1.4 Schematic stages of actuation

This causes the outlet valve to close and the inlet valve to reopen (stages 4, 5). Consequently, the metering chamber refills and the system is ready for the next actuation event (Stage 6) (Brindley, 1999).

1.3 Aims & objectives

1.3.1 Project motivation

Although asthma is not presently curable, a range of treatments is available through which the symptoms can be satisfactorily managed, patients achieve a good quality life and can stay economically active. Nevertheless, there are still huge numbers of asthma sufferers, estimated to be over 235 million worldwide (Anon, 2016 b). The rapid increase of asthma incidence has been evident for the past decades in developed countries such as UK (Anon, 2015) and US. This has coincided with a long period of budgetary restrictions on healthcare services. There are 5.4 million people with asthma in the UK, which means asthma affects one in every 11 people and one in five households. According to the latest data in 2014, 1216 patients died from asthma. At present, the treatment related costs to the NHS is approximately £1 billion per year.

In the US about 1 in 12 people have asthma, which makes total number of 25 million sufferers nationwide. Asthma cost the US about $56 billion in medical costs, lost school and work days, and early deaths in 2007. The health care providers spend almost $9.4 billion a

year on the conditions (Anon, 2011). It is noteworthy to point out that almost half of these expenses are spent on hospitalisation required patients who suffer from acute symptoms (Singh et al., 2007).

It is likely that the number of asthma patients will continue to increase in the foreseeable future. Therefore, a comprehensive scientific understanding and research is crucial to enable product technology and treatment method improvements. Over the past decade, pharmaceutical industries have allocated significant resources to research and development to keep pace with patient needs. For example, the sponsor of this project "Chiesi Farmaceutici SpA" assigns approximately 15 percent of its turnover to research and development (Anon, 2016 a). Utilization of the current technology enables the production of pMDI devices that are capable of generating a self-propelled aerosol cloud containing a large number of particles suitable for respiration. However, the known difficulties associated with the device are (i) high velocity of the aerosol plume, (ii) significant number of large droplets and (iii) patient-device coordination problems (Shaik, 2010). One or more of the mentioned difficulties leads to unwanted oropharyngeal deposition of the drug particles, which reduces the amount of drug available in the lungs and can lead to unpleasant side effects, such as oral thrush. A comprehensive understanding of the processes leading to medical aerosol generation and transport is urgently needed to improve the therapeutic effectiveness of existing drug formulations and to enable rapid innovation. Novel understanding can be unlocked by taking advantage of the available capabilities in the areas of Computational Fluid Dynamics (CFD) applied to healthcare engineering.

The ultimate intention of the research would be to apply the new understanding that is to emerge from this research to the design and development of next-generation inhaler devices meeting the patients' requirements more effectively and conveniently.

1.3.2 Main aim of the project

The research reported in this thesis is a fundamental study of aerosol formation in pMDIs. The aim is to improve understanding of the thermo-fluid dynamic processes leading to droplet generation by constructing numerical models to predict the characteristics of the aerosol cloud as a function of device component geometry and formulation composition.

The project seeks validation of the models by means of systematic comparisons of the model outputs against Phase Doppler Anemometry (PDA) measurements carried out in the Optical Engineering Laboratory in Wolfson School of Mechanical, Electrical and Manufacturing Engineering as well as high quality data in the literature.

Numerical models of the internal flow inside the pMDI and the aerosol source will be developed; these models will be integrated via CFD codes to predict the interaction of the aerosol plume and inhaled air flow. The outcome of the research may serve as the starting point for the evolution of inhaler actuator designs for improved respiratory dose delivery.

1.3.3 Objectives

1. Carry out comprehensive literature review of pMDI technology and of theoretical aspects of the prediction of primary atomisation processes and aerosol plume development
2. Develop theoretical models of (i) thermo-fluid dynamic processes of two-phase propellant flow inside the metering valve and actuator, and, (ii) aerosol formation to capture plume characteristics (e.g. drop size, velocity, flow quality, etc.) as a function of actuator geometric parameters, formulation composition and time.
3. Improvement of spray source description on the basis of item 2, including physical phenomena governing upstream propellant flow inside the actuator
4. To construct CFD model based on item 3 to demonstrate the capability of spray source-air flow interaction
5. An in-depth analysis of the findings of theoretical studies and validation against available experimental data.
6. Draw main conclusions and highlight recommendations for further work.

1.4 Thesis outline

It should be noted that, in the chapters containing original work and contributions to the knowledge, the structure of presentation is as follows: each chapter starts by introducing a conceptual description and image of each model followed by mathematical representations of the model. Once the model is introduced, relevant test cases are described. Next, results for these test cases are provided and validated against high-quality measurement available in public domain or as findings of a parallel experimental project that has been conducted

alongside this numerical/theoretical study. Chapters finish with a discussion to provide further understanding and highlight strengths and weakness of the models.

- Chapter two: This chapter contains the review of the scientific literature on various areas which are directly or indirectly related to the field of pMDI. This includes the topics of (i) two-phase flashing flow models in tubes and apertures, (ii) aerodynamic and flashing atomisation, (iii) proposed mechanisms of pMDI atomisation and, finally, (iv) key literature on the use of CFD in the modelling of pharmaceutical spray injection into flowing or stagnant medium to study interactions between spray and surroundings.
- Chapter three: In this chapter the development of the internal flow model (IFM) of flashing propellant inside twin-orifice system of pMDI is described. Alternative one-dimensional models are assessed based on various scenarios of mass, momentum and heat transfer between vapour and liquid phases, to identify the most applicable model to pMDIs. Predicted spray velocity is validated against PDA measurements for different propellant systems.
- Chapter four: This chapter focuses on developing theoretical models to predict droplet size issuing from a pMDI. Unlike previous approaches, which require tuning of the models by means of adjustable constants, our developed model can predict the final size based on fluid properties and actuator geometric parameters. Theoretical models are constructed of (i) aerodynamic primary atomisation and (ii) flashing primary atomisation followed by secondary aerodynamic fragmentation. The predicted droplet size values are validated against PDA measurements.
- Chapter five: The effect of ethanol content in the propellant formulation is investigated in this chapter. Novel theoretical models of multicomponent mixture flow and atomisation in a pMDI actuator are constructed. The theoretical models include a semi-empirical model of the mixture saturated vapour pressure (SVP) to represent the non-linear behaviour of this quantity as a function of ethanol fraction in mixture. The model predictions of spray velocity and droplet size are validated against PDA measurements.
- Chapter six: This chapter describes the methodology, according to which, more realistic CFD simulations of pMDI aerosol generation and plume development can be

conducted. Our method includes improved definition of spray source on the basis of (i) time-dependent source properties such as velocity, mass flow rate, droplet composition, and (ii) statistical representation of instantaneous droplet size distribution. This is achieved by setting up a demonstration case in the commercial CFD code Star-CCM+, which links the outcomes of the internal flow model (chapters three and five) and the atomisation model (chapter four) through multiple JAVA scripts. Where possible, opportunities were taken to validate the CFD results against PDA measurements of aerosol plume velocity, droplet size and droplet size distributions.

- Chapter seven: This chapter closes the thesis by providing a brief summary of the research work and highlighting the key contributions to original knowledge. Recommendations are made for further works to broaden and deepen the study of this scientific problem.

Chapter Two

Literature Review

Chapter Two: Literature Review

2.1 Introduction

The main characteristic of pMDIs as an inhalation drug delivery method is the capability to produce an aerosol consisting of large numbers of droplets within the respirable size range (below 5 μm). Despite having been on the market for more than half a century, the physical processes that lead to the formation of therapeutic droplets are still poorly understood. What is known is that the atomisation mechanism is highly transient and involves complex interaction of aerodynamic forces and thermo-fluid dynamic effects causing the fragmentation of liquid bulk. Two possible effects have been previously identified as candidate mechanisms, namely (i) air-blast like atomisation and (ii) propellant flashing (Clark, 1991; Finlay, 2001; Versteeg & Hargrave, 2006). The former consist of growth of wave like instabilities on different liquid segments, such as jet, sheet or a droplet, leading to fragmentation of the liquid segment into smaller sub-segments. The latter is caused by rapid depressurisation and, hence, superheating of liquid leading to the formation of tiny vapour embryos. These embryos grow in size and, when they are sufficiently large, a regime change from liquid continuous to vapour continuous takes place. The resulting liquid fragments reorganise themselves into droplets. This chapter presents a general literature review on aerodynamic and flashing atomisation mechanisms and also surveys the literature concerning the atomisation mechanisms that have been proposed specifically for pMDIs.

Thermofluid dynamics of two-phase flashing propellant inside the twin-orifice system of the pMDI also plays a significant role in determining the characteristics of the therapeutic aerosol such as droplet size and droplet velocity. It is understood that propellant expansion and emitted mass flow rate in a pMDI occurs in the critical (choked) flow regime for a substantial fraction of the actuation event. Additionally, towards the end phase of the actuation, flow dynamics is in the sub-critical (un-choked) regime. Thus research work covering two-phase flashing flow through tubes and apertures has been reviewed.

In the field of aerosol delivery devices the use of computational modelling has undoubtedly been valuable to understand the inhaled air flow pattern in the human airways as well as particle dynamics. This has played a significant role in the optimisation of inhaler device functionality by predicting parameters affecting the fate of the particles. The final section of

this chapter gives a review of notable CFD simulations of pharmaceutical sprays and their interaction with surrounding air and, where applicable, enclosure geometry. These interactions include plume-wall impingement or plume-air entrainment.

2.2 Two-phase flashing flow through tubes and apertures

Flow regime dynamics as fluids travel through apertures may be either sub-critical or critical. Critical flow (also known as choked flow) is a limiting condition of mass flow rate. This condition prevails when the mass flow rate does not increase as the pressure of the downstream environment further decreases, while upstream pressure is fixed. Such a condition occurs when the velocity of fluid at the exit plane of an aperture reaches the sonic velocity and the Mach number becomes unity (Hewitt, 2013). Much research has been carried out to study two-phase critical flow through tubes and orifices. Studies were mostly related to safety issued in nuclear industry. Wallis (1980) and Elias & Lellouche (1994) presented comprehensive reviews of the key experimental results and theoretical models. Here we review the key papers which have contributed to theoretical developments in critical two-phase flow.

Theoretical models were developed on the basis of thermodynamic equilibrium and thermodynamic disequilibrium assumptions as well as homogeneous and non-homogeneous two-phase flow regimes. The Homogeneous Equilibrium Model (HEM) was originally named as Isentropic Homogeneous Expansion (IHE) model and developed for low quality and high pressure steam-water flow in converging-diverging nozzles. Starkman et al. (1964). The model also assumes that both phases are at thermal equilibrium and isentropic expansion of the gas phase takes place between the supply reservoir and the nozzle throat. The mass flow rate in subcritical regime can be evaluated as a function of two-phase mixture thermodynamic properties, by means of equation 2-1:

$$G_t = \frac{1}{\bar{v}}\sqrt{2(\bar{h}_0 - \bar{h})} \qquad 2\text{-}1$$

In this expression G_t is the throat mass flux (kg/s.m^2), $\bar{h}$ is two-phase mixture enthalpy (J/kg) where subscript 0, denotes the stagnation condition, $\bar{v}$ is the two-phase mixture specific volume (m^3/kg). By numerical maximisation of equation 2-1 for range of downstream

pressure conditions, the critical mass flux is determined. The range of quality and pressure explored in Starkman's work was 0-0.2 and up to approximately 7 MPa, respectively. Based on model predictions for two-phase mixture of steam-water, the HEM was shown to be appropriate for the prediction of the critical mass flux in long tubes where flow has sufficient residence time to achieve equilibrium condition (Ardron & Furness, 1976).

As an extension to the HEM, the first non-homogenous equilibrium model was put forward by Moody (1965). This model is known as the slip equilibrium model (SEM). The flow inside the nozzle is assumed to take place in the annular regime, where vapour and liquid phases travel with different velocities. The velocity difference is characterised by the slip ratio $S = V_g/V_l$ in which V_g and V_l are gas phase and vapour phase velocities. Moody also assumed that both phases are at thermal and thermodynamic equilibrium. The model treats the slip ratio as an independent variable, which is determined by the following assumptions: no momentum transfer and maximum kinetic energy flux at the exit. This leads to the following expression for the slip ratio as a function of the ratio of the liquid phase and vapour phase densities (i.e. ρ_l and ρ_g):

$$S = \left(\frac{\rho_l}{\rho_g}\right)^{\frac{1}{3}} \qquad 2\text{-}2$$

The model predicted the maximum flow rate of steam/water for pressures ranging between 0.17-21 MPa and flow quality between 0.01 and 1.

Henry (1968) developed a theoretical model for one-dimensional, steady two-phase flow in a constant area duct with evaporation. Homogenous flow regime and incompressibility of liquid were the key modelling assumptions. The model further assumes that friction can be neglected, so the pressure drop is caused by flow acceleration. Neglecting of frictional losses, results in a reversible process, so flow variables will change under isentropic conditions. The following expression is obtained for the critical mass flux:

$$G_t = -\left(\left[x_E\left(\frac{dv_g}{dp}\right)_s + (v_g - v_l)\left(\frac{dx_E}{dp}\right)_s\right]_e\right)^{-1/2} \qquad 2\text{-}3$$

Where v_g and v_l are gas phase and liquid phase specific volumes. x is the flow quality (ratio of the vapour mass to total mass of the two-phase mixture). Subscripts s and e correspond to isentropic conditions and the location of the exit of the orifice, respectively. Subscript E, denotes the equilibrium condition. As a further step to improve model predictions, Henry (1970) introduced a non-equilibrium coefficient N, defined as the ratio actual flow quality to equilibrium flow quality ($N = x/x_E$). Values of N were determined experimentally, having the following range:

$$N = 20x_E \quad for \quad x < 0.05$$
$$N = 1 \quad for \quad x > 0.05 \qquad \text{2-4}$$

By further assuming that the vapour expansion followed polytropic process with an exponent of order 1 (i.e. approximately isothermal), equation 2-5 for the two-phase mass flux was obtained:

$$G_t = -\left(\left[\frac{xv_g}{p} + (v_g - v_l)N\left(\frac{dx_E}{dp}\right)_s\right]_e\right)^{-\frac{1}{2}} \qquad \text{2-5}$$

Where the derivative of equilibrium flow quality was given by:

$$\left(\frac{dx_E}{dp}\right)_s = -\left[\frac{(1-x)\frac{ds_l}{dp} + x\frac{ds_g}{dp}}{s_g - s_l}\right]_E \qquad \text{2-6}$$

Subscript E indicates that all properties and derivatives should be calculated along saturation line corresponding to local exit pressure. For tubes with a sharp edged entrance and L/D (length to diameter) ratios, ranging between 12-100, Henry (1970) proposed that little evaporation takes place up to L/D = 12. This applies to the cases when initially subcooled or saturated liquid enters the tube. Further downstream the mixture flashes and two-phase mixture quality relaxes in an exponential manner towards the tube exit state. Comparisons between the model predictions and available experimental measurement for nozzles and short tubes with water, nitrogen and carbon dioxide as working fluid, showed that the model was in good agreement over a wide range of stagnation conditions. However

for longer tubes, the model over predicts the mass flow rate and hence is not recommended (Wallis, 1980).

Henry & Fauske (1971) argue that the pressure decreases abruptly at the exit plane of the nozzle. So coefficient N for nozzle flow is different to that one corresponds to constant area duct. Therefore, definition of N in equation 2-4 is evolved to the following expression to be applicable to nozzle flows where pressure gradient at the exit is largest:

$$N = x_E/0.14 \quad for \quad x < 0.14$$
$$N = 1 \quad for \quad x > 0.14 \qquad 2\text{-}7$$

The predicted critical flow rate was compared against those of predicted by HEM and HFM as well as sets of available experimental measurements of steam-water (Maneely, 1962; Neusen, 1962) for stagnation pressure of 3.5 MPa. The new model showed best agreement with data across a wide quality range of 0.001 to 0.1.

Lackme (1979) recognized that liquid metastability is one of the key factors which can bring theoretical predictions of critical mass flow rate closer to experimental measurements. For adiabatic and frictionless flow of a superheated liquid through tubes, Lackme (1979) developed a model of critical mass flux prediction. The model incorporates the existence of metastable states between the saturation pressure, p_{sat} and onset of boiling pressure, p_{boil} and was applied to the flashing of hot water at pressures less than 0.2 MPa. Based on examination of experimental measurements of inlet pressure and boiling pressure the following empirical correlation can be deduced for p_{boil} estimation:

$$p_{boil} = k_{met} p_{sat} \qquad 2\text{-}8$$

where k_{met} has a range of 0.95-0.97. Liquid metastability was taken into account by introducing the vaporisation index, y, which was defined as the fractional mass of metastable liquid which is transformed into saturated vapour. Lackme (1979) calculates y based on graphical representation of critical conditions on p-v plane. Model predictions highlighted the role played by metastability as almost 90% of liquid is predicted to be superheated when it is expelled from a tube. Good agreement was achieved between model prediction and measured two-phase void fraction data. Additionally a simple and

compact form of a relationship between the mass flux, the pressure at the onset of boiling and the effective critical quality was developed. This model neglected the length of the portion of the duct with two-phase flow compared with the total length of the duct, as the length of the flashing zone was short in compare to length of the tube.

Based on the work of Lackme (1979), a novel theoretical model for two-phase critical flow of water through a crack was developed by Feburie et al. (1993), so-called the delayed equilibrium model (DEM). The model took into account the existence of metastable liquid in the crack as well as the effect of the two-phase flow pattern. Correlations regarding friction and heat transfer were used for model development. However, none of the empirical parameters were tuned when predictions of mass flux were compared against experimental data; neither in the single-phase flow regime, nor in the two-phase flow regime. The flow through the crack evolves in two stages. Firstly, single-phase liquid flow exists near the crack inlet and expands to a point section where nucleation starts. The nucleation occurs at location where water is superheated and below the saturation pressure. Subsequently, vapour bubbles expand and eventually coalesce into larger bubbles. The fluid was modelled as an interpenetrating continuum of three constituents: saturated liquid, saturated vapour and metastable liquid with no slip between liquid and vapour phases. The following relaxation equation was used to represent the changes in vaporisation index, y in the flow direction, i.e. along the crack:

$$\frac{dy}{dz} = k_y \frac{2P}{A}(1-y)\left[\frac{p_{sat}-p}{p_c-p_{sat}}\right]^{0.25} \qquad 2\text{-}9$$

Where $p_c$is critical pressure and $p_{sat}$is saturation pressure. $2P$ is the perimeter of the crack, A is its cross-sectional area and k_y is an empirical constant, which is evaluated based on a cylindrical pipe geometry to be 0.02. Eventually p is the pressure at location z. This relation expresses that dy fraction of liquid which is transformed from metastable to the saturated liquid phase per unit length is proportional to the remaining fraction of metastable liquid $(1-y)$ as well as a non-dimensional difference between the saturation pressure and the local pressure. The results showed very good agreement with the experimental data in terms of pressure drop along the crack and released mass flux for subcooled inlet conditions. However the model was not capable of incorporating saturated/two-phase inlet conditions.

Giot et al. (1994) extended Feburie's model and made it applicable to all inlet conditions prevailing in steam generator tubes from subcooled liquid and to superheated vapour. Metastable liquid was assumed to undergo isentropic evolution. Giot et al. (1994) included heat transfer between the wall and the fluid for the geometry under consideration. Predictions of mass flow rate were found to be more accurate when metastability was accounted for compared with the results of equilibrium models.

Attou and Seynhaeve (1999) developed a theoretical model of steady-state adiabatic flashing steam/water flow through a pipe. Two physical flow models were considered. Firstly the homogeneous equilibrium model (HEM) and secondly the improved delayed equilibrium model (IDEM). HEM vaporisation is an instantaneous process and takes place when the local pressure reaches saturation pressure. The IDEM model uses a modified relaxation equation, which is valid for initial conditions of subcooled liquid near the saturation state as well as two-phase mixtures:

$$\frac{dy}{dz} = k_y \frac{2P}{A}(1-y)^2 \left(\frac{V_{in}}{V}\right)^{0.1} \left[\frac{p_{sat}-p}{p_c - p_{sat}}\right]^{0.25} \qquad 2\text{-}10$$

In this equation V_{in} and V are the inlet and local velocities, and $k_y$is selected as 0.001. The velocity ratio in this equation is always below unity due to flow acceleration and incorporates an additional delay of vaporisation due to acceleration of the mixture. A systematic comparison of experimental mass flow rates and pressure profiles with results of HEM and IDEM showed that metastability of the liquid phase plays a significant role. The predictions of the IDEM compared favourably with the experimental data especially for inlet conditions close to the saturated state.

According to the materials presented here, it is conclusive that reasonable prediction of two-phase mass flow rate through tubes is strongly dependent on realistic considerations of interphase phenomena along flow path. This includes detailed information of rate of change in mass, momentum and heat between flow phases. In the case where such information is unavailable (such as flashing flow through pMDI actuator) extreme scenarios of interphase phenomenon can provide deeper understanding of flow characteristics.

2.3 Primary atomisation

2.3.1. Aerodynamic atomisation

Term “spray” is described as a dispersion of liquid particles in the surrounding environment containing adequate momentum to provide significant penetration (Yule & Dunkley, 1994). Droplet formation is a result of atomisation, which is the process of bulk fluid fragmentation as a result of external and internal forces during the interaction between liquid segments and the continuous medium. Disintegration takes place when the disruptive forces on the fluid overcome the cohesive forces within the bulk liquid. Here we provide a review on the key aspects of the atomisation mechanism of jet and sheet flow streams. It should be noted that sheet atomisation (2.3.1.3) is the area which is directly implemented in current research. However for the sake of completeness and maintaining continuity in the reviewed material, here we deliver brief overview on liquid jet atomisation as well.

2.3.1.1 Non-dimensional groups

Atomisation is governed by V_{rel}, which is the relative velocity between the surrounding gas and liquid segment, ρ is density, σ is surface tension and μ is the viscosity. L is the characteristic length of the physical phenomena such as droplet diameter, jet diameter or sheet thickness. The relative significance of forces acting on any liquid segment can be quantified by non-dimensional numbers based on these governing parameters. The most widely used dimensionless groups are summarised in Table 2.1.

The Reynolds number, Re, quantifies the relative importance of the viscous forces compared to inertial forces. It is a metric to classify flow in terms of level of internal disturbances resulting in the three well-known flow regimes laminar, transitional or turbulent.

The Weber number, We, expresses the ratio of disruptive aerodynamic forces to the restoring surface tension forces. It is an indicator to distinguish primary and secondary atomisation regimes.

Ohnesorge number, Oh, (also denoted as Z), is a stability metric quantifying the importance of liquid viscous forces to surface tension forces. It is generally known that atomisation quality is poor at high Ohnesorge numbers as strong viscous effects lead to pronounced damping of liquid instabilities (Yule & Watkins,2005).

Group name	Symbol	Definition	Equation
Reynolds	Re	$\frac{\text{Inertia}}{\text{Viscouse}}$	$\frac{\rho L V_{rel}}{\mu}$
Weber	We	$\frac{\text{Inertia}}{\text{Surface tension}}$	$\frac{\rho L V_{rel}^2}{\sigma}$
Ohnesorge	Oh	$\frac{\sqrt{\text{Weber}}}{\text{Reynolds}}$	$\sqrt{\frac{\mu^2}{\rho L \sigma}}$

Table 2.1 Common non-dimensional groups used in atomisation community

2.3.1.2 Atomisation of liquid jets

When a liquid column is injected out of a nozzle into a still or moving ambient gas, a competition starts between disruptive aerodynamic forces and the surface tension. The aerodynamic forces tend to excite perturbations of the liquid surface acting against the surface tension force, which tends to hold the bulk fluid together. Viscous forces generally tend to stabilise the liquid geometry. Fluid disintegration takes place as a result of augmentation of perturbations and oscillations on the surface of the liquid. This process is referred to as primary atomisation which usually occurs close to the nozzle region.

Such phenomena have been extensively researched from a theoretical and experimental point of view for probably more than a century. Much work has been carried out to understand the characteristics of the liquid jet at the point of disintegration by examining (i) jet continuous length (providing a metric of disturbance growth rate) and (ii) final droplet size (providing a metric to quantify wave number of the most unstable disturbance).

According to the comprehensive review on jet disintegration by Lefebvre (1980), the earliest investigations in this area were initiated by Bidone (1829) who was interested in topological characteristics of jets released by non-circular nozzles. It was concluded that the break-up length of the jet is directly proportional to the jet velocity for a given fixed jet diameter. It

was also reported that the break-up length is proportional to jet diameter for a given jet velocity.

The mathematical analysis conducted by Rayleigh (1878) studied the amplification of small disturbances and derived a necessary condition for disintegration of low speed jets. The theoretical work was based on a comparison of the surface energy of the disturbed and undisturbed liquid columns. For the case of an inviscid jet, Rayleigh concluded that any disturbance of a liquid jet with a wavelength greater than the jet circumference grows. His results further demonstrated that the disturbance with the fastest growth rate is the one that is responsible for jet break-up. The average droplet size corresponding to the volume of the segments of the liquid jets produced by the fastest growing disturbance is almost twice the diameter of original jet:

$$D_d = 1.89 d_{jet} \qquad \text{2-11}$$

Rayleigh's finding is known to be a widely valid first approximation (Lefebvre, 1980). Weber (1931) extended Rayleigh's analysis by including the influence of viscosity. It was assumed that any disturbance will cause symmetrical oscillations on the jet with the diameter of d_{jet}. In this case if the wavelength of the initial disturbance is below a threshold value of λ_{min}, it will dampen out due to the opposing action of the surface tension forces. On the other hand, if the initial wavelength is larger than λ_{min} surface tension forces amplify the disturbance leading to liquid break-up. One specific wavelength again produces the largest growth rate of disturbances and is, therefore, the most favourable for generation of droplets so-called optimum wavelength, λ_{opt}. Values of λ_{opt} and λ_{min} for viscous and inviscid jets are summarised in Table 2.2:

Wavelength	Viscous flow regime	Inviscid flow regime
λ_{min}	πd_{jet}	πd_{jet}
λ_{opt}	$\sqrt{2}\pi d_{jet}(1+3Oh)$	$\sqrt{2}\pi d_{jet}$

Table 2.2 Optimum wavelengths calculated for viscous and inviscid jets

Ohnesorge (1936) provided the first classification of jet disintegration regimes based on non-dimensionalised Reynolds (Re) and Ohnesorge (Oh) numbers. Using photographic records of jets at the point of disintegration, the observations were classified with reference to significance of inertial, gravitational, surface tension and viscous forces. It was shown that, judging by the rapidity of droplet formation, three different mechanism of jet disintegration occur, based on variations in magnitude of Oh and Re numbers:

- Low Reynolds number: jet breaks-up into relatively large and fairly uniform droplets.
- Intermediate Reynolds number: oscillation of the jet axis governs the disintegration. The magnitude of oscillation increases until completed break-up is achieved. Droplets with a wide range of sizes are produced.
- High Reynolds number: complete atomisation with short break-up length is achieved with product droplets having much smaller size compared with previous two regimes.

In more recent research, Reitz (1978) used previously published data as well as his own to classify disintegration modes based on increasing injection velocity into four regimes:

- Rayleigh breakup: accounts for breakup at low jet velocities. Growth of axisymmetric oscillations on the jet surface induced by surface tension, are responsible for breakup of the liquid core. This regime forms droplets with a size that is larger than the jet diameter.
- First wind-induced break-up: the influence of surface tension is enhanced by aerodynamic excitation due to the relative velocity between the liquid jet and the surrounding gas. This relative velocity causes a local pressure distribution on the jet,

which in turn accelerates the break-up process. Droplets formed by this regime have similar diameters to the jet diameter.

- Second wind-induced break-up: unstable growth of surface waves on liquid jet with short wavelength is the mechanism responsible for generation of droplets. Wave growth is opposed by surface tension forces. The resulting droplet size is much smaller than the jet diameter.
- Atomisation: breakup occurs directly at the nozzle orifice exit plane. The process results in droplets that are much smaller than the original jet diameter.

These regimes are shown in the diagram of Figure 2.1 and the proposed transition criteria are summarised in Table 2.3 based on the work of (Reitz, 1978). In the table We_l and We_g are Weber numbers based on liquid and gas densities, respectively.

Break-up Regime	Velocity (m/s)	Break-up length (L_{bu}/d_{jet})	Droplet diameter (D)	Weber number (We)
Rayleigh	$0-5$	$10-110$	$D > d_{jet}$	$We_l > 8$ $We_g < 0.4$
First wind-induced	$5-10$	$110-60$	$D = d_{jet}$	$0.4 < We_g < 13$
Second wind-induced	$10-18$	$60-100$	$D < d_{jet}$	$13 < We_g < 40.3$
Atomisation	>18	0	$D << d_{jet}$	$We_g > 40.3$

Table 2.3 Different regimes of liquid jet atomisation, typical velocity, breakup length and transit Weber number (Reitz, 1978)

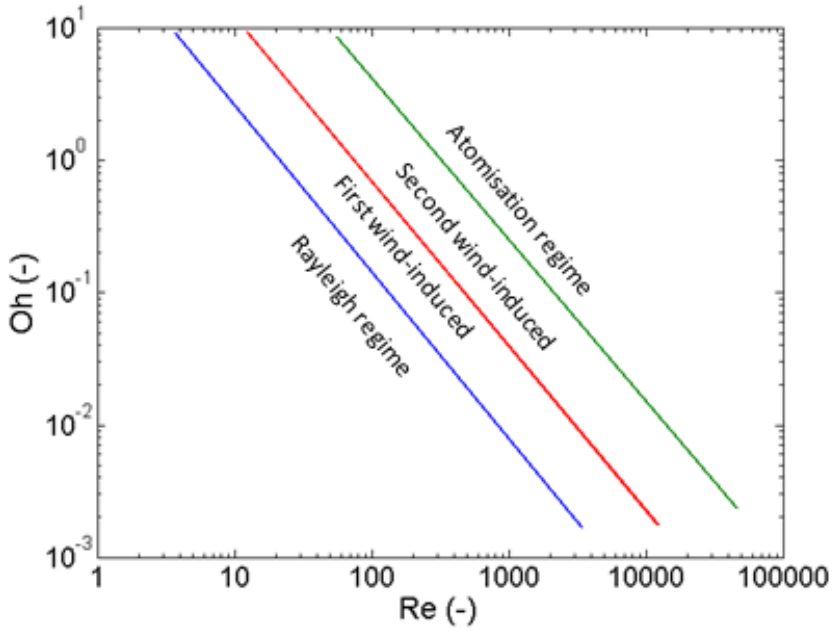

Figure 2.1 Different regimes of liquid jet atomisation as function of Oh and Re numbers after (Reitz, 1978)

2.3.1.3 Atomisation of liquid sheets

If a liquid sheet issues from a nozzle, its later development is governed by the initial sheet velocity as well as physical properties of the gas and liquid. Fraser et al. (1963) identified three distinct modes of sheet disintegration namely: rim, perforated and wave disintegration regimes. In the rim mode, surface tension forces contract the free edge of the sheet into a thick rim which disintegrates further due to jet break-up. This mode is dominant when the viscosity and surface tension of the sheet are high and produces large droplets along with numerous satellite droplets. In the perforated mode, irregularly shaped holes appear on the liquid sheet. These holes grow rapidly in size until the liquid portions of adjacent holes coalesce and form a thick rim. This rim will then disintegrate into droplets of various sizes. Disintegration can also happen as a result of wave propagation on the liquid sheet. In this case, areas of the sheet proportional to half of the oscillation wavelength are detached from the sheet and reorganise themselves into spherical droplet due to surface tension forces.

According to the studies of York et al. (1953) and Dombrowski & Johns (1963) the main mechanism of sheet break-up is the generation of wave-induced instabilities at the interface of liquid and gas phases. As a result of fluctuations in gas and liquid local pressure and velocity, infinitesimal disturbances in the form of waves are generated on the liquid sheet surface. These waves may be either damped, in which case they die away, or, alternatively, may overcome the surface tension forces and grow further in amplitude. The most unstable disturbance has the largest growth rate and, hence, is responsible for sheet disintegration. Eventually sheet disintegration leads to separation of droplets from the liquid bulk. York et al. (1953) conducted a theoretical study of sheet disintegration considering a two-dimensional infinite sheet with a finite thickness. Using calculated local velocities around the disturbed sheet, it was observed that under certain conditions, the disturbance amplitude exponentially grows. It was then concluded that such disturbances are the most dominant ones causing sheet disintegration.

Squire (1953) performed an instability analysis of an inviscid moving liquid film through a stagnant medium. Wave induced instabilities on the liquid surface were considered to be responsible for sheet breakup. The wavelength that is responsible for sheet disintegration (so called optimum wavelength) is the one with maximum growth rate. For $We_g \gg 1$ the wave number K_s, corresponding to the maximum growth rate is obtained by equation 2-12:

$$K_s = \frac{\rho_g V_{rel}^2}{2\sigma} \qquad 2\text{-}12$$

In which V_{rel} is the relative velocity between moving sheet and surrounding gas. Hence optimum wavelength can be calculated using equation 2-13:

$$\lambda_{opt} = \frac{2\pi}{K_s} \qquad 2\text{-}13$$

And

$$We_g = \frac{\rho_g V_{rel}^2 h}{\sigma} \qquad 2\text{-}14$$

Where h is the thickness of the sheet. The maximum growth rate can be worked out using the relation below:

$$\omega_{max} = \frac{\rho_g V_{rel}^2}{(\sigma \rho_l h)^{0.5}} \quad \text{2-15}$$

Fraser et al. (1963) extended Squire's theory to predict the droplet size produced by a low viscosity fan spray sheet. The work assumes the existence of an intermediate stage of unstable ligament formation prior to droplet generation. The wave with maximum growth rate is assumed to detach from the front edge in a form of two cylindrical ligaments per wavelength. The wave number corresponding to the fastest growing wave is calculated from equation 2-12. The diameter of the cylindrical ligament, d_{lig} is:

$$d_{lig} = \sqrt{\frac{4h}{K_s}} \quad \text{2-16}$$

Taking advantage of Rayleigh's analysis (Rayleigh, 1878) the diameter of the droplets generated by the collapse of the ligament can be worked out by using equation 2-11 where the jet diameter is replaced by the ligament diameter:

$$D_d = 1.89\, d_{lig} \quad \text{2-17}$$

Mechanism of sheet disintegration by impaction of liquid sheet by a high velocity air flow was also investigated by Fraser et al. (1963). In their study of flat liquid sheets formed by means of a spinning cup, the atomisation air was introduced through an annular gap located axially symmetrically to the cup. It was observed that wave-induced instabilities formed at the point of air-to-sheet impaction. The existence of an intermittent stage of unstable ligament formation prior to droplet generation was also confirmed.

The influence of the initial sheet thickness on spray characteristics was studied by Rizk and Lefebvre (1980) who used air blast atomisers that were capable of forming flat liquid sheets across the centreline of a two-dimensional air duct. The liquid sheets were exposed to high velocity air from both sides. It was concluded that high values of flow rates and liquid viscosity resulted in the formation of thicker film. It was further reported that thin liquid

films break down to droplets, following the relation of $SMD \propto d_{so}^{0.4}$, where SMD is Sauter mean diameter and subscript SO, denotes spray orifice. This relationship was also confirmed by a separate study by (El-Shanawany & Lefebvre, 1980).

Rizk and Lefebvre (1984) used high-speed flash photography with time increments of 0.2 μs to further investigate sheet disintegration and subsequent droplet formation. A similar mechanism to that proposed by York et al. (1953) and Dombrowski & Johns (1963) was observed in experiments using water as the working fluid and air velocity of 55 m/s. This includes the formation of wave-like instabilities due to interaction of water and air, followed by the formation of unstable liquid ligaments and lastly the formation of droplets. It was also seen that the process of liquid sheet disintegration accelerates and ligaments form closer to the atomiser lip by increasing the air velocity to 91 m/s.

The breakup length of liquid sheets was studied by Arai and Hashimoto (1986), by injecting liquid sheets into co-flowing air. The break-up length is determined based on an average of many observations. It was observed that for a constant sheet thickness, the breakup length decreases by increasing relative velocity between liquid and air. The breakup length showed inverse relation with the liquid viscosity.

In a recent review, Ashgriz (2011) and co-workers provide a comprehensive picture regarding the mechanism of sheet breakup. This review includes the linear and nonlinear instability of a viscous and inviscid liquid sheet, showing the effect of the aerodynamic forces on the growth rate of the initially small perturbations. It appears that nothing new has emerged to significantly change the perception of sheet breakup mechanism and more recent works just developed much more fine details. Nevertheless the materials in section 2.3.1.3 are appropriate context for the current work.

2.3.2 Flash atomisation

Flashing is generally referred to as the development of significant amounts of vapour voidage in a liquid flow as a result of rapid depressurisation. An initially subcooled liquid may become superheated if the pressure drop is large enough for the local pressure in the nozzle throat to fall below the saturation pressure corresponding to the temperature of the fluid. This results in formation of large numbers of small bubbles. These bubbles may grow

rapidly in number and size. Depending on the flow condition or nozzle geometry, flashing can occur either inside or outside of the nozzle. The subsequent fragmentation of bulk liquid is called flash atomisation and is characterised by formation of large numbers of small droplets and usually a wide spray angle. In practical systems, the liquid does not initially contain bubbles, and therefore nucleation is needed to ensure spray formation.

2.3.2.1 Nucleation

Once a liquid is superheated, fluctuations of its thermodynamic properties can result in spontaneous phase transition from the metastable superheated state to a stable two-phase state. Depending on the degree of superheat, there are two types of nucleation processes by which an embryo bubble can be formed: heterogeneous and homogeneous nucleation (Schmelzer, 2003; Lubetkin, 2003). Once the embryo is born, it will grow in size further if its initial size is larger than (or equal to) the critical value of R_c, as estimated by equation 2-18. Otherwise the embryo collapses.

$$R_c = \frac{2\sigma}{p_g - p_\infty} \qquad 2\text{-}18$$

In equation 2-18 σ is the surface tension where p_g and p_∞ are the vapour pressure inside the bubble, and far-field pressure, respectively.

Homogeneous nucleation occurs in absence of pre-existing nucleation sites in the bulk liquid. This type of nucleation takes place in liquids under metastable conditions with sufficiently high degree of superheat.

Heterogeneous nucleation occurs at preferential sites of primary phase such as phase boundaries. This type of nucleation, which is often observed at low levels of superheat, is associated with the existence of metastable gas cavities at the walls of the container, on microscopic particles or in the form of microscopic inert gas bubbles floating in the liquid. The energy required for heterogeneous nucleation is lower than for homogeneous type (Whalley, 1987; Sher et al., 2008). This is due to the fact that prior to superheating, a large number of bubble nuclei with a broad spectrum of sizes is generally present (Jones et al., 1999).

2.3.2.2 Bubble growth in superheated liquid

Bubble growth has been extensively researched by considering the growth of a spherical bubble in a uniformly superheated liquid pool. In such conditions, the growth of a vapour bubble is driven by the differential pressure between the vapour inside the bubble and the far-field liquid and resisted by surface tension, liquid inertia and viscous effects. Dynamics of bubble growth in term of bubble radius, R can be mathematically described using generalised Rayleigh-Plesset equation (Brennen, 1995):

$$R\ddot{R} + \frac{3}{2}\dot{R}^2 = \frac{1}{\rho_l}\left(p_g - p_\infty - \frac{2\sigma}{R} - \frac{4\mu}{R}\dot{R}\right) \qquad 2\text{-}19$$

In which μ and σ are liquid viscosity and surface tension, respectively. ρ_l is liquid density where p_g and p_∞ are vapour and far-field pressures. Superscripts (.) and (..), represent first and second derivatives operators with respect to time, respectively.

As suggested by Plesset & Prosperetti (1977), the process of bubble growth in superheated liquids may be described by four consecutive stages. Initially the size of the nucleus is very small and thus its growth rate is limited by the surface tension force. Assuming that superheat degree is sufficient, in second stage the growth rate shows a linear behaviour until local liquid conditions reaches to the third stage. In the third stage, the liquid layer in the neighbouring of the bubble is cooled down to supply the required heat for evaporation. As the liquid becomes cooler the saturated vapour pressure decreases, accordingly. In this case both inertia and thermal-diffusion control the growth rate of the bubble. The fourth stage is associated with further decrease in growth rate. Now the inertial effects become less significant and the growth rate is predominantly controlled by thermal diffusion. In other words growth rate is governed by the rate at which heat can be provided at the bubble–liquid interface. As the bubble grows large enough, the magnitude of surface tension term ($\sim 1/R$) and viscous term ($\sim \dot{R}/R$) decrease (see equation 2-19) and becomes less significant. Eventually bubble inner pressure reaches the surrounding pressure and growth process terminates.

Rayleigh (1917) simplified equation 2-19 by neglecting effects due to surface tension and viscosity. Under these circumstances, inertial forces and differential pressure determine the bubble growth rate and the following equation may be written:

$$R\ddot{R} + \frac{3}{2}\dot{R}^2 = \frac{p_g - p_\infty}{\rho_l} \qquad 2\text{-}20$$

For a stable nucleus with radius larger than R_c (see equation 2-18), small fluctuations in pressure across the surface of the bubble result in either further bubble growth or bubble collapse. By assuming the liquid and vapour pressures are constant, and for the duration of growth when $R \gg R_c$, equation 2-20 can be solved for $\dot{R}$ as shown by equation 2-21:

$$\dot{R} = \sqrt{\frac{2(p_g - p_\infty)}{3\rho_l}} \qquad 2\text{-}21$$

The constant liquid temperature/constant far-field pressure assumptions studied by Rayleigh are not sufficient to study adiabatic flashing of volatile superheated liquids. This is because evaporation will (i) decrease liquid temperature and hence reduce p_g and (ii) cause increase in void fraction, which causes acceleration pressure drops in flowing liquid systems; these results in $p_\infty$to change. Since the degree of superheat becomes a function of time it is then necessary to include an account of the diffusion of heat towards the bubble surface. This is included in the analysis of Plesset & Zwick (1954). They neglected the effects of liquid inertia and considered the thermally controlled regime of bubble growth in which the effect of temperature reduction of neighbouring liquid layer due to evaporation is also included. Solutions for bubble wall temperature with the assumption of thin thermal boundary layer were obtained. The heat diffusion equation in Lagrange coordinates was solved using successive approximations. The temperature at bubble wall is given by equation 2-22:

$$T - T_\infty = -\left(\frac{\alpha}{\pi}\right)^{1/2} \int_0^t \frac{R^2(x)\left(\frac{\partial T}{\partial r}\right)_{r=R(x)}}{\left[\int_x^t R^4(y)dy\right]^{1/2}} dx \qquad 2\text{-}22$$

In this equation α is the thermal diffusivity and x,y are dummy integration variables to represent time. If variations in bubble radius with respect to time i.e. $R(t)$ are small, then equation 2-22 can be reduced to:

$$T - T_\infty = -\left(\frac{\alpha}{\pi}\right)^{1/2} \int_0^t \frac{\left(\frac{\partial T}{\partial r}\right)_{r=R(x)}}{(t-x)^{1/2}} dx \qquad 2\text{-}23$$

Plesset & Zwick (1954) provided a useful asymptotic solution for bubble growth of thermally controlled regime shown in equation 2-24:

$$\dot{R} = \left(\frac{3}{\pi}\right)^{1/2} \frac{k(T_\infty - T_{sat})}{h_{lg}\rho_g \alpha^{1/2}} \frac{1}{t^{1/2}} \qquad 2\text{-}24$$

Where k is the thermal conductivity of the liquid, h_{lg} is the latent heat, T_{sat} is the saturated temperature and t is the time. Asymptotic solution is developed by neglecting the effects of temperature dependencies on k, ρ_v and h_{lg} as well as assuming linear relation between pressure and temperature. Result showed good agreement with experimental data of Dergarabedian (1960) who employed water as the working fluid over moderate superheat degrees of 6°C. An approximate solution for the thermally growth regime was developed by Forster and Zuber (1954) considering the moving bubble wall to be a spherical heat sink in a stationary medium. Birkhoff et al. (1958) derived an asymptotic solution without assuming a thin boundary layer around the bubble. This solution and the one obtained by Forster and Zuber (1954) were in agreement with the solution of Plesset & Zwick (1954).

An effective combination of the inertia controlled and thermal controlled growth regimes was achieved by Mikic et al. (1970) who employed a linearised Clausius–Clapeyron relation to simplify the non-linear behaviour of the saturated vapour pressure curve. It was assumed that thermal equilibrium prevails in the bubble so that the vapour pressure p_g at any time instant is linked to the bubble wall temperature T_g as shown in relation 2-25:

$$p_g - p_\infty = \frac{\rho_l h_{lg}(T_g - T_{sat})}{T_{sat}} \qquad 2\text{-}25$$

Vapour pressure approximation using equation 2-25 were then combined with equation 2-21 to estimate the bubble growth rate in the inertial controlled regime:

$$\dot{R} = \sqrt{\frac{2\rho_g h_{lg}(T_g - T_{sat})}{3\rho_l T_{sat}}} \qquad 2\text{-}26$$

In equation 2-26 and 2-24, T_{sat} is substituted by T_g (gas temperature at bubble wall) which was a more realistic representative of temperature as shown in equation 2-27:

$$\dot{R} = \left(\frac{3}{\pi}\right)^{1/2} \frac{k(T_\infty - T_g)}{h_{lg}\rho_g \alpha^{1/2}} \frac{1}{t^{1/2}} \qquad 2\text{-}27$$

Elimination of T_g from equations 2-26 and 2-27 leads an equation for $\dot{R}$ which can be integrated and yields an expression that is valid over both inertial and thermal controlled growth regimes:

$$R^* = \frac{2}{3}\left[(t^* + 1)^{3/2} - (t^*)^{3/2} - 1\right] \qquad 2\text{-}28\ (a)$$

$$R^* = \frac{R}{B^2/A}, \qquad t^* = \frac{t}{B^2/A^2} \qquad 2\text{-}28\ (b\text{-}c)$$

$$A = \left[\frac{2}{3}\frac{(T_\infty - T_{sat})h_{lg}\rho_g}{T_{sat}\rho_l}\right]^{1/2}, \qquad B = \left[\frac{12}{\pi} Ja^2 \alpha\right]^{1/2} \qquad 2\text{-}28\ (d\text{-}e)$$

$$Ja = \frac{\rho_l c_{p,l}(T_\infty - T_{sat})}{\rho_g h_{lg}} \qquad 2\text{-}28\ (f)$$

In the set of equations 2-28 for values of $t^* \ll 1$ Rayleigh solution can be obtained in which growth rate is controlled by pressure difference and inertia, whereas for $t^* \gg 1$ the asymptotic solution of Plesset & Zwick (1954) predicts the growth rate in which heat inflow to the bubble is the controlling factor.

Considering the good track record of the approximate solutions provided in this section, it is conclusive that dynamics of bubble growth expressed by 2-19, may be reasonably approximated by solutions of inertial controlled and thermally controlled regimes. Such approach reduces the difficulties and time consumption associating with obtaining detailed solution of equation 2-112-19, where still is capable of incorporating key physics governing bubble growth dynamics.

2.3.2.3 Flash atomisation and droplet size

Generally, systematic increase of the liquid temperature beyond its saturated temperature at prevailing condition, i.e. $T > T_{sat}$, leads to the formation of smaller droplets. Void development accelerates the flow and increases disturbances inside and outside of the liquid element. Reitz (1990) conducted a photographic study of flash atomisation and observed that the atomising jet could be subdivided into an intact inner core and its surrounding small ligaments. It was concluded that flashing reduces the size of the inner core as well as the size of the surrounding droplets.

Wiener (1958) highlighted flashing as the principal mechanism of atomisation of pressurised liquids. The phenomenon is caused by abrupt pressure drop and subsequent heat transfer between the liquid and gas phases during a very brief period of time. The process is assumed to be adiabatic as well as mass transfer dominant. Wiener (1958) calculated the percentage of propellant 12 vaporised at 21 °C during primary atomisation of a spray actuation event (actuator press and fire), using a simple adiabatic heat balance equation:

$$m_{f(\%)} = \frac{c_{p_l}(T_l - T_{wb})}{h_{lg}} \times 100 \qquad 2\text{-}29$$

Where $m_{f(\%)}$ is the flashed mass of the propellant represented in percentage. T_l and T_{wb} are the initial liquid temperature and wet bulb temperature, respectively and c_{p_l} is the heat capacity of liquid. Calculation showed that for propellant 12 at 21 °C, 27% of its mass can turn into vapour.

The idea of flash atomisation of a jet as a result of liquid nucleation was brought forward by Brown and York (1962). The proposed process involved regular generation of low pressure

eddies due to the geometrical imperfections inside the nozzle. These eddies create regions with low pressure leading to bubble formation. The bubbles are then carried downstream regions by the flow. Eventually the jet breaks up due to the gradual growth of the bubbles. Brown and York (1962) used photographic counting methods to derive an empirical correlation linking the droplet mean diameter D_{10} (m), to the Weber number and temperature of the flow in the expansion chamber (space with enlarged volume across flow path) for water and propellant 11:

$$D_{10} = \left(\frac{4220 \ - 9.3T_{ec}}{We_g}\right) \times 10^{-6} \qquad 2\text{-}30$$

In this equation T_{ec} (K) is the expansion chamber temperature.

Theoretical work to predict droplet size produced by flashing was carried out by Sher and Elata (1977). The work considered the formation process of spray from a pressurised can containing propellant as the working fluid. The process was described as rapid growth of bubbles as the can releases propellant into the atmosphere. Continual growth results in adjacent bubbles touching each other, forming larger void volume and fragmenting the liquid. The geometric arrangement of bubbles was assumed to be a close packed array. Hence vapour and liquid volume fraction are $\pi/6$ and $1 - \pi/6$, respectively. At this point, regime change is assumed to take place and the energy contained in the exploding bubbles will be partly transformed into droplet surface energy. It was also assumed that droplets follow a log-normal distribution. Using these assumptions, an expression was derived to relate mean spray droplet size to fluid thermo-physical properties and flow parameters:

$$D_d = \frac{\alpha\sigma}{\rho_l}\left[\frac{h_{lg}^2 \bar{p}^2 M^2}{C_{p_l}\rho_l \bar{T}^3 R'^2 D_{th}^{0.5}}\right]^4 \frac{\exp(-2.5\ln^2\sigma_g)}{\Psi^4(\Delta p)^4} \qquad 2\text{-}31$$

Where $= 1.266/\eta m^{2/3}$, in which η is the fraction of bubble energy which transforms into droplet surface energy and m is the volume density of vapour nuclei. $\bar{p}$ and $\bar{T}$ are the absolute average values inside and outside the pressurised can. M is the molecular weight of the propellant and Ψ is assumed to be 1. D_{th} is the thermal diffusion coefficient. R' is the universal gas constant and σ_g is the geometric standard deviation of the assumed

distribution. Eventually Δp is the pressure difference. Comparison of the model results against measured droplet size did not show a very good match against the observation. The main difficulty of the model was a *priori* determination of the many of the parameters required by equation 2-31. It should also be mentioned that experimentation showed that the nozzle configuration had no significant effect on droplet size. The nozzle diameter does not explicitly appear in equation 2-31; the nozzle throat only acts as a space for nucleation and bubble growth.

Solomon et al. (1985) investigated the droplet size issued from twin-orifice system, using propellant 11 and Jet A/dissolved air. The emitted mass flow rate from the valve and spray orifices were estimated with the locally homogeneous model (LHM) and separated flow model (SFM). The flow model was linked to a droplet size correlation adopted from the work done by Lefebvre (1980), which was originally derived for pre-filming airblast atomisers. The model predictions of droplet size showed reasonable agreement with the measured data obtained by laser diffraction particle sizer. By comparing the results of propellant 11 (flashing case) and Jet A/air (non-flashing case), It was found that flashing generally increased the atomisation quality judged by reduced droplet size.

A theoretical model for predicting the size of droplets in a superheated water spray due to thermal fragmentation was presented by Razzaghi (1989). The atomisation process is divided into three consecutive stages. The first stage is formation of primary droplets as a result of aerodynamic breakup. The size of the droplet at this stage was assumed to be proportional to the wavelength of instability on liquid surface. The duration of primary droplet formation is considered to be sufficiently short for conditions to be adiabatic (i.e. no heat exchange with the surrounding air), so the droplet and jet temperatures are identical. Consequently, the primary droplets will be superheated. The second stage in Razzaghi's model is nucleation and growth of vapour cavities inside the superheated droplets. The criterion of flashing inception is based on the non-dimensional degree of superheat adopted from the experimental work of Bushnell and Gooderum (1968):

$$\frac{T_l - T_{sat}}{T_l} \geq 0.1 \qquad 2\text{-}32$$

Where T_l is superheated liquid temperature. Further growth of the bubble inside the droplet leads to thinning of the surrounding liquid film up to a point where the bubble bursts. In the final stage, after bubble bursting the remaining mechanical energy (due to the stretched liquid film) and thermal energy in the liquid are partly transformed into surface energy through which "tertiary droplets" with smaller size are formed. The number of tertiary droplets is determined by uniform random number generator algorithm within the range of 1 to 10. This mechanism is illustrated in Figure 2.2.

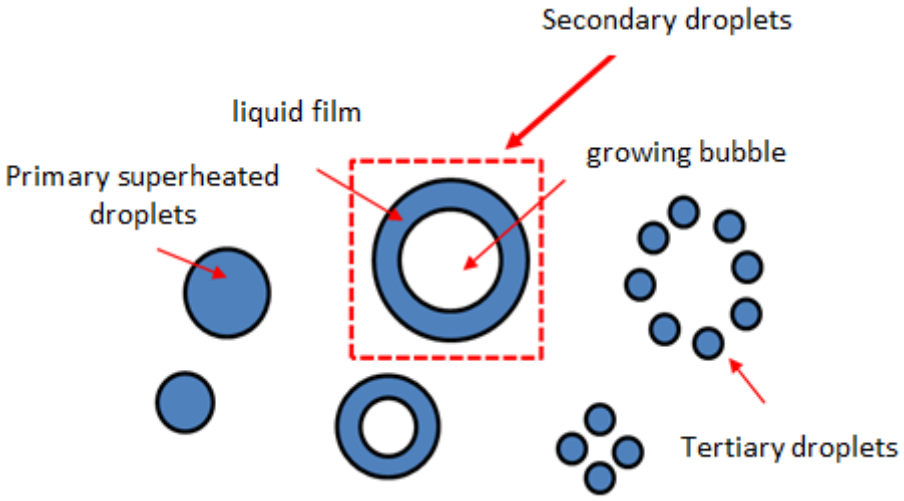

Figure 2.2 Schematic of primary, secondary and tertiary droplets formed as a result of thermal fragmentation adapted from (Razzaghi, 1989)

The results showed that the average droplet size increases from 6 µm to 14 µm as the discharge pressure decreases from 10 MPa to 2.5 MPa. A similar trend was observed when the initial temperature was reduced from 550 K to 475 K.

Park & Lee (1994) studied the effect of the internal flow pattern inside a spray nozzle on the behaviour of the flashing spray, by examining photographs of sprays from circular transparent nozzles of superheated water. The internal flow regime appeared to respond to increases in superheat level by changing from bubbly to slug flow and subsequently to annular flow regime. It was also observed that by increasing the degree of superheat, finer and more uniform droplet sizes were produced. At low superheat levels, a large intact core

region was observed, where the droplets are mainly formed around the edges of the spray. Further increase of superheat degree at the prevailing pressure resulted in a more violent bubble growth process. Subsequently, bubble collision and coalescence inside the nozzle formed liquid slugs. Discharging of these slugs at the nozzle exit caused rearrangement into stretched ligaments and then disintegration into fine droplets. Further increase in superheat resulted in the formation of a vapour core and thin liquid annulus moving along the walls of the nozzle, which is termed the annular flow regime. As the fluid is released out of the nozzle it disintegrates into fine droplets.

Domnick & Durst (1995) carried out experimental work using phase Doppler particle analysis, laser Doppler anemometry and laser sheet visualisation to study the behaviour of flashing flow of propellant 12 while moving through a constriction (see Figure 2.3). It was observed that, due to the generation of low pressure recirculation zones near the entry to the constriction, liquid nucleation and growth of bubbles were initiated. The volume of this recirculation zone increased as a result of continued bubble growth until it reached a threshold where after it collapsed. The fluid in the recirculation zone was periodically transported by the mean flow towards the nozzle exit leading to periodic bubble cloud generation. It was observed that flashing preferentially takes place along the walls of nozzle geometry.

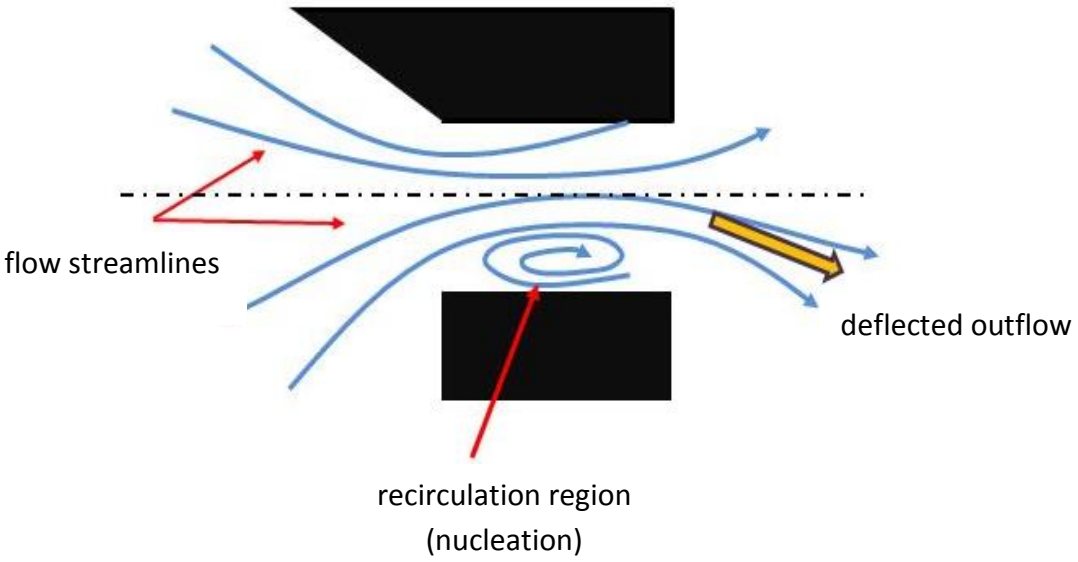

Figure 2.3 Schematic of flashing flow through a constriction based on the work of (Domnick and Durst, 1995)

Yildiz et al. (2002, 2004, 2006) conducted a series of studies of flashing jet characteristics as a function of initial conditions with relevance to sudden release of liquefied gases into the ambient environment. By employing optical diagnostic techniques such as particle image velocimetry (PIV), Phase Doppler Anemometry (PDA) and high-speed imaging (HSI) the mean droplet diameter, breakup pattern and spatial velocity distributions of HFA134 flashing jets were investigated. The measured droplet size was found to be directly correlated with the degree of superheat. Interestingly, it was also reported that the droplet centreline velocity did not depend on degree of superheat. The influence of upstream pressure was also investigated and it was shown that this parameter had a direct relationship with jet velocity and inverse relationship with the mean droplet size. In terms of breakup pattern, for the same initial pressure and superheat, it was concluded that a jet that emerges from a larger nozzle shows a more explosive breakup pattern. It was also observed that increase of the degree of superheat up to 6.4 °C changed the breakup pattern from slow expansion to violent shattering.

2.4 Secondary atomisation

Following formation, droplets may be transported to regions where strong aerodynamic loads can potentially deform droplets and lead to further disintegration. This mechanism is termed secondary atomisation. The dominant parameters governing droplet breakup are disruptive aerodynamic forces and the restorative surface tension forces. The ratio of these forces is the Weber number. Droplet viscosity opposes fragmentation and dissipates energy supplied by aerodynamic forces. These effects are represented by the Ohnesorge number representing the relative magnitude of viscous to surface tension forces. Viscous forces are known to be dominant for Oh values larger than 0.1, below which fragmentation is almost independent of this parameter.

Depending on the prevailing conditions and aerodynamic load, secondary atomisation may occur differently. The exact regime of droplet breakup occurs is predominantly a function of the Weber number and is identified by breakup morphology.

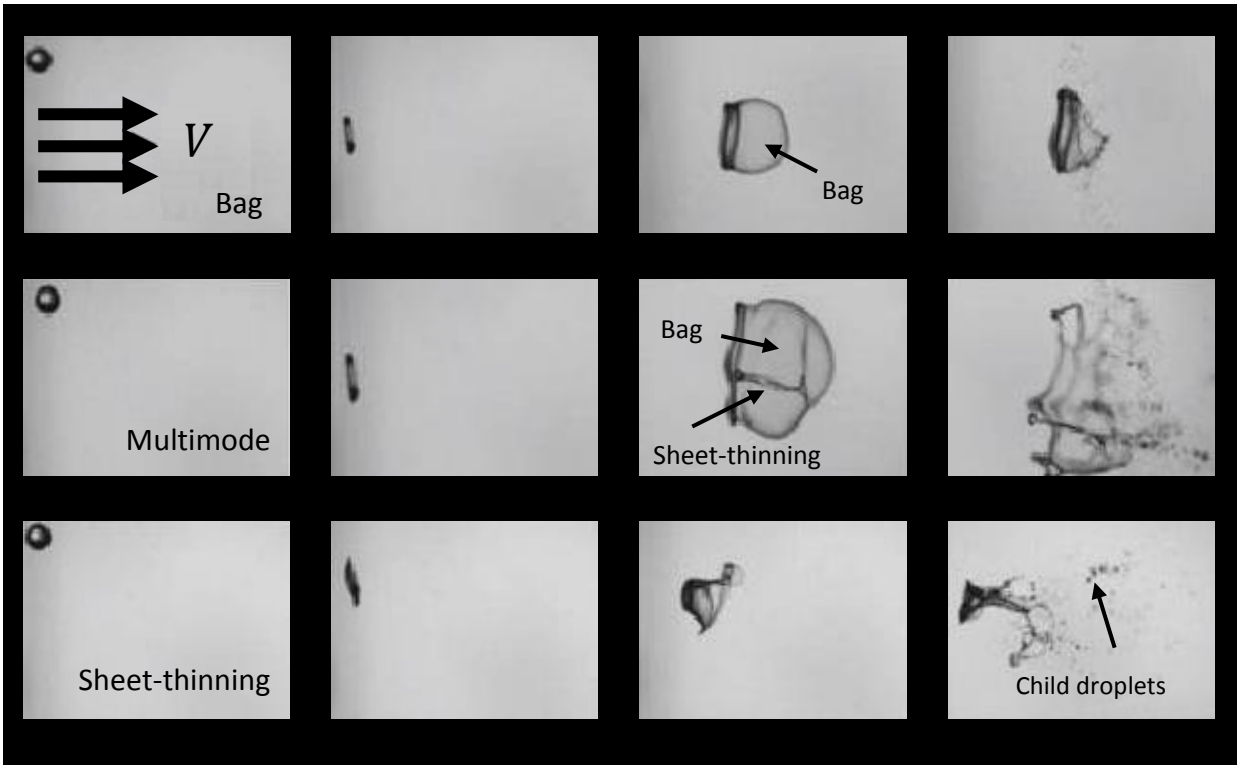

Figure 2.4 Visual representation of different secondary atomisation regimes proposed by (Guildenbecher et al., 2009)

Breakup Regime	Weber number (We)
Vibrational (no breakup)	$\sim 0 < We_g < \sim 11$
Bag	$\sim 11 < We_g < \sim 30$
Multimode	$\sim 30 < We_g < \sim 80$
Sheet	$\sim 80 < We_g < \sim 350$
Catastrophic	$We_g > \sim 350$

Table 2.4 Different regimes of droplet secondary atomisation and transit Weber number for Oh <0.1 (Guildenbecher et al., 2009)

Figure 2.4, proposed by Guildenbecher et al. (2009) shows rows of images corresponding to the initial, middle and final stages of a droplet breakup event, illustrating different breakup regimes. The transit Weber number is from one regime to another is summarised in Table 2.4.

As discussed by Lee & Reitz (2001) secondary atomisation occurs in five distinct regimes. The first regime is known as “vibrational breakup” which occurs as a result of the formation of a non-uniform pressure distribution over the droplet surface causing geometric deformation. As a result of the restoring action of the surface tension force, cyclic deformation occurs and the droplet shape oscillates. This breakup regime does not always occur, proceeds much more slowly than the other regimes, and results in formation of large droplets. Therefore it is ignored as being the first regime of droplet fragmentation and “bag breakup” regime is considered as the first breakup mode (Liu & Reitz, 1997).

The second regime occurs at low Weber number and is termed “bag breakup” regime. During bag breakup, flow separations around the deformed droplet, results in a positive pressure difference between the leading stagnation point and the wake. This pushes the centre of the deformed droplet downstream leading to formation of a bag-like configuration (Han & Tryggvason, 2001). The outer edge of the liquid segment forms a toroidal ring to which the bag is attached. The bag bursts into small child droplets and, subsequently, the ring itself breaks up and reorganises itself into a small number of larger liquid segments (See the top row of Figure 2.4). The Weber number associated with the initiation of this breakup regime in known as the critical Weber number. For cases with $Oh < 0.1$, studies show that the critical Weber number is 11 ± 2 (Guildenbecher et al., 2009). A wide range of droplet sizes is produced in the bag regime. As confirmed by Chou and Faeth (1998) the mean droplet size formed from the ring material was around 30% of the parent drop diameter, whereas the mean droplet size formed from the breakup of the bag was 4% of the parent drop diameter.

The third regime is known as “Multimode breakup” occurs at intermediate Weber numbers between those of bag breakup and sheet-thinning breakup. The mechanism appears to be a combination of these two breakup modes (See the second row of Figure 2.4). The formation of a bag is accompanied by the presence of a core droplet leading to ligament formation in

the centre of the bag. This configuration is known as stamen (Pilch & Erdman, 1987; Dai & Faeth, 2001). It is currently not known why bag breakup occurs at low intensity of aerodynamic forces and sheet-thinning occurs at higher intensity. However, it is postulated that unstable surface waves determine the precise details of the breakup regime (Guildenbecher et al., 2009).

The fourth regime is known as "sheet-thinning" breakup, which occurs at higher relative velocities between liquid and surrounding gas and hence higher Weber number. Deformation of liquid segments in this regime establishes a sheet-like configuration at the droplet periphery. This sheet stretches into ligaments, which eventually disintegrates into large numbers of child droplets. The process continues until the droplet is completely atomised or alternatively reaches a size where aerodynamic forces are insignificant. In the latter scenario, a core droplet remains when the atomisation mechanism terminates (Hsiang & Faeth, 1992).

The final regime of breakup occurs at extremely high Weber numbers and so-called "catastrophic breakup". The formation and growth of wave-like instabilities on the leading edge of the deformed droplet are observed during this breakup mode. These waves are believed to be of the Rayleigh – Taylor type (which are generated due to the acceleration of the dense liquid segment into the lighter ambient) and penetrate the droplet while growing in amplitude. This results in disintegration of the droplet from the inside. It is proposed that the wavelength of instability is directly correlated to the size of the child droplets (Joseph et al., 1999; Hwang et al., 1996). This type of breakup regime is only observed in shock tube experiments where extremely high relative velocities can be provided. It is not expected that this breakup mode will be observed in typical sprays (Faeth et al., 1995).

2.5 Atomisation mechanism of pMDI

pMDI is unique in terms of its ability to form a fine aerosol plume with large numbers of droplets predominantly in the size range 1-5 µm but the details of atomisation mechanism of the device is poorly understood (Versteeg & Hargrave, 2006; Finlay, 2001; Gavtash et al., 2014). To date, two candidate mechanisms are conjectured, namely (i) propellant flashing (Finlay, 2001; Clark, 1991; Versteeg et al., 2006; Dunbar, 1997) and (ii) aerodynamic atomisation (Clark, 1991; Gavtash et al., 2014).

Fletcher (1975) conducted comprehensive research focusing on both theoretical and experimental aspects of the thermo-fluid dynamics of flashing propellant flow through a twin-orifice system. Initial investigations were conducted on CFC propellant mixtures with 50:25:25 w/w % of propellants 12, 11 and 114. Flow visualisation inside the expansion chamber and near-orifice region was achieved using 8000 fps rotating prism camera along with 7 kW xenon arc lamp as the source of illumination. A qualitative description of the atomisation mechanism was put forward, which suggested that liquid bulk size reduction was initiated inside the expansion chamber, followed by subsequent breakup as the flow passed through the spray nozzle. In order to determine the spray size distribution, small quantities of less volatile pMDI surfactant Span 85 were dissolved in the propellant mixture. The residual droplets were collected in a sedimentation cylinder and allowed to sediment for 15 hours onto a series of glass slides. The mass median diameter of the residual particles was found to be 4.9 µm and 7.8 µm, for 0.25 mm and 0.58 mm orifice diameter respectively. The following empirical correlation for mass median diameter (MMD) as a function of spray orifice diameter d_{so} for solution formulation was developed:

$$MMD = 1.6 \times 10^{-2}\, d_{so} \qquad 2\text{-}33$$

Fletcher (1975) also developed mathematical representations of steady, two-phase propellant flow through twin-orifice systems for continuous discharge. The model was constructed to predict mass flow rate through valve and spray orifices as a function of thermodynamic properties of upstream flow in the chambers. These predictions are made under subsonic and choked discharge conditions, separately. Results showed that the prediction of exit velocity under choked discharge conditions was more in line with experimental data, compared with the one predicted under subsonic conditions.

Clark (1991) extended Fletcher's work and carried out a comprehensive study to determine the atomisation mechanism responsible for the generation of respirable aerosols by pMDIs. His work was aiming to link the generated droplet size to the pressure and temperature in the expansion chamber. In order to estimate the initial droplet diameter generated just outside the spray orifice, Clark also used propellants with known amounts of dissolved surfactants. The size of the residual aerosols, after the volatile propellant evaporates away, was measured with an aerodynamic particle sizer (APS) with a particle sizes range of 0.5 to

15 microns. Clark conjectured that the dominant atomisation mechanism of the pMDI was due to aerodynamic forces similar to air-blast atomisation. He proposed that the propellant is pre-atomised into liquid ligaments during its passage from the metering chamber to the expansion chamber. Next, two-phase propellant mixture enters the spray orifice in the form of liquid ligaments and rapidly expanding propellant vapour. The vapour flow squeezes and shears off liquid ligaments from which smaller liquid segments are generated. These exit the spray orifice as small spherical droplets. In air-blast atomisation the propellant vapour pressure and the quality of a two-phase mixture at the entry of the atomiser nozzle, are the most significant controlling factors governing the droplet size. Clark correlated the experimental droplet size data with the peak expansion chamber pressure p_{ec} and vapour quality x_{ec} to obtain an empirical correlation for the mass median aerodynamic diameter (MMAD in μm) as defined by equation 2-34:

$$MMAD = \frac{C}{x_{ec}^{0.46}\left(\frac{p_{ec} - p_{amb}}{p_{amb}}\right)^{0.56}} \qquad 2\text{-}34$$

where p_{amb} is ambient pressure. Clark (1991) reported good fit with measured data for continuous and metered discharge using the constant C = 8.02 μm and 1.82 μm, respectively. Clark (1991) also expanded the theoretical work of Fletcher (1975) by developing a mathematical model of quasi-steady, two-phase flow of propellants to evaluate metered pMDI discharges. The predicted flow velocity, pressure and temperature inside an actuator were shown to be in good agreement with experimental measurements.

Although Clark's correlation for droplet size has been the most influential contribution to date, the model is empirical. As was noted above, the constant C of equation 2-34 has dimension of length. Clark (1991) used equation 2-34 to capture the trends relating to the effects of formulation parameters on droplet size. However, the length-scale determining physical processes are hidden in the parameter C. Clark needed different values of C for continuous and metered discharge, so this constant is not universal and may need to be adjusted on a case-by-case basis, limiting the predictive power of the equation.

Dunbar & Miller (1997) and Dunbar et al. (1997) measured droplet size and velocity of pMDI sprays containing HFA134 and a mixture of propellant 11/12 (28:72 w/w %) in stationary

ambient air. Measurements showed that pMDI sprays are unsteady, three-dimensional and characterised by high initial drop velocities and production of large numbers of small droplets. It was reported that HFA134 produced smaller mean drop size than the propellant 11/12 mixture formulation. This was attributed to higher vapour pressure of HFA134 by around 33% compared with propellant 11/12 mixture. In a separate study a small quantity of drug (Salbutamol) was added to propellant 11/12. This was found to cause a significant increase to the mean drop size at 100 mm away from spray orifice which was attributed to retarded evaporation rate of the droplets when drug is added to the formulation.

Dunbar also developed a theoretical model of propellant inside the pMDI. While deriving mathematical relations for two-phase propellant flow through orifices Dunbar and Miller (1997) assumed that only the vapour phase chokes and the liquid phase was treated as incompressible. This assumption resulted in large spray velocity in the order of 200 m/s, which did not match with his PDA measurements. Dunbar (1996) further attempted to shed light on the atomisation mechanism of pMDIs by examining a wide range of droplet size correlations with good track record in the field of industrial atomisation. However, it was found that Clark's model (equation 2-34) was the most useful droplet size correlation. When it was applied in conjunction with their internal flow model to generate instantaneous drop size in metered discharge, Dunbar & Miller (1997) found that it was necessary to employ C=8.02 as the constant. A Rosin-Rammler distribution was used to generate the droplet source in a CFD model using to predict the development of aerosol plume in stationary ambient air.

Wigley et al. (2002) characterised a HFA227 aerosol produced by a pMDI in the near-orifice region (x/D_{so}=6.2, where x is the measured distance and D_{so} is the spray orifice diameter) utilising a PDA system. Similar to Dunbar et al. (1997) measurements, it was found that the spray exhibits highly transient and complex variations, including variations of spray plume exit direction. Measured velocity and droplet size showed reasonable match with their model of internal flow of propellant when used with Clark's drop size correlation in conjunction with C = 1.82 μm. This suggests that the details of the internal flow model as well as the selection of the constant in Clark's atomisation correlation are important for successful predictions.

Versteeg & Hargrave (2006) studied the fundamentals of pMDI plume development in the near-orifice region of commercial pMDI actuator and also visualised the two-phase flow regime in the expansion chamber of a simplified transparent model. Laser-based high-speed imaging revealed that the spray event consists of three distinct stages:

1. Initial transient phase, covers the start-up duration of the injection. This involves narrow pulses of spray with generation of large droplets around 50 µm.
2. Main quasi-steady phase, which is fully developed spray with gradual spray density variations related to changes of pressure and vapour mass fraction of the two-phase mixture inside the expansion chamber. Striated spray is also noticeable in this phase highlighting spatially varying droplet concentration. Respirable droplets are formed during this phase.
3. Final phase, consists of a gradually narrowing spray with decreasing droplet number density. Due to the formation of larger liquid ligaments during this stage, larger droplets with size up to 150 µm are generated.

Lastly by observation of the flow pattern in the expansion chamber it was pointed out that an annular flow regime prevails over a substantial fraction of the actuation event. It was proposed that propellant flashing in the spray nozzle during the second phase (quasi-steady) of the injection may play a major role in the production of respirable droplets. Imaging of the nozzle exit region revealed the formation of a sizeable liquid pool stripping of ligaments from this accumulated liquid pool around the outer cone of the nozzle appeared to be the main source of much larger droplets.

2.6 CFD modelling of pharmaceutical sprays

Computer aided simulation is now extensively used across all fields of engineering and science. This route is now popular and beneficial more than ever, due to commercially available and powerful computational packages. The design of aerosol delivery devices in pharma industry is no exception. In this field of science, the published research can be categorised into three main classes which are aerosol plume development and transport in (i) stationary ambient, (ii) enclosed geometry with (or without) co-flowing air and (iii) USP throat, biological throat and more comprehensive models of the upper airway up to the 5^{th} generation of bronchi. The key interest is to estimate deposition and understanding the

factors governing the underlying physics of this process. In this section we review the key studies which utilised computational modelling of fluid flow and particle dynamics to unlock different aspects of aerosol delivery.

Lagrangian particle tracking is the most widely used method for simulating the effects of particles injected into a flow. In this method, the flow field (continuous phase) is determined initially and the particles or droplets (discrete phase) are subsequently traced through the established flow field (Gosman & loannides, 1983; Durst et al., 1984). The approach assumes that a negligible local volume fraction (typically < 5%) is occupied by the particles (Sommerfeld, 1992). Groups of particles with the same properties and characteristics (e.g. diameter, density, velocity, temperature, etc.) are represented by computational parcels (Sommerfeld, 1992). The method is able to provide detailed information regarding particle behaviour, and by linking it to appropriate sub-models, additional physics such as particle evaporation, particle-wall impaction and turbulent dispersion of the particles may also be predicted. Depending on the particle mass loading (ratio of particle mass and total two-phase mixture mass) the effect of particles on the continuous phase may or may not be neglected. In the case of low mass loading, the transfer of heat, mass and momentum between particles and continuous phase can be ignored (Wong et al., 2012). This method of calculation is called a one-way coupled calculation. In cases where particle mass loading is substantial or where significant mass transfer occurs as a result of droplet evaporation, the effects of discrete phase are no longer negligible on the continuous phase. Therefore an iterative, two-way coupled calculation is more appropriate to capture the features of the particles and the flow field (Wong et al., 2012). In this case, initially, the continuous phase equations (i.e. Navier-Stokes equations) are solved (Versteeg & Malalasekera, 2007) and subsequently the particles are tracked using the Lagrangian tracking algorithm - also known as discrete phase modelling (DPM) (Sommerfeld, 1992). Next, the aerodynamic influence of particles (i.e. drag) on the continuous phase, as well as evaporation of the droplets and energy exchange with the gas phase are calculated. These contributions due to interphase momentum, mass and heat transfer are subsequently applied to the fluid flow equation as source terms. Fluid equations are then solved again and pressure, velocity, temperature and other scalars are updated.

Further discrete phase iterations are performed using the recently updated flow field until the convergence criteria are met.

Wong et al. (2012). and Worth Longest & Holbrook (2012) provided comprehensive reviews of the application of CFD in the context of development and optimisation of inhaler device and particle deposition in the upper airways and lungs. The research included the description of previous CFD utilisation in the analysis of the commercial pMDIs. It was concluded that CFD can be used as an effective tool to predict and optimise the performance of the inhalers. However, this has to be done alongside experimental validation. It was also noted that particles can be accurately tracked through an airflow using two-way coupled calculations. However, these papers also pointed out that this process is highly computationally expensive, and the required computational resource is directly correlated to the number of particles presented in the computational domain.

In the field of drug delivery, one of the early implementations of CFD to study inhaler design was carried out by Versteeg et al. (2000). The research involved a CFD model to predict the steady air flow behaviour through an Astra Zeneca Pulmicort® pMDI actuator. In the numerical simulation a spray plume source was injected into a United States Pharmacopeia Induction Port (USP-IP) and particle trajectories were evaluated using Lagrangian particle tracking. High levels of turbulence were observed in the actuators due to the presence of several recirculation zones in the pMDI mouthpiece region where the developing spray jet interacts with the air flows. Based on the CFD result of plume injection into the USP-IP, it was concluded that the droplet trajectories are initially dictated by inertia. Nevertheless, owing to the interaction of the aerosol plume with surrounding air, evaporation of the droplets and air entrainment by the jet, the plume slows down and droplet size reduction occurs. The turbulent dispersion of the particles was also applied to the simulation using the stochastic random walk model and particle deposition was visualised. It was found that significant amounts of particle deposition occurred on the horizontal section of the USP-IP. It was difficult to obtain an exact quantitative match between CFD results and experiments, but the model achieved fair agreement with PIV measurements.

In similar work, Harrington et al. (2001) developed a CFD model discussing aerosol formation and development from a pMDI considering the interphase interaction between

drug particles and air. The study was aimed at characterisation of drug deposition in a USP-IP and a human oral cavity model. The human oral cavity was reconstructed from MRI scans acquired whilst inhalation through a pMDI was taking place. The model was capable of considering the interaction between phases, droplet boiling, and turbulent dispersion of particles as well as particle deposition. The majority of deposition in the USP-IP was found to be on its horizontal segment, which was in good qualitative agreement with experiments. In the case of the biological throat model, the main obstruction for the plume penetration appeared to be the tongue where significant deposition was predicted to take place. By comparing the deposition in the USP-IP and the biological throat model it was evident that the level of deposition at the back of biological throat was higher than the USP-IP, which also matched with previous experimental findings.

The steady flow of inhaled air, fuel vapour (JP-8) behaviour and ultrafine particle (less than 0.1 μm) in simplified human upper airway geometry was simulated by Zhang & Kleinstreuer (2003). The geometry of the respiratory tract was partitioned into two major regions representing (i) mouth to trachea as one segment followed by (ii) the bronchial tree as the second segment. The study was carried out under different breathing modes, namely, low $Q_{air} = 15$ l/min, medium $Q_{air} = 30$ l/min and high $Q_{air} = 60$ l/min. It was observed that the inlet flow rate had a significant impact on the vapour fuel deposition fraction. As the inlet flow rate rose, the deposition fraction of the vapour fuel reduced. It was also concluded that, at low inhalation flow rates, the distributions of temperature in oral airways affected the velocity field specifically in the trachea implying that higher local temperatures caused faster continuous phase velocity. There was negligible effect of temperature variations for medium to high inhalation flow rates. Lastly, the vapour fuel deposition fractions in the model segments were found to be independent of inhaled air temperature variations 263K < T_{air} < 310K in the upper airways. Nevertheless, the localised concentration of vapour may be affected by non-isothermal flow in this region.

Zhang et al. (2004) proposed a novel highly idealised mouth throat geometry and compared aerosol deposition with two standard USP-IPs. The study was carried out both experimentally and numerically for 30, 60 and 90 l/min inhaled air flow. Gravimetry was used to measure the deposition in the aforementioned geometries experimentally for 2.5, 5 and 6 μm particles; the results were compared with in-vivo deposition data in the human

oropharynx. It was concluded that the amount of deposition is considerably higher for the idealized mouth-throat geometry compared with the USP-IP. The total deposition efficiency curve for the idealised mouth-throat showed a good match with in-vivo average curve of Stahlhofen et al. (1989). On the other hand, the USP-IP data fell considerably below the in vivo averaged curve. It was proposed that the idealised geometry is more suitable than USP-IPs for in-vitro testing of pharmaceutical aerosols. A CFD model of particle deposition was developed by implementing both Lagrangian particle tracking and Eddy Interaction Model (EIM). The latter is a DPM sub-model that accounts for successive interactions between particles and turbulent eddies during their lifetime within the computational domain. After the end of the life time of one eddy, the particle interacts with the next eddy. This resolves the chaotic motion of particles in a turbulent flow (Gosman & loannides, 1983). The inhaled air flow was solved using the Reynolds Averaged Navier-Stokes (RANS) equations in conjunction with the $k-\omega$ turbulence model. The predicted total deposition in the highly idealised mouth-throat was found to be in relatively good agreement with the measured data only after the application of a near-wall correction function to the turbulence fluctuating velocity components, in the EIM.

Kleinstreuer et al. (2007) undertook a comprehensive study to examine the effect of various propellants, nozzle diameter and spacers on droplet transport and deposition. They modelled a pMDI actuator linked to a geometry model of the human upper airway and simulated an inhalation air flow rate of 30 l/min in conjunction with injections of the propellant particulate phase. For HFA and CFC propellants, nozzle diameters of 0.25 mm and 0.5 mm were utilised, respectively. The spray source was constructed based on assumed values of mass flow rate and spray angle. The former was determined in a way to produce initial velocity of around 150 m/s, for both propellants and nozzle diameters. Enhanced Taylor Analogy Breakup (ETAB) atomisation model was used to predict the generated droplets.

Multiple regions of recirculation were observed within the actuator and the attached spacer. Due to the abrupt volume expansion from the mouthpiece to the spacer region, significant droplet velocity reduction was evident. The decrease in velocity resulted in increased droplet residence time in the spacer, which, in turn, caused enhanced droplet evaporation. For both CFC and HFA driven pMDIs, the deposition in the oral cavity was significantly

reduced when a spacer was used. A higher fraction of droplets reached the lung which was in good agreement with in-vitro and in-vivo measurements. By comparing the HFA-propelled and CFC-propelled pMDIs, it was concluded that performance of HFA-driven pMDI was better than CFC-driven one. By using an identical nozzle diameter of 0.25 mm for both propellants, it was detected that a greater portion of droplets reaches to the lung with HFA as the propellant. This was attributed to the higher vapour pressure and lower surface tension of HFA causing finer atomisation. Lastly, the influence of nozzle diameter was also investigated on atomisation characteristics. The CFD results were experimentally validated and clarified that a smaller nozzle diameter is associated with the release of smaller droplets.

In order to optimise the lung delivery of sub-micron particles, Worth Longest et al. (2007) developed a CFD model, which was capable of predicting transport and deposition of a capillary-generated aerosol (Albuterol sulfate - ρ=22.1 kg/m^3). The spray source is defined using an externally, numerically defined capillary aerosol generator (CAG). Source variables are selected based on reasonably assumed values of mass flow rate (25 mg/s), inlet velocity (443 m/s), temperature (100 °C) and range of droplet size (0.1-60 µm). This was sprayed into a standard USP port (USP, 2005) through a capillary tip having a diameter of 57 µm. The spray was accompanied by 30 l/min of co-flow air (typical breathing flow rate). Lagrangian particle tracking was used to obtain the particles trajectories in conjunction with the EIM model (Gosman & loannides, 1983) to consider turbulent dispersion of the particles. Particle evaporation was also considered in the model. The numerical prediction of the spray angle (approximately 29 degrees) agreed with previous reports. Furthermore, the CFD predictions of mass fraction of deposited particles in evaporating and non-evaporation cases were 13.3% and 13.1%, respectively. These compared favourably with the experimental mean total mass fraction of 14.6 $\pm$ 1.1%. The mass median diameter (MMD) predicted by the CFD simulation at the outlet face of induction port was 3.07 µm for the case of non-evaporating particle and 3.45 µm for the case of evaporating droplets. Laser diffraction particle size analysis gave a value of 3.06 µm, which proved to be a very good match between the model and experiments.

By using the same spray source of Worth Longest et al. (2007) the effects on the particle deposition of spray momentum and mouth-throat geometry characteristics were studied by Worth Longest et al. (2008). In order to characterise the effect of spray momentum,

capillary aerosol generated particles were compared with ambient aerosols with the same particle size distribution and 30 l/min of air co-flow. To evaluate the impact of geometry, a standard USP-IP and realistic mouth-throat geometry were studied. It was observed that the effect of spray momentum is more pronounced in the USP-IP deposition. According to the quantified findings in the case of USP-IP, the deposition may be reduced by a factor of 3.5 (from 14.7% to 4.2%) by decreasing the spray momentum. In the mouth-throat model geometry, however, the decrease factor for total deposition was found to be only 1.7 (from 20.8% to 12.2%) for the same decrease in spray momentum. The higher level of deposition of spray and ambient aerosol in the mouth-throat geometry was attributed to the simpler geometry of the USP-IP, which lacks particle-tongue impaction. Furthermore, it was noted that the deposition of ambient aerosols was much larger in mouth-throat models than in the USP-IP. For capillary aerosol generation spray source the particle size was an additional parameter that should be taken into consideration. For particles greater than 3 μm, the deposition patterns in mouth-throat and USP-IP were very similar and only differed by 10 %. On the other hand, for particle sizes smaller than 3 μm the deposition in the USP-IP is 300% lower than in mouth-throat models.

The deposition pattern of monodispersed particles in an idealised mouth-throat geometry was studied numerically by Matida et al. (2006) using mean flow tracking, large eddy simulation (LES) and finally shear stress transport (SST) with EIM. 20,000 particles with a density of 912 kg/m^3, and diameters of 2.5 μm, 3.7 μm and 5 μm, respectively, were injected from an inlet with a diameter of 3 mm and an initial velocity of 65 m/s. Steady air flow with a volumetric flow rate of 32.2 l/min accompanied the injected particles. The predicted deposition fraction appeared to be in good agreement with measured data obtained by Dehaan & Finlay ,(2004). In this study, experiments showed an average deposition value of 60% for all of the particles. Simulation results show that standard LES predicted 50% deposition, whereas SST/EIM predicted 90% deposition and mean flow tracking (i.e. without accounting for turbulence effects on particle motion) around 20%. It was concluded that LES appears to capture the relevant flow features that SST/EIM cannot replicate, mainly in the wake of the inlet jet and in near-well regions.

The effect of the duration of the aerosol generation was studied by Worth Longest et al. (2009). The work involved a deposition study of aerosol through a mouth-throat model and

the USP-IP. The capillary aerosol generation time varied from 1 to 4 seconds while the dose mass of the spray source was fixed for all aerosol generation periods. The CFD result indicated that, as the aerosol injection time increases from 1 to 4 second, the deposition fraction in the mouth-throat model and the USP-IP drops by almost 30% and 60%, respectively. It should be stated that due to the sudden release of particles into the domain, a large momentum source is created during the initial formation of aerosols: the so called "burst effect". The presence of this burst leads to particle deposition enhancement. Increasing the duration of aerosol spray generation, results in dissipation of the burst effect, which reduces the associated deposition. For all aerosol generation times, the CFD deposition predictions were in good agreement with in-vitro results. Thus, it was concluded that a good strategy to reduce deposition is to increase the aerosol generation time at a constant dose mass.

The influence of flow pathways and air inlet on the deposition in a USP throat and the inhaler device itself were investigated by Worth Longest & Hindle (2009). Similar to Worth Longest et al. (2009), a capillary aerosol generation source was utilised. The aerosol was injected into a USP-IP accompanied by 30 l/min of co-flow air through prototypes of the inhaler body and mouthpiece with large and small air inlets. The inhaler body was cylindrical with length and diameter of approximately 70 mm and 26.4 mm, respectively. Two small circular air inlets with diameter of 3 mm were situated on the sides of the inhaler body. In another geometry, the effect of inlet air quantity was investigated by introducing multiple inlets positioned at the back of the inhaler body. This produced an effective inlet flow area of 352 mm^2. Results implied that the configuration of the flow pathway, near the nozzle, and the diameter of the air inlet, drastically influence the particle deposition level. As the diameter of inlet air reduces, the turbulence intensity inside the mouthpiece significantly rises and hence increases drug deposition within the mouthpiece. It was concluded that turbulence intensity and effective diameter of the mouthpiece are two major design parameters that directly influence particle deposition.

A study of pMDI spray parameters was undertaken using commercial CFD code FLUENT by Oliveira et al. (2010 a). A spray source was modelled assuming that it is emitted from a pMDI into a three dimensional cubic test box at ambient conditions with a co-flow air. The air was flowing into the test box at a constant velocity of 5 m/s. 100 µg of Ventolin particles

were injected as non-evaporating solid particles with typical actuation duration of 0.1 second. The initial velocity of the particles was set to 30 m/s in horizontal direction. The particle diameters were in the range of 1.22 µm to 49.5 µm with a Rosin-Rammler distribution. The drug particles were defined as solid material, which assumes that complete flash evaporation of propellant takes place instantaneously after the aerosol emerges from the spray orifice. Lagrangian particle tracking and two-way coupled calculations were selected to obtain particle trajectories and consider the effect of discrete phase on continuous phase. It was found that the particle velocity starts from a maximum value and adapts to the air flow mean velocity in a relatively short time. This was due to the rapid momentum transfer from the particulate to the gas phase. On the other hand, acceleration and perturbation of the air flow field was evident particularly in the spray source region near the spray orifice where the particles strongly interact with the surrounding air. Moreover, in a similar study, the cubic test box was replaced by a spacer. To refine the model a time-varying mathematical representation of the inhalation and exhalation velocity profile was included to the simulation Oliveira et al. (2010 b). The inhalation cycle velocity was introduced using a sine function with a magnitude of approximately 5 m/s whereas the exhalation cycle with zero velocity. It was assumed that the inhalation phase duration is 1/3 of the total breathing cycle. According to the post-processed result of the air flow inside the spacer, a large recirculation zone was observed straight after the inlet area of the spacer due to the sudden expansion. It was then observed that the recirculation zone traps and slows down the particles, which leads to a substantial particle velocity reduction. The decrease in velocity results in reduced inertial particle deposition. Finally, the authors stress the importance of high quality experimental data and further customisation of the software to obtain reliable results.

2.7 Summary and conclusion

In this chapter a comprehensive review of various topics which directly and indirectly relate to different aspects of pMDI was presented. The review of theoretical models of two-phase flow through tubes and apertures suggested that prediction of mass flow rate is directly linked with the assumptions made to describe interphase mass, momentum and heat transfer between flow phases. Various models are presented in the literature which were based on homogeneous and non-homogeneous flow regime, and based on thermodynamic

equilibrium and dis-equilibrium. In the case of pMDI no definitive knowledge regarding these processes is known. Therefore extreme scenarios of interphase phenomenon can be evaluated to provide deeper understanding of flow characteristics. Slip equilibrium model (SEM) is useful when momentum transfer between phases does not occur and phases travel with different velocities. The Homogeneous equilibrium model (HEM) is appropriate for the prediction of the critical mass flux in long tubes with sufficient residence time for the fluid to reach thermodynamic equilibrium. Henry (1968) discusses that flow does not reach equilibrium in short tubes and proposed a model accounting for finite rate of masse transfer resulting in improved prediction of mass flow rate. The Homogeneous Frozen Model (HFM) has been shown by Clark (1991) to perform adequately in pMDI applications where both nozzles are short. Effect of liquid metastability can also be included in models using empirical correlations (Attou & Seynhaeve, 1999; Feburie et al., 1993). However, the difficulty of these correlations is that they are case specific and the values of empirical constants need to be adjusted on a case-by-case basis as working fluid and geometry of the tube changes. Thus, there is a need to provide more detailed consideration of the effects of metastability in the context of flows of evaporating pMDI propellant formulations.

The review of the atomisation literature revealed that there is still no universally accepted atomisation mechanism for pMDI. Clark (1991) suggested that primary atomisation may be due to an aerodynamic mechanism (akin to air-blast/air-assist atomisation) or a flashing mechanism (akin to effervescent atomisation). Therefore, these mechanisms are included in the review. Aerodynamic atomisation of a fluid stream occurs when disruptive aerodynamic forces overcome the surface tension and viscous forces. This manifests itself in terms of growing of disturbances on the liquid, leading to its disintegration and formation of droplets. In the case of flash atomisation, rapid growth of the localised bubbles in metastable liquid element leads to disintegration and reducing liquid length scale. Following formation, droplets may be transported to regions where strong aerodynamic loads can potentially deform droplets and lead to further disintegration. Due to high velocity of pMDI sprays inside and near-orifice region, such mechanism appears to be locally significant.

With reference to pMDI application, Clark developed a correlation that captures the influence of the volatility of the formulation on the final size of the droplets, but it contains an adjustable constant with dimension of length. In terms of theoretical models, no

predictive models are available at present with the capability to predict droplet size from first principles. Fundamental study of primary atomisation in pMDIs is needed to understand the physical process governing the formation of therapeutic droplets.

CFD modelling in the development of pharmaceutical sprays was also reviewed and it is concluded that the most widely used approach in previous studies is the Lagrangian particle tracking framework to simulate the discrete phase and to obtain particle trajectories. When the mass loading of the discrete phase is significant, two-way coupled calculations must be performed to obtain sufficient accuracy in particles trajectories calculations. In the case of spray injection into geometry, steady co-flow air 30 l/min were used in almost all of the studies. The majority of the studies were considering the USP-IP or biological mouth-throat geometry as the preferred computational domain in order to study the deposition fraction of the particles.

One shared shortcoming which is observed in the CFD practices was the definition of the spray source (e.g. initial droplet velocity, size distribution temperature, etc.). This element of the modelling has received less attention to date and is the key factor in establishing initial condition of the spray which in turn governs the fate of the spray in far-field. The literature suggests that the spray source is so far defined based on assumed values or experimental data which are case specific. No attempt has been made to link the properties of the spray source to the flow conditions inside the actuator and spray orifice using commercial CFD codes. There is a significant need for accurate models if more realistic CFD simulations are to be conducted.

Chapter Three

Internal Flow Model of pMDI

3 Chapter Three: Internal Flow Model of pMDI

3.1 Introduction

The phenomenological flow model of Fletcher (1975) and Clark (1991), which its basis was later implemented by Dunbar and Miller (1997), has greatly contributed towards the understanding of propellant flow in pMDI twin-orifice systems. The original work of Fletcher and Clark was developed based on two main assumptions:

i. thermodynamic equilibrium in the metering and expansion chambers, and
ii. homogeneous frozen flow through the valve and spray orifices.

Fletcher's model was formulated for continuous discharge of the propellant and subsequently developed by Clark for metered discharge. Although the outcome of the models was in reasonable general agreement with their experimental results, a number of problems remained unsolved:

- The measured expansion chamber temperature was greater than the saturation temperature corresponding to expansion chamber pressure. This implies that the liquid is superheated and the two-phase mixture is metastable in this space.
- The velocity of the plume outside the spray orifice was underestimated.
- Two-phase flow regime played a major part in determining the spray flow rate, but experimental evidence relating to the nature of the flow in pMDI actuators was insufficient to provide a firm basis for theoretical developments.
- Droplet size was not predicted from first principles.

Although the phenomenological model has satisfactory track record, the afore-mentioned drawbacks suggest that there are still opportunities for the model to be pushed forward scientifically. Atomisation will be studied in chapter 4 of this thesis. The aim of this chapter is to develop a novel one dimensional (1-D) numerical model of the propellant flow inside a pMDI actuator with focus on mass flow rate and fluid conditions in the spray orifice just prior to emergence of the aerosol plume . It should be noted that considerable differences in the predicted flow rate and pressure ratios from various 1-D models of flashing propellant flows have been identified previously (Huff, 1985). Thus, the task at hand is to compare the performance of alternative 1-D models of flashing propellant flow in pMDI applications. The

outcomes of internal flow model are temporal flow characteristics inside the twin-orifice system such as pressure/temperature inside the chambers and quantification of propellant evaporation in these volumes. Predicted near-orifice spray velocity will be validated against PDA measurement for different propellant systems and actuator geometric properties. The model developed in this chapter will be used in the following chapters to construct a predictive atomisation model (chapter 4), and specify a time dependent pMDI spray source for CFD simulations (chapter 6).

3.2 Internal flow model (IFM)

3.2.1 Conceptual image of flow models in pMDI

3.2.1.1 HFM/HEM/SEM

Four distinct scenarios of two-phase flow interphase phenomena through orifices are considered namely (i) Homogeneous Frozen Model (HFM), (ii) Homogeneous Equilibrium Model (HEM), (iii) Slip Equilibrium Model (SEM) and (iv) Hybrid Homogeneous Frozen Model (H-HFM). These models are schematically shown in Figure 3.1. All models are homogeneous, i.e. vapour and liquid phase are interpenetrating continua. In the HFM model, the flow travels from the reservoir to the nozzle exit without mass transfer: no evaporation takes place and hence the size of any pre-existing, finely dispersed vapour bubbles is constant. At the other extreme, the HEM model assumes that vapour and liquid undergo mass transfer such that vapour bubbles traveling through the nozzle grow to their maximum size corresponding to the thermodynamic equilibrium at the prevailing state at the nozzle exit. In the HFM and HEM models, both phases here are also traveling with the same velocity. The conceptual image associated with the SEM model involves an annular liquid film traveling along the walls of the nozzle and the vapour flowing in the core. Similar to HEM, this vapour core is corresponding to maximum evaporation rate corresponding to thermodynamic equilibrium condition at the nozzle exit. Here the phases are travelling with different velocities.

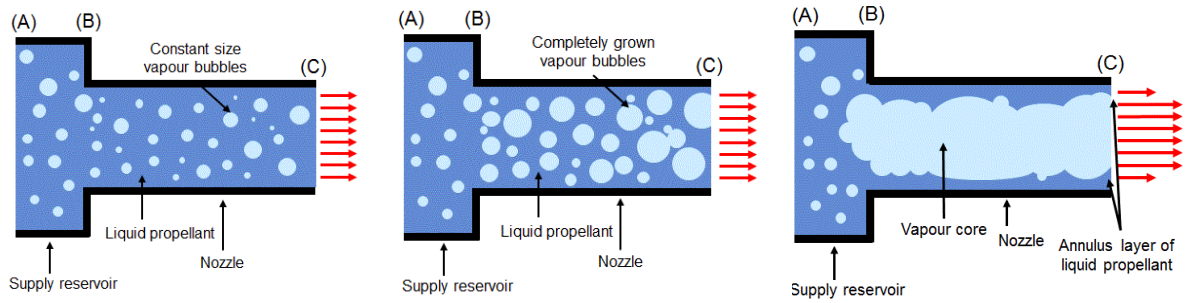

(a) HFM **(b) HEM** **(c) SEM**

Figure 3.1 Schematic of flow models through nozzle

3.2.1.2 Hybrid-HFM

Figure 3.2 shows a schematic of the flow process for vapour-liquid propellant mixture from the reservoir through the spray orifice constriction for the Hybrid-HFM (H-HFM) model. It is known that the most significant length scale reduction takes place inside spray orifice: from the order of 100 μm down to the range 1-10 μm (Versteeg et al., 2006).

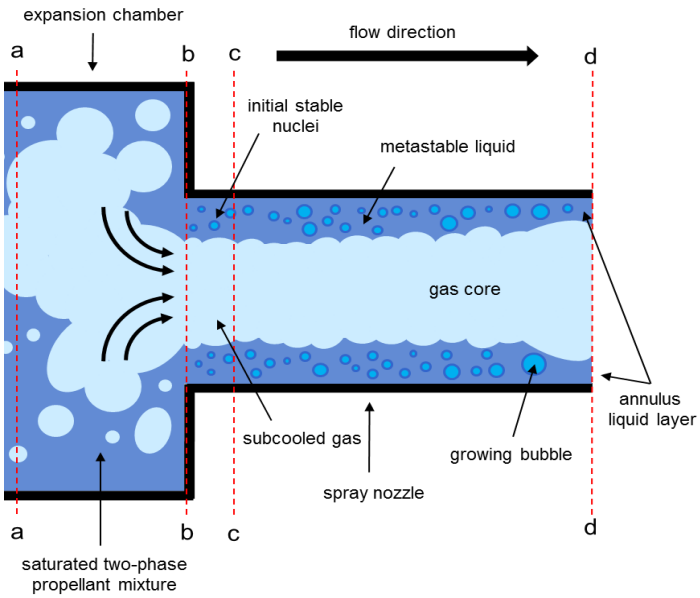

Figure 3.2 Schematic of Hybrid-HFM

Therefore the H-HFM model is only applied to flow through spray orifice. The term hybrid indicates the incorporation of finite mass transfer rate into frozen assumption. Flow visualisations suggest that propellant liquid from the expansion chamber enters the spray nozzle by flowing along the walls and the reservoir vapour forming the core flow (Versteeg et al., 2006). As the mixture enters the spray orifice (section b-b), it accelerates and, as a consequence, experiences a rapid pressure drop. This rapid depressurisation turns the liquid to metastable liquid. This metastability results in formation of bubble embryos (between sections b-b & c-c). The resulting bubble embryos may then grow and if the growth is sufficient, a vapour-liquid equilibrium state can be reached. If the radius of bubble nuclei between sections b-b & c-c are larger than a critical value, the resulting nuclei can grow explosively as the flow travels through the spray orifice (between sections c-c & d-d). This phenomenon is widely known as flash boiling. The population of nuclei per unit volume of the liquid as well as the critical nucleus size are functions of the degree of superheat of the liquid for homogeneous and heterogeneous nucleation (Sher et al., 2008). In absence of frictional loss, the growth of bubbles and evaporation of the metastable liquid propellant is solely responsible for flow acceleration and the subsequent pressure drop between inlet and exit of the spray nozzle.

3.2.1.3 Flow inside chambers

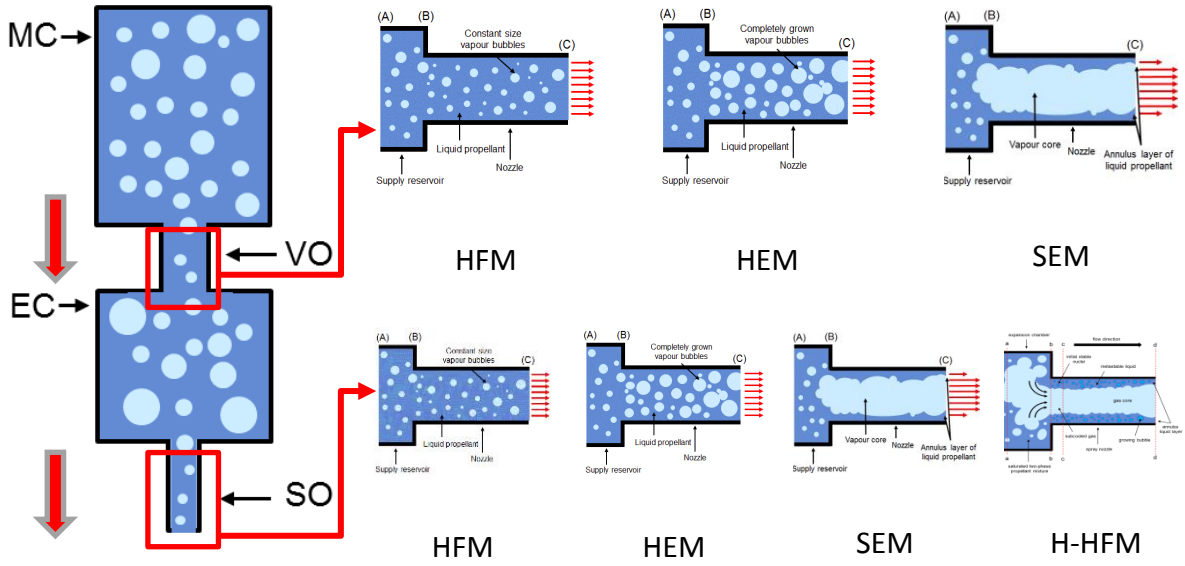

Figure 3.3 Schematic of propellant flow inside chambers

As the propellant flows through the orifices (using one of the orifice models schematically shown in Figure 3.3), the fraction of liquid inside the upstream chamber reduces. Subsequently propellant evaporates and the vapour fills the voidage in the chambers. Our model paradigm is developed based on ideal mixing of vapour and liquid phases. This means that the phases are truly mixed as they are uniformly distributed across the two-phase mixture.

3.2.2 General modelling assumption

In this section, the relevant and global modelling assumptions, established throughout the modelling are set and described as follows:

- General modelling assumptions:
  - ✓ One-dimensional flow: variations of the propellant flow occur in the flow direction. This assumption implies that any other changes (in transport or thermodynamic properties) perpendicular to the flow path are negligible.
  - ✓ Quasi-steady flow: flow discharge process through the actuator is assumed to be quasi-steady suggesting that for any small and finite time interval, the conditions of the flow in actuator compartments follows steady conditions. This assumption is previously used in other work (Clark, 1991; Dunbar and Miller, 1997; Ju et al., 2010).

- ✓ Adiabatic flow: due to the rapid nature of the metered discharge the residence time of the propellant flow in the spray orifice is too short (order of 20 μs) for significant heat transfer to take place between the actuator and the propellant.
- ✓ Zero nozzle entrance velocity of the phases (i.e. large upstream reservoir compared with throat diameter)
- ✓ Fluid energy budget: variations in propellant temperature and kinetic energy are due to evaporation and expansion caused by local pressure differences. Any contribution due to surface energy is neglected.
- ✓ Gravity: The effect of gravitational force on the propellant flow is neglected in the calculations.
- ✓ Isentropic expansion inside the nozzle (adiabatic and frictionless flow)
- ✓ Portion of drug in the propellant is very low (typically less than 1%). So the model development concentrates on the study propellant expansion and propellant vapour-liquid interactions (chapter 5 of this thesis considers the effect of non-volatile excipients in the formulation, particularly ethanol)

3.3 Equations of flow models through orifices

3.3.1 Single phase flow discharge

At the start of the actuator depression, the initial discharge through the valve orifice will be single phase and liquid only, which is evaluated using equation 3-1:

$$G_{sp} = C_{d,vo}\left(2\frac{p_{0,mc} - p_{amb}}{v_l}\right)^{\frac{1}{2}} \qquad 3\text{-}1$$

Where $G_{sp}$is the single liquid phase mass flux. $p_{0,mc}$and p_{amb} are initial pressure inside metering chamber and ambient pressure prevailing in the expansion chamber at t = 0, respectively, and v_l is liquid specific volume. Finally $C_{d,vo}$ is the discharge coefficient of valve orifice.

3.3.2 Two-phase flow discharge

The continuity and momentum equations for homogenous two-phase mixture in nozzle of constant cross section (such as A), neglecting the effects of wall friction are shown by equations 3-2 & 3-3 respectively:

$$\dot{m} = \frac{AV}{\bar{v}} = GA \quad 3\text{-}2$$

$$-Adp = \dot{m}dV \quad 3\text{-}3$$

In which $\dot{m}$ and V are the mass flow rate and velocity, respectively. $\bar{v}$ is the two-phase mixture specific volume and G is the two-phase mass velocity (mass flux). Combining 3-2 and 3-3 yields:

$$-dp = GdV \quad 3\text{-}4$$

And two-phase mixture specific volume and enthalpy are defined as equations 3-5a-b):

$$\bar{v} = xv_g + (1-x)v_l \quad 3\text{-}5a$$

$$\bar{h} = xh_g + (1-x)h_l \quad 3\text{-}5b$$

Where subscripts g and l denote the related gas phase and liquid phase property, respectively. v is the specific volume and h is the enthalpy. Eventually x is the two-phase flow quality defined as the ratio of vapour mass to the total mass of the two-phase mixture.

3.3.2.1 HFM

3.3.2.1.1 Modelling assumptions:

- Homogeneous flow regime: liquid and gas phases are fully mixed and distributed uniformly. Thus the mixture properties can be described by means of mass-weighted average properties.
- Complete momentum transfer between phases: both phases travel with the same velocity
- Liquid is considered as incompressible and vapour phase behaves as ideal gas

- Frozen flow composition: No mass transfer along the flow path from the supply reservoir to the throat. This assumption is valid, because the fluid residence time in the orifice is short and hence there is not enough time for a significant amount of transfer of heat and mass between the two phases.
- Choked flow: if the pressure ratio of downstream and upstream reservoir ($\eta = p_{ds}/p_{us}$), becomes less than the critical value corresponding to critical pressure, ($\eta_c = p_c/p_{us}$), the mass flow rate does not increase by further decrease in downstream pressure.

3.3.2.1.2 Subsonic discharge

For a subsonic isentropic flow the one-dimensional Euler equation can be integrated along the orifice as follows:

$$\frac{1}{2}(V_t^2 - V_0^2) = -\int_0^t \bar{v}\, dp \qquad 3\text{-}6$$

Where $\bar{v}$ is evaluated from equation 3-5a. The integration takes place between the supply reservoir (denoted by subscript 0) to the throat (denoted by subscript t). The frozen flow assumption suggests that the flow quality remains unchanged (no mass transfer, so $x_0 = x_t = Const.$). Furthermore, the incompressible liquid assumption specifies the change in liquid specific volume along the integration path is negligible ($v_{l,0} = v_{l,t}$). Pursuing the isentropic assumption for the gas expansion ($p_0 v_{g,0}^{\gamma} = p v_g^{\gamma} = Const.$) and taking the upstream flow to be at stagnation conditions ($V_0 = 0$), equation 3-6 can be analytically integrated as follows:

$$(1 - x_0)v_{l,0}(p_0 - p_t) + x_0 \frac{\gamma}{\gamma - 1}\left(p_0 v_{g,0} - p_t v_{g,t}\right) = \frac{1}{2}V_t^2 \qquad 3\text{-}7$$

Let us define the variable η, denoting the ratio of throat pressure to upstream pressure as equation 3-8:

$$\eta = p_t/p_0 \qquad 3\text{-}8$$

In conjunction with isentropic gas flow assumption, equation 3-7 yields:

$$\frac{p_t v_{g,t}}{p_0 v_{g,0}} = \eta^{\frac{\gamma-1}{\gamma}} \qquad 3\text{-}9$$

Using equation 3-5a, the average specific volume of the mixture can be written as follows:

$$\overline{v_t} = \eta^{-\frac{1}{\gamma}} x_0 v_{g,0} \left[\left(\frac{1-x_0}{x_0} \right) \left(\frac{v_{l,0}}{v_{g,0}} \right) \eta^{\frac{1}{\gamma}} + 1 \right] \qquad 3\text{-}10$$

By substitution of 3-7 and 3-9 into equation 3-6 followed by some re-arrangements, it is possible to obtain:

$$G_t = C_d \left(\frac{p_0}{x_0 v_{g,0}} \frac{2\eta^{\frac{2}{\gamma}}}{\left[\left(\frac{1-x_0}{x_0} \right) \left(\frac{v_{l,0}}{v_{g,0}} \right) \eta^{\frac{1}{\gamma}} + 1 \right]^2} \left[\left(\frac{1-x_0}{x_0} \right) \left(\frac{v_{l,0}}{v_{g,0}} \right) (1-\eta) + \frac{\gamma}{\gamma-1} \left(1 - \eta^{\frac{\gamma-1}{\gamma}} \right) \right] \right)^{\frac{1}{2}} \qquad 3\text{-}11$$

Where C_d is the discharge coefficient. Equation 3-11 is also derived by Clark (1991 - page 165) using definition of speed of sound in homogeneous two-phase flow. In the subsonic discharge regime, the nozzle throat pressure is equal to the downstream pressure of the reservoir. Thus, by having the knowledge of upstream conditions, equation 3-11 gives the mass velocity at the throat for this case.

3.3.2.1.3 Critical discharge

For the case of critical discharge, the throat pressure in equation 3-7 is no longer equal to the downstream reservoir pressure as the choking pressure is generally higher. This pressure is also known as critical pressure, p_c and the pressure ratio corresponding to critical pressure is denoted as η_c:

$$p_t = p_c \;\rightarrow\; \eta = \eta_c$$

Since the critical pressure is not known and must be solved iteratively, as part of the solution procedure using Fletcher's (1975 – page 92) equation 3-12:

$$\left(\frac{1}{\eta_c}-1\right)+X_c\frac{\gamma}{\gamma-1}\left(\eta_c^{\frac{1-\gamma}{\gamma}}-1\right)=\frac{\gamma X_c}{2}\left(\frac{1}{X_c}+1\right)^2 \qquad 3\text{-}12$$

Where:

$$\frac{1}{X_c}=\left(\frac{1-x_0}{x_0}\right)\left(\frac{v_{l,0}}{v_{g,0}}\right)\eta_c^{\frac{1}{\gamma}} \qquad 3\text{-}13$$

Equation 3-12 is obtainable when velocity at spray orifice exit is equated to two-phase speed of sound (Fletcher 1975). For the case where the quality x_0 in equation 3-13 is close to unity, one may conclude the following:

$$\left(\frac{1-x_0}{x_0}\right)\left(\frac{v_{l,0}}{v_{g,0}}\right)\ll 1 \qquad 3\text{-}14$$

And hence:

$$\frac{1}{X_c}\to 0$$

This would lead to a simplified version of 3-13 to predict critical pressure ratio for high quality two-phase flow, which is also familiar from isentropic gas dynamics (Abramovich, 1976):

$$\eta_c=\left(\frac{2}{\gamma+1}\right)^{\frac{\gamma}{\gamma-1}} \qquad 3\text{-}15$$

3.3.2.2 HEM

3.3.2.2.1 Modelling assumptions:

The modelling assumptions used to derive HEM equations are presented as follows:

- Homogeneous flow regime: liquid and gas phases are fully mixed and distributed uniformly across the flow. Thus the mixture properties can be described by means of mass-weighted average properties.
- Complete momentum transfer between phases: both phases travel with the same velocity
- Liquid is considered as incompressible
- Both phases are at thermal and thermodynamic equilibrium at the spray orifice exit i.e. properties of the phases correspond to those of a static, equilibrium two phase system with plane interfaces.
- Surface tension effects are neglected.

3.3.2.2.2 Subsonic discharge

For subsonic discharge, neglecting the kinetic energy of the two-phase mixture in upstream reservoir, the velocity at any section of the nozzle can be calculated using the adiabatic energy equation 3-16 (Starkman et al., 1964):

$$V_t = \sqrt{2(\bar{h}_0 - \bar{h})} \qquad 3\text{-}16$$

Substitution of equation 3-16 in continuity equation has shown by equation 3-2 yields:

$$G_t = C_d \frac{1}{\bar{v}} \sqrt{2(\bar{h}_0 - \bar{h})} \qquad 3\text{-}17$$

The average enthalpy of two-phase mixtures is computed by equation 3-5 b) and C_d is the discharge coefficient of the orifice.

3.3.2.2.3 Critical discharge

For a set of stagnation conditions of the supply reservoir, the critical mass discharge occurs at the pressure ratio where the maximum throat flow rate is achieved. However, it is not possible to derive an expression for critical pressure ratio similar to equation 3-12 for frozen flow model. In order to determine choking conditions for a given fluid pressure and temperature in the upstream reservoir, the pressure ratio is systematically reduced from 1 to 0 in small steps. At each step the mass velocity is evaluated and the maximum mass flow rate can be determined (Starkman et al., 1964) for the given upstream conditions.

3.3.2.3 SEM

3.3.2.3.1 Modelling assumptions:

- Separated flow regime: two-phase flow pattern inside the orifice is annular (with no entrainment), meaning that vapour flows in the core and liquid film moves along the walls of the nozzle.
- No momentum transfer between the phases: phases have different velocities in the nozzle and are related using the slip ratio, $S = V_g/V_l$.
- Liquid is considered as incompressible
- Both phases are at thermal and thermodynamic equilibrium at the spray orifice exit i.e. properties of the phases correspond to those of a static, equilibrium two phase system with plane interfaces.
- Surface tension effects are neglected.
- Isentropic expansion inside the nozzle

3.3.2.3.2 Subsonic discharge

In the subsonic discharge regime, continuity equation (equation 3-2) can be also represented by equation 3-18a (or 3-18a3-18b):

$$G = \frac{\dot{m}}{A} = \frac{\alpha}{x}\frac{\dot{m}_g}{A_g} = \frac{\alpha}{x}\frac{V_g}{v_g} \qquad \text{3-18a}$$

$$G = \left(\frac{1-\alpha}{1-x}\right)\frac{\dot{m}_l}{A_l} = \left(\frac{1-\alpha}{1-x}\right)\frac{V_l}{v_l} \quad \text{3-18b}$$

In above equations subscripts l and g represents liquid related and gas related properties and α is two-phase void fraction is determined by means of equation 3-19 (Whalley, 1987).

$$\alpha = \frac{1}{1 + \left(\frac{1-x}{x}\right)\left(\frac{v_l}{v_g}\right)S} \quad \text{3-19}$$

The energy equation is expressed using equation 3-20:

$$h_0 = x_0 h_{g0} + (1 - x_0)h_{l0} = x\left(h_g + \frac{V_g^2}{2}\right) + (1-x)\left(h_l + \frac{V_l^2}{2}\right) \quad \text{3-20}$$

This equation may be combined with equation 3-18 (a) and, using the definition of slip ratio S, gives the following relation for mass velocity (Moody, 1965):

$$G_t = \frac{\dot{m}}{A} = C_d \sqrt{\frac{2(\overline{h_0} - \bar{h})}{\left(xv_g + (1-x)v_l S\right)^2\left(x + \frac{1-x}{S^2}\right)}} \quad \text{3-21}$$

Specific enthalpy of the mixture in calculated using equation 3-5a3-5 (b) and flow quality can be obtained using the isentropic assumption:

$$x = \frac{s_0 - s_l}{s_{lg}} \quad \text{3-22}$$

Equation 3-21 demonstrates that the mass velocity G is a function of slip ratio S. Maximisation of G with respect to S yields the following relation for the slip ratio (Moody, 1965):

$$S = \left(\frac{v_g}{v_l}\right)^{1/3} \qquad 3\text{-}23$$

3.3.2.3.3 Critical discharge

In order to determine the choking conditions, the maximum flow rate through the nozzle has to be evaluated. Similar to HEM no specific equation can be derived for pressure ratio calculation. The same procedure as described for HEM critical discharge needs to be implemented. The pressure ratio is systematically reduced from 1 until the maximum mass velocity is found; the corresponding pressure ratio is the choking pressure ratio.

3.3.2.4 Hybrid-HFM

The HFM model assumes no evaporation in the spray orifice, whereas the equilibrium models assume that the fluid is in thermodynamic equilibrium at the spray orifice exit: i.e. maximum evaporation. The Hybrid-HFM model considers intermediate levels of propellant evaporation inside spray nozzle. This recognises that finite mass transfer rates will occur during bubble growth and the fluid state inside the spray orifice does not achieve thermodynamic equilibrium. Thus, the fluid is metastable.

3.3.2.4.1 Modelling assumptions

- Homogeneous nuclei distribution in liquid layer
- Adiabatic and spherical bubble growth under thermodynamic and thermal equilibrium
- Inclusion of thermodynamic disequilibrium by considering propellant metastability and vaporisation index
- Isentropically expanding core gas and isentropically evolving metastable liquid
- Condensation of initial gas inside the expansion chamber as it experience rapid pressure drop is neglected.
- Complete momentum transfer between phases: both phases travel with the same velocity , hence $V_g = V_l$.

3.3.2.4.2 Mixture constituents and mixing rule

As the mixture flows through the spray orifice from supply reservoir, a pressure drop is experienced by flow at the constriction (between supply reservoir and nozzle inlet). This creates metastable propellant, which in turn leads to formation of bubble embryos in the metastable liquid. The resulting bubbles grow in size and cause pressure drop along the nozzle. Subsequently, this pressure drop promotes further evaporation of liquid phase. Evaporation of a certain mass of metastable liquid converts it into saturated vapour (located inside the growing bubbles) and a small layer of saturated liquid (surrounding the bubble). The saturated vapour inside the supply reservoir experiences the pressure drop also, and becomes subcooled inside the nozzle. The propellant mixture will, in general, consist of four separate constituents, which are (i) subcooled core gas, (ii) superheated metastable liquid, (iii) saturated gas and (iv) saturated liquid. Distributions of these constituents are schematically shown in Figure 3.4 by means of distinct colour coding.

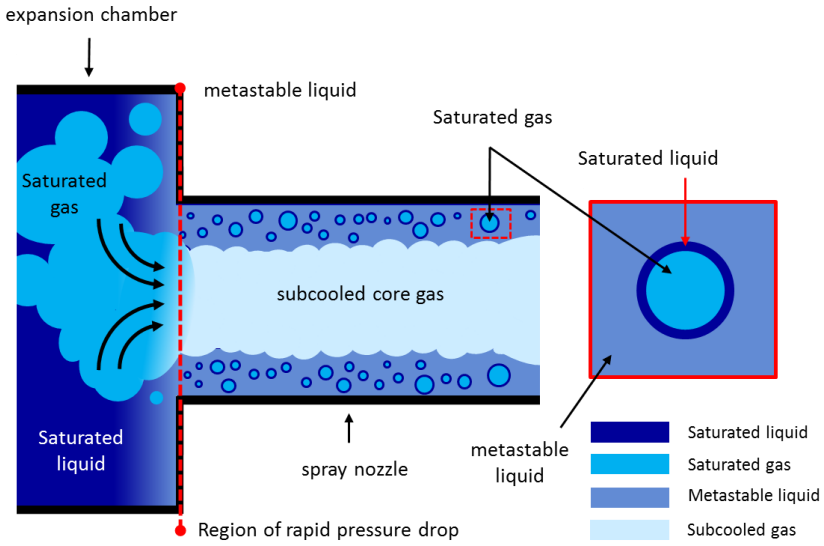

Figure 3.4 Schematic of mixture constituents inside expansion chamber and spray nozzle

Let the initial mass fraction of vapour and liquid inside the supply reservoir (expansion chamber) to be expressed by x_0 and $(1 - x_0)$, respectively. Let the mass fraction of additional vapour inside the nozzle (due to bubble growth) be denoted by x_{RP}. In the current model it is assumed during evaporation only a fraction of metastable liquid is converted into saturated liquid and vapour. This fraction converted to saturated thermodynamic state is represented by y as described by (Feburie et al., 1993) and (Attou &

Seynhaeve, 1999) and is known as vaporisation index. The remaining $(1-y)$ fraction of metastable liquid experiences isentropic evolution. Such representation allows us to describe specific volume and specific enthalpy of the mixture by means of mass weighted mixing rule, as expressed by equations 3-24 and 3-25.

$$\bar{v} = x_0 v_{g,core} + (1-x_0)\left[(1-y)v_{l,M} + (y-x_{RP})v_{g,sat} + x_{RP}v_{l,sat}\right] \quad 3\text{-}24$$

$$\bar{h} = x_0 h_{g,core} + (1-x_0)\left[(1-y)h_{l,M} + (y-x_{RP})h_{g,sat} + x_{RP}h_{l,sat}\right] \quad 3\text{-}25$$

In equation 3-24 and 3-25, subscripts sat denotes saturated specific properties, which are evaluated along the saturation line at local pressure. $v_{l,M}$ and $h_{l,M}$ are the specific volume and enthalpy of metastable liquid. These properties are determined by linear extrapolation of subcooled liquid properties in metastable domain (the region bounded by the saturated liquid line and spinodal curve) along lines of constant entropy (Attou & Seynhaeve, 1999). Subscript $core$ represents the properties related to core gas. The core gas goes under isentropic expansion and hence its specific volume, $v_{g,core}$, is calculated using equation 3-26:

$$v_{g,core} = v_{g,0}\left(\frac{p_0}{p}\right)^{1/\gamma} \quad 3\text{-}26$$

To evaluate equations 3-24 and 3-25, y and x_{RP} and pressure drop at spray orifice constriction, need to be represented which are taken care of in the following sub-sections.

3.3.2.4.3 Two-phase flow at constriction entrance

The sudden pressure drop associated with abrupt contraction of two-phase fluid from a large reservoir to the spray orifice is assumed to take place very rapidly, so without heat and mass transfer between the phases. The pressure drop is obtained using the following expression (ESDU 89012, 1989):

$$p = p_0 - \Phi^2 \times \Delta p_{sp} \quad 3\text{-}27$$

Where p is the pressure at the nozzle inlet and p_0 is the upstream pressure of supply reservoir and Δp_{sp} is the single phase (liquid phase) pressure drop corresponding to the case where liquid is flowing alone at same mass flow rate as two-phase mixture. The two-phase multiplier, Φ^2, is evaluated as (ESDU 89012, 1989):

$$\Phi^2 = 1 + x\left[\left(\frac{v_{g,in}}{v_l}\right) - 1\right] \quad 3\text{-}28$$

where $v_{g,in}$ is related to the vapour specific in the supply reservoir, $v_{g,0}$, using isentropic expansion relation:

$$v_{g,in} = v_{g,0}\left(\frac{p_0}{p}\right)^{1/\gamma} \quad 3\text{-}29$$

The single phase pressure drop Δp_{sp}, is calculated using equation 3-30:

$$\Delta p_{sp} = \frac{G^2}{2\rho_l}\left\{1 - \left(\frac{A_{SO}}{A_0}\right)^2 + \left(\frac{1}{C_c} - 1\right)^2\right\} \quad 3\text{-}30$$

In this equation, G is the mass flux, A_{SO} and A_0 are the cross sectional area of spray orifice and upstream reservoir, respectively. C_c is the single phase contraction coefficient for the orifice, which can be calculated using the following relation:

$$C_c = ae^{b(A_{SO}/A_0)} + ce^{d(A_{SO}/A_0)} \quad 3\text{-}31$$

Where the coefficients are presented in Table 3.1:

Coefficient	a	b	c	d
Value	0.5979	0.1253	0.003628	4.479

Table 3.1 Coefficients for empirical relation of single phase contraction coefficient (ESDU 89012, 1989)

3.3.2.4.4 Determination of vaporisation index (y)

Vaporisation index y in effect describes the kinetics of evaporation. This quantity is generally introduced in the literature based on empirical correlations (Hardy & Mali, 1983; Feburie et al., 1993). Attou and Seynhave (1999) introduce a relaxation equation to evaluate the development of the vaporisation index in evaporating two-phase pipe flows (see section 2.2). In present work we obtain y by assuming all mixture constituents are travelling inside the nozzle with identical velocity. By applying a separate energy balance on the moving liquid layer inside the nozzle, after some bubble growth inside the liquid, the local mean enthalpy of the liquid layer is:

$$\overline{h_l} = h_{l,0} - \frac{V^2}{2} \qquad 3\text{-}32$$

On the other hand, a mass weighted average representation of liquid only mean enthalpy yields the following equation:

$$\overline{h_l} = (1-y)h_{l,M} + (y - x_{RP})h_{l,sat} + x_{RP}h_{g,sat} \qquad 3\text{-}33$$

By equating the right hand side of equations 3-32 and 3-33, and subsequently performing some rearrangements, y can be calculated as follows:

$$y = \frac{\left(h_{l,M} - h_{l,0} - \frac{V^2}{2}\right) + x_{RP}h_{lg,sat}}{h_{l,M} - h_{l,sat}} \qquad 3\text{-}34$$

3.3.2.4.5 Determination of vapour production by bubble growth (x_{RP})

Mass fraction of produced vapour,x_{RP} is directly linked to bubble size development, which is included in the model using approximate solutions of Rayleigh-Plesset equation (hence subscripted as RP). As discussed in chapter 2 section 2.3.2.2, and described by Lienhard and Day (1970) and Plesset & Sadhal (1984), the theory of bubble growth in superheated liquids can be reasonably split into two separate regimes, which both are approximate solution to Rayleigh-Plesset equation. Initially, the first regime (inertial controlled regime) will dominate; the liquid superheat is large and liquid inertia acts as an opposing factor in constraining bubble growth rate and the velocity of the growth is approximately constant. The second regime is the thermal controlled growth regime during which the limiting factor of the growth is the inflow of thermal energy. Here the liquid superheat is not as large since its temperature reduces during vaporisation. Both size growth regimes are calculated using equations 3-35a-b) (Plesset & Zwick, 1954; Forster & Zuber, 1954) and the slowest growth rate is then recognised as "the growth rate" by the model (3-35a-c)):

$$\left(\frac{dD_b}{dt}\right)_{inertial} = 2\left(\frac{2v_l}{3}\,(p_b - p_{amb})\right)^{\frac{1}{2}} \qquad 3\text{-}35a$$

$$\left(\frac{dD_b}{dt}\right)_{thermal} = 2\left(\frac{c_p v_g (T_b - T_{sat,amb})}{v_l h_{lg}}\right)\alpha^{1/2} t^{-1/2} \qquad 3\text{-}35b$$

$$\frac{dD_b}{dt} = min\left\{\left(\frac{dD_b}{dt}\right)_{inertial}, \left(\frac{dD_b}{dt}\right)_{thermal}\right\} \qquad 3\text{-}35c$$

In equations 3-35a-c), D_b is the bubble diameter. Here α represents thermal diffusivity ($= k/\rho c_p$). When the bubble diameter has been calculated, the vapour mass fraction within the liquid due to bubble growth,x_{RP} can be worked out from the following relation:

$$x_{RP} = \frac{n_b \pi {D_b}^3}{6 v_g m_l} \quad 3\text{-}36$$

In which m_l is the mass of the liquid segment flowing into the spray orifice over actuation time step of Δt. n_b is the number of initial bubble nuclei in the superheated liquid. Senda et al. (1994) studied the nucleation of mixtures of n-pentane and n-hexane and proposed the following expression for the number of bubble nuclei per unit volume, N_b is a function of liquid degree of superheat under steady state conditions:

$$N_b = A \exp(\frac{B}{\Delta\theta}) \quad 3\text{-}37$$

where $= 5.757 \times 10^{12}$, $B = -5.279$ and $\Delta\theta$ is the degree of superheat defined by equation 3-38.

$$\Delta\theta = T_l - T_{sat,amb} \quad 3\text{-}38$$

The parameters of Senda's equation are expected to be fluid dependent and, if the nucleation regime is heterogeneous, may also depend on the container geometry. Experimental data for HFA propellants would be required to determine the relevant parameter values. In the present work, the following expression was used:

$$N_b = C_b A \exp(\frac{B}{\Delta\theta}) \quad 3\text{-}39$$

Equation 3-39 assumes that an exponential dependence of the number of nuclei on superheat $\Delta\theta$ is correctly represented by Senda's equation, but uses a correction factor C_b as an adjustable parameter. Since HFAs are much more volatile than n-pentane and n-hexane, it would be reasonable to expect that the number of bubble nuclei per liquid unit volume would be higher than indicated by equation 3-37. The absolute number of nuclei is then calculated by equation 3-40:

$$n_b = N_b Vol_l \quad \text{3-40}$$

In which Vol_l is the volume of the liquid segment flowing into the spray orifice during time Δt:

$$Vol_l = (1 - x_0)\dot{m} v_l \, \Delta t \quad \text{3-41}$$

3.3.2.4.6 Determination of liquid layer void fraction (α_l)

The void fraction of liquid layer as a result of bubble growth can be calculated using equation 3-42:

$$\alpha_l = \frac{x_{RP}/v_{lM,sat}}{x_{RP}/v_{lM.sat} + (1 - x_{RP})/v_{g,sat}} \quad \text{3-42}$$

Where $v_{lM,sat}$ is the mass weighted average of saturated liquid and metastable liquid, specific volumes, obtainable from equation 3-43:

$$v_{lM.sat} = \frac{(1-y)}{(1-x_{RP})} v_{lM} + \frac{(y - x_{RP})}{(1-x_{RP})} v_{l,sat} \quad \text{3-43}$$

3.3.2.4.7 Conservation equations

Continuity, momentum and energy equations are written in differential form for flow of propellant mixture along the nozzle (z-direction), leading to the following system of first-order ordinary differential equations:

$$\frac{d(\dot{m})}{dz} = 0 \quad \text{3-44}$$

$$\frac{d(\dot{m}V)}{dz} + \frac{dp}{dz} = 0 \quad \text{3-45}$$

$$\frac{d}{dz}\left[\dot{m}\left(\bar{h}+\frac{V^2}{2}\right)\right]=0 \qquad 3\text{-}46$$

Using the analogy with single phase critical flow through converging ducts, the mass flow rate through the spray orifice reaches a maximum when the velocity of a two-phase propellant mixture equals the two-phase mixture speed of sound (i.e. $M=1$). Hence, the mass flow rate value is selected in a way that corresponding flow velocity hits sonic velocity at the exit of the spray orifice. In the present method the sonic velocity a is given by equation 3-47a.

$$a=\bar{v}\sqrt{\frac{-\xi_h}{\xi_h\psi_v-\xi_v\psi_h+\xi_v\bar{v}+\Gamma\xi_v\varphi_h-\Gamma\xi_h\varphi_v}} \qquad 3\text{-}47a$$

Where:

$$\xi_h=(1-x_0)\left(h_{l,sat}-h_{l,M}\right)$$

$$\xi_v=(1-x_0)\left(v_{l,sat}-v_{l,M}\right)$$

$$\varphi_h=(1-x_0)\left(h_{lg,sat}\right)$$

$$\varphi_v=(1-x_0)\left(v_{lg,sat}\right)$$

3-47b

$$\psi_v=x_0\left.\frac{dv_{g,0}}{dp}\right|_s+(1-x_0)\left[(1-y)\left.\frac{dv_{l,M}}{dp}\right|_s+x_{RP}\frac{dv_{g,sat}}{dp}+(y-x_{RP})\frac{dv_{l,sat}}{dp}\right]$$

$$\psi_h=x_0\left.\frac{dh_{g,0}}{dp}\right|_s+(1-x_0)\left[(1-y)\left.\frac{dh_{l,M}}{dp}\right|_s+x_{RP}\frac{dh_{g,sat}}{dp}+(y-x_{RP})\frac{dh_{l,sat}}{dp}\right]$$

$$\Gamma=\frac{n_b}{6m_l}\frac{{D_b}^3}{{v_g}^2}\frac{dv_{g,sat}}{dp}$$

The detailed derivation of speed of sound relation is presented in appendix A. Derivation conducted based on the method proposed by (Bouré et al., 1976) and later used by Feburie et al. (1993) and Attou & Seynhaeve (1999).

3.3.2.4.8 PIF algorithm

Critical mass flow rate can be seen as the maximum possible value of the mass flow rate and the minimum impossible value corresponding to fixed thermodynamic condition at the inlet and device geometry. The combination of these two aspects defines the basis of the possible-impossible flow (PIF) algorithm summarised as below (Attou & Seynhaeve, 1999; Feburie et al., 1993):

1) Guess of the mass flow rate
2) Forward marching integration of equations 3-44, 3-45 and 3-46.
3) During integration, if the flow velocity reaches sonic velocity (equation 3-47a) before the end of the spray nozzle, the guessed mass flow rate is too large and flow is impossible ($\dot{m}_{imp}$). Calculation terminates and a possible mass flow ($\dot{m}_{pos}$) rate needs to be re-guessed based on equation 3-48:

$$\dot{m}_{pos} = \frac{\dot{m}_{imp}}{1+\delta} \qquad 3\text{-}48$$

   where δ is a tuneable factor of PIF; its initial value is selected as 0.5.
4) During integration, if the flow velocity does not reach sonic velocity and the exit calculated pressure is larger than the downstream pressure, then the flow is critical and possible. However, the guessed mass flow rate needs to be increased ($\dot{m}_{imp}$) by equation 3-49, so flow velocity would hit sonic velocity at the nozzle exit plane.

$$\dot{m}_{imp} = \dot{m}_{pos}(1+\delta) \qquad 3\text{-}49$$

   Critical mass flow rate is obtained when ϵ is smaller than specified tolerance of 0.001.

$$\epsilon = (\dot{m}_{imp} - \dot{m}_{pos})/\dot{m}_{pos} \qquad 3\text{-}50$$

3.4 Near-orifice expansion model

As diagrammatically shown in Figure 3.5, in choked conditions, the pressure at spray orifice exit p_{SO}, is higher than the downstream atmospheric pressure, p_{amb}. Thus the emerging mixture experiences an abrupt pressure drop as it is expands to the pressure of the surroundings outside the nozzle exit. Fletcher (1975) suggests that this discontinuity results in abrupt vapour expansion, which accelerates the flow by ΔV in the near-orifice region. For the continuous discharge, Fletcher (1975) computed the velocity jump by means of an axial momentum balance on the diverging control volume of the emerging mixture distinguished by dashed red line. Equation 3-51 is therefore obtainable:

$$\Delta V = V_{NO} - V_{SO} = \frac{p_{SO} - p_{amb}}{G} \qquad 3\text{-}51$$

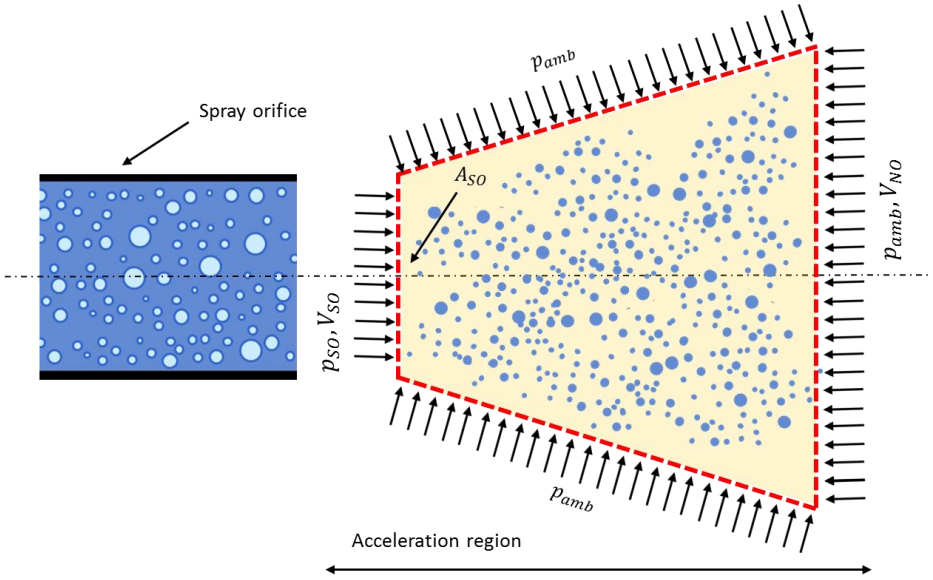

Figure 3.5 Distribution of pressure in emerging spray in near-orifice region

Although the equation is derived for continuous discharge originally, here we apply this principle to metered discharge, which is consistent with quasi-steady assumption proposed by Clark (1991). In equation 3-51, subscripts “NO” and “SO” denotes near-orifice and spray orifice exit regions respectively.

3.5 Fluid state inside chambers

The conditions in the metering chamber and expansion chamber are assumed to be homogeneous and in thermodynamic equilibrium. The thermodynamic state of the two-phase propellant mixture can be defined in terms of the quality and temperature. These quality and temperature can be related to the average specific volume and average specific enthalpy of the propellant in a chamber using equations 3-52a-b):

$$\bar{v} = \frac{m_C}{Vol_C} = v_{l,sat}(T) + x v_{lg,sat}(T) \qquad \text{3-52a}$$

$$\bar{h} = \frac{H_C}{m_C} = h_{l,sat}(T) + x h_{lg,sat}(T) \qquad \text{3-52b}$$

For given mass m_C and enthalpy H_C in a chamber, elimination of x from equations 3-52a-b) results in the following non-linear equation for the propellant temperature in the chamber:

$$\frac{\bar{v} - v_{l,sat}(T)}{v_{lg,sat}(T)} - \frac{\bar{h} - h_{l,sat}(T)}{h_{lg,sat}(T)} = 0 \qquad \text{3-53}$$

The thermodynamic properties of the propellant are defined on the saturation line and hence they are unique functions of temperature. Equation 3-53 is a non-linear equation for the unknown chamber temperature, which may be solved using the Newton-Raphson method of finding the roots of a non-linear equation. When T is computed, the quality of the two-phase mixture in a chamber can be calculated by substitution of its value in equation 3-52a) (or 3-52b).

The instantaneous mass of propellant, m_C within a chamber is a function of time. As the metered discharge process progresses, the instantaneous mass in a chamber is equal to the difference of mass flowing into and out of a chamber through orifices at any time and may be found using equation 3-54:

$$\frac{dm_C}{dt} = \dot{m}_{in,C} - \dot{m}_{out,C} \qquad 3\text{-}54$$

Integration of the equation 3-54 from the start of actuation event when $t = 0$, to an intermediate time when $t = \tau$, yields:

$$m_C(t) = m_C(0) + \int_{t=0}^{t=\tau} \dot{m}_{in,C}(t)dt - \int_{t=0}^{t=\tau} \dot{m}_{out,C}(t)dt \qquad 3\text{-}55$$

Where $m_C(0)$ is the initial propellant mass in a chamber. Moreover, $\dot{m}_{in,C}(t)$ and $\dot{m}_{out,C}$ denote the mass flow rate into/out of a chamber, respectively. Similar to the propellant mass in a chamber, the enthalpy of a chamber is also a function of actuation time. The energy conservation equation for a chamber can be written as follows:

$$\frac{dH_C}{dt} = Vol_C \frac{dp}{dt} + \dot{m}_{in,C}h_{in,C} - \dot{m}_{out,C}h_{out,C} \qquad 3\text{-}56$$

After integration the chamber enthalpy at any actuation instant can be calculated using equation 3-57:

$$H_C(t) = H_C(0) + Vol_C\,[p(0) - p(t)] + \int_{t=0}^{t=\tau} h_{in,C}(t)\dot{m}_{in,C}(t)dt - \int_{t=0}^{t=\tau} h_{out,C}(t)\dot{m}_{out,C}(t)dt \qquad 3\text{-}57$$

Where $H_C(0)$ is the initial enthalpy in the chamber. $\dot{m}_{in,C}(t)$ and $\dot{m}_{out,C}$ are the mass flow rate into and out of a chamber respectively. In section 3.2.2 the velocity inside the chamber is assumed to be negligible compared with velocity inside spray orifice. Hence the kinetic energy in this region can be disregarded. Therefore $h_{in,C}$ and $h_{out,C}$ would be identical to the specific enthalpies of the propellant mixture in the chambers. It is worth mentioning that for the case of metering chamber the term $\dot{m}_{in,C}$ is zero as there is no mass flow rate into this space.

For the sake of simplicity the Euler forward differencing numerical algorithm was chosen to solve equation 3-55 and 3-57.

3.6 Thermodynamic properties of propellant

Thermodynamic property evaluation of the internal flow models uses linkage of the model to NIST-REFPROP. This method of data evaluation encompasses high level of accuracy and also enables us to consider wide range propellants and their mixtures. The program is developed by the US National Institute of Standard and Technology (NIST) and its main purpose is to distribute data of transport and thermodynamic properties of most commonly used fluids in industry (as well as their mixtures) including a wide range of hydrocarbons and refrigerants. The code implements the most accurate models to estimate the properties using FORTRAN subroutines. REFPROP linkage to MATLAB is achieved using a customised external function which can be frequently called during calculations.

3.7 Result and Discussion

3.7.1 Internal flow model general variables

3.7.1.1 Test case and temporal resolution

The duration of a typical pMDI actuation event is 100 to 400 ms for the range of practical metering chambers (Clark, 1991; Dunbar et al., 1997). From theoretical point of view, an optimised value of time step is selected to capture the flow transient with sufficient accuracy. This is achieved by investigating effect of time step on spray velocity using a range of different Δt values as illustrated in Figure 3.6. For HFA227 propellant system, the modelling parameters of the case are summarised in Table 3.2. The values of discharge coefficient are adopted based on the charts produced by Clark (1991, pages 112 and 114). This suggests that for D_{vo} of 0.7 mm, discharge coefficient value is approximately 0.6 which is also confirmed by Dunbar (1996). For the case of D_{so}, Clark (1991) reports a mean discharge coefficient value of 0.7 for a wide diameter range of 0.29-1.02 mm, which is used in this work. According to the figure for 2 ms and 1 ms time step, the velocity profile is unstable. Time step size reduction down to 0.5 ms, eliminates all the oscillations. Further decrease of the time step size to 0.25 ms shows a stable solution with predicted velocity values that are substantially identical to the 0.5 ms solution except for a small increase of the initial velocity peak. Further reduction of time step to 0.075 ms yields no further change. Thus numerical integration time step of 0.25 ms was selected and this has proved to be a satisfactory choice of time step for other cases.

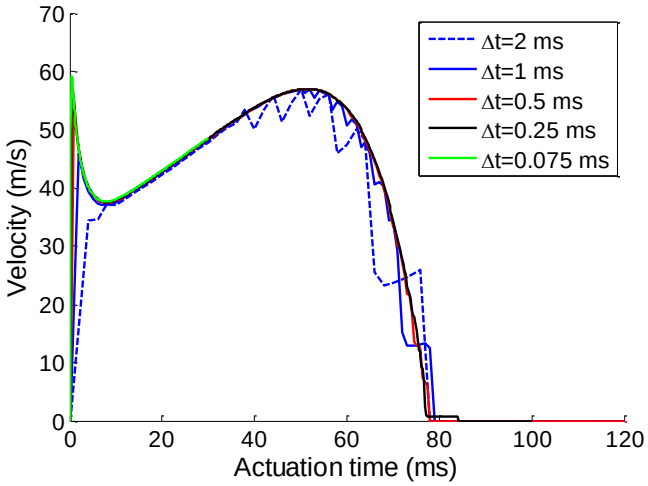

Figure 3.6 Temporal discretisation study - two-phase flow velocity calculated for different time step values

Parameter	Value	Parameter	Value
Vol_{mc}	25 µl	D_{vo}	0.7 mm
Vol_{ec}	25 µl	D_{so}	0.4 mm
$C_{d,vo}$	0.6	$C_{d,so}$	0.7
T_{amb}	295 K	L_{so}	0.75 mm

Table 3.2 Modelling parameters of the default test case

3.7.1.2 Solution variables

In this section we examine in more detail the temporal behaviour of the solution variables of the pMDI for the case with HFA227 as the propellant and modelling parameters introduced in Table 3.2. In this section the predictions of H-HFM model are obtained using equation 3-37 (i.e. C_b=1) for nuclei population. Figure 3.7 (a-b) represents the temporal variation of pressure inside the expansion and metering chambers.

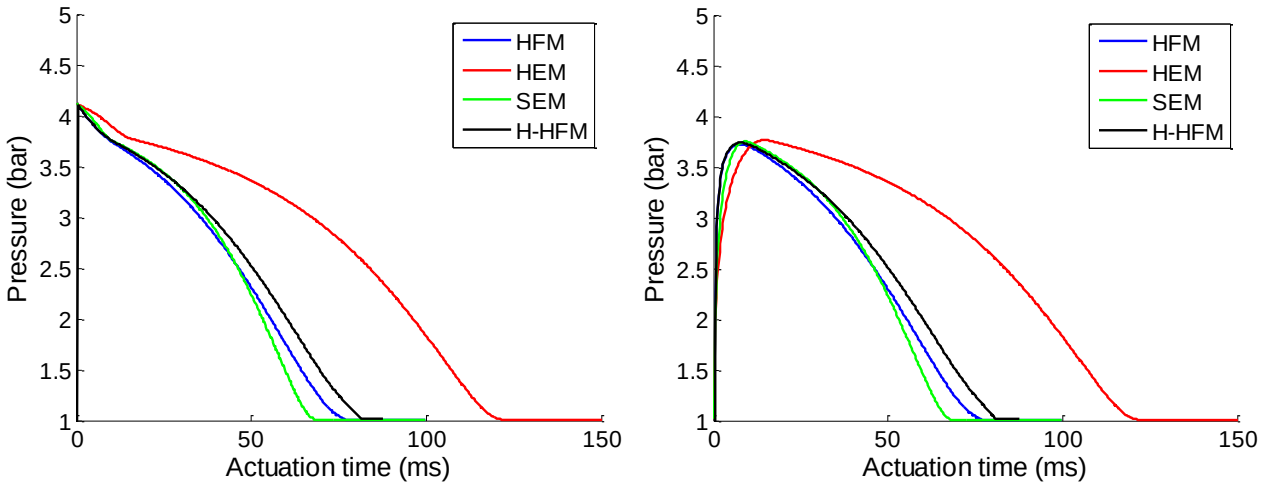

(a) metering chamber **(b) expansion chamber**

Figure 3.7 Temporal evolution of propellant flow pressure for different orifice flow models

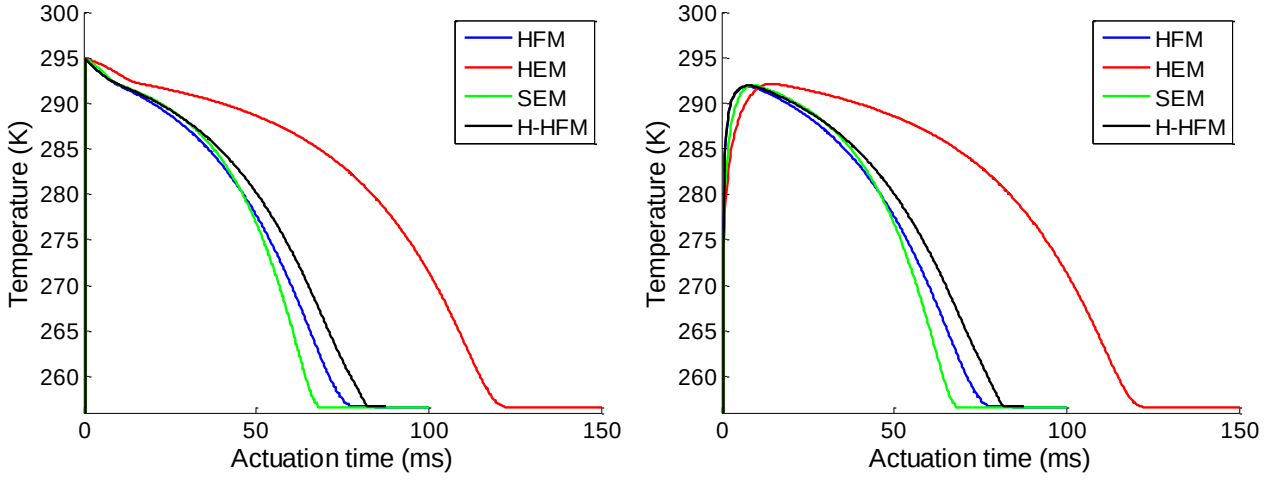

(a) metering chamber **(b) expansion chamber**

Figure 3.8 Temporal evolution of propellant flow temperature for different orifice flow models

It can be seen that the broad trends of the pressure-time traces are similar for all different orifice flow models. It should be noted that the overall duration of the actuation events is longer for HEM than the rest of the models, as HEM predicts lower mass flow rates (see section 3.7.2 for more details). Figure 3.7 (a), shows that the pressure inside the metering

chamber monotonically falls from its initial value corresponding to saturated vapour pressure of HFA227 at ambient temperature. This pressure fall is linked with continuous emptying of the metering chamber during the actuation. Figure 3.7 (b) shows that the actuation causes the pressure in the expansion chamber to rise rapidly initially, after the valve orifice is opened.

This rapid rise corresponds to the initial inflow of propellant liquid, most of which evaporates once it is inside this space. The expansion chamber pressure increases until it reaches a maximum. This increase in pressure is due to the gradual propellant accumulation in this space as a result of imbalance between the propellant inflow through valve orifice, being larger than propellant outflow from spray orifice. This leads to expansion chamber filling. After the maximum point on the trace is reached, the pressure then more gradually decreases as this space in being emptied out by flow out of the spray orifice until atmospheric pressure is attained.

Figure 3.8 (a-b) represents the temporal temperature trend in the actuator chambers. The temperature behaviour follows the pressure variations, because of the thermodynamic equilibrium assumption prevailing in the chambers, linking pressure and temperature together.

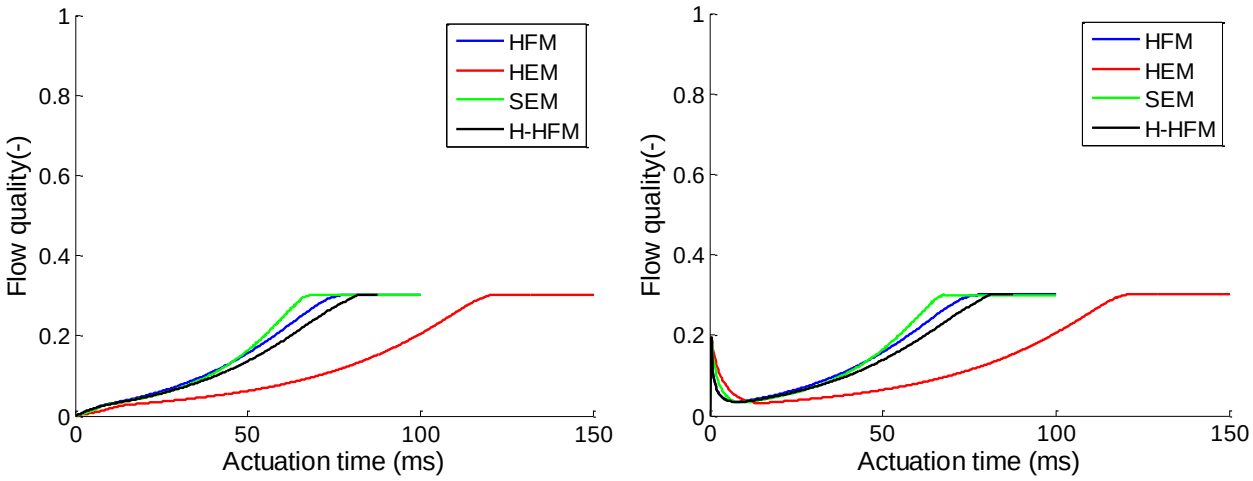

(a) metering chamber **(b) expansion chamber**

Figure 3.9 Temporal evolution of propellant flow quality for different orifice flow models

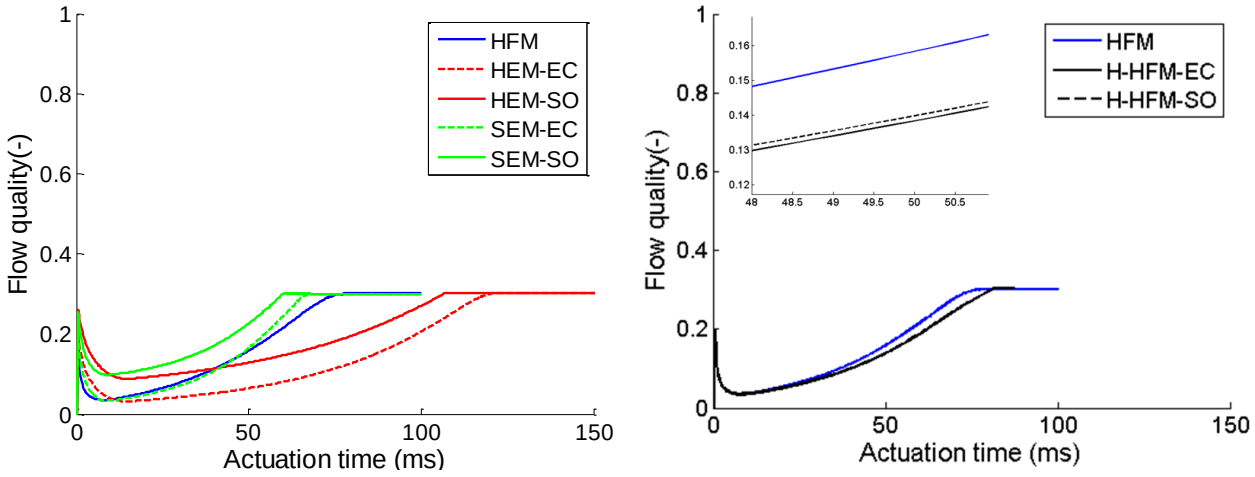

(a) HFM, HEM, SEM **(b) HFM, H-HFM**

Figure 3.10 Comparison of temporal propellant flow quality inside expansion chamber and at spray orifice exit

All traces in both chambers settle at 256.65 K which corresponds to saturation temperature of HFA227 at atmospheric conditions. Evaporation of propellant in pMDI actuator is represented by quality of two-phase flow in the chambers, in Figure 3.9 (a-b). As expected, the quality in the metering chamber rises continuously. The value of the quality at the start of the actuation is zero as the metering chamber contains only saturated liquid at ambient conditions. Once the actuation starts, the liquid flows through the valve orifice. In order to fill the voidage in the metering chamber space, evaporation of the liquid begins and the mass fraction of the vapour increases. The quality in the expansion chamber is set to start from an undefined (arbitrarily set to zero) as there is no propellant presented in this space. Subsequently, it instantaneously reaches 0.2 as the initial discharged liquid from valve orifice adiabatically evaporates in the expansion chamber. As more propellant enters the expansion chamber, vapour production is inhibited and quality decreases until a minimum is reached, which corresponds to the end of expansion chamber filling. After the minimum point, flow quality increases more gradually which eventually reaches to the final value of approximately 0.3. This value corresponds to the equilibrium quality for adiabatic expansion of HFA227 from ambient temperature of 295 K, to atmospheric pressure.

Mass transfer characteristics of each orifice flow model are demonstrated by comparing the flow quality in the expansion chamber and at the spray orifice exit. This is shown in Figure 3.10, where flow quality in the expansion chamber is shown with dashed traces and flow quality at the spray orifice exit is signified by means of solid lines. It can be seen that the quality at the spray orifice is generally higher than expansion chamber quality for HEM and SEM. Figure 3.10 (b) indicates that the quality at spray orifice exit of H-HFM model is just marginally above the expansion chamber. This suggests that - with the assumed nucleation parameters in equation 3-37 for bubble number density - the production of vapour in spray orifice is minimal and flow characteristics of H-HFM, is very similar to HFM. This issue is revisited in section 4.4.3, which contains a parametric study of the effect of the assumed bubble number density on atomisation.

Figure 3.11 (a-b), shows the average mass flow rate of propellant mixture through valve and spray orifice. It can be seen that all traces show similar qualitative behaviour in time. Once the valve orifice is opened, mass emission from the metering chamber is highest due to the large pressure difference between metering and expansion chamber, at the initial stages of actuation. As pressure in the expansion chamber quickly increases, the mass flow rate drops as the expansion chamber pressure increases. When the pressures in the metering and expansion chambers are only slightly different, changes in mass flow rate through valve orifice become a lot more gradual until the metering chamber empties. The differences in magnitude of mass flow rate depend on the amount of vapour produced by each orifice flow model. The zoomed-in inset of mass flow rate in Figure 3.11 (a) shows the subtle difference of HFM and H-HFM predictions.

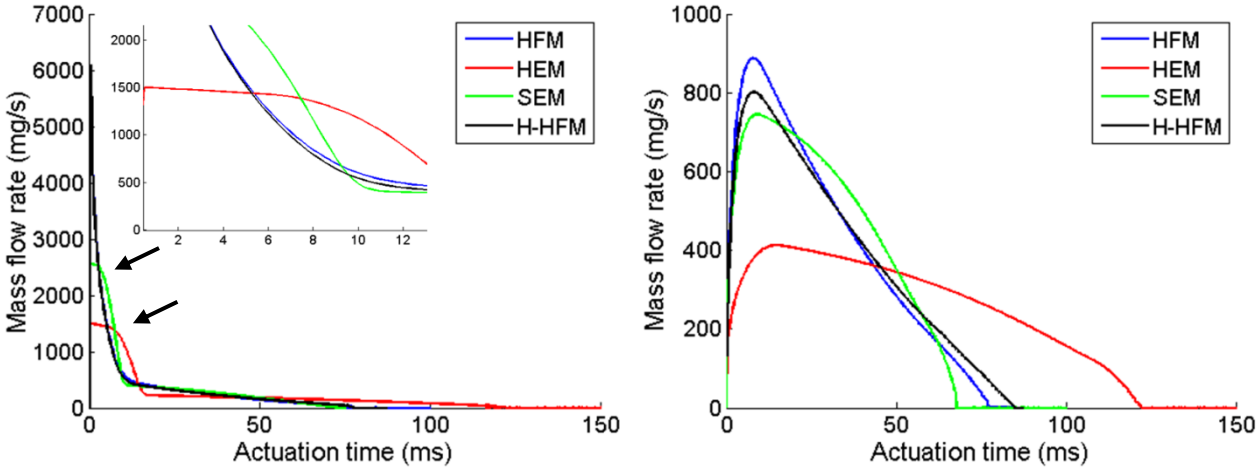

(a) Valve orifice **(b) Spray orifice**

Figure 3.11 Comparison propellant mass flow rate using different orifice flow models

Figure 3.11 (b) shows the mass flow rate through the spray orifice, predicted by the four different models. It is observed that mass flow rate initially increase rapidly as the pressure inside the expansion chamber increases during the filling stage. This trend is primarily a result of less evaporation leading to greater portion of liquid in the discharged mixture. As a consequence, the average density of the emitted mixture increases and hence the mass flow rate through spray orifice rises up to a maximum value. At this time as shown in Figure 3.10, a minimum point in expansion chamber quality is observed after which evaporation in this space increases. This leads to emission of two-phase mixture with reduced liquid portion which in turn reduces the mixture average density. After the maximum mass flow rate, by increase in evaporation mass flow rate decreases continuously, until the discharge concludes.

Figure 3.12 (a-b) shows the predicted temporal spray velocity at the spray orifice exit and in the near-orifice region for the implemented orifice flow models. For SEM model, here the velocity is reported as average two-phase velocity (i.e. $V = G_t \overline{v_t}$). The instants when the critical and sub-critical discharge regimes occur are indicated on the diagrams. Figure 3.12 shows that the discharge regime spray orifice immediately becomes critical after the instantaneous rise of the velocity magnitude during the first time step.

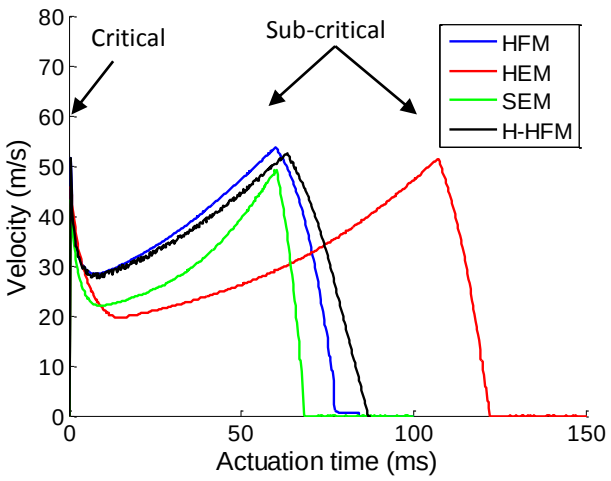

(a) Spray orifice exit

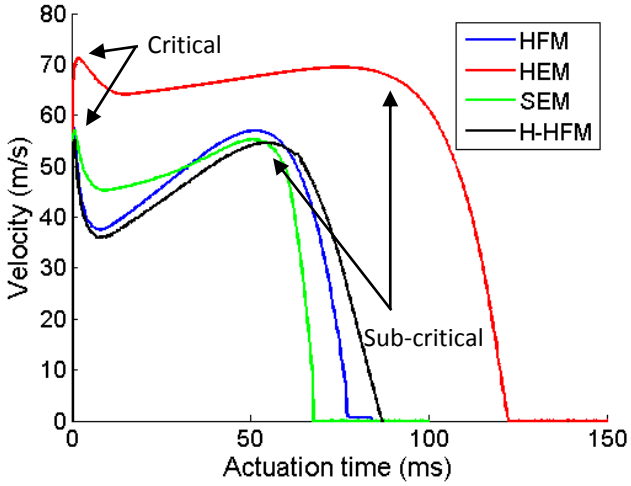

(b) Near-orifice region

Figure 3.12 Temporal plume velocity for different orifice flow models

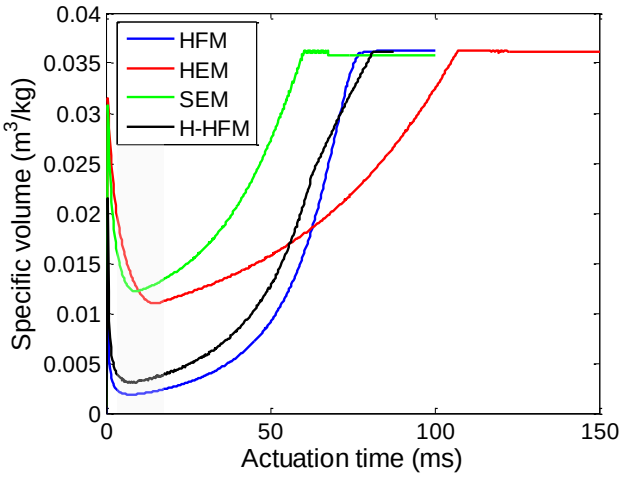

Figure 3.13 Temporal evolution of two-phase propellant mixture specific volume

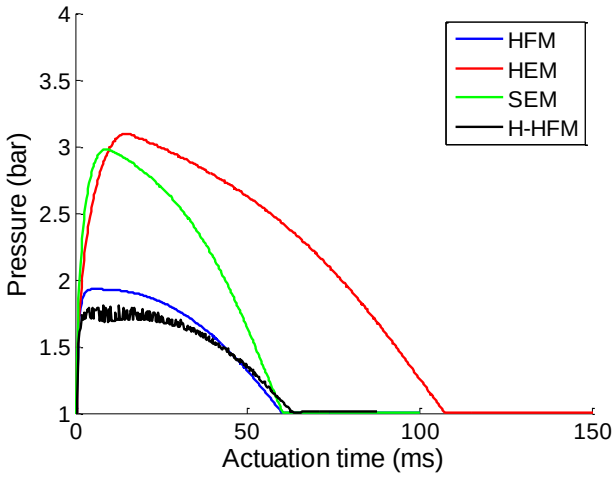

Figure 3.14 Temporal evolution of spray orifice pressure

The initial rise corresponds to discharge of initial of high quality vapour/liquid mixture, through spray the orifice. After this point a subsequent fall in the velocity is observed. The minimum point on the velocity curve, after 10 - 20 ms, corresponds to the condition of maximum expansion chamber pressure and maximum mass flow rate out of the spray orifice. Figure 3.13 shows that the average specific volume of the two-phase mixture has a minimum (highlighted region) and the expansion chamber pressure has a maximum at the

same time as the minimum point observed on the velocity curves. Thus, during the expansion chamber filling stage, evaporation is inhibited as the pressure rises and less vapour is in the two-phase mixture. The effect of changes in the specific volume is large compared to those in the velocity, so the net effect is that the mass flow has a maximum. From this minimum point, velocity gradually increases until it reaches a second maximum where the discharge regime becomes sub-critical. Here the velocity rise is roughly linear and links with the expansion chamber emptying stage. Finally, the mass in the chambers depletes completely and the velocity sharply decays until it reaches zero when the pressure in the expansion chamber equals the atmospheric pressure. The larger magnitudes of near-orifice velocities during critical discharge is a result of higher pressure at spray orifice exit, which resolves itself to ambient pressure by the abrupt acceleration in the near-orifice region. The values of pressure at spray orifice exit are shown in Figure 3.14 for different flow models.

3.7.2 Comparison between orifice flow models

As presented in section 3.7.1.2, implementation of the different orifice flow models predicts the same overall range for pressure and temperature magnitudes. Results also indicate that flow quality range between of 0 – 0.28 in all actuator compartments. According to results of the previous section, the most responsive parameter to alternative orifice flow models is the duration of the actuation event. Considering Figure 3.7 (a) as an example, let the duration predicted by HFM to be the reference. This duration is predicted to be 77 ms. In the HFM no vapour is produced along flow path from supply reservoir through the orifice. Thus, the available flow energy is used to emit more liquid and, hence, the metering chamber is emptied quicker compared with H-HFM for which duration is predicted slightly longer, around 81 ms. This is due to the partial bubble growth in metastable propellant through spray orifice. Additionally, since some vapour is produced, the average density of two-phase mixture decreases and therefore mass flow rate through the spray orifice decreases compared with HFM. Thus the metering chamber empties more slowly.

For the case of HEM, complete evaporation is achieved at the exit of the orifice. In this case mass flow rate is further reduced and the duration increases considerably to 121 ms. Event duration predicted by the SEM is the shortest among the models considered here, about

68 ms, which is correlated to mass emission predicted by the model over approximately 25-55 ms (see Figure 3.11 (b)).

The mass flow rate magnitude determines overall event duration. According to Figure 3.11 (a) one interesting feature is the magnitude of the mass flow rate through the valve orifice at the initial stages of the actuation. Figure 3.11 (a) suggest that HEM and SEM predict very slow decrease of mass flow rate over the first 8 ms and 3 ms of the actuation event, respectively. One the other hand HFM and H-HFM shows an almost instantaneous decrease from the very beginning of the actuation. Such trend is attributable to choking of valve orifice. HFM and H-HFM predicts that the valve orifice is subsonic from the beginning of the actuation. HEM and SEM suggest that valve orifice operates at choked regime for some times during the beginning of actuation (around 8 ms for HEM and 3 ms for SEM after actuation). Thus the mass flow rate is limited over this duration compared with HFM and H-HFM.

For the case of spray orifice mass flow rate, Figure 3.11 (b) shows the magnitudes of traces are considerably affected by using different orifice flow models. Results suggest that the peak mass flow rate is ordered from highest to lowest as HFM, H-HFM, SEM and HEM. It is evident that there is an inverse correlation between the peak mass flow rate and event duration.

Predicted velocities show noticeable difference for different models as well. According to Figure 3.12 (a), HFM and H-HFM predict the highest velocity within the range of 28 m/s to 53 m/s, with HFM being marginally higher. The predicted velocity by HEM and SEM is approximately the same and is within the range of 20 m/s to 50 m/s. For the flow velocity in the near-orifice region, the magnitude of the velocity is considerably higher during critical discharge regime, because the pressure at the spray orifice exit is higher than the downstream atmospheric pressure. This pressure difference imposes an additional thrust force on the flow and, hence, causes acceleration and velocity increase in the near-orifice region. When the discharge switches to the sub-critical regime, the throat and downstream pressure becomes equal and hence the flow does not accelerate further after emerging from the spray orifice. This leads to both traces following the same pattern from this point until the end of the actuation. The acceleration is directly proportional to the difference

between the pressure at the spray orifice and prevailing ambient pressure and is inversely proportional to the mass flow rate. For a fixed ambient pressure, Figure 3.14 and Figure 3.11 (b) suggest that the maximum pressure difference and lowest mass flow rate are predicted by the HEM. Thus, the highest predicted acceleration is associated with this model. The predicted range of spray orifice pressure by SEM is almost identical to HEM and H-HEM. However, the SEM mass flow rate is higher than its HEM counterpart and hence offsets the amplitude of the near-orifice velocity.

3.7.3 Spatial distribution of flow variables in spray orifice (H-HFM predictions)

Examining solution variables along the spray orifice may bring deeper understanding regarding effect of liquid evaporation on two-phase flow development. Therefore, predictions of relevant flow variables by the H-HFM model along spray orifice are presented in this section.

3.7.3.1 Test case and spatial resolution

The modelling parameters are the ones summarised in Table 3.2 with C_b=1. Additionally the diameter of the expansion chamber is assumed to be 1.2 mm. Results are presented for two particular timestamps of 10 ms and 40 ms along the actuation. These times approximately corresponds to initiation and intermediate stages of developed plume, whose significance is due to bulk of spray production (Versteeg et al., 2006). The initial conditions of the flow at these timestamps are summarised in Table 3.3.

Time (ms)	Absolute nuclei population C_b=1	Superheat degree (K)	Mass flow rate (kg/s)	x_{ec} (-)	T_{ec} (K)	p_{ec} (bar)
10	551	14.72	9.1081	0.0341	291.91	3.74
40	267	14.38	4.8569	0.0966	284.96	2.97

Table 3.3 Initial condition of metastable two-phase flow prior to spray orifice entrance

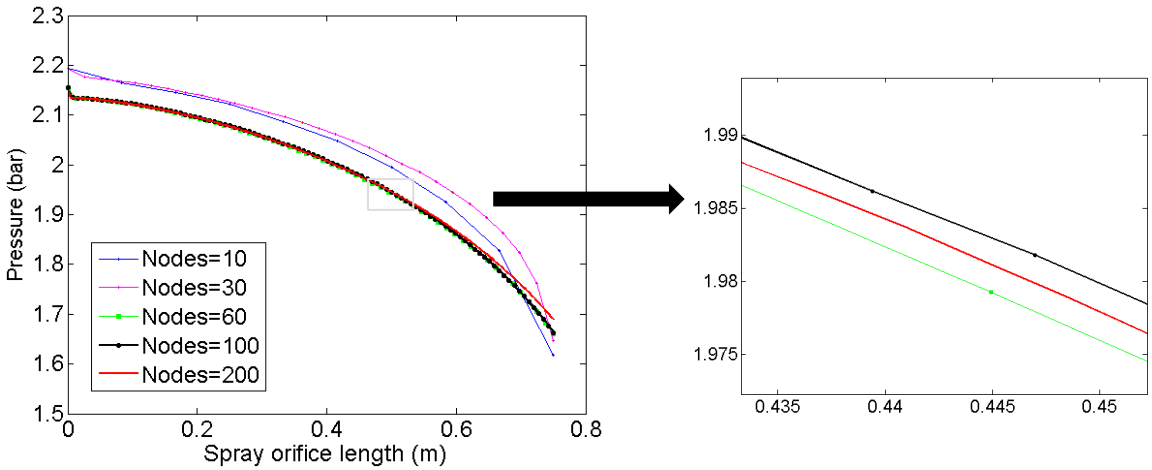

Figure 3.15 Spatial discretisation study - two-phase flow pressure drop along spray orifice for different node numbers

Figure 3.15 shows variations of pressure along spray orifice for different numbers of computational nodes along the spray orifice increasing from 10 to 200. Pressure traces are computed for initial conditions corresponding to 10 ms, shown in Table 3.3. Figure 3.15 suggests that for 10 and 20 number of nodes pressure variations show evident difference from 0.23 mm onwards. Increasing number of nodes to 60, 100 and 200, results in minimal difference in pressure traces. However increasing nodes from 100 to 200 led to obtaining converged solution in around 7 times longer duration. Here we used 100 nodes to arrive at grid independent solution over reasonable computation time.

3.7.3.2 Solution variables

Figure 3.16 to Figure 3.21 present the spatial development of flow characteristics. Each figure consists of two diagrams, each corresponding to a particular timestamp (10 ms or 40 ms), respectively. The initial conditions of the flow at these timestamps are summarised in Table 3.3. Figure 3.16 shows spatial distribution of the liquid layer void fraction (equation 3-42) along the spray orifice, which is a metric to demonstrate propellant evaporation in each liquid segment. The extent of evaporation depends on the initial superheat degree and number of nuclei in the liquid layer.

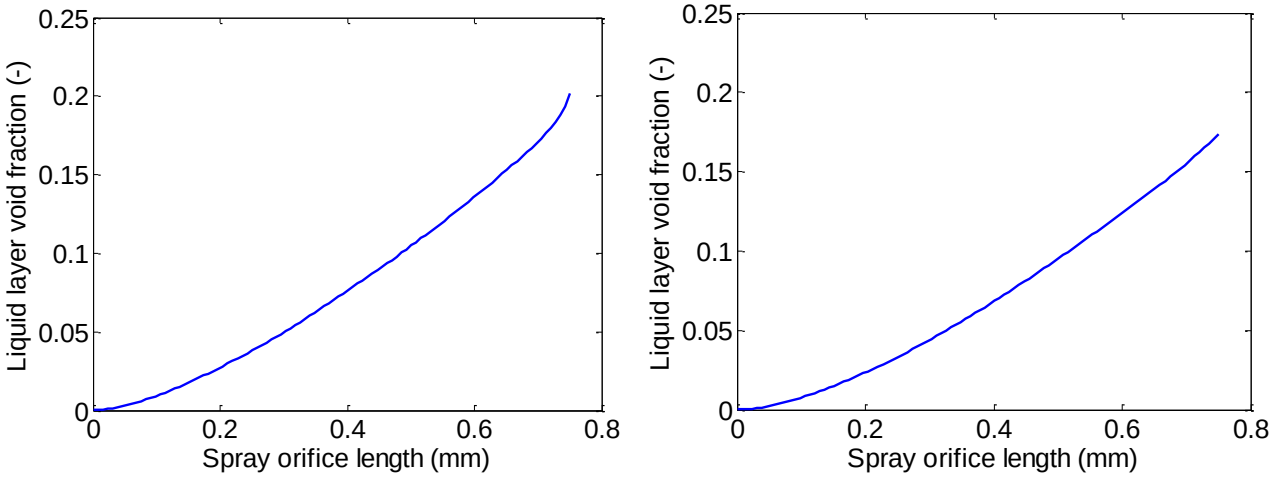

(a) 10 ms **(b) 40 ms**

Figure 3.16 Spatial distribution of liquid void fraction along spray orifice at different instants of actuation event

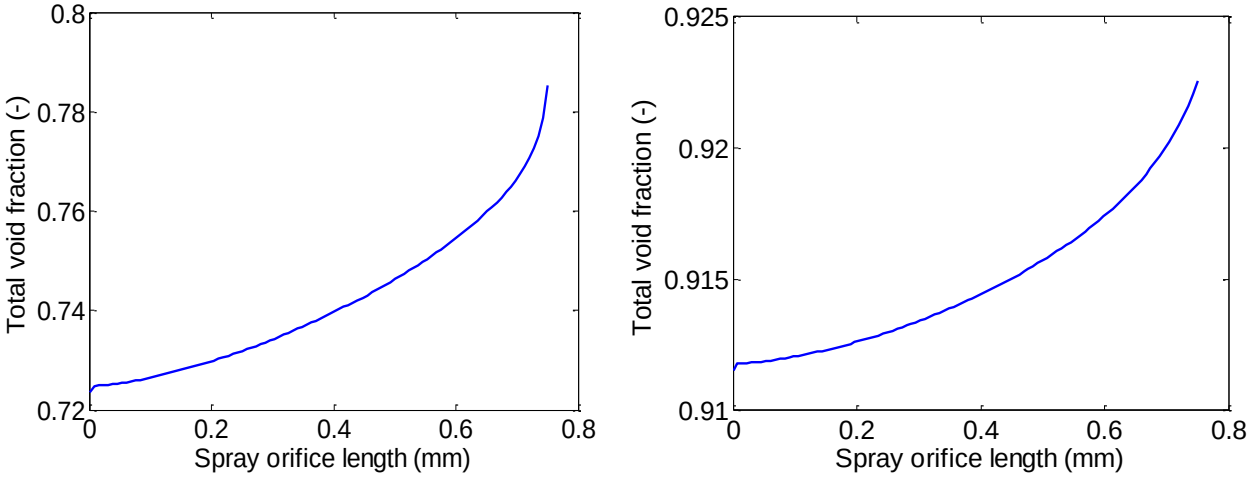

(a) 10 ms **(b) 40 ms**

Figure 3.17 Spatial distribution of total void fraction along spray orifice at different instants of actuation event

Figure 3.17 shows the spatial development of the total void fraction inside the spray orifice. Similar to Figure 3.16, the void fraction increases with distance in the spray orifice. However, the changes to the magnitude of the total void fraction are small. This indicates that the contribution of liquid layer evaporation to total amount of vapour phase inside the spray orifice is comparatively small.

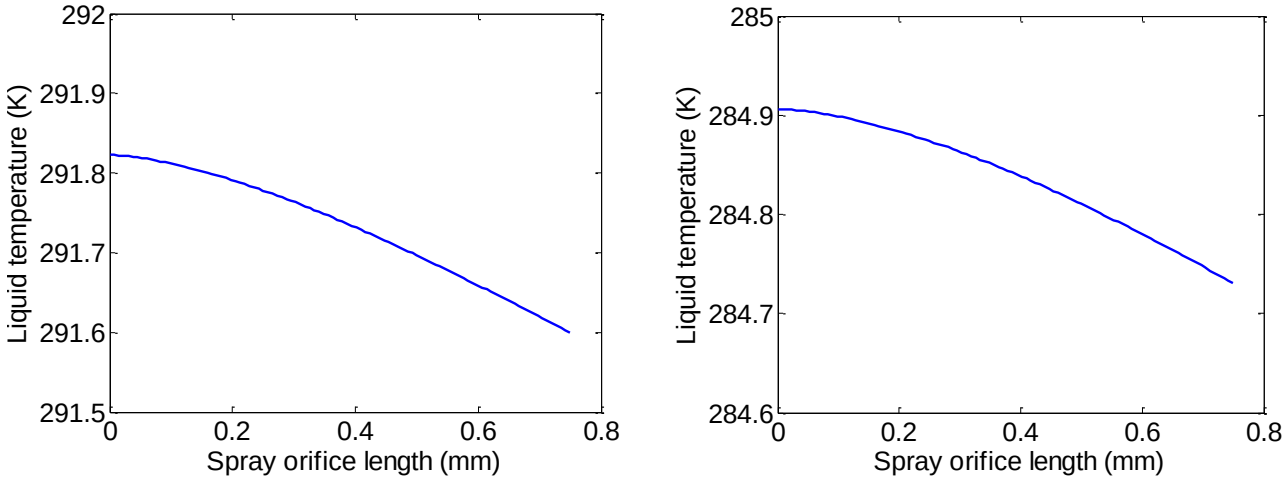

(a) 10 ms **(b) 40 ms**

Figure 3.18 Spatial distribution of liquid temperature along spray orifice at different instants of actuation event

As evaporation takes place inside the spray orifice under adiabatic conditions, the liquid temperature drops (see Figure 3.18). According to the figure, temperature changes are very small, because the amount of evaporation in the spray orifice is limited. It should be mentioned that the amount of evaporation is in two-way coupled linkage with the changes in the prevailing pressure. Propellant evaporation in conjunction with expansion of the core gas results in a pressure drop, which, in turn, enhances further evaporation. Axial pressure variations are shown in Figure 3.19. These traces show a substantial drop of the pressure, starting from the initial value at the spray orifice entry calculated by equations 3-27 to 3-31 and continuously dropping as the flow travels towards the spray orifice exit. The magnitude of the pressure at the constriction inlet depends on the mass flow rate travelling through the nozzle, itself being a function of expansion chamber initial conditions, nozzle geometry and nuclei population. The traces show that the rate of change of pressure increases rapidly as the flow approaches the spray orifice exit plane. A large proportion of propellant evaporation and core gas expansion occurs towards the end of the spray orifice.

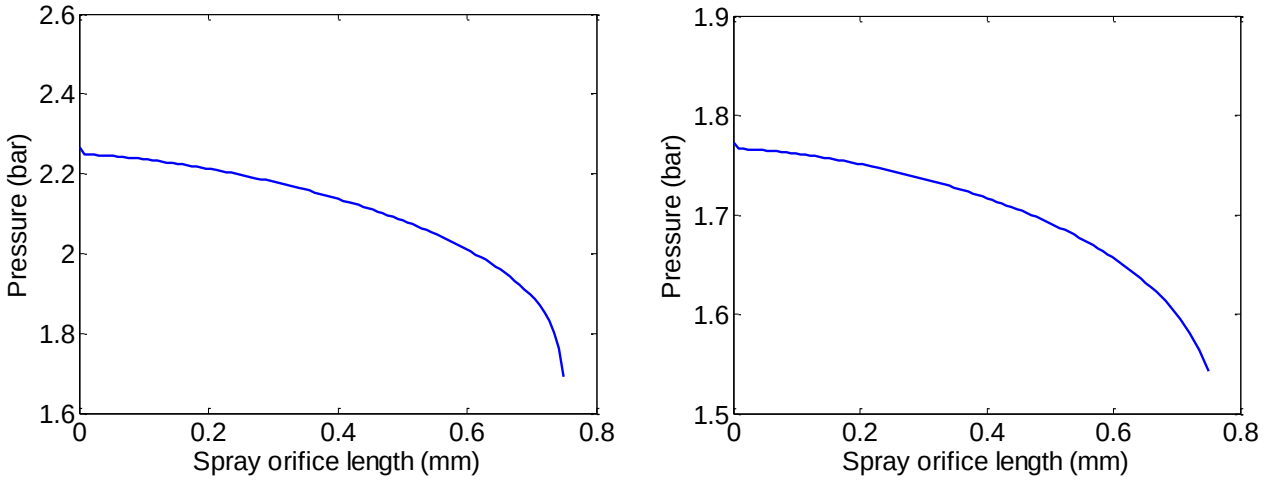

(a) 10 ms **(b) 40 ms**

Figure 3.19 Spatial distribution of pressure along spray orifice at different instants of actuation event

The axial pressure drop as a result of evaporation and core gas expansion, results in acceleration of the flow inside the spray orifice. The variations of the fluid velocity, the two-phase speed of sound (equation 3-47 (a)) and the corresponding Mach number are illustrated in Figure 3.20. This shows that the velocity gradually increases along the spray, but the flow acceleration becomes greater towards the nozzle exit. This increase in acceleration occurs as a consequence of the rapid pressure drop.

Figure 3.20 shows that the sonic velocity (dashed line) remains almost constant along the nozzle and drops at the spray orifice exit where flow velocity hits the sonic velocity. Here is the point where the Mach number equals unity. Variations of Mach number are also shown by means of green traces along the nozzle. Figure 3.21 demonstrates the distribution of vaporisation index which quantifies the amount of metastability of the spray orifice liquid. A rising trend of vaporisation index is observable, which highlights the increasing transformation of metastable liquid to saturated liquid due to bubble growth and vapour production.

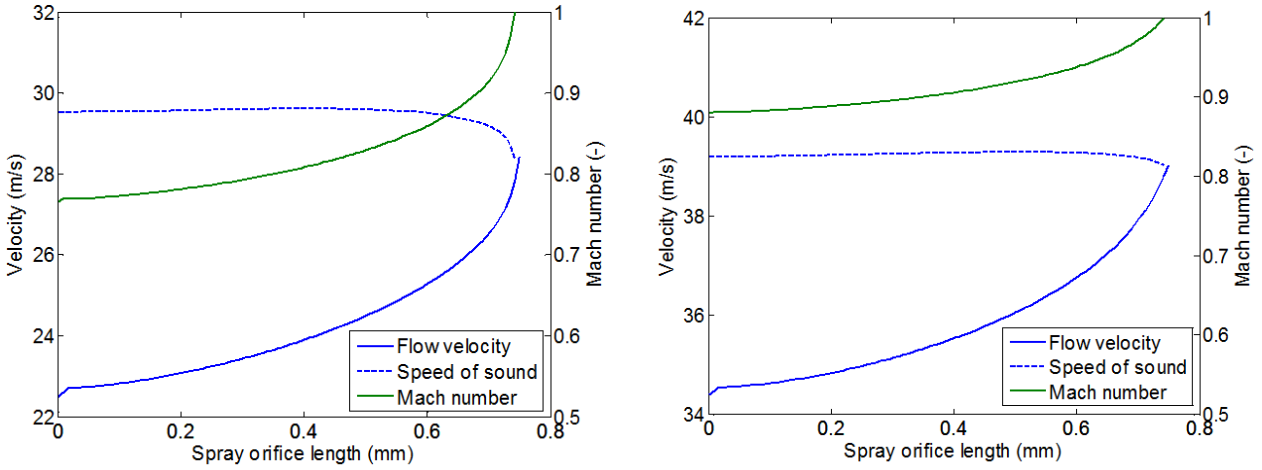

(a) 10 ms **(b) 40 ms**

Figure 3.20 Spatial distribution of two-phase mixture velocity, speed of sound and Mach number along spray orifice at different instants of actuation event

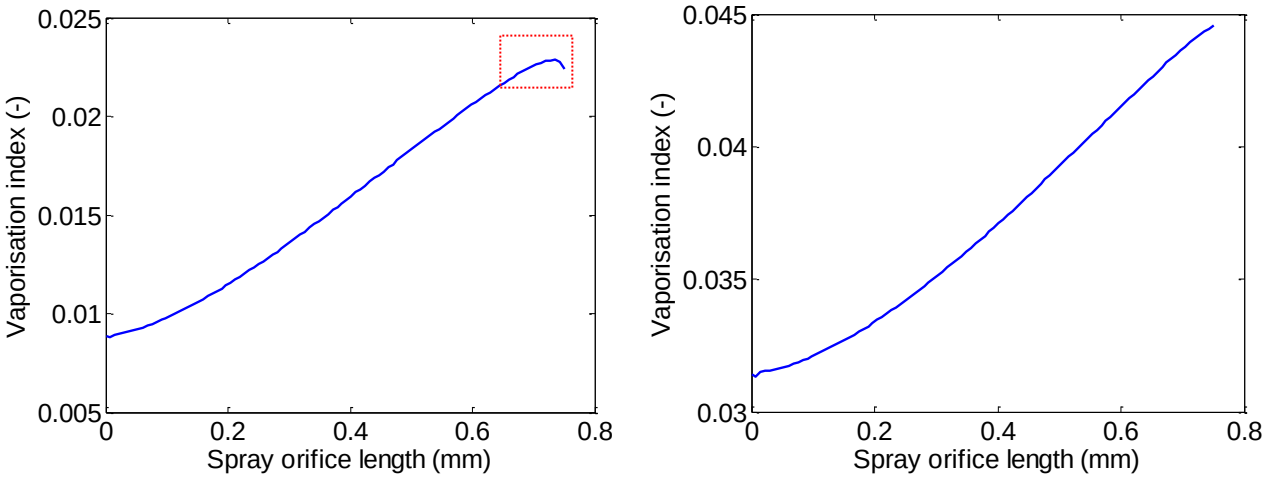

(a) 10 ms **(b) 40 ms**

Figure 3.21 Spatial distribution of vaporisation index along spray orifice at different instants of actuation event

It should be noted that the magnitude of the values is generally very small. This suggests that large portion of liquid (i.e. $1 - y$ fraction) remains metastable whilst it is emitted into the surroundings at the spray orifice exit, which is in line with numerical observation of Lackme (1979). At 10 ms the rate of change of pressure near the orifice exit is extremely

rapid, the gradient of the vaporisation index curve gradually decreases until it becomes negative this is indicated in Figure 3.21 (a) with a red dashed box. This implies that the predicted rate of evaporation does not keep pace with the decreasing pressure, so that the degree of metastability of the liquid is predicted to increase by small amount.

3.7.4 Velocity validation against PDA measurement

In this section the outcome of internal flow model in terms of spray velocity is compared against PDA measurements. Three sets of measured data are used; the corresponding modelling parameters and test conditions are presented section 3.7.4.1. Once the test cases are introduced, further analysis is performed on the measured data in section 3.7.4.2, to make it directly comparable to internal flow model predictions.

3.7.4.1 Test cases and measured velocity

3.7.4.1.1 PDA measurement of parallel project

These sets of PDA data are the outcome of a parallel experimentally-based project carried out by Ben Myatt, a co-worker in the Thermofluids research group at Loughborough University. Some analysis related to these PDA measurements can be found in Myatt et al. (2015 a-b) and further details will be reported elsewhere in future. Geometric properties of the actuator and test conditions are summarised in Table 3.4.

Parameter	Value	Parameter	Value
Vol_{mc}	50 µl	D_{vo}	0.7 mm
Vol_{ec}	50 µl	D_{so}	0.3 mm
$C_{d,vo}$	0.6	$C_{d,so}$	0.7
T_{amb}	295 K	L_{so}	0.75 mm

Table 3.4 Geometric and modelling parameters of the test case Myatt et al. (2015 a-b)

PDA results correspond to a series of 30 spray events at 15 mm away from spray orifice are shown in Figure 3.22 for HFA134 and HFA227 placebo propellant systems. Plume velocities were ensemble averaged over 10 ms time bins.

3.7.4.1.2 PDA measurement of Dunbar et al., (1997)

This set of PDA measurements was obtained by Dunbar et al. (1997) as shown in Figure 3.23. The corresponding parameters of the test case are shown in Table 3.5. Each data point was collected from a minimum number of five actuations and averaged over 20 ms time bins. The point of measurement was at 25 mm distance from the spray orifice. Finally, the propellant system used in this work was HFA134.

Parameter	Value	Parameter	Value
Vol_{mc}	63 µl	D_{vo}	0.7 mm
Vol_{ec}	17.6 µl	D_{so}	0.5 mm
$C_{d,vo}$	0.6	$C_{d,so}$	0.7
T_{amb}	295 K	L_{so}	0.75 mm

Table 3.5 Geometric and modelling parameters of the case of (Dunbar et al., 1997)

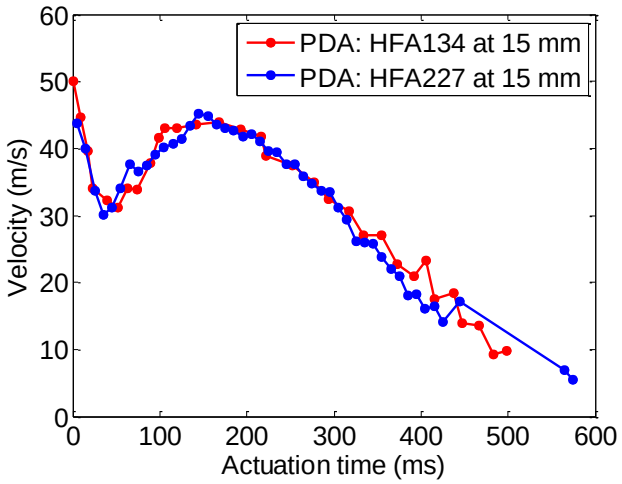

Figure 3.22 PDA measurement of plume velocity for HFA134 and HFA227 at 15 mm away from spray orifice

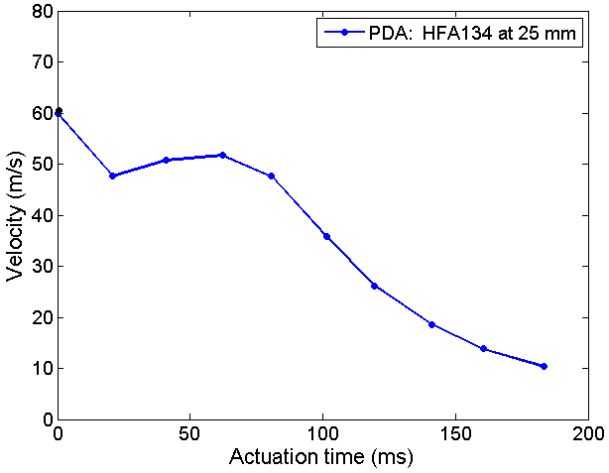

Figure 3.23 PDA measurement of plume velocity forHFA134 at 25 mm away from spray orifice by (Dunbar et al.,1997)

3.7.4.1.3 PDA measurement of Wigley et al., (2002)

The test parameters related to this data set are shown in Table 3.6. Data were collected from series of 10 actuation events and measurements were taken at 2.6 mm away from spray orifice. Velocity values were averaged over 5 ms time windows and the system propellant was HFA227. These measurements are shown in Figure 3.24.

Parameter	Value	Parameter	Value
Vol_{mc}	25 µl	D_{vo}	0.7 mm
Vol_{ec}	25 µl	D_{so}	0.4 mm
$C_{d,vo}$	0.6	$C_{d,so}$	0.7
T_{amb}	295 K	L_{so}	0.75 mm

Table 3.6 Modelling parameters of the default test case

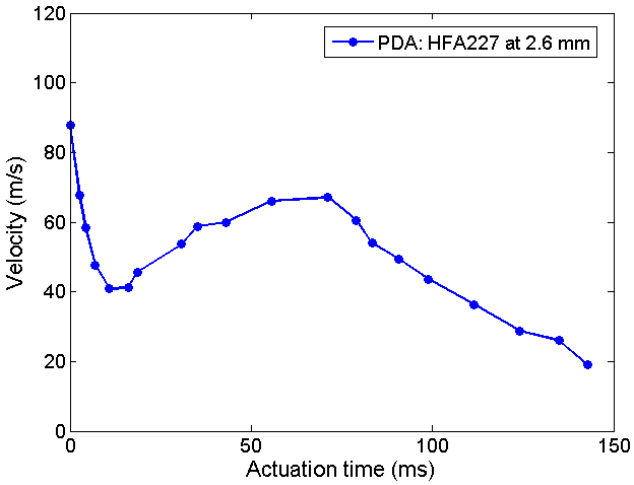

Figure 3.24 PDA measurement of plume velocity

for HFA227 at 2.6 mm away from spray orifice by Wigley et al. (2002)

3.7.4.2 Near-orifice extrapolation

Comparison of model predictions against PDA data requires further analysis on PDA measurements. The internal flow model predicts velocity values immediately outside the spray-orifice. This is a fictitious point where all superheated HFA has flashed off and the spray has accelerated through the shock at the exit of the spray orifice (see Figure 3.5). Current phenomenological models do not contain an account of the axial development of flow in this region. Therefore models do not allow us to calculate a distance where the HFA flashing and the spray acceleration are complete. However, Clark (1991) implies that the relevant changes take place within a short axial distance from the actuator nozzle. On the other hand PDA measurements presented in sections 3.7.4.1.1 and 3.7.4.1.2, are conducted at 15 mm and 25 mm away from the spray orifice, which are strictly far-field measurements ($x/D = 50$). In this case, if the velocity decay rate with respect to distance was known, this could be used to extrapolate PDA results to any assumed near-orifice position corresponding to model prediction. In the current validation activity, it is assumed that near-orifice region covers the initial 10 mm from the spray orifice exit plane. This distance is closest to spray orifice at which velocity values can be measured by PDA with reasonable accuracy, as determined by test protocol of parallel experimentally based project. By getting any closer to spray orifice than 10 mm, velocity values may be affected by dense spray effect and related data drop out.

Extrapolation of PDA data to near-orifice region requires knowledge of the axial plume velocity decay rate. If the spray plume follows quasi-steady jet/plume relationships, the velocity would be inversely proportional to the distance from the effective plume source location. This is also termed as "apparent plume source" in Fletcher (1975-section 4.1). This behaviour is shown in equation 3-58 in non-dimensional format:

$$\frac{V_{cl}}{V_{ref}} = \frac{C}{(x - x_s)/D_{so}} \qquad 3\text{-}58$$

Where V_{cl} and V_{ref} are plume centreline and reference velocity respectively. C is the model constant and D_{so} represents the diameter of the spray orifice. Parameter x is the distance to actuator orifice and x_s is the distance from the spray orifice exit to the effective source location. The nonlinear least squares method using the Levenberg-Marquardt algorithm was implemented in Matlab to determine the best-fit model constants in equation 3-58 from axial distributions of plume centreline velocity in the PDA data sets.

3.7.4.2.1 Plume centreline velocity fits

- **Parallel project**

Variation of plume centreline velocity with respect to axial distance from the spray orifice is presented in Figure 3.25. The value at each point is averaged over the entire emission duration. Figure 3.25 suggests that changes in velocity are fairly gradual especially as one travels away from the spray orifice. By performing non-linear fit on the data, coefficients of equation 3-58 read the ones presented in Table 3.7. Such coefficients results in R^2 values of to be greater than 0.98.

Coefficient	C	V_{ref}	x_s
HFA134	57.27	58.44	9.83
HFA227	71.56	41.74	10.63

Table 3.7 Constants in equation 3-58 for parallel experimental project centreline velocity

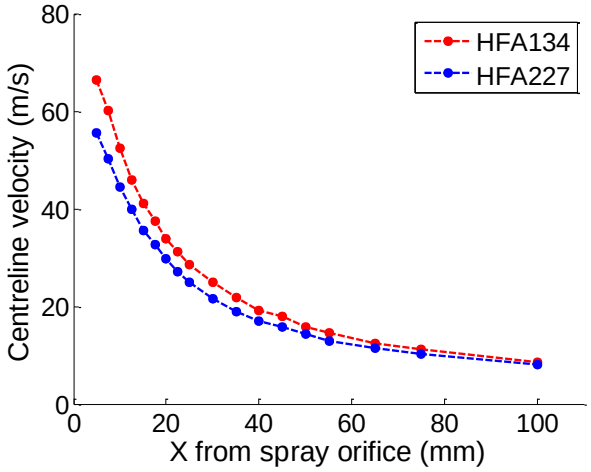

Figure 3.25 PDA measurement of plume velocity for HFA134 and HFA227 at 15 mm away from spray orifice

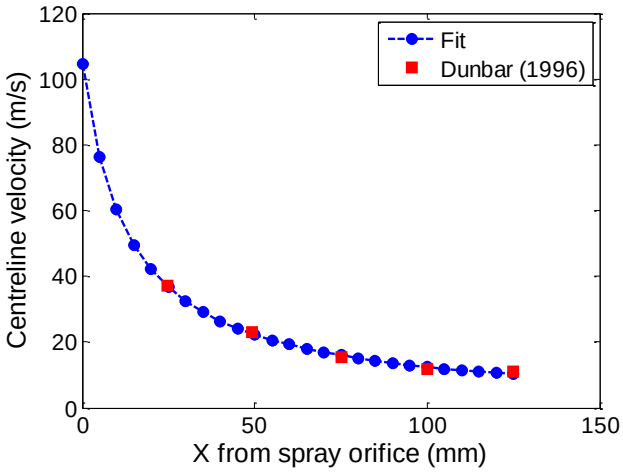

Figure 3.26 PDA measurement of plume centreline velocity for HFA134 and HFA227

- **Dunbar (1996)**

The centreline velocity data are shown by discrete square markers in Figure 3.26. This data is gathered from Dunbar (1996) which and are part of the same experiment which are published in (Dunbar et al., 1997). Here the data suggest that plume velocity can reasonably follow quasi-steady formulation. The best-fit coefficients are presented in Table 3.8; a goodness of 0.99 was achieved.

Coefficient	C	V_{ref}	x_s
HFA134	53.19	53.21	13.51

Table 3.8 Constants in equation 3-58 for the case of (Dunbar, 1996)

- **Wigley et al. (2002)**

For these measurements, axial velocity data was not available. Therefore the PDA trace could not be extrapolated to 10 mm away from the spray orifice, to maintain consistency with the previous comparison. However, it should be noted that Wigley et al. (2002) compared model predictions directly to the measured data, since the PDA data were taken very close to the spray orifice.

3.7.4.3 Validation of velocity predictions

Near-orifice velocity of the plume is predicted using the four different orifice flow models and is compared with PDA measurements of parallel experimental project, Dunbar et al. (1997) and Wigley et al. (2002), as shown in Figure 3.27 and Figure 3.28. Geometric and modelling parameters of the test cases are summarised in Table 3.4 - Table 3.6, respectively. The extrapolated PDA data are shown in the figures by means of the black dashed line. Predictions of alternative orifice flow models are colour coded as shown in the legends. In all figures, the predictions of H-HFM are shown by means of discrete black circles. These predictions correspond to different initial conditions of the flow inside the expansion chamber, at different instants during the actuation. This is done due to time consuming nature of this algorithm which makes it difficult to implement this algorithm for the entire actuation event.

Figure 3.27 (a-b) shows that the temporal trend of velocity is reasonably captured by all models. It can be observed that HEM over predicts near-orifice plume velocity for the entire actuation duration. This is also the case for the vapour phase velocity predicted by SEM which shows even larger over prediction than HEM.

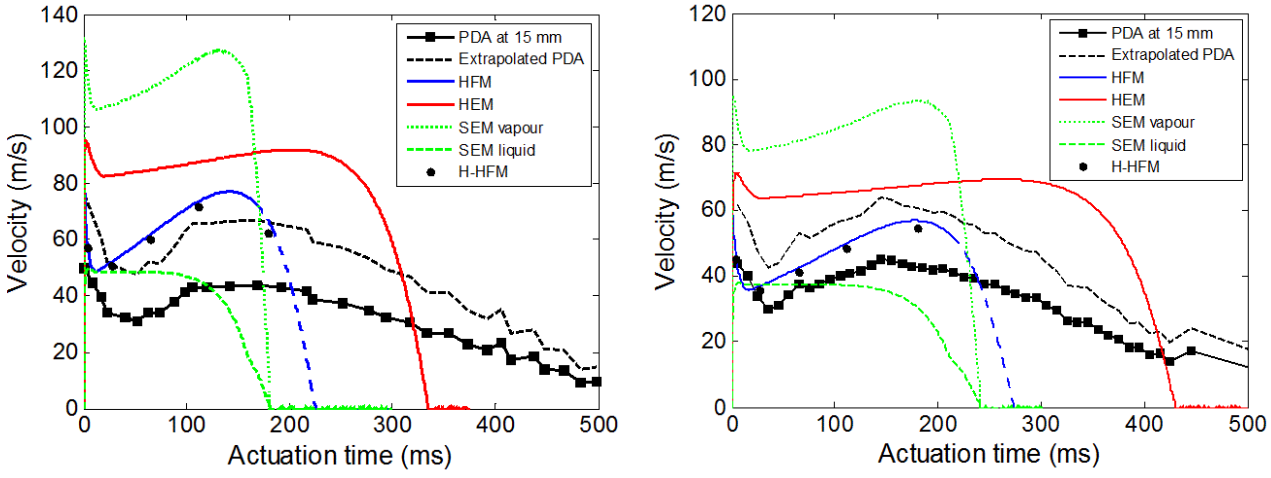

(a) HFA134 **(b) HFA227**

Figure 3.27 Near-orifice prediction of plume velocity using different orifice flow models compared with PDA measurement

These rapid velocities is due to the high predicted pressure at the spray orifice exit by these models, which imposes a great driving force leading to rapid flow acceleration.

On the other hand, the liquid velocity predicted by SEM is below the extrapolated PDA data over the whole actuation event. The velocity predictions of HFM and H-HFM, however, show good agreement with the extrapolated PDA data for HFA134 and HFA227. For HFA134 the frozen model outcomes follow the PDA trace up to 200 ms; for HFA227 this time is around 230 ms. These instants correspond to approximately 95% emission of the original propellant mass. From these moments onwards, the model predictions show a rapid reduction of velocity due to adiabatic cooling of the propellant when the metering chamber is empty, signalling the end of aerosol generation. The velocity decay of PDA curves is more gradual and takes place over a longer time scale. This more gradual velocity decay at the end of the plume is likely to be caused by ambient to actuator heat transfer, providing an external energy source for propellant evaporation. This leads to emission of the tiny remnant mass in the metering chamber and expansion chamber; these phenomena are not considered in the present model.

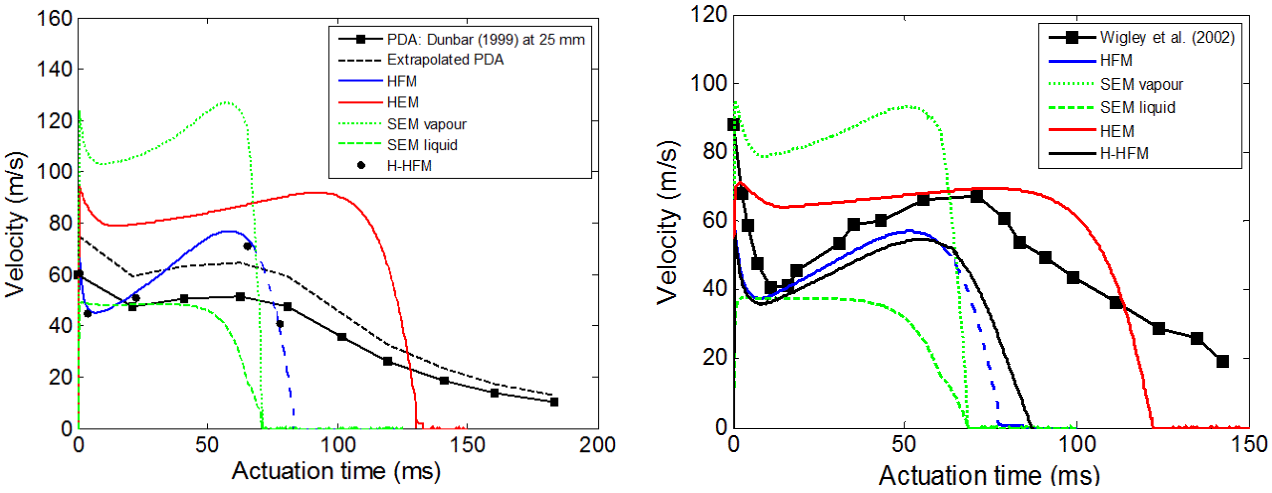

(a) PDA measurement of Dunbar et al. (1997) **(b) Wigley et al. (2002)**

Figure 3.28 Near-orifice prediction of plume velocity using different orifice flow models compared with PDA

It should be noted that the timing of the velocity minimum are somewhat mismatched with the PDA curves. This is probably due to the mixing effect of the plume and ambient air in the spray orifice downstream which reduces velocity gradients and stretches the curve.

Figure 3.28 (a) shows predicted velocity using different models compared against the PDA measurements of (Dunbar et al., 1997). Similar to previous case, broad time trend of velocity is captured by the models. It is evident that the prediction of HEM and SEM vapour phase is far larger than extrapolated PDA curve. On the other hand, the SEM liquid phase velocity under predicts the measured values over the entire actuation event. The predictions of HFM and H-HFM, are again closest to the PDA data.

Model predictions are compared directly with the PDA measurement of Wigley et al. (2002) in Figure 3.28 (b). Results confirm the previous findings regarding the temporal trend and velocity magnitude predicted by each model. With reference to current set of PDA measurements, initial and secondary velocity peaks are underestimated by HFM and H-HFM by around 15 m/s and 11 m/s, respectively. However, the predicted temporal behaviour of the spray velocity is close to the measured data during the 63 ms from the device actuation that corresponds to the emission of 95% of the original mass.

These results suggest that predictions of the internal flow model can be compared successfully with the extrapolated PDA data and the velocity magnitude is predicted within the correct range. The predicted duration of the actuation events is shorter, because 95% of mass is emitted over approximately 70 ms after which adiabatic cooling of the remnants of formulation causes a sharp decay in predicted velocity. PDA data, however, shows a much more gradual decrease in velocity that is attributable to heat input through the actuator walls. It is worth mentioning that Dunbar rejects the existence of two velocity extrema and hypothesised that data dropout in dense spray regions was responsible for velocity minimum existence. However, more recent PIV measurements by Crosland et al. (2009) , as well as PDA measurements of Wigley et al., (2002) and Myatt et al., (2015 a-b) support the existence of both velocity extrema.

3.7.5 Plume velocity and duration trends

In this section we demonstrate the capability of the model further, by applying permutations to modelling parameters and study the effects of them on plume velocity and duration. It should be noted that due to limited data in the literature, most of the comparisons are qualitative. Attempts are made to validate the trends of solution variables against published observations where possible. The HFM model was used as the candidate model to explore the modelling parameters, because it showed reasonable agreement between the predictions of this model and PDA measurements in section 3.7.4.3. Modelling parameters of the tests are summarised in Table 3.9. It should be noted that expansion chamber volume and valve orifice diameter are identical for all test cases and are 25 µl and 0.7 mm, respectively. Similarly, discharge coefficients are identical for all cases and are 0.6 for spray orifice and 0.7 for valve orifice.

Model parameter														
Test case	D_{so} mm					Vol_{mc} µl			T_{amb} K			Propellant		
1	0.4					25			295			HFA227	HFA134	CFC12
2	0.4					25			285	295	303	HFA134		
3	0.4					25	50	63	295			HFA134		
4	0.2	0.32	0.48	0.7	0.9	25			295			HFA227		

Table 3.9 Modelling parameters of the default test case

3.7.5.1 Test case 1

Figure 3.29 (a-b) shows the predicted near-orifice velocity and plume duration of the pMDI for different propellant systems. The velocity is averaged over 95% mass emission duration. Results suggest that HFA227 shows the lowest velocity, whereas CFC12 and HFA134 have a higher mean velocity, respectively. It can be seen that the velocity shows an inverse

relation with spray duration. This behaviour has been justified by Clark (1991) as arising from differences in the saturated vapour pressure of the propellants: the higher the vapour pressure, the greater the driving force of the spray and, hence, the velocity becomes higher. For ambient temperature of 295 K, the saturated vapour pressure of HFA134 is 6.05 bar, CFC12 is 5.96 bar and HFA227 is 4.12 bar and the predicted actuation-averaged spray velocities are in corresponding order. The faster the plume velocity is, the quicker the mass discharge, so the metering chamber depletes in a shorter time period. These trends are confirmed by experimental measurements of Clark (1991, section 6.2.2.4.5) which determined peak spray velocity using thrust transducer technique, and concluded that exit velocity is higher for propellants with higher vapour pressure.

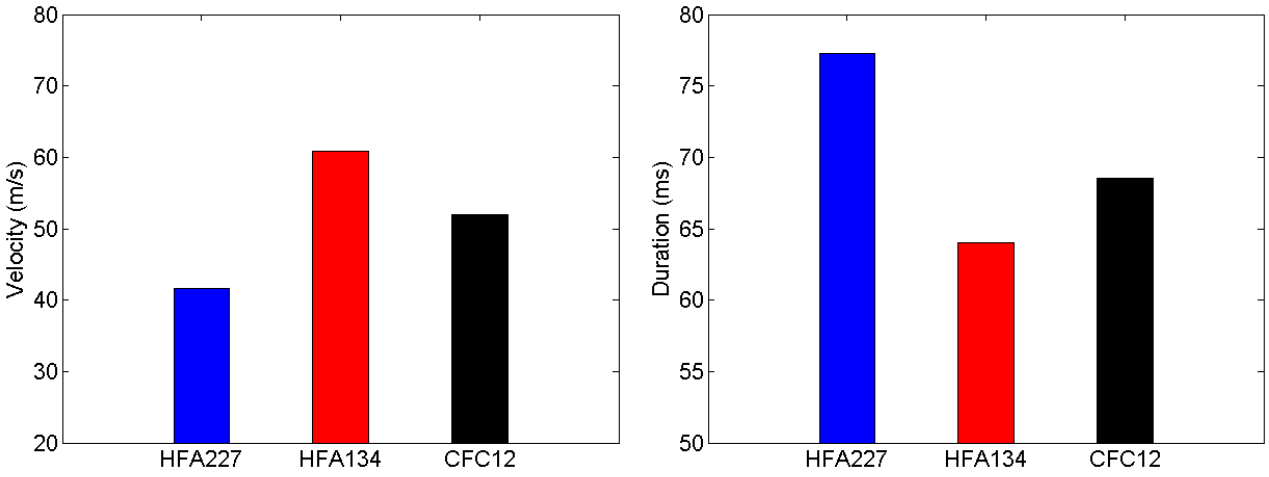

(a) Velocity **(b) Plume duration**

Figure 3.29 Prediction of mean plume characteristics for three different propellants

Measured data showed that exit velocity for HFA134 and CFC12 are around 38 m/s and 36 m/s. For HFA227 this value is considerably lowered to approximately 29 m/s. Gabrio et al. (1999) use plume force as a metric to determine plume velocity and also confirms that HFA227 produces slowest plume where HFA134 and CFC12 exhibit almost identical velocities. Model prediction also lines up with measurements by Hochrainer et al. (2005) of plume tip velocity of sprays formed by CFC12 and HFA227. Their results as shown in Figure 3.30 suggest that generally HFA227 produces a slower plume, especially during the initial transient.

3.7.5.2 Test case 2

The effect of vapour pressure is further explored on plume velocity by examining different ambient temperature for HFA134 propellant system. This enables investigation of a pressure range of 4 bars to 8 bars. Figure 3.31 shows that by increasing the ambient temperature from 285K to 305K, the plume velocity increases by almost 40%.

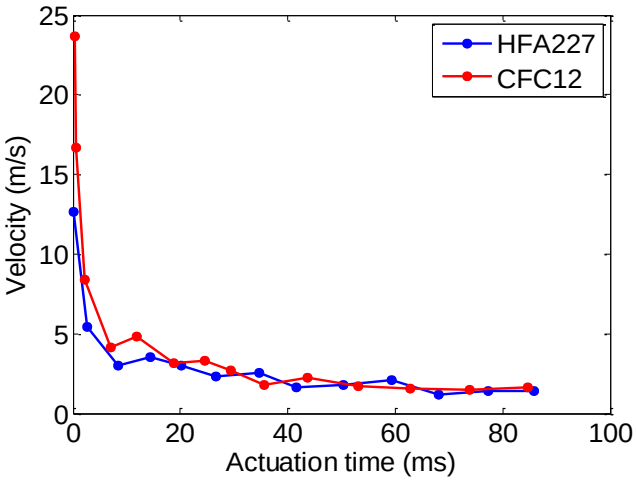

Figure 3.30 Plume velocity measurement of Hochrainer et al. (2005)

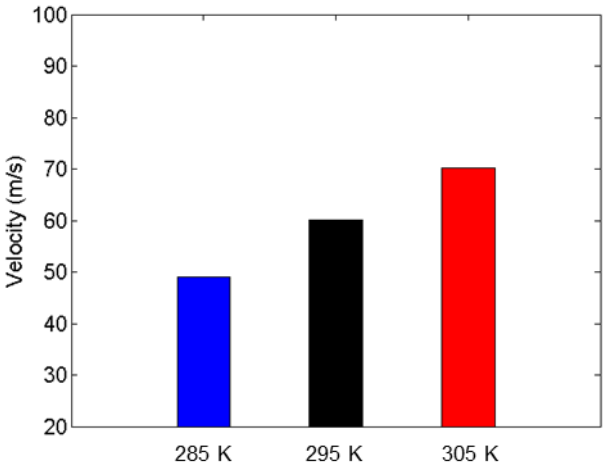

Figure 3.31 Prediction of mean plume velocity for different ambient temperature

3.7.5.3 Test case 3

Figure 3.32 (a-b) shows the mean velocity of the spray for different metering chamber sizes of 25 µl, 50 µl and 63 µl, for HFA134 propellant system. Results indicate that plume velocity is almost independent of the metering chamber size. This trend is in line with the measurements of Clark (1991) and Gabrio et al. (1999), who did not find a strong correlation between metering chamber size and plume velocity. On the other hand, the size of the metering chamber directly correlates to the plume duration as a larger metering chamber requires more time to deplete. This trend is also observed by Clark (1991) who computed actuation duration for 100 µl and 50 µl metering valves with nominally similar valve and spray orifice diameters of 0.6 mm. It is reported that spray duration was approximately proportional to volume of metering chamber.

3.7.5.4 Test case 4

The influence of spray orifice diameter on plume mean velocity and spray duration is investigated and presented in Figure 3.33 (a-b). The abscissa of the figures represents the non-dimensional diameter ratio for a fixed valve orifice diameter of 0.7 mm.

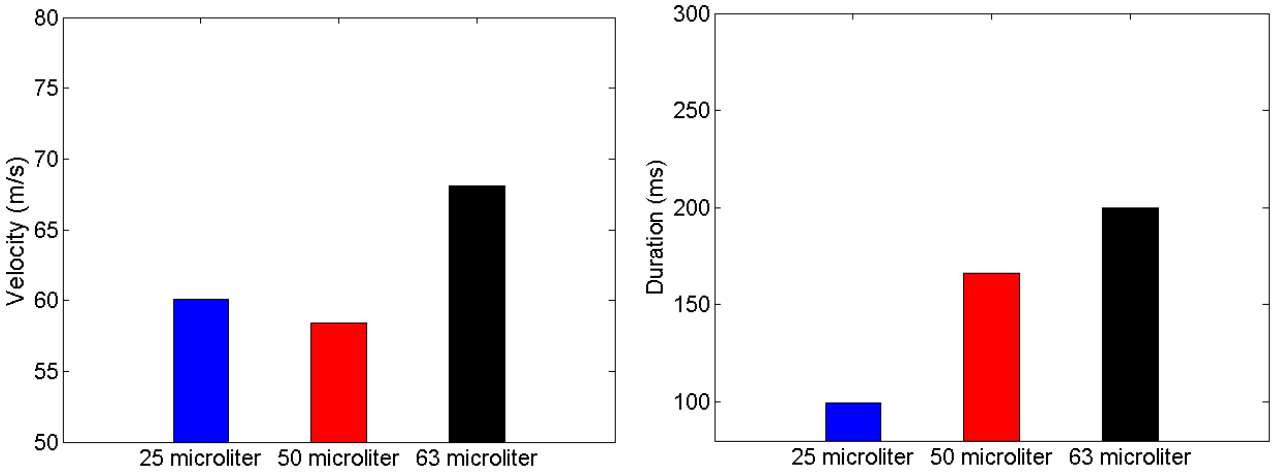

(a) Velocity **(b) Plume duration**

Figure 3.32 Prediction of plume characteristics for three different metering chamber volumes

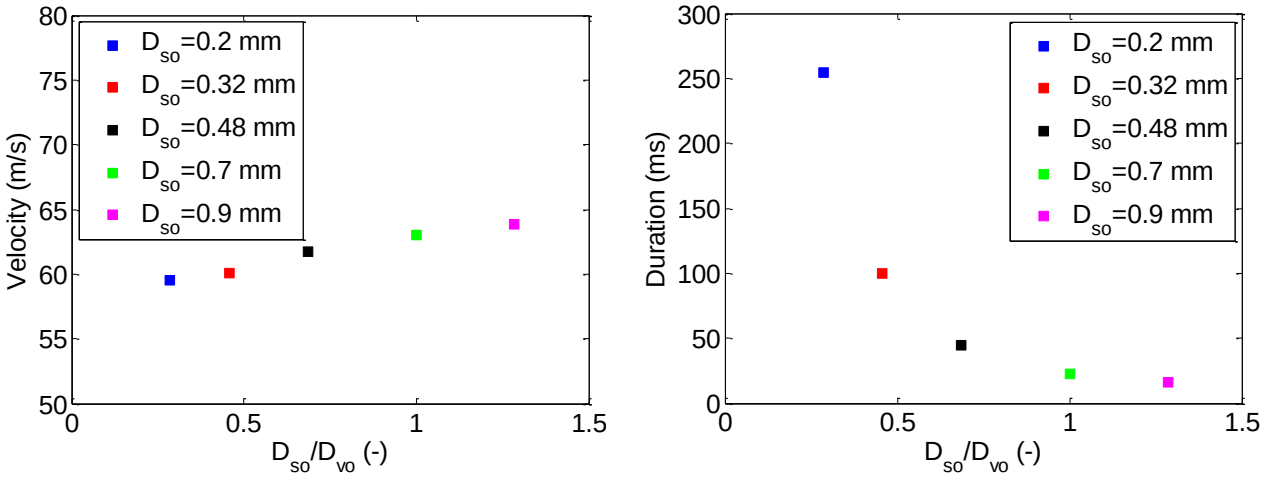

(a) Velocity **(b) Plume duration**

Figure 3.33 Prediction of plume characteristics for three different spray orifice diameters

Modelling predictions suggest that by increasing the spray orifice size, velocity of the plume increase. This trend agrees with the ones reported by Clark (1991) and Gabrio et al. (1999). However, modelling predictions suggests that by increasing the spray orifice diameter by 70%, only 7% increase in velocity takes place, whereas, for the same propellant system and diameter ratios of smaller than unity, Clark's (1991) measurement shows that by doubling the size of spray orifice, around 20% acceleration is obtained. In agreement with the previous work (Clark, 1991; Brambilla et al., 1999; Ganderton et al., 2002; Lewis et al., 1998; Lewis et al., 2004; Lewis et al., 2006; Lewis, 2007) the plume duration increases as the spray orifice diameter decreases. Reduction of the cross-sectional area of the spray orifice leads to lower mass emission per time unit and, hence, slower metering chamber depletion. Figure 3.33 (b) shows that by decreasing in spray orifice size, the changes in plume duration become less pronounced. This trend was also observed in measurements by Lewis et al., (2006).

3.8 Summary and conclusions

In this chapter, a range of 1-D models of flashing propellant flow through the twin-orifice system of pMDI were presented. The following existing models were implemented for application to assess their validity for metered pMDI flows: the homogeneous frozen model (HFM), the homogeneous equilibrium model (HEM) and the slip equilibrium model (SEM). A novel hybrid-homogeneous flow model (H-HFM) was also developed. This model has the capability to address liquid metastability and evaporative mass transfer in the spray orifice.

Temporal behaviour of solution variables of the propellant flow through the twin-orifice system was presented and it was observed that the trends were similar to the ones obtained by Clark (1991). The duration of the spray is predicted to be different for different flow models due to the large differences in predicted mass flow rate. In general, the predictions of H-HFM were found to be similar to those for HFM. This was due to the small evaporation rate predicted by H-HFM in conjunction with nucleation parameters that were used previously by Senda et al. (1994) for n-pentane/n-heptane mixtures. Results suggest that the magnitude of pressure, temperature and flow quality inside the chamber is almost independent of the implemented orifice flow model. However, the flow quality at the spray orifice exit is greater for HEM and SEM compared with HFM and H-HFM predictions.

Flow velocity at the spray orifice exit shows inverse relation to the amount of evaporation, so the HFM predicts the highest spray orifice exit velocity, whereas the H-HFM prediction is marginally lower, and the HEM/SEM shows the lowest spray orifice exit velocity predictions. This trend reverses when the near-orifice velocity is considered. Higher pressure at spray orifice exit is predicted for the equilibrium models in which more evaporation is predicted to take place. Thus the flow accelerates more in near-orifice region.

To seek validation, the model predictions of near-orifice velocity were compared against temporal measurement of plume velocity using optical diagnostic techniques (PDA). For three separate sets of measurement, the velocities predicted by HEM and SEM vapour phase were found to be consistently larger than the measured values. The SEM liquid phase velocity on the other hand was consistently well below the plume velocity. The predictions of the HFM and H-HFM models were always in the correct order of magnitude and exhibited the correct temporal trends reported in previous work.

To further assess the model, parametric variations of modelling variables were applied to study their effect on plume velocity and duration. Due to limited data in the literature and lack of data presentation in temporal format, the comparison was made qualitatively. Results show that effect of saturated vapour pressure of the propellant is one of the significant factors which determine the plume velocity and duration. This factor was studied using different propellants and ambient temperatures. As supported by previous works changing in metering chamber volume only influences the plume duration, whereas spray velocity remains approximately unaffected. Model outcomes indicate that reduction of spray orifice cross-sectional area leads to formation of a faster and shorter plume. This trend was also observed by Clark (1991) and Gabrio et al. (1999).

Chapter Four

Atomisation Model of pMDI

4 Chapter Four: Atomisation Model of pMDI

4.1 Introduction

Pressurised metered dose inhalers are distinguished by their unique ability to form a fine aerosol plume with large numbers of droplets predominantly in the size range 1-5 μm. The mechanism responsible for droplet generation from bulk formulation is known to be transient, turbulent and highly complex (Versteeg & Hargrave, 2006; Finlay, 2001; Gavtash et al. 2014), but the details are poorly understood. Two possible effects have been previously identified as candidate mechanisms of liquid bulk disintegration, namely (i) propellant flashing (Finlay, 2001; Clark, 1991; Versteeg et al., 2006; Dunbar, 1997) and (ii) aerodynamic atomisation (Clark, 1991, Gavtash et al., 2014).

Flashing is the process of rapid growth of the gas phase after exposing a pressurised fluid to abrupt pressure drop. The liquid content in the mixture becomes superheated and the vapour nuclei in the mixture rapidly grow up to a point where disintegration of the bulk liquid is caused, generating fine droplets. This mechanism of droplet generation is called flash boiling atomisation. Initial bubble nuclei can be present in the liquid if it is sufficiently superheated (Sher et al., 2008). The twin-orifice arrangement of a typical pMDI allows rapid depressurisation when propellant flows (i) from the metering chamber into the expansion chamber space through the valve orifice, (ii) from expansion chamber through the spray orifice constriction and (iii) when the two phase propellant mixture is expelled into the ambient having atmospheric pressure (Finlay, 2001).

Clark (1991) conjectured that the dominant atomisation mechanism of the pMDI was aerodynamic breakup similar to air-blast atomisation. Propellant is understood to be pre-atomised into liquid ligaments during its passage from the metering chamber to the expansion chamber. Two-phase propellant formulation was understood to enter the spray orifice in the form of liquid ligaments and rapidly expanding propellant vapour. The vapour flow was assumed to deform liquid ligaments and generating smaller liquid segments, which finally exit the spray orifice as small spherical droplets. It was concluded that the propellant vapour pressure and, furthermore, the amount of vapour produced in expansion chamber as a result of evaporation were the most significant controlling factors governing the droplet size. Clark correlated the experimental droplet size data with the peak expansion chamber

pressure p_{ec} and vapour quality x_{ec} to obtain an empirical correlation for the mass median aerodynamic diameter (MMAD) as defined by equation 4-1:

$$MMAD = \frac{C}{x_{ec}^{0.46}\left(\frac{p_{ec} - p_{amb}}{p_{amb}}\right)^{0.56}} \qquad 4\text{-}1$$

Where p_{amb} = ambient pressure. Clark (1991) reported good fit to measured data for continuous and metered discharge using the constant C = 8.02 and 1.82, respectively. Dunbar et al. (1997); Dunbar and Miller (1997) applied C = 8.02 in combination with a transient CFD model to find the values of droplet size at a particular time using instantaneous values of x_{ec} and p_{ec}. Although Clark's correlation has been the most influential one up to date, the model is empirical. The constant C of equation 4-1 has dimension of length. Equation 4-1 successfully captures the trends that relate formulation parameters to the final size of the droplets, but the length-scale determining physics is not described by the expression. This limits the predictive power of the equation. Other studies (Stein & Myrdal, 2004; Brambilla et al., 1999; Ivey et al., 2014) have developed empirical correlations for spray droplet size requiring measurement of the residual droplet size from binary liquid sprays containing HFA propellant and a non-volatile excipient. Thus none of the existing approaches predicts droplet size from first principles.

The aim of this chapter is to present a novel theoretical approach to the prediction of the size of droplets produced by pMDIs without the need for empirical adjustments. Two separate models are constructed based on (i) aerodynamic atomisation using the linear instability sheet atomisation (LISA) framework (Senecal et al., 1999), and (ii) hybrid-aerodynamic/flashing atomisation using combination of LISA, the approach of (Sher & Elata, 1977) linked with secondary break-up. The hybrid atomisation model enables us to explore the possibility of droplet formation based on either of aerodynamic or flashing modes of atomisation. Since atomisation is strongly dependent on flow rate, velocity and properties of fluid (Lefebvre, 1989), both atomisation models require accurate predictions of the mentioned parameters. According to chapter 3, section 3.7.4.3, HFM and H-HFM were the most successful models in predicting near-orifice spray velocity when

comparing the predictions against PDA measurements. These internal flow models are used in conjunction with the atomisation models to predict issued droplet size.

4.2 Conceptual image of pMDI atomisation

Internal flow visualisation studies using optical nozzles suggest the existence of a thin annular liquid sheet inside the spray orifice during a substantial fraction of the spray event (Versteeg et al., 2006). This sheet contains liquid formulation that is accelerated through the spray orifice along with a propellant vapour core. The liquid sheet provides the fundamental initial liquid length scale, from which respirable droplets are subsequently formed when the liquid emerges from the spray orifice. Preliminary estimates based on these visualisations show that the thickness h of the annular layer is around 10 μm. On the other hand a typical pMDI spray orifice has a radius of R_{SO}= 200 μm. Hence, the ratio of the layer thickness and spray orifice radius is much smaller than unity and the thin annular liquid sheet can be treated as a flat sheet.

As propellant enters the spray orifice, the pressure drops rapidly. According to the HFM, no mass transfer takes place between liquid and vapour phase, i.e. evaporation is inhibited (Clark, 1991). In this case where no bubbles nucleate, atomisation would occur due to an aerodynamic breakup mechanism which is assumed to take place at spray orifice exit. This mechanism is represented by LISA framework (Senecal et al., 1999; York et al., 1953; Dombrowski & Johns, 1963), which uses the analogy with flat sheet break-up. Wave-induced instabilities at the interface of liquid and HFA gas phases will grow in amplitude and are responsible for sheet disintegration and formation of unstable cylindrical ligaments.

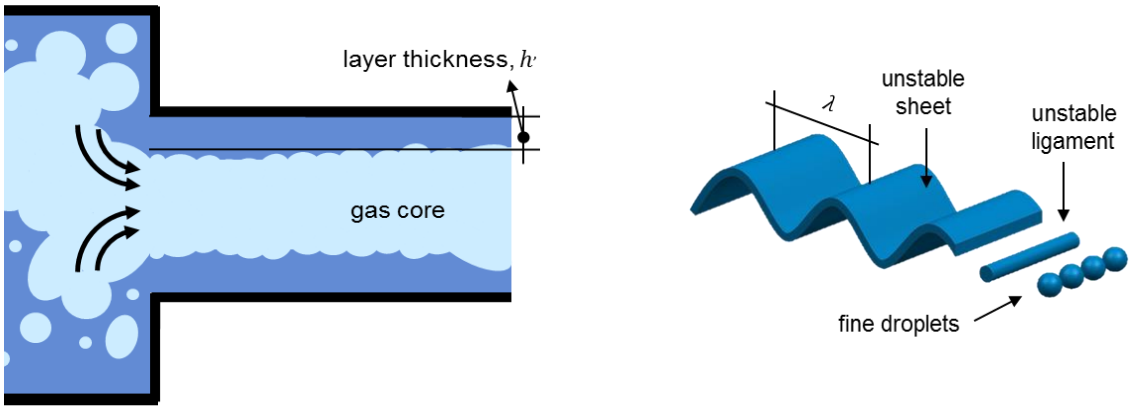

Figure 4.1 Schematic of droplet generation from annular liquid sheet, using LISA mechanism in pMDI

These ligaments are assumed to move normal to their axis. Eventually, as a result of capillary forces, the ligaments are broken apart further and contract into spherical droplets. The assumed mechanism is schematically shown in Figure 4.1.

In the hybrid atomisation model, the process consists of two distinct scenarios. According to the H-HFM, a rapid pressure drop is experienced by propellant at the upstream edge of spray orifice, which leads to vapour bubble nucleation at this location and in the vena contracta that is understood to be occurring just downstream (Domnick & Durst, 1995). One scenario assumes the same aerodynamic breakup mechanism as before with the difference that some propellant evaporates at the liquid surface and is released into the propellant gas core, causing reduction of the liquid sheet thickness. The droplets are subsequently formed by aerodynamic atomisation based on the above-mentioned LISA model (see Figure 4.2 (a)). In the second scenario, bubbles remain intermingled with the liquid phase and during the growth process, they cause disturbances and fragmentation of the liquid sheet (Sher & Elata, 1977) into liquid blobs. This process is shown in Figure 4.2 (b). Blobs then interact with the high-speed vapour core and the resulting aerodynamic loading produces fine droplets due to secondary aerodynamic atomisation.

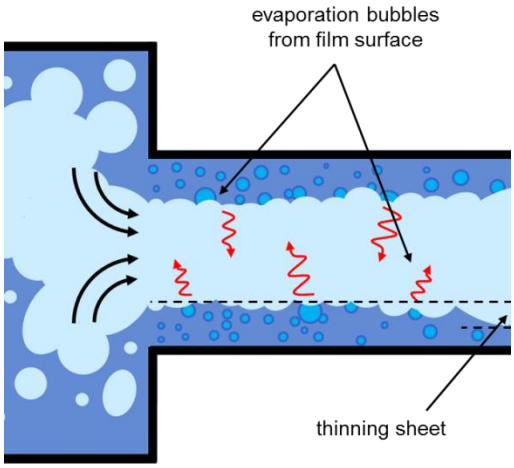

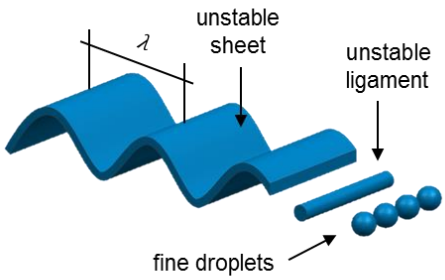

(a) Droplet generation from annular liquid sheet, using LISA mechanism

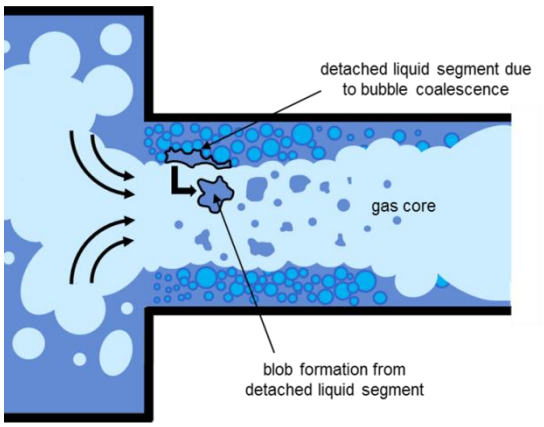

(b) Liquid blob formation

due bubble growth and liquid layer disruption

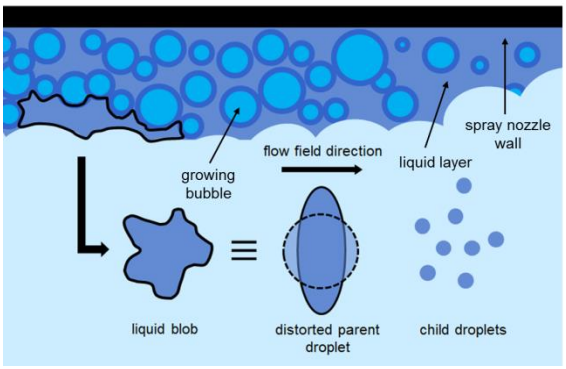

(c) Liquid blob disintegration

to fine droplets in TAB regime ($We_g < 50$)

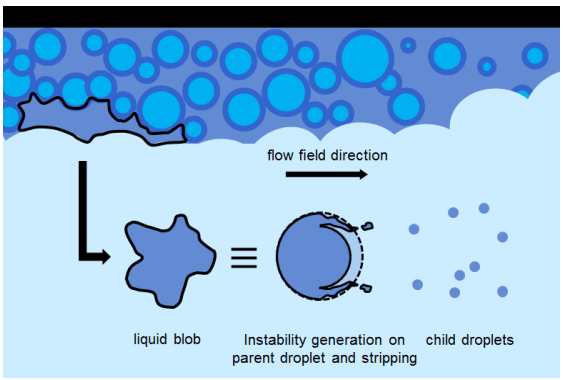

(d) Liquid blob disintegration

to fine droplets in KH regime ($We_g \geq 50$)

Figure 4.2 Schematic of hybrid atomisation model

The exact nature of the secondary mechanism by which final droplets are produced, is decided on the basis of the local gas-phase Weber number for the liquid blobs. Preliminary calculations suggest that the prevailing gas Weber number inside the spray orifice is within the range where multimode secondary break-up is most probable i.e. $20 < We_g < 80$. The multimode breakup can be best represented by two separate secondary mechanisms - sheet-thinning and vibrational deformation (Zeoli & Gu, 2006). These mechanisms are incorporated in the hybrid atomisation model. These models are mathematically represented by Kelvin Helmholtz (KH) (Reitz, 1987) and Taylor Analogy Breakup (TAB) (O'Rourke & Amsden, 1987), respectively. Conceptual models of TAB and KH models in pMDI spray orifice are illustrated in Figure 4.2 (c) and Figure 4.2 (d), respectively.

4.3 Theoretical models

4.3.1 General modelling assumptions

The key modelling assumptions that are applied throughout the atomisation modelling development are as follows:

- Annular configuration of the initial liquid phase inside the spray orifice
- Flat sheet approximation: the emergent annular sheet can be considered as a flat sheet ($h/R_{SO} \ll 1$)
- Relative velocity between annular liquid flow and vapour core flow is approximately equal to two-phase flow discharge velocity. This assumption is also used by (Senecal et al., 1999; Schmidt et al., 1999; Razzaghi, 1989)

4.3.2 Governing equations

4.3.2.1 Annular layer thickness

As remembered from chapter 3, section 3.3.2.3, the void fraction for a homogenous two-phase flow is determined by equation 3-19 (Whalley, 1987):

$$\alpha = \frac{1}{1 + \left(\frac{1-x}{x}\right)\left(\frac{v_l}{v_g}\right)} \qquad 3\text{-}19$$

As shown in Figure 4.3 schematically, the definition of the void fraction for one-dimensional flow yields equation 4-2 for an annular flow:

$$\alpha = \frac{A_g}{A_{SO}} = \left(\frac{D_g}{D_{SO}}\right)^2 \qquad 4\text{-}2$$

Where A_g and A_{SO} are the cross sectional area occupied by the gas and the spray orifice, respectively. Since $D_{so} = 2h + D_g$, the thickness of the annulus can be worked out from equation 4-3.

$$h = \frac{D_{SO}}{2}\left(1 - \sqrt{\alpha}\right) \qquad 4\text{-}3$$

Where D_{SO} is the spray orifice diameter, D_g is the diameter occupied by the gas phase and h is the layer thickness.

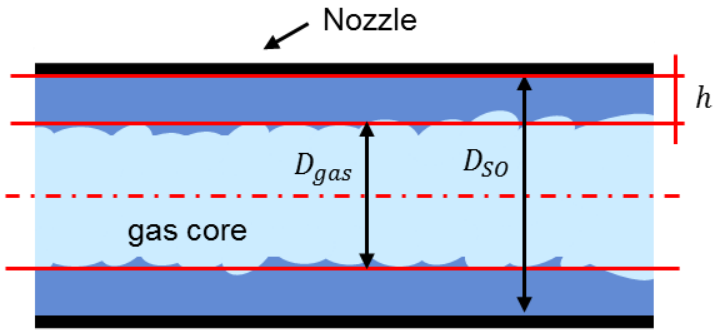

Figure 4.3 Schematic of annular flow topology inside spray orifice

Hence, the thickness h of the annular liquid layer in a spray orifice with diameter D_{SO} can now be estimated using equations 3-19 and 4-3 from the flow quality and the specific volumes of the liquid and the gas phase, which are all generated by the internal flow model.

4.3.2.2 Aerodynamic atomisation (LISA)

Senecal et al. (1999) developed a dispersion equation for liquid sheets with small sinusoidal disturbances, which yielded equation 4-4 for the growth rate ω_r , of the most unstable disturbance:

$$\omega_r = \frac{1}{\tanh(k\acute{h}) + \Gamma}\left[-2\nu_l k^2 \tanh(k\acute{h}) + \sqrt{4\nu_l^2 k^4 \tanh(k\acute{h}) - \Gamma V_{rel}^2 k^2 - [\tanh(k\acute{h}) + \Gamma]\left[-\Gamma V_{rel}^2 k^2 + \frac{\sigma k^3}{\rho_l}\right]}\right] \quad 4\text{-}4$$

Where $\acute{h}$ is the half sheet thickness of the annular layer ($\acute{h} = h/2$). Γ is the density ratio between the gas and liquid phase (i.e. ρ_g/ρ_l), ν is the kinematic viscosity and k (=$2\pi/\lambda$) is the wave number. As we apply this equation to pMDI flow, Here the liquid properties correspond to HFA liquid phase, and gas properties correspond to HFA gas phase.

Two wave-generation regimes were recognised by Senecal et al. (1999): (i) short waves that are dominated by viscous and surface tension effects and (ii) long waves, which are governed by inertial and surface tension effects. The regimes can be distinguished on the basis of the gas cut off Weber number (Senecal et al., 1999).

$$We_g = \frac{\rho_g V_{rel}^2 \acute{h}}{\sigma} \quad 4\text{-}5$$

If $We_g > 27/16$, then short waves are generated. Otherwise long waves are dominant responsible for break-up. For the case of short waves, Senecal et al. (1999) give the following simplified version of equation 4-4:

$$\omega_r = -2\nu_l k^2 + \sqrt{4\nu_l^2 k^4 + \Gamma V_{rel}^2 k^2 - \frac{\sigma k^3}{\rho_l}} \quad 4\text{-}6$$

Numerical maximisation of equation 4-6 with respect to wave number (i.e. $d\omega_r/dk$) yields the maximum growth rate, ω_{max} as a function of wave number, k. Corresponding wave number of maximum growth rate is denoted by K_s. The diameter of the ligament d_{lig} at the point of disintegration is assumed to be linearly proportional to the reciprocal of wave number K_s:

$$d_{lig} = \frac{2\pi C_{lig}}{K_s} \quad 4\text{-}7$$

Where C_{lig} is ligament constant and has a value of 0.5 (Hutcheson et al., 2008; Ghose et al., 2014).

In the long wave regime, viscosity has negligible effect on wave growth and hence K_s can be obtained using inviscid analysis (Squire, 1953) as mentioned by Senecal et al. (1999):

$$K_s = \frac{\rho_g V_{rel}^2}{2\sigma} \quad 4\text{-}8$$

The ligament diameter at break-up point can be obtained from mass balance. By assuming that two ligaments form per wavelength, equation 4-9 can be obtained:

$$d_{lig} = \sqrt{\frac{8\acute{h}}{K_s}} \quad 4\text{-}9$$

Regardless of the responsible wave regime for break-up, the diameter of the droplets can be obtained based on capillary instability analysis of the initial ligaments:

$$D_d = 1.88 d_{lig}(1 + 3Oh)^{1/6} \quad 4\text{-}10$$

In which Oh denotes the Ohnesorge number defined by equation 4-11:

$$Oh = \sqrt{\frac{\mu_l^2}{\rho_l \sigma d_{lig}}} \quad 4\text{-}11$$

4.3.2.3 Hybrid atomisation

4.3.2.3.1 Onset of different atomisation regimes

Determination of the onset of atomisation regime is based on spatial comparison of liquid layer void fraction, α_{lay} (equation 3-42 which used with subscript lay) against critical void fraction, α_c. Critical void fraction is strongly dependent on bubble nuclei topological arrangement inside the liquid layer. In the absence of any visual evidence, an arbitrary assumption has to be made in order to determine droplet size scale. Therefore the simplest assumption would be a primitive cubic system (PCS) arrangement of nuclei inside the liquid layer. This assumption is also used in previous works (Sher & Elata, 1977; Senda et al., 1994;

Kawano et al., 2006). Such nuclei geometric arrangement suggests that the critical void fraction occurs when growth is sufficient for adjacent bubbles to touch each other. In a PCS arrangement the corresponding void fraction is $\alpha_c \cong 0.52$.

If $\alpha_{lay} < \alpha_c$ everywhere along the spray nozzle, aerodynamic atomisation based on LISA model prevails at the spray orifice exit plane. However, if at any point along spray nozzle $\alpha_{lay} \geq \alpha_c$, bubbles are assumed to touch each other, the liquid layer fragments and liquid blobs (also termed as parent droplet) are formed. Here flash-boiling atomisation prevails inside the spray nozzle. The liquid blobs are then exposed to aerodynamic force of the vapour core and disintegrate by one of the assumed secondary atomisation mechanism, into number of fine child droplets.

4.3.2.3.2 Parent droplet formation by flashing

Once the void fraction criterion is satisfied, bubble bursting leads to liquid layer disintegration. The arrangement of the initial bubble nuclei within the liquid segment has a direct impact on the size of the product liquid droplets. In this model two possible arrangements are considered for the bubbles based on the liquid layer thickness namely two-dimensional (2D) and three-dimensional (3D) PCS arrangements. Homogeneous distribution of nuclei leads to identical average distance, l_{ave} between any two adjacent bubbles.

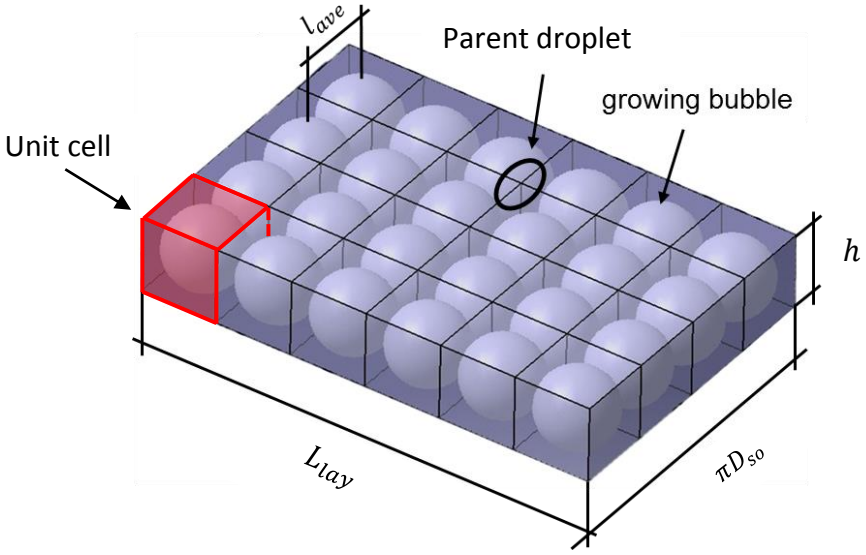

Figure 4.4 2D nuclei arrangement in liquid layer

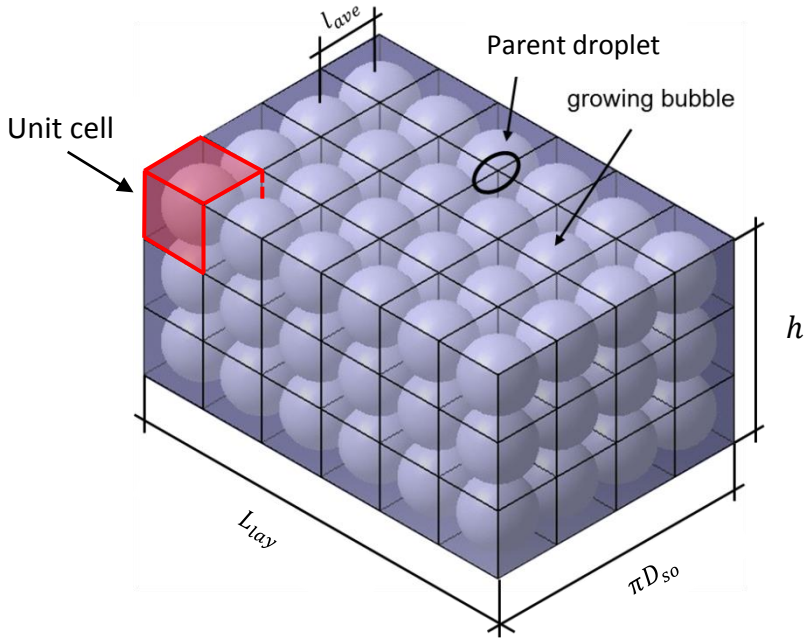

Figure 4.5 3D nuclei arrangement in liquid layer

If this average distance is larger than the layer thickness, then there is no space for the nuclei to be placed on top of each other, along the thickness of the layer. Therefore, one bubble per unit cell is appropriate as shown in Figure 4.4. Thus a 2D arrangement is the topological nuclei arrangement and average distance between two bubbles can be calculated as follows:

$$l_{ave} = \sqrt{\frac{A_{lay}}{n_b}} \qquad 4\text{-}12$$

Where A_{lay} is the surface area of the liquid layer ($= \pi D_{so} \times L_{lay}$) and n_b is the absolute number of bubbles in liquid layer calculated by equation 3-40. As a result, number of parent droplets (shown by circle in Figure 4.4), n_d is twice the number of bubble nuclei (per bubble nucleus one droplet is formed from the top segment surface and one from bottom segment surface).

On the other hand, if the average distance between two bubbles is smaller than the liquid layer thickness, a 3D arrangement of nuclei lattice would occur. In this case, there is a possibility for the nuclei to be situated on top of each other along the layer thickness (as shown in Figure 4.5). In this situation the average distance is estimated using equation 4-13:

$$l_{ave} = \sqrt[3]{\frac{Vol_{lay}}{n_b}} \qquad 4\text{-}13$$

Where Vol_{lay} is the liquid layer volume and is calculated using the expression below:

$$Vol_{lay} = \pi D_{so} \times L_{lay} \times h \qquad 4\text{-}14$$

Where L_{lay} is the length of liquid layer segment ($= V.\Delta t$ where V is local flow velocity and Δt is time step over which liquid flows into spray orifice). For this case, the residual liquid surrounding each of the bubbles is used for one droplet formation. Thus, the number of droplets is equal to the number of bubbles in the liquid segment. At the point where condition $\alpha_{lay} \geq \alpha_c$ is satisfied, the size of the residual droplets is calculated based on the mass balance on the liquid layer and formed parent droplets:

$$D_p = \sqrt[3]{\frac{6m_l(1-\alpha_c)v_{l,c}}{n_d\pi}} \qquad 4\text{-}15$$

Where the m_l is the mass of the liquid layer flowing into the spray orifice.

4.3.2.3.3 Child droplet formation

A parent droplet undergoes further disintegration due to being exposed to high velocity HFA gas phase, flowing inside spray nozzle. This interaction produces the final fine droplets. These final droplets are also termed child droplets. In accordance with Faeth et al. (1995), determination of the appropriate secondary atomisation regime depends on the prevailing droplet Weber number ($We_g = \rho_g V^2 D_p/\sigma$). Flow calculations suggest that the transitional Weber number should be in the range of $20 < We_g < 80$. As noted by Faeth et al. (1995) multimode secondary breakup occurs with in this range, resembling a combination of bag and sheet-thinning breakup modes (Lefebvre, 1988; Ashgriz, 2011; Guildenbecher et al., 2009). Bag and sheet-thinning modes are best represented by TAB and KH secondary atomisation models (Zeoli & Gu, 2006), respectively. Realistically, the transition between TAB and KH is a continuous function of Weber number. There is no guideline in the literature to establish a single transitional Weber number from TAB to KH. However, modelling is simplified by assuming that each model is activated over distinct regions of gas Weber number (Faeth et al., 1995). Therefore, we use the average Weber number of 50 (average of 20 and 80) as the transition criterion. For gas Weber numbers below 50, TAB model is activated. For Weber numbers above 50, KH model is activated.

4.3.2.3.3.1 TAB model

According to O'Rourke & Amsden (1987), the non-dimensionalised equation of motion of the oscillating droplet is:

$$\frac{d^2\acute{y}}{dt^2} = \frac{2}{3}\frac{\rho_g}{\rho_l}\frac{V^2}{{r_p}^2} - \frac{8}{\rho_l}\frac{\sigma}{r_p^3}\acute{y} - \frac{5\mu_l}{\rho_l r_p^2}\frac{d\acute{y}}{dt} \qquad 4\text{-}16$$

Where $\acute{y}$ is non-dimensionalised distortion parameter defined as $y' = 2\acute{x}/r_p$ ($\acute{x}$ is the displacement of droplet equator from its equilibrium position). In equation 4-16, r_p is the radius of parent droplet calculated from equation 4-15 ($r_d = D_d/2$) and t is the time.

Assuming that the droplet-ambient relative velocity is constant and is equal to the local prevailing velocity in the spray orifice and then equation 4-16 can be analytically integrated and solved for each liquid blob which is produced by the procedure described in 4.3.2.3.2. The solution reads as follows:

$$\acute{y}(t) = \frac{We_g}{12} + e^{-t/t_d}\left[\left(\acute{y}(0) - \frac{We_g}{12}\right)\cos(\omega t) + \left(\frac{d\acute{y}/dt}{\omega} + \frac{\acute{y}(0) - We_g/12}{\omega t_d}\sin(\omega t)\right)\right] \quad 4\text{-}17$$

Where:

$$\frac{1}{t_d} = \frac{5\mu_l}{2\rho_l r_p^2} \quad 4\text{-}18$$

And:

$$\omega^2 = \frac{8\sigma}{\rho_l r_p^3} - \left(\frac{1}{t_d}\right)^2 \quad 4\text{-}19$$

If $\acute{y} > 1$ at some point during the oscillation, then child droplet is generated from the blob and its size is calculated as follows (O'Rourke & Amsden, 1987)

$$D_d = \frac{D_p}{1 + \frac{8K\acute{y}^2}{20} + \frac{\rho_l r_p^3 (d\acute{y}/dt)^2}{\sigma}\left(\frac{6K-5}{120}\right)} \quad 4\text{-}20$$

Where K is equal to 10/3 (O'Rourke & Amsden, 1987).

4.3.2.3.3.2 KH model

As derived by Reitz (1987), the wave length Λ of the disturbance with maximum growth rate, which is responsible for pinching off child droplets from parent droplet, is calculated from equation 4-21:

$$\frac{\Lambda}{D_p} = \frac{9.02(1 + 0.45Oh^{0.5})(1 + 0.4Ta^{0.7})}{\left(1 + 0.87We_g^{1.67}\right)^{0.6}} \quad 4\text{-}21$$

The corresponding growth rate Ω of the most unstable wavelength is:

$$\Omega\left(\frac{\rho_l D_p^3}{\sigma}\right)^{0.5} = \frac{(0.34 + 0.38We_g^{1.5})}{(1+Oh)(1+1.4Ta^{0.6})} \quad 4\text{-}22$$

Where D_p is the diameter of the parent droplet, Oh is the Ohnesorge number as defined by equation 4-11 with the length scale of D_p and eventually Ta is the Taylor number defined by the following expression:

$$Ta = Oh\sqrt{We_l} \quad 4\text{-}23$$

In which We_l is the Weber number defined based on liquid phase density. The resulting child droplets are linearly proportional to the wavelength of instability:

$$D_d = 2B_0\Lambda \quad 4\text{-}24$$

Where B_0 is a model constant set equal to 0.61 based on the work of Reitz (1987).

4.3.2.4 Near-orifice droplet size

The HFM and H-HFM internal flow models are linked with the atomisation models. These models suggest that the propellant emerging from the spray orifice is superheated. The superheat will cause flashing in the near-orifice (denoted by "NO") region immediately outside the spray orifice (denoted by "SO"), resulting in increased flow quality. Conservation of energy assuming adiabatic conditions enables us to evaluate the near-orifice quality using equation 4-25:

$$x_{NO} = \frac{h_{l(T,SO)} - h_{l,(sat,amb)}}{h_{lg,(sat,amb)}} \quad 4\text{-}25$$

In equation 4-25, h_l and $h_g$are the enthalpies of liquid and vapour respectively, and h_{lg} is the latent heat. The subscript sat, amb denotes saturation state at ambient condition. Change in quality corresponds to a reduction of droplet mass is obtainable from equation 4-26:

$$m_{d,NO} = (1 - x_{NO})m_{d,SO} \quad 4\text{-}26$$

Where $m_{d,NO}$ is the reduced droplet mass in near-orifice region and $m_{d,SO}$ is droplet mass at spray orifice exit, obtainable from equation 4-27:

$$m_{d,SO} = \frac{\pi D_d^3}{6v_{l(T,SO)}} \quad 4\text{-}27$$

Evaporation of volatile formulation components will bring the droplets to thermodynamic equilibrium. This has to be accounted for, since it constitutes a further size reduction mechanism. The size of the droplet after the flashing (near-orifice) is calculated using equation 4-28:

$$D_{d,NO} = \sqrt[3]{\frac{6m_{d,NO}v_{l(sat,amb)}}{\pi}} \quad 4\text{-}28$$

4.4 Results and discussion

In this section the outcomes of the atomisation models are presented. Firstly, relevant model predictions for LISA and Hybrid model are described and discussed using test case output from the HFM and H-HFM internal flow models generated in chapter 3. Subsequently, results are validated against the PDA data obtained by the parallel experimental project and data gathered from the literature. It should be noted that H-HFM model involves coupling of the bubble growth equation with the governing equations of homogeneous two-phase flow in iterative mode. The resulting computations are very time consuming. It is, however, possible to carry out instantaneous atomisation calculations based on assumed stagnation conditions since the model assumes quasi-steady state. For the purpose of comparison of the atomisation models in conjunction with HFM and H-HFM, the results involving the latter, as the internal flow model, are presented at five key instants of the atomisation event. These instants correspond with key stages of actuation such as initial start-up, expansion chamber filling and expansion chamber emptying

The next step is to conduct parametric study on nuclei population and investigate its effect on the atomisation mechanism and on the droplet size as predicted by the model. Finally, the outcome of a short parametric study regarding the factors affecting droplet size

(propellant, temperature, actuator geometry) is presented and an attempt is made to compare these model predictions with trends reported in the literature.

4.4.1 Atomisation models predictions

4.4.1.1 Test case and modelling parameters

In current section we examine the temporal solution variables of our aerodynamic and hybrid atomisation models. The modelling parameters are similar to the ones introduced in chapter 3, section 3.7.1.1. For the reader's convenience we repeat modelling parameters in Table 4.1. HFA227 is used in this study as the propellant system and the time step was selected as 0.25 ms.

Parameter	Value	Parameter	Value
Vol_{mc}	25 µl	D_{vo}	0.7 mm
Vol_{ec}	25 µl	D_{so}	0.4 mm
$C_{d,vo}$	0.6	$C_{d,so}$	0.7
T_{amb}	295 K	L_{so}	0.75 mm

Table 4.1 Modelling parameters of the default test case

4.4.1.2 Aerodynamic atomisation (LISA)

Figure 4.6 to Figure 4.9 show the predictions of LISA (aerodynamic) atomisation model in conjunction with HFM internal flow model. Figure 4.6 presents the temporal variations of liquid layer thickness inside the spray orifice from which droplets are generated. It can be seen that layer thickness initially increases quickly up to a maximum point. The timing of this maximum corresponds to the filling stage of the expansion chamber when more liquid enters than leaves this space.

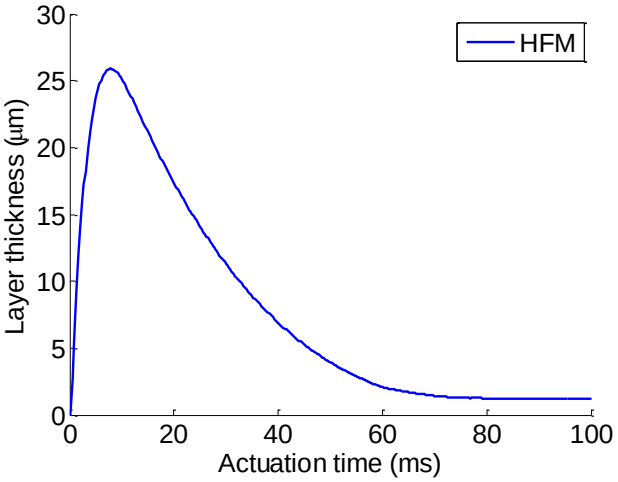

Figure 4.6 Temporal evolution of annular layer thickness inside spray orifice

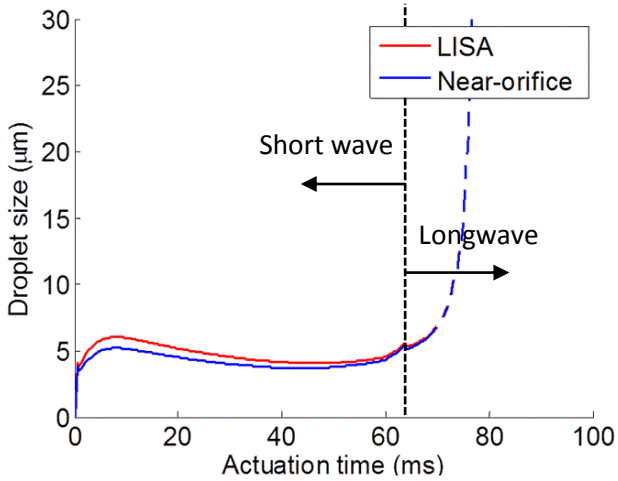

Figure 4.7 Predicted droplet size before and after near-orifice flashing

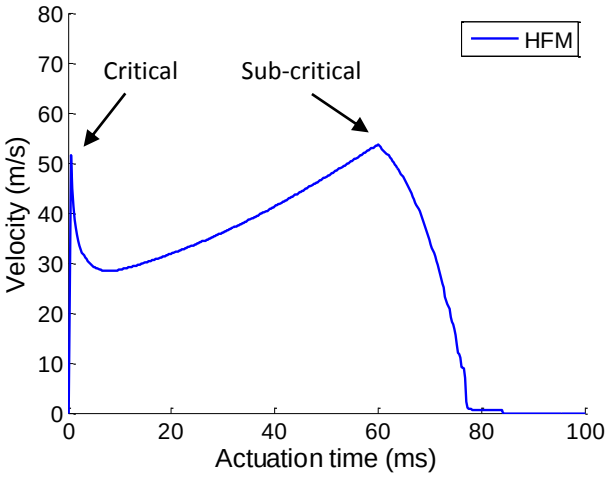

Figure 4.8 Spray velocity at spray orifice exit

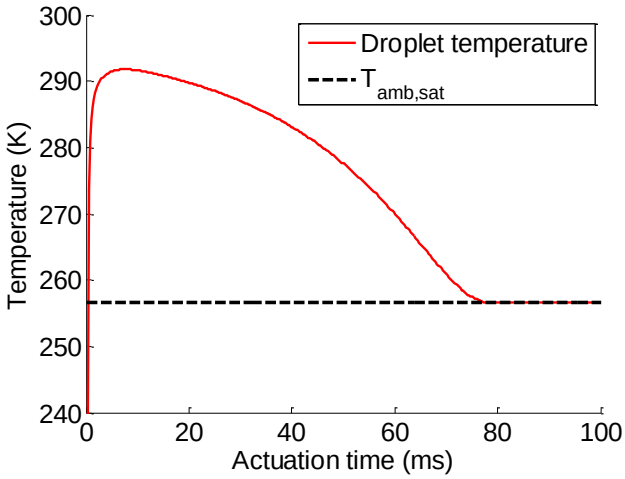

Figure 4.9 Temporal droplet temperature before and after near-orifice flashing

Therefore, more liquid travels through the spray orifice, which forms a thicker layer. After this point the liquid layer thickness reduces more gradually during the emptying stage of the expansion chamber, when more liquid evaporates in the expansion chamber.

The liquid annulus is the precursor liquid entity from which liquid ligaments and hence spray droplets are formed. Temporal traces of predicted droplet size at spray orifice exit using LISA (equation 4-10) and near-orifice region (equation 4-28) are shown in Figure 4.7. Since the main energy source of droplet fragmentation is the spray orifice exit velocity, here we show this variable in Figure 4.8, for the reader's convenience. Results suggest that both

droplet size traces (equations 4-10 and 4-28) show very similar patterns over the whole actuation event. The regions where “short waves” or “long waves” are dominant responsible for atomisation, are shown by means of arrows and annotations in Figure 4.7. With reference to Figure 4.7, the predicted droplet size rapidly rises to 4 µm, which is reached at a time that corresponds to the occurrence of initial velocity peak. After this, droplet size more gradually increases up to 6 µm over a short duration of 7 ms as a consequence of the velocity decrease during expansion chamber filling. The available energy for atomisation reduces as the velocity decreases by 20 m/s and hence larger droplets are formed. From here onwards droplet size gradually decreases by continual increasing of the velocity up to the point where the second velocity peak occurs at around 63 ms. The inverse relationship between velocity and droplet size, which is captured by these predictions, confirms the previous findings of Clark (1991), Dunbar et al. (1997), Wigley et al. (2002) and Myatt et al. (2015 a-b).

After the second velocity peak, the velocity sharply reduces due to a rapid reduction in propellant mass flow rate associated with metering chamber depletion. At this point the adiabatic assumption results in sharp velocity reduction and internal flow predictions become poor. The inverse relation of velocity/droplet size for aerodynamic atomisation causes unrealistically high droplet size predictions. The results become meaningless; the reduced degree of confidence in the results is indicated by means of a dashed line. Figure 4.7 shows that conditions at the spray orifice exit responsible for primary atomisation in the “short wave” regime i.e. We_g (equation 4-5) $>$ 27/16, prevail when t < 65 ms. Our internal flow model predicts that approximately 95% of the propellant mass has been emitted by that time, so only 5% of metering chamber mass is emitted as (unrealistically) large droplets in the “long wave” regime. Nevertheless, the LISA model captures the production of the large bulk of the droplets.

The difference between the two traces marked LISA and near-orifice in Figure 4.7 shows the effect due to flashing of the superheated droplets in the near-orifice region. The droplet size reduces by a further 1 µm at the first peak in the trace. After this, the differences between the traces become gradually less. This is due to the increased evaporation in the expansion chamber, which cools the fluid before it enters the spray orifice (see also Figure 4.9, which shows the droplet temperature at the spray orifice exit). The dashed line

indicates the saturated temperature of HFA227 droplets at atmospheric pressure. This is the final temperature of all droplets after superheated fluid has flashed off and thermodynamic equilibrium with ambient conditions is reached. The figure suggests that, as time advances, the amount of superheat reduces, so less additional size reduction due to near-orifice flashing takes place during the later stages of the actuation event.

4.4.1.3 Hybrid atomisation

Figure 4.10 to Figure 4.15 show the predictions of the hybrid atomisation model in conjunction with H-HFM internal flow model for the test case with input conditions presented in Table 4.1. Temporal discretisation was selected as 0.25 ms and spray orifice length was subdivided into 100 computational grid cells (see chapter 3, section 3.7.3.1). For the actuator geometric parameters and propellant system in Table 4.1, the temporal distribution of the number of bubbles in the layer is shown in Figure 4.10 using C_b = 1. It can be seen that the nuclei population inside the liquid layer which flows into spray orifice, initially increases during the filling stage of expansion chamber up to a maximum and afterwards decreases monotonically as this space empties out. The void fraction of the liquid layer is shown in Figure 4.11. The temporal trend and magnitude of this quantity is a result of interaction between number bubble nuclei, degree of superheat and velocity of the flow. The latter determines the residence time of the bubbles inside the spray orifice. According to the liquid layer void fraction prediction, it seems that internal flashing of liquid layer is not the dominant atomisation mechanism as α_{lay} is consistently below α_c (shown with dashed line). Hence, the hybrid atomisation model with nucleation parameter C_b set equal to unity suggests that droplets are produced only by the aerodynamic mechanism represented by the LISA model.

Figure 4.12 shows the temporal evolution of liquid film thickness. The time trend is similar to the one described in Figure 4.6. The trends seem to suggest that the layer thickness and number of nuclei roughly increase in the same way, which keeps the void fraction almost constant. Here we include the film thickness presented in Figure 4.6 for the sake of comparison.

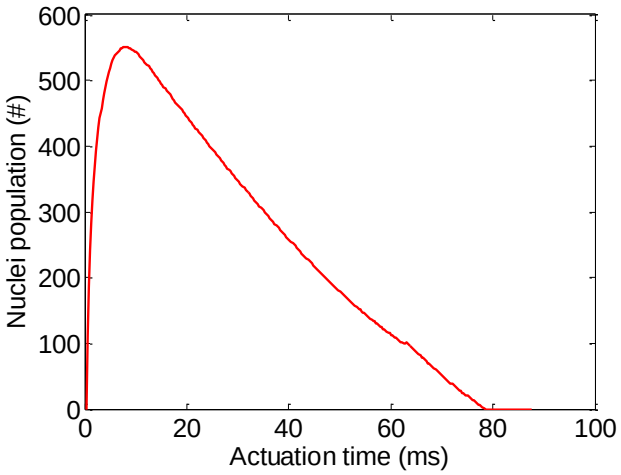

Figure 4.10 Temporal evolution of nuclei population, in liquid layer flowing into spray orifice

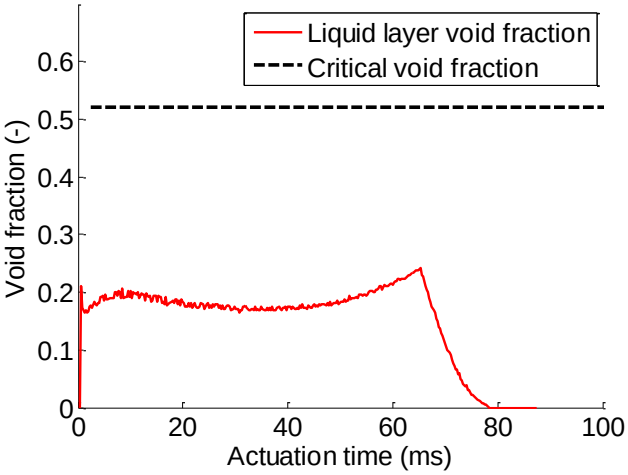

Figure 4.11 Temporal evolution of liquid layer void fraction

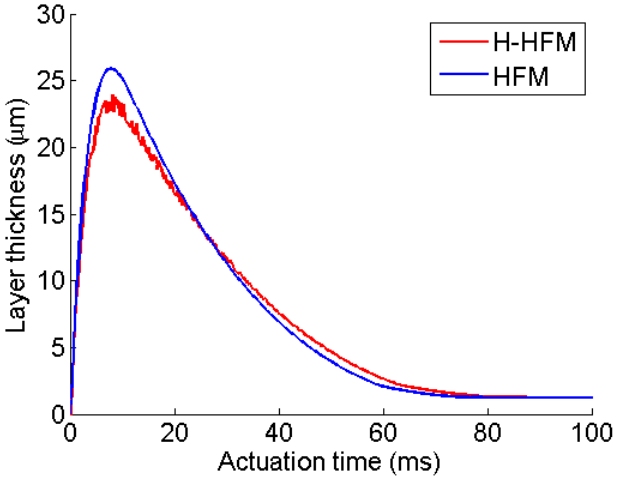

Figure 4.12 Temporal evolution of annular layer thickness inside spray orifice

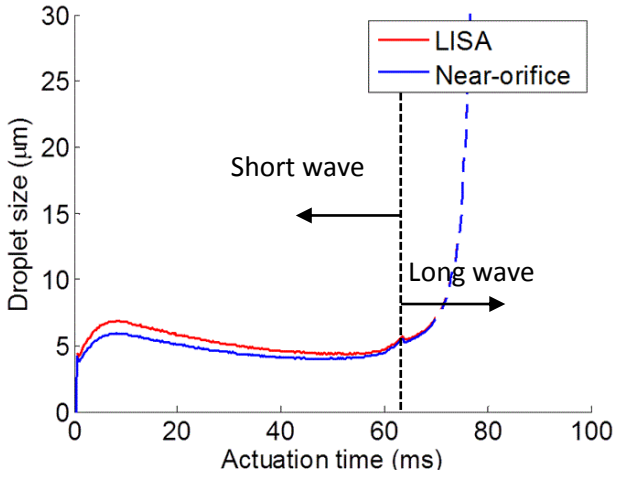

Figure 4.13 Predicted droplet size before and after near-orifice flashing

It can be seen that the peak film thickness for H-HFM is around 3 µm smaller than the value predicted using HFM as internal flow model. This is due to the evaporation of the layer as a result of bubble growth inside the spray orifice. As assumed by the hybrid atomisation model, if the void fraction criterion is not met, i.e. bubbles do not grow sufficiently to disrupt the liquid segment from inside; bubbles will evaporate from the film surface and diminish the liquid film thickness.

The predicted droplet size is shown in Figure 4.13. Here the temporal trend of droplet size is similar to Figure 4.7 and the inverse relationship between the velocity predicted by H-HFM (shown in Figure 4.14) and droplet size is again clearly established. Pre-flashed droplet size

in Figure 4.13 and Figure 4.7, reveals that the droplet size predictions in Figure 4.13 are around 0.75 µm larger than the one shown in Figure 4.7, at the peak (i.e. 7 ms). Considering this is tiny amount, it exists because the velocity predicted by H-HFM is slightly smaller than the value predicted with HFM at the same time instant (also see Figure 3.12 (a)). As a result, the atomisation energy is slightly less for the H-HFM case.

Figure 4.15 shows that the temperature of the droplet at spray orifice exit (red trace) is slightly reduced compared with original liquid temperature in expansion chamber. This is due to minor evaporation of the liquid inside the spray nozzle prior to atomisation.

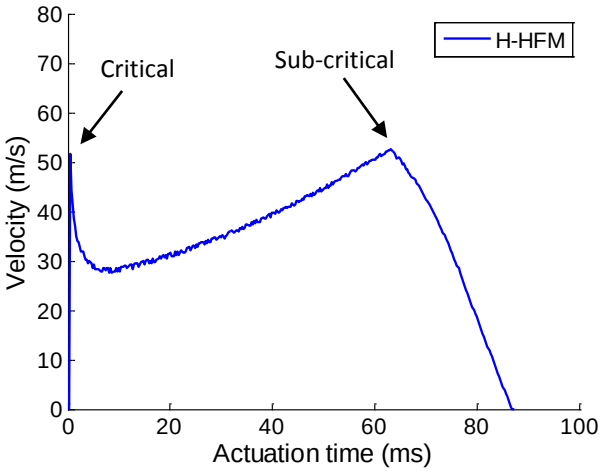

Figure 4.14 Temporal evolution of annular layer thickness inside spray orifice

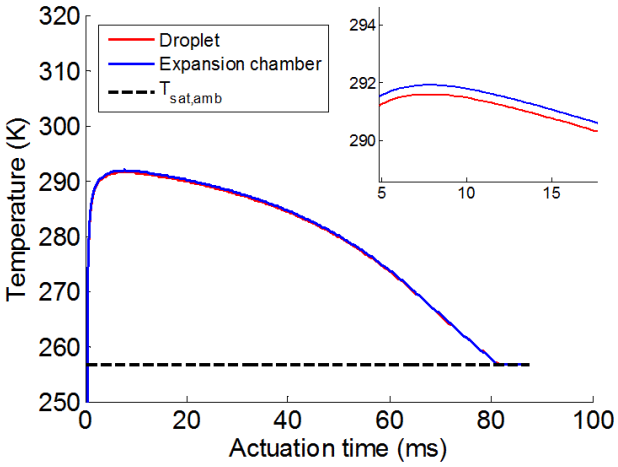

Figure 4.15 Predicted droplet temperature before and after near-orifice flashing

4.4.2 Droplet size validation against PDA measurements

In this section the outcomes of the aerodynamic and hybrid atomisation models are compared with PDA measurements. Three sets of measured data are used, the corresponding modelling parameters and test conditions of which were presented in chapter 3, section 3.7.4.1. The measured data are introduced in the following section.

4.4.2.1 Test cases and measured droplet size

4.4.2.1.1 PDA measurements of parallel project

One set of PDA measurements used for atomisation model validation is part of the parallel experimental project. The test parameters and conditions were presented in chapter 3, section 3.7.4.1.1 and are restated here in Table 4.2. The measurement point is at 15 mm from the spray orifice and the data is averaged over 10 ms time bin. The measured droplet

size, represented using arithmetic mean diameter, D_{10}, and Sauter mean diameter (SMD) D_{32}, is shown in Figure 4.16. The corresponding formula used to computed these mean diameters from PDA data are given below:

$$D_{10} = \frac{\sum_{i=1}^{n} n_i D_i}{\sum_{i=1}^{n} n_i} \qquad and \qquad D_{32} = \frac{\sum_{i=1}^{n} n_i D_i^3}{\sum_{i=1}^{n} n_i D_i^2} \qquad 4\text{-}29\ (a\text{-}b)$$

Parameter	Value	Parameter	Value
Vol_{mc}	50 µl	D_{vo}	0.7 mm
Vol_{ec}	50 µl	D_{so}	0.3 mm
$C_{d,vo}$	0.6	$C_{d,so}$	0.7
T_{amb}	295 K	L_{so}	0.75 mm

Table 4.2 Geometric and modelling parameters of the test case Myatt et al. (2015 a-b)

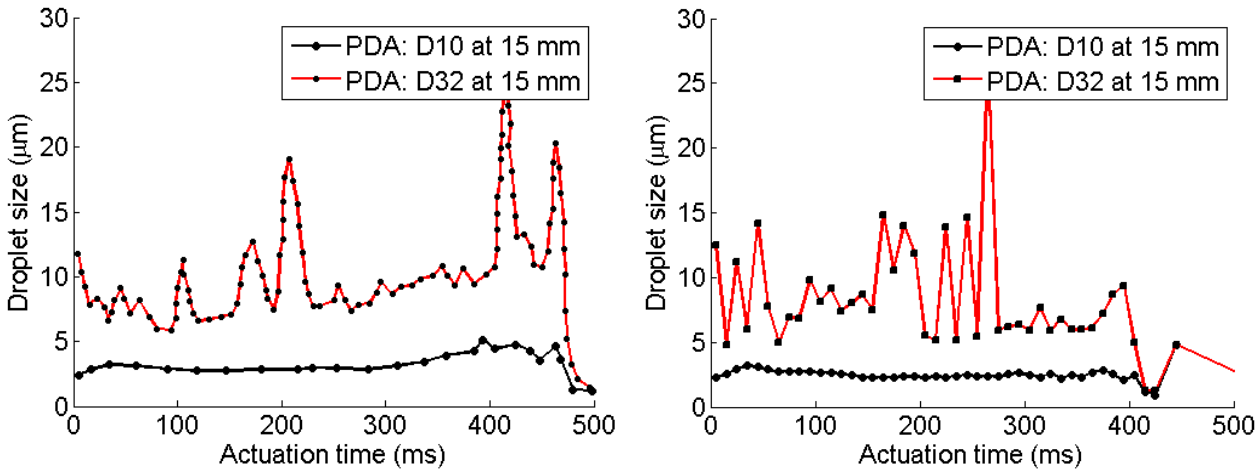

(a) HFA134 **(b) HFA227**

Figure 4.16 Temporal measurement of droplet size presented by D10 and D32 at 15 mm away from spray orifice Myatt et al. (2015 a-b)

4.4.2.1.2 PDA measurements of Dunbar et al. (1997)

This set of PDA measurements is obtained from Dunbar et al. (1997) for HFA134. The parameters of the test case are summarised in Table 4.3. The point of measurement is at 25 mm from the spray orifice and the time bin for data averaging is 20 ms. This set of data is reported based on volume mean diameter (VMD), denoted as D_{30}, using the following expression. Data is shown in Figure 4.17 (a):

$$D_{30} = \left(\frac{\sum_{i=1}^{n} n_i D_i^3}{\sum_{i=1}^{n} n_i} \right)^{1/3} \qquad 4\text{-}30$$

Parameter	Value	Parameter	Value
Vol_{mc}	63 µl	D_{vo}	0.7 mm
Vol_{ec}	17.6 µl	D_{so}	0.5 mm
$C_{d,vo}$	0.6	$C_{d,so}$	0.7
T_{amb}	295 K	L_{so}	0.75 mm

Table 4.3 Geometric and modelling parameters of the case of (Dunbar et al. 1997)

4.4.2.1.3 PDA measurement of Wigley et al. (2002)

This set of measurement corresponds to HFA227 propellant system with the parameters summarised in Table 4.4. The measurements are conducted at 2.6 mm from the spray orifice and the time bin used for data averaging is 5 ms. The values of D_{10} and D_{32} are used to represent droplet size as shown in Figure 4.17 (b).

Parameter	Value	Parameter	Value
Vol_{mc}	25 µl	D_{vo}	0.7 mm
Vol_{ec}	25 µl	D_{so}	0.4 mm
$C_{d,vo}$	0.6	$C_{d,so}$	0.7
T_{amb}	295 K	L_{so}	0.75 mm

Table 4.4 Modelling parameters of the case of Wigley et al. (2002)

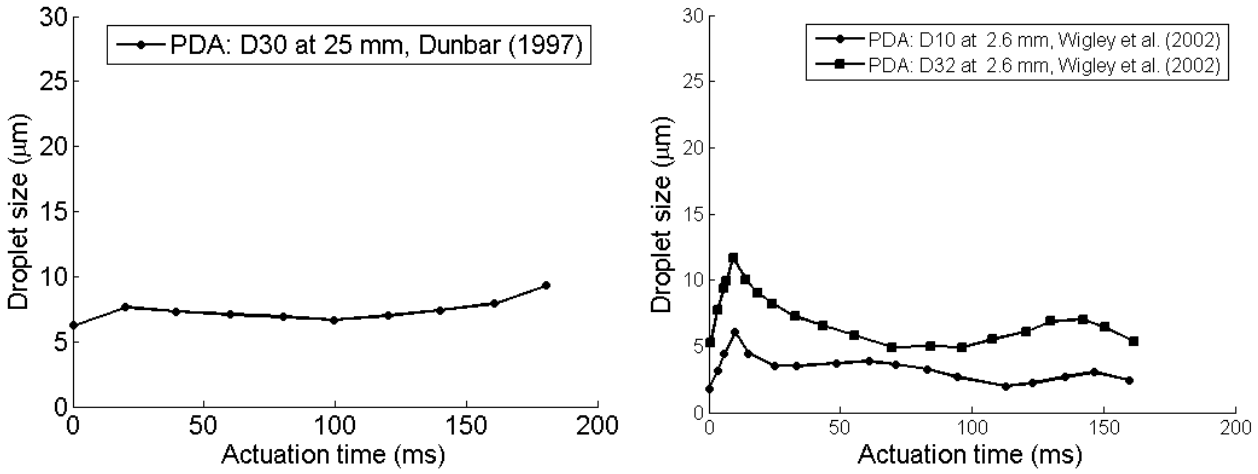

(a) D30, HFA134 at 25 mm away from spray orifice by (Dunbar et al. 1997)

(b) D10 & D32, HFA227 at 2.6 mm away from spray orifice by Wigley et al. (2002)

Figure 4.17 Temporal measurement of plume droplet size

4.4.2.2 Near-orifice extrapolation

As described in chapter 3 section 3.7.4.2, model predictions correspond to near-orifice region, which are assumed to cover the initial 10 mm distance from the spray orifice. In order to directly compare our model predictions to the PDA measurements, we would ideally need to back extrapolate droplet size data to a distance of 10 mm from spray orifice. This requires information relating to the axial decay of droplet size due to evaporation. Among the test cases used in this study, such detailed data was only available for PDA

measurement of the parallel experimental project. For mean metrics of D_{10} and D_{32}, the measured centreline plume droplet size for HFA134 and HFA227 propellant systems are shown in Figure 4.18. The figure suggests that D_{10} and D_{32} exhibit an ascending trend over the first 20 mm for D_{10} and over the first 50 - 60 mm for D_{32}. More detailed assessment of these data within the experimental project has revealed that these rising trends are most probably due to the effect of PDA data dropout in the dense spray region. For the case of D_{32}, the magnitude of the size change is also very large due to the sensitivity of this metric to production of small numbers of very large droplets. Thus, the axial D_{10} data in regions $x < 20$ mm was judged to be unreliable.

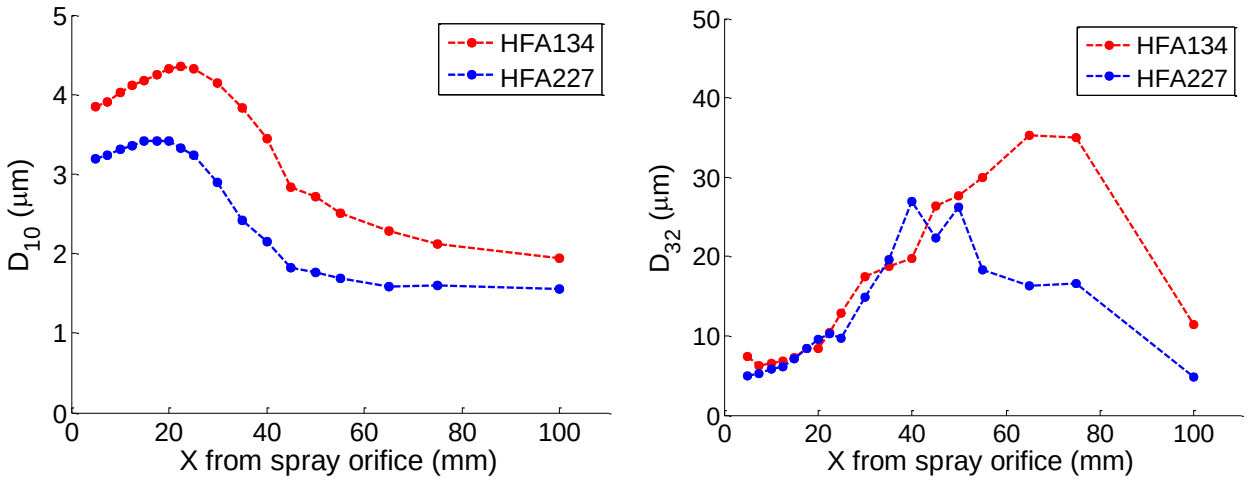

(a) D10 **(b) D32**

Figure 4.18 Axial variation of plume centreline droplet size for different propellants

Extrapolation of PDA drop size data towards a near-orifice source location at 10 mm is, therefore, not feasible. Validation of the predicted droplet size requires additional numerical modelling that can account for the interactions between the aerosol plume and its surroundings (see chapter 6 of this thesis). Here we verify the order-of-magnitude of the droplet size predicted by the atomisation models as well as the temporal trends of the model predictions by comparison with the PDA data.

4.4.2.3 Validation of droplet size predictions

Temporal droplet size predictions using the LISA and hybrid-atomisation models are with PDA measurements from the parallel experimental project in Figure 4.19 (a-b) for HFA134 and HFA227 propellant system, respectively. Predictions of the hybrid-atomisation model

(dots) are presented at five instants in time with different flow initial conditions (pairs of temperature and quality) inside the expansion chamber. These initial conditions correspond with key stages of actuation such as initial start-up, expansion chamber filling and expansion chamber emptying. The initial conditions at the selected time instants are summarised in Table 4.5 and Table 4.6 for HFA134 and HFA227, respectively.

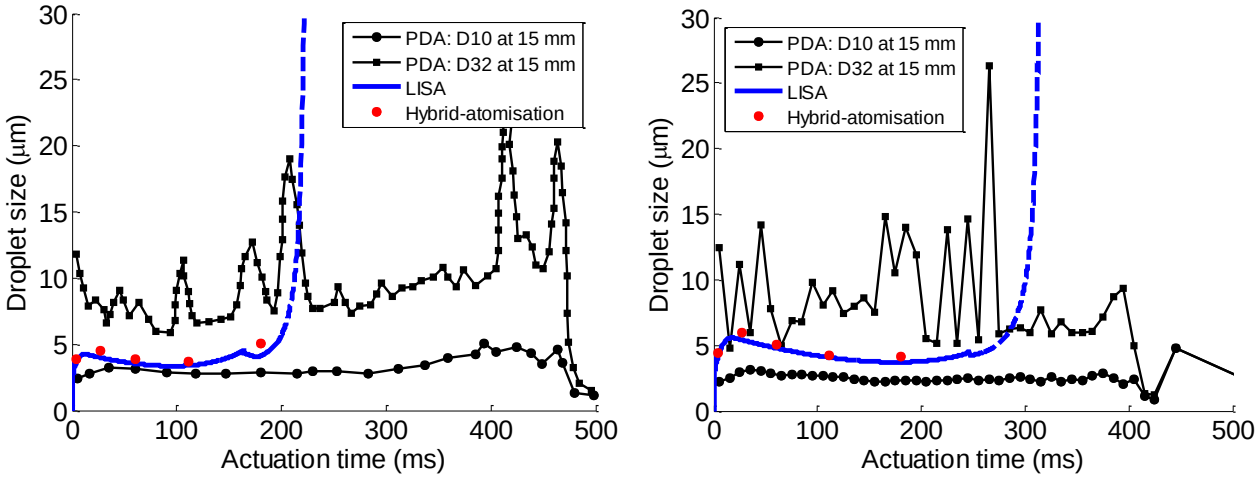

Figure 4.19 Near-orifice prediction of plume droplet size compared with PDA measurements for HFA134 (a), and HFA227 (b)

It should be noted that the atomisation model predicts "the most representative drop size" (Senecal et al. ,1999) without further specifics, moreover, the model does not include a distribution parameter to indicate variability of droplets size. Thus, comparison of the predictions of the LISA model to PDA metrics is necessarily approximate. Here the measured D_{10} and D_{32} are both used as indications of the order-of-magnitude of the droplet size for validation of the model predictions and for consistent comparison of temporal trend.

The results show that the temporal trend of the predicted droplet size closely follows the measured trend of D_{10}, for both propellants. It can be seen that the initial peak, followed by the gradual decrease in droplet size is well captured by the model. It is worth mentioning that the timing of the model peak does not match exactly with the corresponding one for the measured D_{10}. The discrepancy may be due to high rate of momentum transfer between the emerging plume and the surrounding ambient air, leading to plume slowing down. This is also observed in velocity traces in Figure 3.27. As a consequence the droplets arrive later at the point of PDA measurement results in stretching the duration of the curve.

Instant (#)	Time (ms)	T_{ec} (K)	x_{ec} (-)
1	4	288.79	0.05
2	37	290.41	0.03
3	60	286.51	0.06
4	111	278.84	0.11
5	180	259.21	0.21

Table 4.5 Initial conditions of hybrid-atomisation model for HFA227

Instant (#)	Time (ms)	T_{ec} (K)	x_{ec} (-)
1	3	287.66	0.06
2	24	290.65	0.03
3	69	286.02	0.06
4	113	278.52	0.11
5	160	266.56	0.18

Table 4.6 Initial conditions of hybrid-atomisation model for HFA134

Figure 4.19 shows that the predictions of LISA and hybrid-atomisation model are very similar in magnitude. It was noted previously that the hybrid-atomisation model generally predicts liquid layer void fraction around 0.2, which is below the critical void fraction values for

flashing inception. Hence, the atomisation is predicted to be dominated by the aerodynamic mechanism and results are generated by the algorithm based on LISA. The slight difference between blue trace (LISA) and the dots (H-HFM) is due to minor differences in the velocity prediction of both models and described previously. The results also show that the predicted droplet size magnitude is bounded by D_{10} and D_{32} up to 200 ms for HFA134, and 250 ms for HFA227 - which corresponds to emission of approximately 95% of the propellant mass in metering chamber. It should be noted that the erratic nature of the measured D_{32} values is associated with unrepresentatively large effect of small numbers of large spray droplets, resulting in large fluctuations in the temporal trace, sometimes with magnitudes of 10 μm to 20 μm. In spite of this limitation, D_{32} provides a useful upper bound for the sake of order of magnitude comparison with prediction outcomes.

In general, the drop size predictions of the present model agree more closely with the measurement represented by $D_{10.}$ In the literature of industrial atomisers, LISA outcomes are more commonly compared with D_{32} (Senecal et al., 1999; Park et al., 2009), which is more widely used in spray applications. For pMDI sprays, however, both D_{10} and D_{32} metrics are significant. The former is most representative of the large number respirable droplets with diameters below 10 μm, whereas D_{32} captures information relating to the much smaller number of larger droplets with diameter above 20 μm, which are likely to deposit in the mouth and throat. As indicated previously, the comparison is made on an order-of-magnitude basis, so the result that the LISA prediction is more in line with D_{10} indicates that we can conclude that, for pMDI applications, the model makes satisfactory predictions of the therapeutically useful, smaller droplets produced by pMDIs emitted as part of 95% of the pMDI propellant mass.

The results of atomisation model are compared against the PDA measurement of (Dunbar et al., 1997) in Figure 4.20. Since the size distribution of these measurements is unknown, it is not possible to reconstruct the D_{10} and D_{32} values to compare against modelling prediction. However, the comparison is still effective for order of magnitude comparison and understanding of the temporal trends. Figure 4.20 shows that the temporal trend of the predicted droplet size is in line with the PDA measurements. Important features of the trace such as initial peak and gradual size reduction are observable in both measurement and predictions. Furthermore, the droplet size magnitude is predicted within the correct order.

Similar to the previous case, aerodynamic atomisation is the dominant mechanism since the layer void fraction does not exceed the critical value of 0.52. The results indicate that the predictions of the hybrid-atomisation model are again very close to those of LISA. It should be noted that the measured data in this case is averaged over 20 ms time bins.

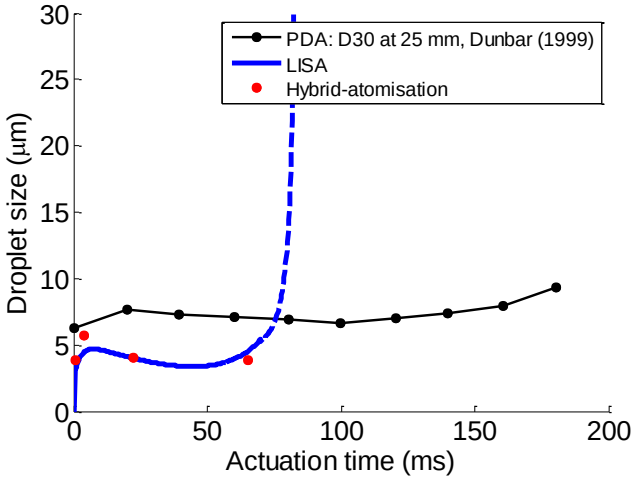

Figure 4.20 Comparison of predicted near-orifice plume droplet size against PDA measurement of (Dunbar et al., 1997)

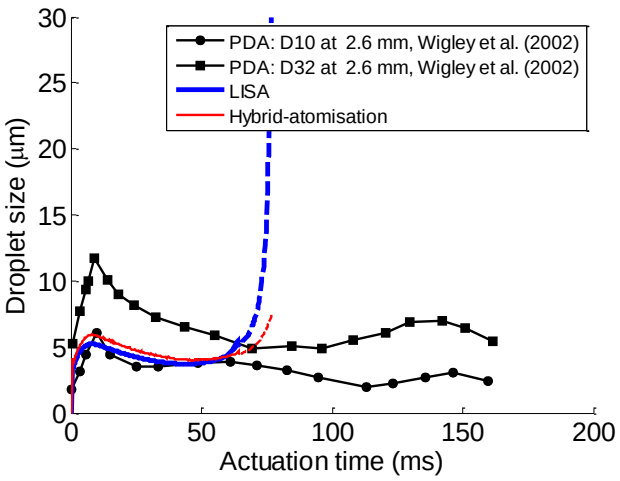

Figure 4.21 Comparison of predicted near-orifice plume droplet size against PDA measurement of (Wigley et al., 2002)

This causes the temporal trace to exhibit much smoother trend leading to diminishing of the curve extrema. Such dependency of data representation on time bin size makes the data set to be only suitable for order-of-magnitude comparison.

The final validation case is against the PDA measurement of (Wigley et al., 2002), shown in Figure 4.21. Similar to previous cases the modelled temporal profile is very well captured. The droplet size predictions by the hybrid-atomisation model are close to those of the LISA model, which suggests that the aerodynamic mechanism is dominant in these simulations. The magnitude of the droplets is again in good agreement with the D_{10} curve and the predicted droplet size is bounded by D_{10} and D_{32}, over 63 ms of the actuation over which 95% of metering chamber mass is predicted to be emitted. The results suggest that the timing of the predicted droplet size peak is earlier than the measured peak by about 2 ms. The good agreement with model predictions is probably due to the fact that the PDA measurement point is located very close to spray orifice (2.6 mm). As a result the plume velocity is not compromised by plume to air momentum transfer and hence droplets are

also less affected by heat gain from the entrained air. Since the droplets arrive quickly at the measurement point, size reduction due to much evaporation is not significant.

4.4.3 Parametric study of nuclei population

4.4.3.1 Nuclei population correction factor

According to the predictions of the hybrid-atomisation model in previous sections, none of the examined cases seem to produce droplets in flashing regime and the dominant atomisation mechanism is predicted to be aerodynamic. While the occurrence of flashing is reported by other scholars (Finlay, 2001; Lewis, 2007), one probable reason for the absence of flashing in the numerical model is underestimation of nuclei population by equation 3-39 in conjunction with C_b=1, as restated here:

$$N_b = C_b A \exp(\frac{B}{\Delta\theta}) \qquad 3\text{-}39$$

where $\mathrm{A} = 5.757 \times 10^{12}$,$\mathrm{B} = -5.279$ and $\Delta\theta$ is the degree of superheat. As mentioned earlier, the constants in this equation were derived from tests on stagnant reservoirs with hydrocarbon fluids, which are much less volatile than HFAs. Furthermore, observations suggest that expansion chamber flow is highly turbulent which itself can lead to the formation of transient locally low pressure zones with the potential to increase nucleation sites compared with the predictions of equation 3-39. Thus, it is expected that the number of nuclei associated with atomisation of HFA propellants may be considerably larger. A correction factor C_b, in equation 3-39, can be tuned to examine the effect of an increase of the number of nuclei. The test case with modelling parameters summarised in Table 3.4 is re-evaluated by increasing C_b to 20 and 50, respectively. Without detailed knowledge of the actual nuclei population, these values were tuned by trial and error in order to illustrate the main features of the model results when flashing is the dominant mechanism. It should be noted that the population of nuclei for the studied cases are not dense enough for 3D nuclei arrangement in liquid layer to occur. Thus in what follows, 2D nuclei arrangement prevails inside the layer.

4.4.3.2 Droplet size

Predictions of the hybrid-atomisation model for HFA134 and HFA227 when C_b=20 and 50 are shown in Figure 4.22 and Figure 4.23. The types of droplet predicted to occur by the algorithm are indicated by colour coding and are shown in the legend. Figure 4.22 (a) suggests that at the first three instants, droplets with diameter of 4.5 µm – 5 µm are generated by aerodynamic atomisation. This implies that, whilst the number of nuclei has increased substantially, the growth of bubbles is still not sufficient to lead to layer disruption and blob detachment i.e. critical void fraction criterion is not reached. However, at the fourth and fifth instants, the model predicts that multimodal atomisation mechanism takes place. It is predicted that flashing occurs inside the spray orifice as soon as the local layer void fraction reaches the critical value. This leads to layer disintegration and formation of 23 µm primary propellant blobs from the liquid layer. As determined by local gas Weber number, these blobs undergo KH secondary mechanism, which produces a drop size of 5.5 µm at fourth instant. TAB is the dominant secondary mechanism at fifth instant, reducing blob size to 10 µm. Flashing of the droplets in the near-orifice region leads to further size reduction and the droplet size lies within the range of 3.8-9.5 µm.

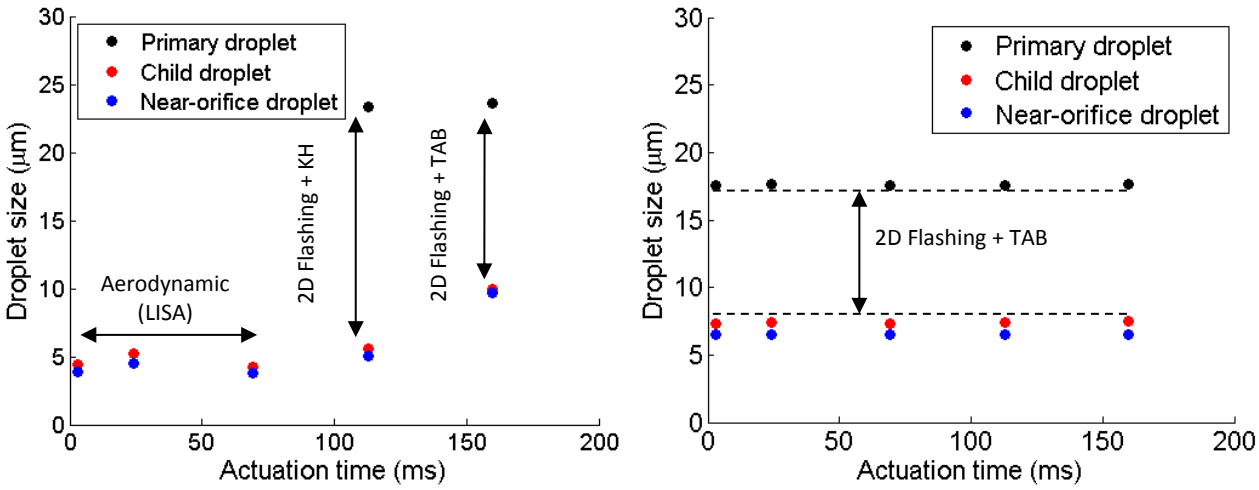

(a) Cb=20 **(b) Cb=50**

Figure 4.22 Temporal droplet size predicted by hybrid-atomisation model as a function of nuclei population, for HFA134

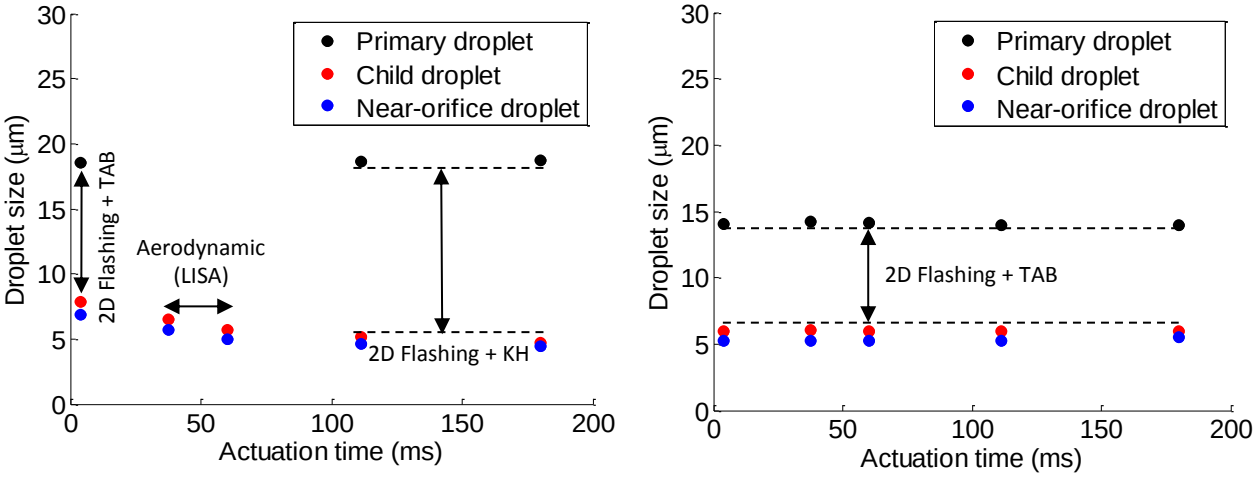

(a) Cb=20 **(b) Cb=50**

Figure 4.23 Temporal droplet size predicted by hybrid-atomisation model as a function of nuclei population, for HFA227

Figure 4.22 (b) presents the case when C_b=50. At all instants of actuation, the increase in nuclei population results in void fraction values that reach the critical value of 0.52 somewhere along the spray nozzle. This means that flashing is the dominant mechanism and primary droplets are formed at a distance along the spray nozzle. Uniform primary droplet size of 17.5 µm is observed at all instants. This uniformity is due to the assumption of PCS arrangement of the nuclei which leads to accumulation of considerable liquid mass around the corners of each unit cell, at the point of critical void fraction of 0.52. The prevailing range of gas phase Weber number lies between 20 and 40, so the child droplet sizes shown in Figure 4.22 (b) are formed due to cyclic distortion of primary blob, governed by TAB model, being around 7.5 µm. After flashing their superheated contents, these droplets exhibit a diameter around 6.5 µm.

For the case of HFA227, at the first instant the primary droplet (blob) of 18.5 µm is formed which is further reduced in size by TAB model to 7.8 µm. At the second and third instants aerodynamic atomisation (LISA) predicts droplet size around 6.5 µm and 5.5 µm respectively. At the next two flashing instants primary droplets with 18.5 µm size are formed. The local Weber number suggests that the primary droplet is fragmented to child droplets by the KH model. Child droplet size of 5.1 µm and 4.7 µm are formed, respectively. Flashing of the droplets in the near-orifice region leads to further size reduction and the droplet size lies within the range of 4.5-6.8 µm. For the case of C_b=50, primary droplet sizes are almost

identical at all instants, around 14 μm. The range of Weber numbers determines that the child droplet sizes governed by TAB, being approximately 6 μm in diameter. Eventually flashing after exiting the spray orifice reduces the size to a range of 5.2-5.5 μm.

Figure 4.23 (a) shows that temporal behaviour and order-of-magnitude of the droplet size can still be captured by hybrid model when of C_b=20, confirming the possibility of prevailing multimode atomisation mechanism if the number of nuclei is sufficient. When nuclei population further increases to 50, the assumed PCS arrangement of growing bubbles within the liquid layer dictates the resulting droplet size. Nevertheless the order-of-magnitude of droplet size is still predicted reasonably.

For both propellants the predicted mechanism is multimode atomisation when nuclei population is increased by factor of 20. Once nuclei population is increased by factor of 50, atomisation mechanism shifts into the flashing regime where constant droplet-time trend is predicted. This suggests that, at least from theoretical perspective, both flashing and aerodynamic atomisation mechanisms produce reasonable values of the final droplet size. The key factors which govern the migration of atomisation mechanisms from one mode to another are appeared to be nuclei population and their topological arrangement inside the liquid segment.

4.4.4 Factors influencing droplet size

To further demonstrate the atomisation model the main factors affecting predicted droplet size are explored and the droplet size trends with respect to modelling parameters are compared against the ones reported in the literature.

4.4.4.1 Method of droplet size averaging

Section 4.4.2 did not show very significant differences between the predictions of LISA and hybrid-atomisation model when aerodynamic mechanism is dominant. However, the temporal variations of the droplet size represented by the HFM+LISA models are appreciably time efficient. So such combination is used for the current study. Temporal droplet size is averaged over the fraction of the actuation event duration where 95% of the metering chamber mass is emitted i.e. $\left(\sum_{i=1}^{n} m_{SO,i}\right)/m_{mc} = 95\%$. The average size calculated using 4-31:

$$\overline{D_d} = \frac{\sum_{i=1}^{n} m_{l,i} D_{d,i}}{\sum_{i=1}^{n} m_{l,i}} \quad \text{4-31}$$

Where $\overline{D_d}$ is averaged droplet size and subscript i denotes time step and n is the total number of time steps. m_l is the mass of the liquid which fragments into number of droplet with diameter D_d.

4.4.4.2 Effect of saturated vapour pressure

The effect of saturated vapour pressure is investigated by employing different propellants in the model. Figure 4.24 (a) shows the variation of average droplet size with respect to different propellants. It can be seen that the HFA227 results yield the largest size whereas HFA134 and CF12 results are relatively similar in size, with HFA134 being marginally smaller. This behaviour correlates with the saturated vapour pressure of the modelled propellants, which is inversely proportional to the emitted droplet size. Such trends were also observed in the measurements of Baeckstroem and Nilsson (1988) and Harnor et al. (1993) for CFC propellant systems. The fact that HFA134 shows smaller droplets compared with CFC12 is also confirmed by previous studies comparing HFA systems with CFC (Dunbar et al. ,1997, Leach, 1999). Brambilla et al. (1999) also reported that MMAD produced by HFA227 formulation is around 20% larger than the HFA134 formulation.

The effect of vapour pressure is further investigated by using HFA134 at various ambient temperatures as vapour pressure modifier, as shown in Figure 4.24 (b). For HFA134 propellant results suggest that the average droplet size reduces by around 70% when temperature increases from 285 K to 305 K. This trend is also reported by Polli et al. (1969) in CFC based systems and Stein & Myrdal (2004) for HFA134.

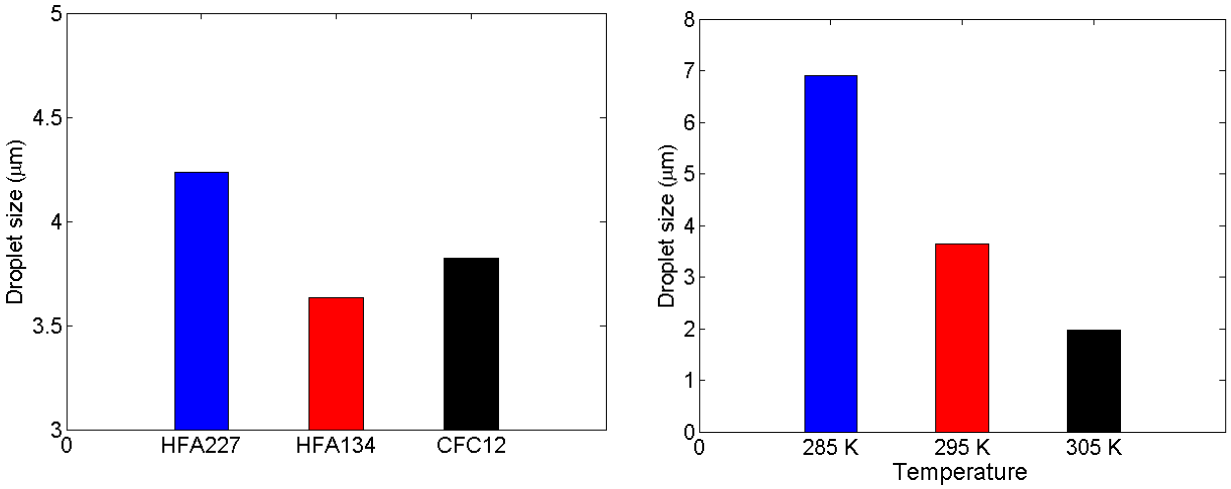

(a) different propellant **(b) different temperatures**

Figure 4.24 Prediction of average droplet size by LISA atomisation model

4.4.4.3 Effect of expansion chamber volume

The effect this parameter on droplet size is shown in Figure 4.25 (a). This indicates that the difference in average droplet size is subtle (7%) as expansion chamber volume increases up to four times. This negligible change is also reported by Stein & Myrdal (2004) using pMDI injection into large-volume chambers. Lewis (2007) and Stein et al. (2014) also pointed out the minimal effect of expansion chamber volume on drug delivery characteristics of practical pMDIs due to the fact that the volume of the valve stem is the main contributor and the actuator sump volume comprises a small fraction of the whole system.

4.4.4.4 Effect of spray orifice diameter

The model predictions suggest that the diameter of the spray orifice also has negligible effect on the droplet size. For the actuators with valve orifice diameter of 0.7 mm and utilising HFA134 as propellant system, Figure 4.25 (b) indicates that increase in spray orifice diameter from 0.2 mm to 0.48 mm has practically no effect on droplet size. In previous measurements conducted by (Berry et al., 2003) it was observed that average initial droplet diameters increased by only about 10% as the spray orifice diameter increased from 0.29 to 0.49 mm which also considered as a small change. In general, it is well known trend that droplet size is reduced by decreasing spray orifice diameter (Meakin et al., 2000; Lewis 2007; Ranucci et al., 1992). This disparity is due to the assumption linked with LISA model

suggesting that the formed droplet is stripped off the surface of the liquid film. Therefore the size of the generated droplets is not strongly dependent on the thickness of the layer inside spray orifice which itself is function of spray orifice diameter as described by equation 4-3.

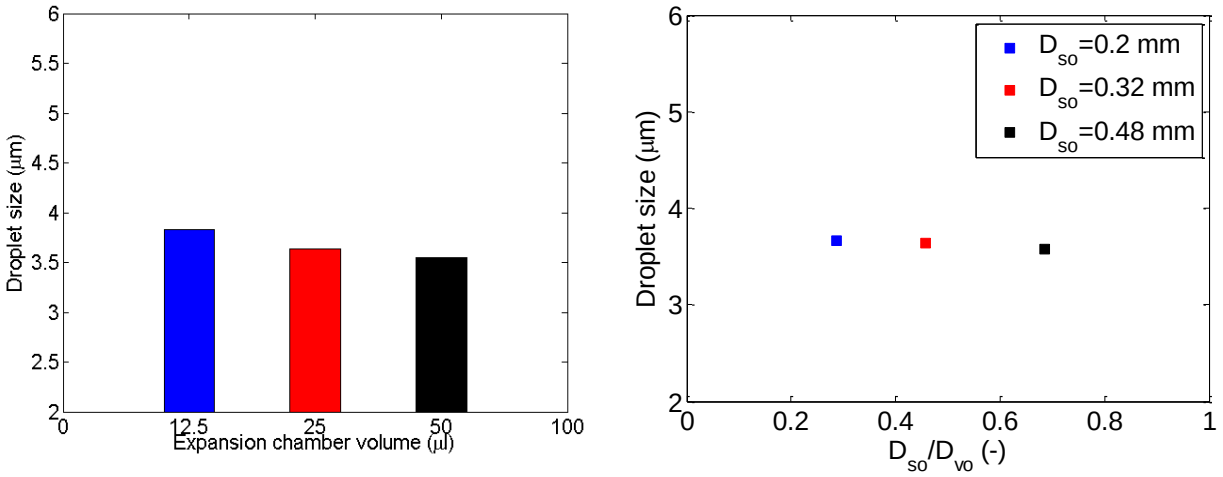

(a) **(b)**

Figure 4.25 Prediction of average droplet size by LISA atomisation model with respect to different expansion chamber volumes (a), and different spray orifice diameter (b)

4.5 Summary and conclusion

In this chapter novel theoretical approaches were developed to predict the size of the droplets issued from a pMDI from first principles. Two different atomisation models were constructed to reflect previously proposed aerodynamic and flashing atomisation mechanisms by (Finlay, 2001; Clark, 1991; Versteeg et al., 2006; Dunbar, 1997; Gavtash et al., 2014). The aerodynamic atomisation model was developed based on the breakup of a flat liquid sheet. The flashing model spatially tracks the evaporation rate of the liquid layer and determines whether growing of the bubbles is sufficient to disrupt the liquid layer. Both models are linked to the internal flow model through which flow parameters throughout the spray orifice and particularly at the point of liquid layer breakup are predicted.

Predictions of the new atomisation models were compared against different sets of PDA measurements, mostly mean diameter metrics D_{10} and D_{32}. All sets of comparison showed that the temporal behaviour of droplet size is well captured by the atomisation models and

the droplet size is predicted with in the correct range, for the duration of 95% of metering chamber mass emission. For the sets of measurements, which were taken at some distance further from the spray orifice (Myatt et al., 2015 a-b), the predicted size was larger than the measured D_{10} values, which can be attributed to some further size reduction in the measured data due to evaporation. For measurements at distances very close to the spray orifice (Wigley et al., 2002) the evaporation time is negligible and PDA D_{10} data showed very good agreement with predicted drop size values.

In all of the cases, predictions of the hybrid-atomisation model were very similar to those by the LISA model suggesting that the evaporation was not enough to disrupt the liquid layer and transition the atomisation to flashing regime. It was conjectured that this is due to the uncertainty of the values of parameters of the nuclei population equation 3-37. (Senda et al., 1994), when applied to pMDI. The nuclei population was increased to C_b=20 to demonstrate the outcome of the model when a combination of aerodynamic and flashing atomisation mechanisms occurs. Sheet-thinning (KH) and vibrational (TAB) secondary atomisation were activated at different instants of time in this case. Further increase of this parameter to C_b=50 generated an atomisation regime where only flashing was predicted to be responsible for the production of primary droplets. The vibrational (TAB) mechanism governed the production child droplets. This study suggests that the occurrence of multimode atomisation in pMDI is possible depending on the number of nuclei at the inlet of the spray orifice, which itself is a function of the degree of superheat and the actuator geometry.

The predicted drop size was again compared with PDA measurements. It was observed that the broad trend of droplet size still emerges when the nuclei population increases by C_b=20 and multimode atomisation mechanism occurs. By increasing nuclei population by C_b=50 an almost constant droplet size was predicted. This is attributable to the assumed PCS nuclei arrangement inside the layer, which leaves considerable amount of liquid mass around the grown bubble inside a unit cell, which undergoes further aerodynamic atomisation. This comparison between model trends and PDA data would suggest that aerodynamic atomisation is the most likely mechanism controlling the droplet size in pMDIs.

Finally, the factors affecting droplet size were investigated using LISA atomisation model. As supported by the literature, an inverse relationship between droplet size and vapour pressure of propellant was observed. Increase in ambient temperature also leads to decrease in droplet size. Furthermore, the effect of spray orifice diameter did not shown to have significant effect on the predicted final droplet size. This is attributable to LISA model original assumption, suggesting that droplet generation in short wave regime does not strongly dependent to liquid layer thickness inside spray orifice.

Chapter Five

Internal Flow and Atomisation Models of Propellant/ethanol Mixture Inside pMDI

5 Chapter Five: Internal Flow and Atomisation Models of Propellant/ethanol Mixture Inside pMDI

5.1 Introduction

Most established chlorofluorocarbon (CFC) pMDIs, were developed as suspensions in which the active pharmaceutical ingredient (API) is dispersed in the liquefied propellant system with the aid of a surfactant (Gupta et al., 2003). Later on and as required by Montreal protocol (Montreal Protocol, 1987), conventional propellants were substituted by hydrofluoroalkane (HFA) propellants HFA227 and HFA134. Approved surfactants were found to be effectively insoluble in HFAs and formulations with co-solvents were developed to overcome this problem (Vervaet & Byron, 1999). Further problems with the stability of HFA suspension formulations led many companies to develop solution pMDIs. Ethanol is commonly used as excipient in marketed inhalers such as Airomir (UCB Pharma), Atrovent Duovent (Boehringer Ingelheim) and Beclojet (Chiesi SA) (Pilcer G. & Amighi K., 2010). Excipients are inactive ingredients which are implemented to improve the physical/chemical stability of the API (Pilcer G. & Amighi K., 2010). However, their advantages are sometimes offset by the fact that addition of ethanol can potentially compromise device performance as assessed by the resultant plume particle size distribution and delivered dose (Hickey 1996; Whitham & Eagle, 1994). The main focus of this chapter is modelling of the effects of the presence of ethanol in the formulation.

One possible source of device deficiency is due to changes of the thermophysical properties of the formulation, specifically saturated vapour pressure (SVP), as the ethanol is added to the formulation. It is known that the vapour pressure of a pMDI formulation influences the atomisation process and the size of the emitted droplets within the inhaler dose (Smyth & Hichkey, 2002; Smyth et al. 2002; Stefely et al., 2000; Tzou, 1998).

The internal flow model, which was thus far developed for pure propellants, is extended to cover HFA/ethanol two-component mixtures in a twin-orifice system of a pMDI. Raoult's law is by far the most common way of describing SVP of mixtures, but departures from this model are well known in the literature (Vervaet & Byron, 1999; Mason et al., 2014; Gavtash et al., 2016). A comprehensive database of the saturated vapour pressure of binary mixtures of HFA134/ethanol and HFA227/ethanol was produced. The data was fitted over a wide

range of ethanol concentration and temperature. The resulting empirical model, which includes a realistic definition of formulation SVP, was implemented within the homogeneous frozen flow model (HFM) and linked to the LISA atomisation model to predict droplet size. These models are chosen as they predicted most reasonable spray velocity (chapter 3) and droplet size (chapter 4). Plus, looking ahead at implementation of source model in CFD (chapter 6), economical source description is needed to capture key physics without unnecessary computational overhead. This is achievable by using HFM and LISA.

5.2 Saturated vapour pressure (SVP) measurement

5.2.1 Experimental procedure

5.2.1.1 pMDI can manufacture

pMDI canisters of different ethanol containing formulation were manufactured. A wide range of ethanol concentrations (10%-90% w/w) was considered. This range was primarily chosen to support internal flow calculations and CFD calculations of evaporating droplets since these will contain only ethanol after the propellant evaporates as the spray mixes with inhaled air.

Predetermined quantities of ethanol solutions were weighed into tared cut edge C128 aluminium cans (Presspart). The headspace of all pMDI canisters (containing bulk formulation) was purged with HFA spray shots. This action reduces the amount of air present inside the cans, which has the potential to alter the measured pressure in the canister headspace. Using Pamasol P2016 laboratory scale (see Figure 5.1), crimping and filling equipment, the cans were sealed with BK 357 continuous spray valves (Bespak, UK) and filled to a specific weight of either HFA134 or HFA227 propellant. During the filling stage, the weight of the cans was continuously monitored to avoid the possibility of manufacturing failure by exceeding the specified weight and hence inaccuracy of the desired solution composition. The sealed cans were then placed in a tray with the failed ones positioned upside down and discarded from the next phase of the experiment (see Figure 5.1-right).

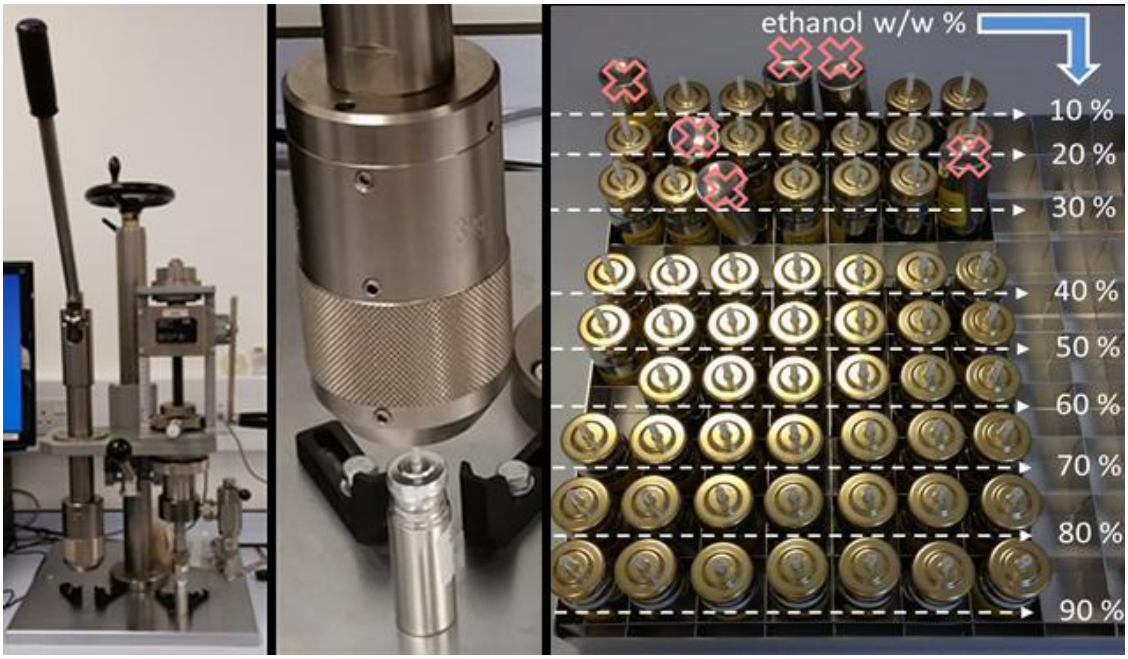

Figure 5.1 Filling and crimping stage using Pamasol P2016 laboratory scale (left and middle); Prepared cans in tray (right)

5.2.1.2 Environmental control

The original intention was to measure the formulation SVP over a wide temperature range. The temperature range was selected (i) to provide the range of conditions necessary for the internal flow model and (ii) to be technically feasible using simple means of temperature control. The target temperatures and those actually achieved during the experiments are summarised in Table 5.1.

		Cooling bath			Environmental chamber	
Target Temperature (C°)		-20	-10	0	20	30
Measured temperature (C°)	HFA134	-16.6	-11.3	0.3	20	30
	HFA227	-17.1	-11.8	0.2		

Table 5.1 Target and measured temperature

In order to achieve appropriate high temperature (20°C and 30°C) measurement environments, cans were left to equilibrate for minimum of 60 minutes inside a calibrated environmental chamber (Westech, UK) enclosure system prior to measurement (temperature probe was readable from 15 to 35 ± 1°C). The 60 minute period was determined to be adequate for the purpose of pMDI hardware and formulation equilibrium arrival since only 30 minute equilibrium period was reported in a previous experimental study (Mason et al., 2014).

For 0°C temperature, a standard ice bath was prepared by crushing ice cubes into small pieces (around 1 cm). This maximised the surface area and allowed the ice to make contact with the walls of the canisters and bath container leading to uniformly distributed temperatures. Ice was periodically added to the flask to maintain the temperature. For -10°C and -20°C temperatures, salt/ice cooling baths (see Figure 5.2) were employed with the weight ratios of approximately 1:9 and 1:3, respectively. The container is initially filled with crushed ice as for setting up the 0°C ice bath; the desired salt quantity is then added by sprinkling it over the ice to achieve the required temperature (Ledgard 2007).

Changes in temperature during measurements were continuously monitored. For this purpose, two calibrated Hanna HI147-00 thermometers (temperature readable from -50°C to 150°C ± 0.3°C) were employed. One thermometer was placed to monitor the temperature adjacent to the canister shell while the other one monitored the tray side temperature. It proved to be substantially more difficult to control the conditions during vapour pressure measurements at lower temperature (0, -10, -20 °C) mainly as a result of ice melting during the experiment. Immediate action was taken to restore the temperature if it deviated from the target value by more than 1 °C by addition of ice. One other difficulty associated with cooling baths is to try to avoid contact between condensed moisture and the stem hole. For the cases where the pressure inside the can is sub-atmospheric, any water contact with the stem hole could lead water to be sucked into the canister and perturb solution composition and potentially lead to inaccurate measurement. Strenuous efforts were made to make sure that the canisters head (valve stem and valve ferrule) were kept out of the coolant.

Figure 5.2 Standard ice bath to provide 0°C (left figure); Salt/ice (1:3 ratio) bath to provide -20°C

5.2.1.3 Measurement procedure

Vapour pressure was measured using a MMD-30E electronic diaphragm gauge (0-30 bar) readable to 0.05 bar. For each canister, five headspace gauge pressure readings were taken with at least 120 seconds rest before repeating the measurement. The connection to the electronic pressure gauge was used to depress the canister valve for five seconds to provide enough time for the vapour to fill the diaphragm space homogenously and to deliver a steady reading. The reading was then recorded and the whole process was repeated on further two canisters and an average vapour pressure determined. Care was taken to prevent misalignment of the valve depressing action, which could cause propellant leakage and false measurement.

5.2.2 Measurement results

Saturated vapour pressure data are summarised in Table 5.2 and Table 5.3, for HFA134 and HFA227 based mixtures, respectively. These measurements are also shown in Figure 5.4 and Figure 5.3 as functions of ethanol mole fraction and temperature.

ethanol (% w/w)	HFA134 Saturated Vapour Pressure (bar) ± Std				
	T = -16.6 °C	T = -11.3 °C	T = 0.3 °C	T = 20 °C	T = 30 °C
10	1.30 ±0.15	1.8 ±0.10	2.80 ±0.10	5.35 ±0.10	6.85 ±0.10
20	1.40 ±0.10	1.90 ±0.05	2.90 ±0.05	5.30 ±0.2	6.70 ±0.15
30	1.35 ±0.10	1.75 ±0.10	2.85±0.05	5.00 ±0.15	6.30 ±0.20
40	1.30 ±0.10	1.75 ±0.05	2.70 ±0.05	4.70 ±0.15	5.95 ±0.20
50	1.25 ±0.05	1.60 ±0.05	2.50 ±0.05	4.35 ±0.10	5.35 ±0.20
60	1.00 ±0.05	1.30 ±0.05	2.10 ±0.05	3.70±0.20	4.70 ±0.15
70	0.80 ±0.05	1.05 ±0.05	1.75 ±0.05	3.00 ±0.05	3.75 ±0.05
80	0.45 ±0.05	0.65 ±0.05	1.10 ±0.05	2.00±0.15	2.60 ±0.10
90	0.20 ±0.05	0.30 ±0.05	0.55 ±0.05	1.20 ±0.10	1.40 ±0.10

Table 5.2 Collected SVP data for HFA134/ethanol mixture (N = 5)

ethanol (% w/w)	HFA227 Saturated Vapour Pressure (bar) ± Std				
	T = -17.1 °C	T = -11.8 °C	T = 0.2 °C	T = 20 °C	T = 30 °C
10	0.80 ±0.05	1.10 ±0.10	1.70 ±0.2	3.50 ±0.10	4.50 ±0.10
20	0.80 ±0.05	1.10 ±0.05	1.60 ±0.20	3.20 ±0.10	4.05 ±0.10
30	0.60 ±0.05	0.90 ±0.05	1.40 ±0.15	2.90 ±0.10	3.65 ±0.10
40	0.50 ±0.05	0.75 ±0.05	1.15 ±0.20	2.55 ±0.15	3.20 ±0.05
50	0.35 ±0.05	0.60 ±0.05	0.90 ±0.15	2.10 ±0.05	2.60 ±0.10
60	0.20 ±0.05	0.40 ±0.05	0.60 ±0.15	1.60±0.05	2.10 ±0.05
70	0.10 ±0.05	0.25 ±0.05	0.40 ±0.10	1.10 ±0.05	1.50 ±0.05
80	0.05 ±0.05	0.10 ±0.05	0.25 ±0.1	0.70±0.05	1.05 ±0.05
90	0.05 ±0.05	0.05 ±0.05	0.05 ±0.10	0.40 ±0.05	0.50 ±0.05

Table 5.3 Collected SVP data for HFA227/ethanol mixture (N = 5)

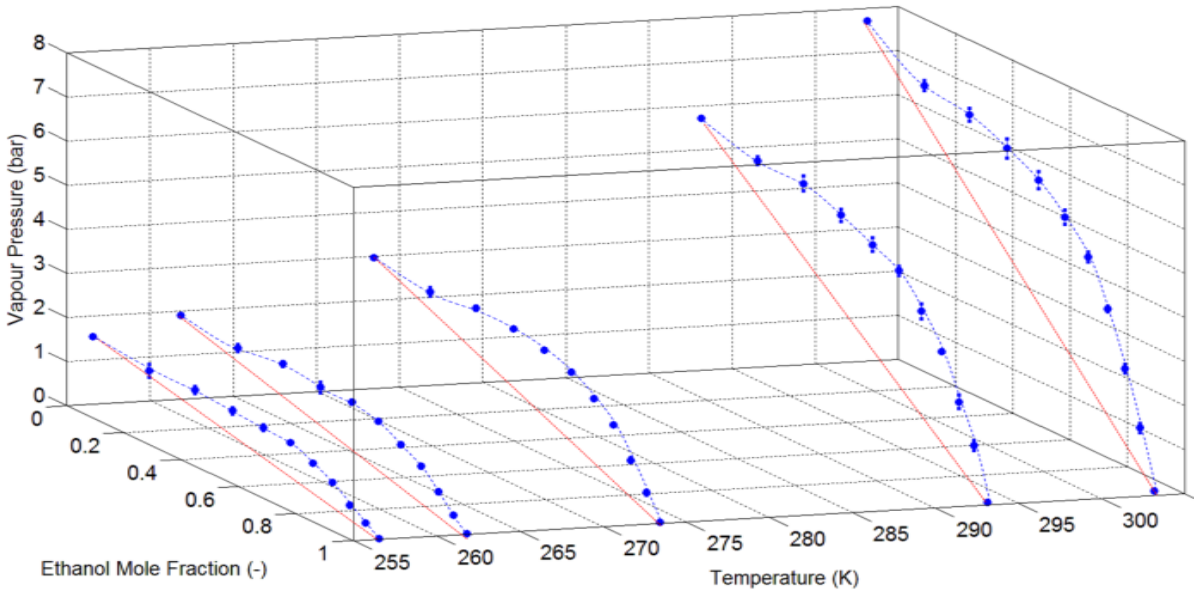

Figure 5.3 Saturated vapour Pressure (SVP) of HFA134/ethanol binary mixture, as functions of temperature and ethanol mole fraction

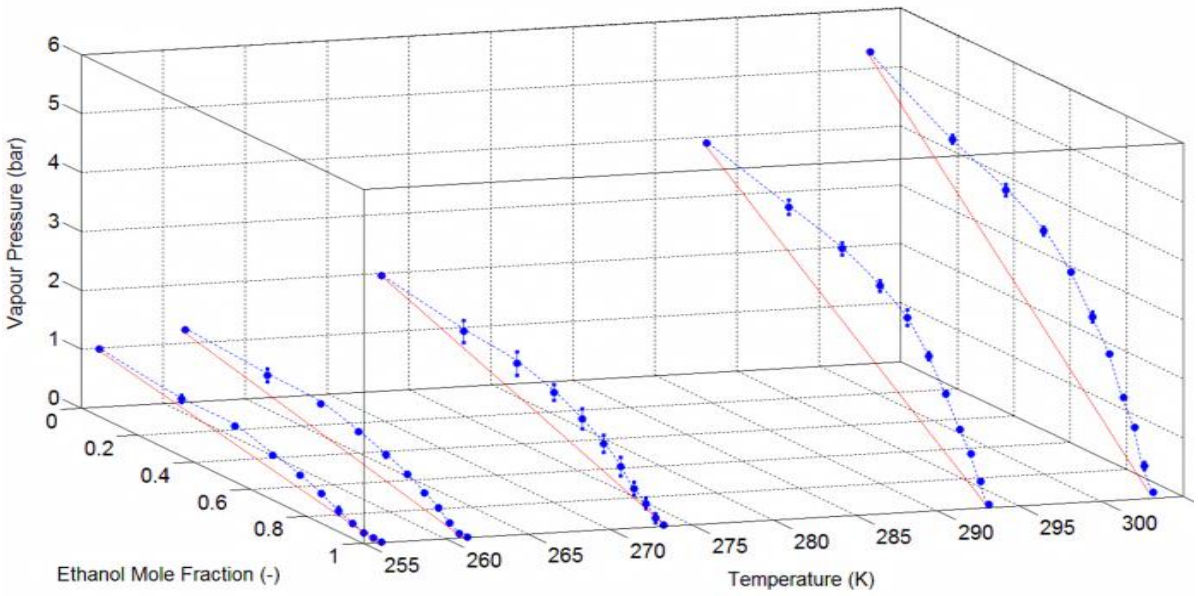

Figure 5.4 Saturated vapour Pressure (SVP) of HFA227/ethanol binary mixture, as functions of temperature and ethanol mole fraction

Boundary values of the curves corresponding to pure HFA and ethanol from the NIST database are included in the figures. The straight solid line on the graphs indicates Raoult's law theoretical model of vapour liquid equilibrium (VLE) of binary mixtures. These lines are included in the figure to visually aid the reader to observe the vapour pressure deviation from Raoult's law. For both propellant/ethanol binary systems, an increase of the ethanol concentration causes a decrease in the vapour pressure. Figure 5.4 and Figure 5.3, show positive deviations from Raoult's law. This implies that net repulsive forces exist between the molecular species in HFA/ethanol mixtures, resulting in larger amounts of HFA entering the vapour phase and, hence, higher SVP values.

To evaluate the validity of the measured data set, Figure 5.5 and Figure 5.6 compare the present measurements of saturated vapour pressure of HFA227/ethanol and HFA134/ethanol blends, respectively, against available data in the public domain. Due to the limited literature on such binary mixtures, the assessment can only be carried out for high temperatures close to room temperature. The trace with blue markers in Figure 5.5, which covers HFA227/ethanol mixtures, represents the values of current measurement at 293.15 K. The black traces distinguished by square and diamond symbols are the published ones conducted at 294.65 K and 283.17 K, respectively (Vervaet & Byron, 1999; Kleiner & Sadowski, 2007). The figure indicates that the trend and magnitude of the current measurement is consistent with previous studies. All traces show a general decrease in vapour pressure as ethanol concentration increases. Noticeably, the values measured at 293.15 K are much closer to the ones measured at 294.65 K, rather than those obtained at 283.17 K. This is an expected pattern since vapour pressure is known to be a strong function of temperature.

The traces in Figure 5.6 with blue and red markers are vapour pressure of HFA 134/ethanol measured at 293.15 K and 303.15 K, respectively. These results are compared with previously measured values at 294.65 K (black line with squares) and at 298 K (black line with diamonds) (Smyth et al. 2002; Vervaet & Byron, 1999). Again the trends and the magnitude of the current measurements are in good agreement with published data.

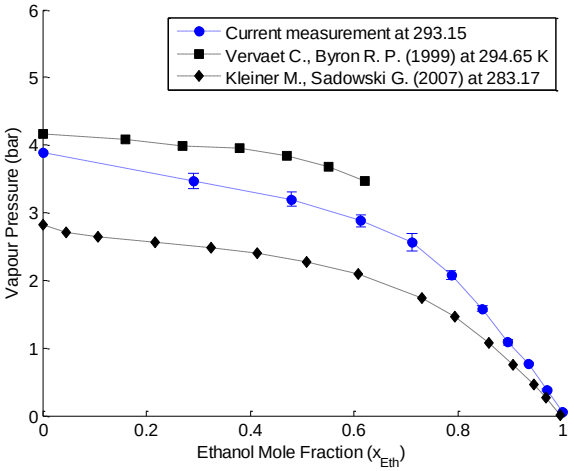

Figure 5.5 HFA227/ethanol measured SVP compared with available data in the literature

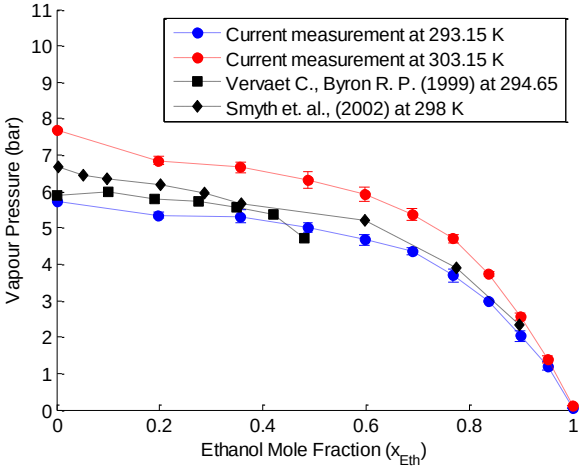

Figure 5.6 HFA134/ethanol measured SVP compared with available data in the literature

5.3 Empirical model of saturated vapour pressure (SVP)

5.3.1 Model development

In order to develop an empirical equation a non-dimensional function Π_v^* is introduced and is defined as follows:

$$\Pi_v^*(x_E, T) = \frac{p_{mix}(x_E, T) - p_E(T)}{p_H(T) - p_E(T)} = (1 - x_E)[1 + f(x_E, T)] \qquad 5\text{-}1$$

Where x_E is ethanol mole fraction inside the mixture. In equation 5-1, $p_{mix}(x_E, T)$ denotes the measured SVP value of the HFA/ethanol mixture, which is a function of ethanol mole fraction and temperature. $p_H(T)$ and $p_E(T)$ are saturated vapour pressure of pure HFA and ethanol respectively, which are functions of temperature only. The term $(1 - x_E)$ represents Raoult's law, which expresses the linear relationship between SVP and molar ethanol concentration. The factor $[1 + f(x_E, T)]$ represents the departure of the measured SVP values from Raoult's law. The chosen non-dimensional representation recognises that the largest contribution to the temperature-dependence of the SVP of HFA/ethanol mixture is due to the temperature-dependence of the SVP of the pure substances. It is an advantage of the chosen functional form that the highly accurate NIST values of the SVP of the pure substances (i.e. $p_H(T)$ and $p_E(T)$) from REFPROP, used thus far in the internal flow model (see chapter 3), can be built in. Additionally, this practice generally improves the compactness of the fit as it eliminates the great differences in scale between two of the

variables (i.e. non dimensional function and mole fraction are both of order 1). Nonlinear least squares method using Levenberg-Marquardt algorithm in Matlab was implemented to construct a two-dimensional surface fit for each propellant-ethanol mixture. Based on trial and error, bivariate polynomial functions with different orders where examined to obtain a reasonably accurate model of the Raoult's law departure function of $f(x_E, T)$:

$$f(x_E, T) = ax_E + bx_E^2 + cx_E T + dx_E^3 + ex_E^2 T + fx_E T^2 \quad 5\text{-}2$$

The coefficients of the equation for each propellant/ethanol mixture are summarised in Table 5.4. Using the reported coefficients in conjunction with equations 5-1 and 5-2, the following values for the goodness of the fit were computed: R^2 is 0.98 and 0.99 for HFA227 and HFA134 respectively.

Coefficient	a	b	c	d	e	f
HFA134	-57.73	4.325	0.4202	0.01125	-0.005239	-0.000759
HFA227	0.613	-6.784	0.0171	-2.666	0.03957	-7.149×10^{-5}

Table 5.4 SVP polynomial departure function coefficients

The fitted surface and corresponding residual graph for each propellant/ethanol blend is illustrated in Figure 5.7 to Figure 5.10. Figure 5.7 and Figure 5.9 suggest that the general descending trend of SVPs as ethanol content increases is captured by the fitted surfaces. The convex surface shown in Figure 5.7 (most visible around ethanol mole fraction line of 0.4), suggests the level of interaction between temperature and ethanol concentration is appreciable in HFA134/ethanol blends. The surface being relatively flat along the temperature axis, Figure 5.9, on the other hand indicates the minimal role of interactions between ethanol concentration and temperature in determining the SVP of HFA227/ethanol mixtures.

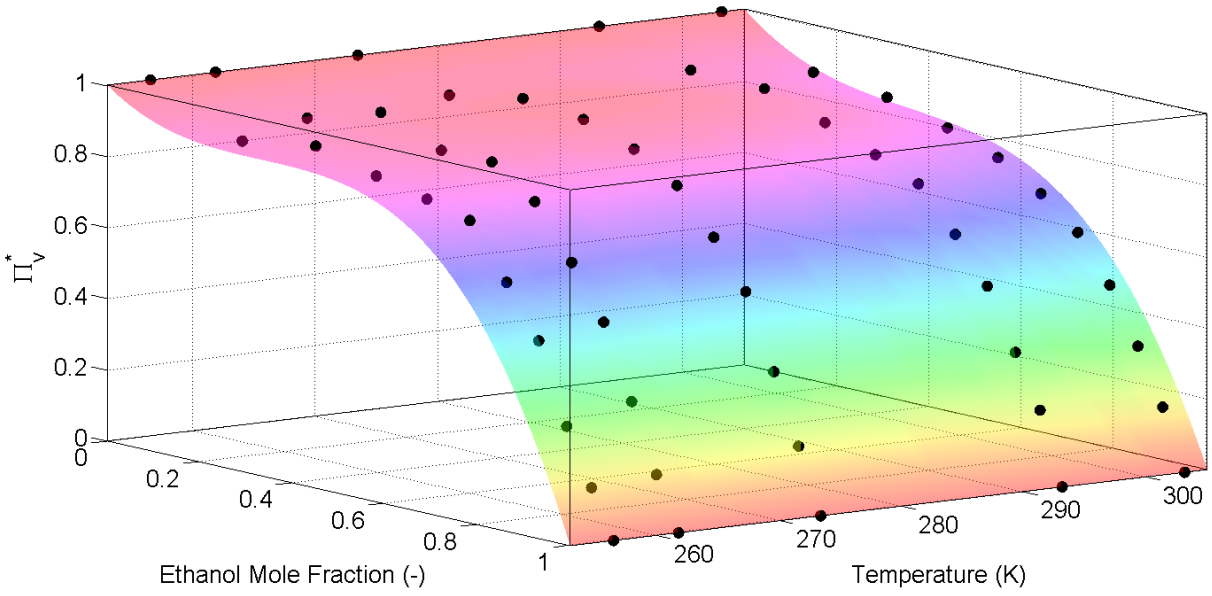

Figure 5.7 Surface fit of HF134/ethanol non-dimensional pressure function over measured temperature and ethanol mole fraction ranges

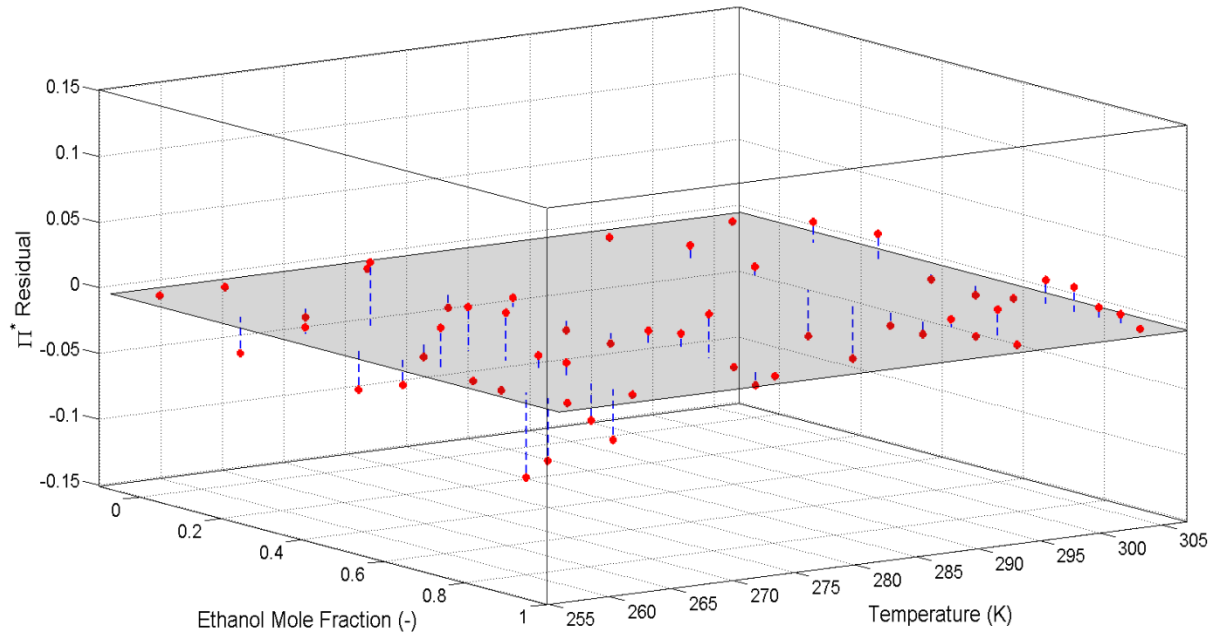

Figure 5.8 HFA134/ethanol non-dimensional pressure post-fit residuals over measured temperature and ethanol mole fraction ranges

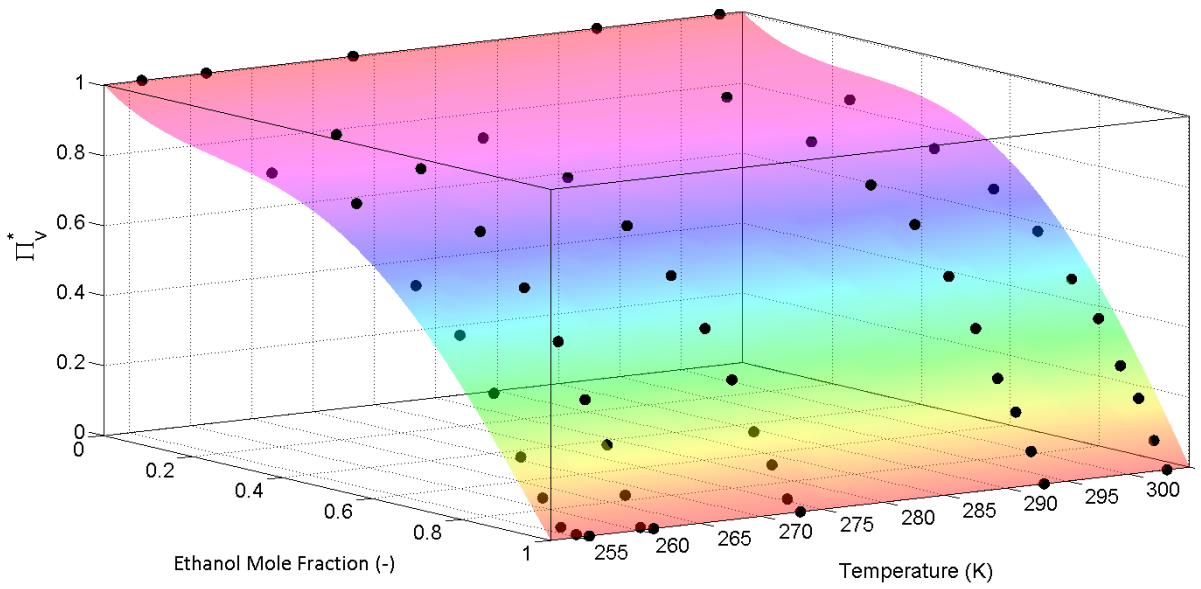

Figure 5.9 Surface fit of HFA227/ethanol non-dimensional pressure function over measured temperature and ethanol mole fraction ranges

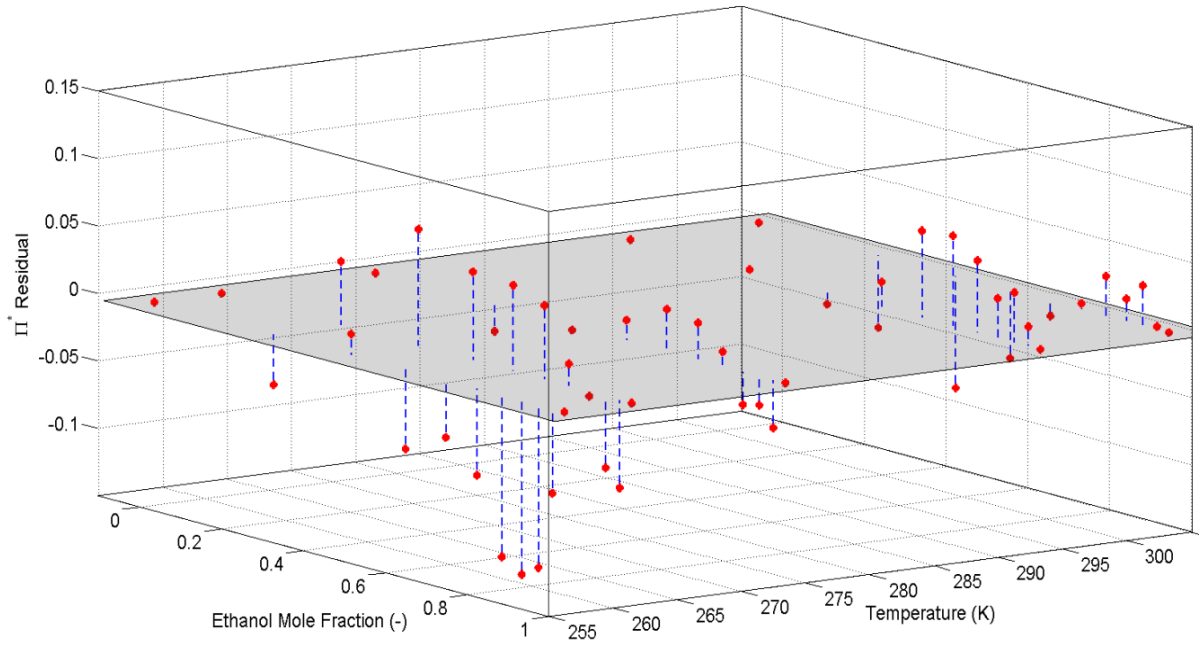

Figure 5.10 HFA227/ethanol non-dimensional pressure post-fit residuals over measured temperature and ethanol mole fraction ranges

Comparison of Figure 5.8 and Figure 5.10 reveals that the magnitude of Π^* function residual for HFA227/ethanol mixture is generally greater than the ones computed for HFA134/ethanol. For both binary blends, the residuals of the best-fit functions show peaks at the low end of temperature values and high end of ethanol concentrations. However, this is not too serious, since these temperatures are only reached towards the very end of the actuation, corresponding to mass emission around 5% of the total mass in metering chamber. As discussed in chapter 3, section 3.7.4.3 the final 5% of mass emission is governed by external heat transfer between actuator and surrounding, which is not included in current model.

5.3.2 Model validation

The validity of the new empirical SVP model is further assessed by comparing its outcome against the measurements of Vervaet and Byron (1999), Kleiner and Sadowski (2007) and Smyth et al., (2002) as shown in Figure 5.11 and Figure 5.12. As witnessed by the figures, model outcomes illustrate very good agreement with the published data, for both propellant mixtures.

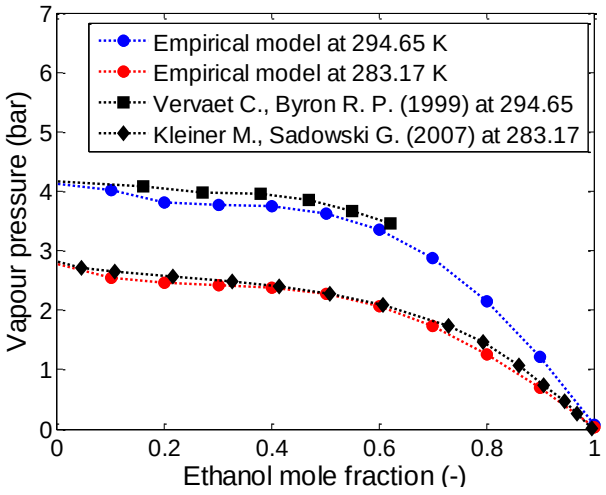

Figure 5.11 HFA227/ethanol predicted SVP values compared with available data in the literature

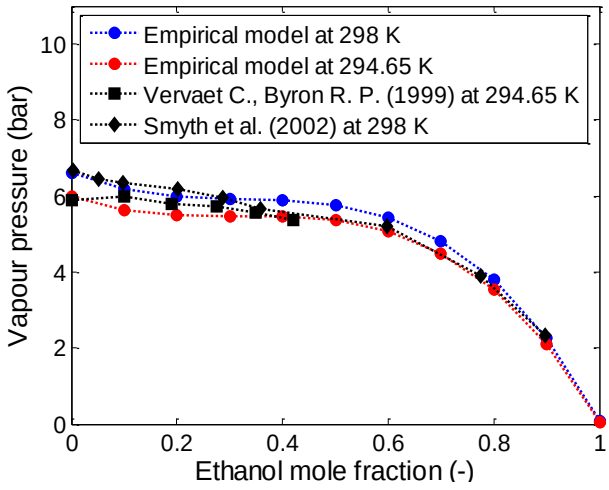

Figure 5.12 HFA134/ethanol predicted SVP values compared with available data in the literature

5.4 Flow model of mixture formulation

The mixture model extends the homogeneous frozen model (HFM) of Fletcher (1975) and Clark (1991). This capability enables us to incorporate the effect of ethanol on the formulation and to predict the plume characteristics as a function of formulation composition. Thus, the key features of the metered discharge applied to mixture formulation flow are similar to the ones presented in chapter 3 for single component propellant flow. However, thermodynamic and transport properties of the formulation are modified to represent the ethanol contribution to the liquid phase, and, more importantly, its effect on saturated vapour pressure.

5.4.1 Conceptual image of mixture formulation model

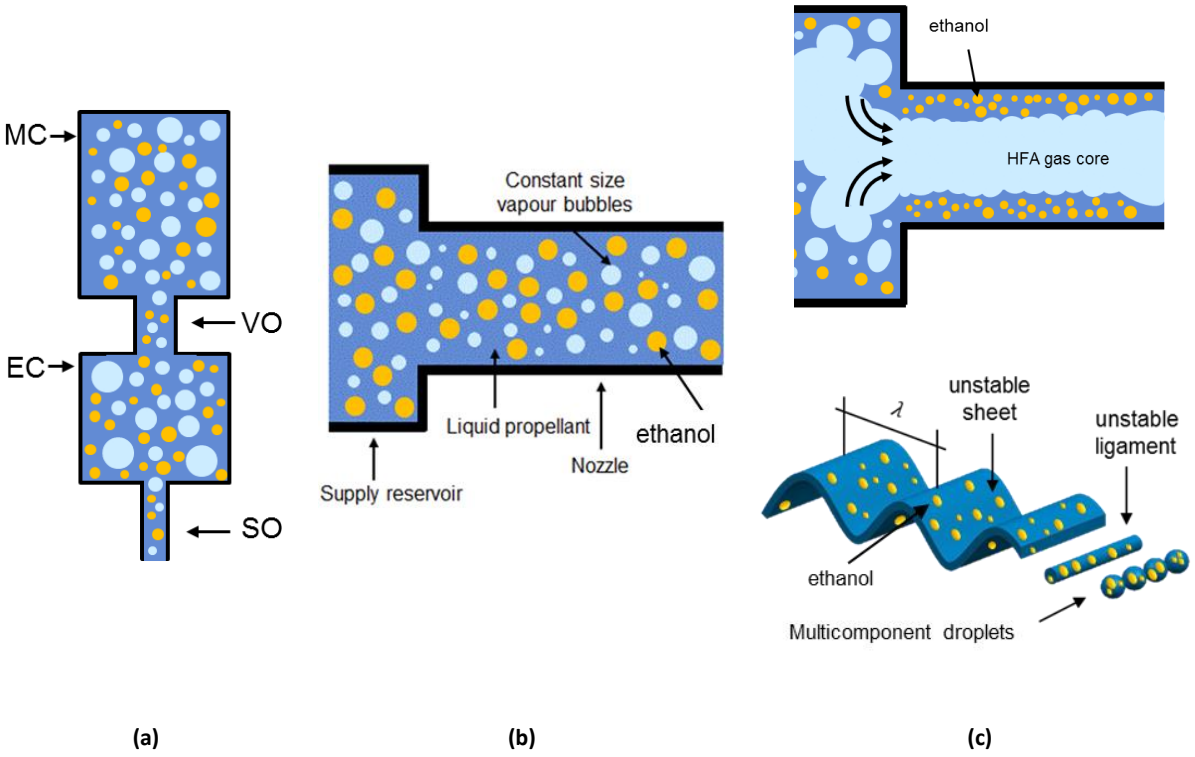

Figure 5.13 Schematic of mixture flow models through nozzle

With reference to the flow state inside the chambers, Figure 5.13 (a) illustrates that the liquid phase consist of ideally mixed ethanol (orange circles) and HFA (dark blue background) in all pMDI compartments. As the flow emission takes place, HFA constituent of the solution evaporates and develops the vapour phase (bright blue circles). Homogeneous distributions of mixture constituents are assumed as before. Our modelling concept of mixture formulation flow through the spray orifice is similar to the one described by HFM model

(see chapter 3, section 3.2.1.1). There is no mass transfer from liquid phase to gas phase in orifices from supply reservoir to the throat. Here the mixture constituents are assumed to be homogenously mixed (see also Figure 5.13 (b)). As described in chapter 4, section 4.2, the precursor liquid film forms inside the spray orifice on which wind induced instabilities either grow of attenuate. The disturbance with the fastest growth rate is responsible for sheet disintegration into cylindrical ligaments. These ligaments are assumed to move normal to their axis. Eventually as a result of capillary forces, ligaments are broken apart further and contract into multicomponent spherical droplets. The assumed mechanism is schematically shown in Figure 5.13 (c).

5.4.2 Modelling assumptions

The modelling assumptions, which are established throughout the simulation of multicomponent flow in twin-orifice system, are mainly the ones applied to single component propellant flow presented in chapter 3, sections 3.2.2 and 3.3.2.1.1. For reader's convenience, here we restate the key assumption used in model development along with the ones specifically related to current model.

- General modelling assumptions are as follows:
  - ✓ Quasi-steady, one-dimensional, adiabatic and reversible (isentropic) flow
  - ✓ Zero nozzle entrance velocity (i.e. large upstream reservoir compared with throat diameter)
  - ✓ Fluid energy budget: variations in propellant temperature and kinetic energy are due to evaporation and expansion caused by local pressure differences. Any contribution due to surface energy is neglected.
  - ✓ Gravity: The effect of gravitational force on the propellant flow is neglected in the calculations.
  - ✓ Homogeneous two-phase flow regime: Mixture liquid phase and gas phase are mixed thoroughly, so liquid and vapour phase are flowing at the same velocity.
  - ✓ Conditions in metering chamber and expansion chamber: All species are at thermodynamic and thermal equilibrium inside the chambers.
  - ✓ Isentropic expansion inside the nozzle (adiabatic and frictionless flow)
  - ✓ Irreversible phase change from liquid to vapour phase

- ✓ Frozen flow composition: No mass transfer along the flow path from the supply reservoir to the throat. This assumption is most valid when fluid residence time in the orifice is short and hence there is not enough time for a significant amount of transfer of heat and mass between the two phases.
- ✓ Choked flow: As the two-phase mixture velocity reaches to the sonic speed, the mass flow rate becomes independent of the throat pressure.

- Mixture formulation modelling assumption:

  - ✓ Homogeneous liquid mixture (Interpenetrating continua): HFA and ethanol are homogeneously mixed in liquid phase. Hence, a pseudo fluid having the mass-weighted averaged properties of each constituent represents the multicomponent solution as a whole.
  - ✓ Ethanol is assumed to act as non-evaporating species so the vapour phase contains HFA vapour only. This assumption is supported by considerably lower ethanol SVP comparing with HFA227 and HFA134 over the modelling temperature range of 240K – 300K.

5.4.3 Governing Equations

5.4.3.1 General considerations

To define the sets of equations in a compact format, it is necessary to introduce a new group of variables for mixture representation. The mass fraction of liquid ethanol is denoted by Y_E and is formulated by equation 5-3.

$$Y_E = \frac{m_{l,E}}{m_{l,H} + m_{l,E}} \quad 5\text{-}3$$

And hence:

$$Y_H = 1 - Y_E \quad 5\text{-}4$$

Where subscripts E and H, represent ethanol and HFA related properties. Since HFA is the only evaporating species, the mixture flow quality x_{mix} can be defined as the mass of HFA vapour phase over the total mass inside the chamber:

$$x_{mix} = \frac{m_{g,H}}{m_{mix,C}} = \frac{m_{g,H}}{m_{g,H} + m_{l,H} + m_{l,E}} \quad 5\text{-}5$$

And finally, based on the assumption of interpenetrating continua, the average of any extensive thermodynamic property of the liquid solution such as $\bar{\Phi}_{ls}$ (assuming liquid phase as the unit) and overall fluid such as $\bar{\Phi}_{mix}$, is defined as the mass weighted average of each species constituent:

$$\bar{\Phi}_{ls} = Y_H \Phi_{l,H}(T) + Y_E \Phi_{l,E}(T) \quad 5\text{-}6$$

$$\bar{\Phi}_{mix} = x_{mix} \Phi_{g,H}(T) + (1 - x_{mix})\left[Y_H \Phi_{l,H}(T) + Y_E \Phi_{l,E}(T)\right] \quad 5\text{-}7$$

5.4.3.2 HFM of multicomponent formulation

For sub-critical discharge conditions, equation 5-8 is used to calculate the mass velocity of multicomponent, two-phase mixture through orifices. This equation is the same as equation 3-11:

$$G_{t,mix} = C_d \left(\frac{p_{0,mix}}{x_{0,mix} v_{g,0}} \frac{2\eta_{mix}^{\frac{2}{\gamma}}}{\left[\left(\frac{1 - x_{0,mix}}{x_{0,mix}}\right)\left(\frac{\bar{v}_{ls,0}}{v_{g,0}}\right)\eta_{mix}^{\frac{1}{\gamma}} + 1\right]^2} \left[\left(\frac{1 - x_{0,mix}}{x_{0,mix}}\right)\left(\frac{\bar{v}_{ls,0}}{v_{g,0}}\right)(1 - \eta_{mix}) + \frac{\gamma}{\gamma - 1}\left(1 - \eta_{mix}^{\frac{\gamma-1}{\gamma}}\right)\right] \right)^{\frac{1}{2}} \quad 5\text{-}8$$

Where subscript 0 represents conditions in supply reservoir. $x_{0,mix}$ can be calculated from equation 5-5, $\bar{v}_{ls,0}$ can be calculated from the general form presented by 5-6, and finally $v_{g,0}$ is the specific volume of the vapour phase i.e. HFA vapour. η_{mix} denotes the ratio of throat mixture pressure to upstream mixture pressure:

$$\eta_{mix} = p_{t,mix} / p_{0,mix} \quad 5\text{-}9$$

As described in chapter 3, section 3.3.2.1.3, under critical discharge condition where the velocity of two-phase flow approaches the two-phase speed of sound, η_{mix} in equation 5-8 can be calculated using the equation 5-10 (Fletcher, 1975):

$$\left(\frac{1}{\eta_{c,mix}}-1\right)+X_{c,mix}\frac{\gamma}{\gamma-1}\left(\eta_{c,mix}^{\frac{1-\gamma}{\gamma}}-1\right)=\frac{\gamma X_{c,mix}}{2}\left(\frac{1}{X_{c,mix}}+1\right)^2 \quad 5\text{-}10$$

Where:

$$\frac{1}{X_{c,mix}}=\left(\frac{1-x_{0,mix}}{x_{0,mix}}\right)\left(\frac{\bar{v}_{ls,0}}{v_{g,0}}\right)\eta_{c,mix}^{\frac{1}{\gamma}} \quad 5\text{-}11$$

In equations 5-10 and 5-11, subscript c, represent the critical condition.

5.4.3.3 Multicomponent formulation state inside chambers

The calculation of the conditions inside the metering chamber and expansion chamber uses the homogeneous equilibrium assumption. Thermodynamic properties of the multicomponent two-phase mixture are functions of the prevailing temperature and species fraction in each phase. Since ethanol is assumed to serve as non-evaporating species, the gas phase contains HFA vapour only and the liquid phase is a homogeneously mixed solution of HFA and ethanol. Therefore, equations 5-12 and 5-13 are used to evaluate average specific volume and specific enthalpy of the two-phase mixture:

$$\bar{v}_{mix}=\frac{m_{mix,C}}{Vol_C}=x_{mix}v_{g,H_{sat}}(T)+(1-x_{mix})\left[Y_H v_{l,H_{sat}}(T)+Y_E v_{l,E_{sat}}(T)\right] \quad 5\text{-}12$$

$$\bar{h}_{mix}=\frac{H_{mix,C}}{M_C}=x_{mix}h_{g,H_{sat}}(T)+(1-x_{mix})\left[Y_H h_{l,H_{sat}}(T)+Y_E h_{l,E_{sat}}(T)\right] \quad 5\text{-}13$$

Where subscript C refers to chamber, m is the total mass and Vol is the volume. By performing some algebraic manipulation, x_{mix} is eliminated from equations 5-12 and 5-13 and the resultant equation can be established as follows:

$$\frac{\bar{v}_{mix}-Y_H v_{l,H_{sat}}(T)+(Y_H-1)v_{l,E_{sat}}(T)}{v_{g,H_{sat}}(T)-Y_H v_{l,H_{sat}}(T)+(Y_H-1)v_{l,E_{sat}}(T)}-\frac{\bar{h}_{mix}-Y_H h_{l,H_{sat}}(T)+(Y_H-1)h_{l,E_{sat}}(T)}{h_{g,H_{sat}}(T)-Y_H h_{l,H_{sat}}(T)+(Y_H-1)h_{l,E_{sat}}(T)}=0 \quad 5\text{-}14$$

Equation 5-14 is a nonlinear equation in temperature T and HFA mass fraction Y_H of the liquid phase. This equation can be solved using a Newton-Raphson root finding routine. It

should be noted that equation 5-14 includes two unknown variables of T and Y_H. As evaporation takes place and HFA mass transfers from liquid to vapour phase, liquid phase becomes more enriched with ethanol. In this case an iterative approach was design to solve the equation as follows:

1. Initial guess of, Y_H^* ,(practically can be set to last calculated value)
2. Solve equation 5-14 for T, based on Newton-Raphson root finding routine
3. Calculate x_{mix} from equation 5-12 (or 5-13) using calculated T from Step 2, and guessed Y_H^* value fromStep 1.
4. Evaluate mixture constituens masses (m_g, $m_{l,H}$and $m_{l,E}$) based on species specific volume at T.
5. Calculate new value of Y_H from equations 5-3 and 5-4
6. Stop calculation if equation 5-15 was satisfied:

$$\frac{|Y_H - Y_H^*|}{Y_H^*} \leq \epsilon \qquad 5\text{-}15$$

where ϵ is set to 0.001.

Using the quasi-steady assumption, the instantaneous multicomponent mixture mass and enthalpy in a chamber is determined by applying mass and energy conservation on the chamber (similar to equations 3-54 to 3-57 which are presented in chapter 3, section 3.5). This yields equation 5-16 and 5-17 for instantaneous mixture mass and enthalpy, respectively.

$$m_{mix,C}(t) = m_{mix,C}(0) + \int_{t=0}^{t=\tau} \dot{m}_{mix,C_{in}}(t)dt - \int_{t=0}^{t=\tau} \dot{m}_{mix,C_{out}}(t)dt \qquad 5\text{-}16$$

$$H_{mix,C}(t) = H_{mix,C}(0) + V_C[p_{mix}(0) - p_{mix}(t)] + \int_{t=0}^{t=\tau} \bar{h}_{mix,C_{in}}(t)\dot{m}_{mix,C_{in}}(t)dt - \int_{t=0}^{t=\tau} \bar{h}_{mix,C_{out}}(t)\dot{m}_{mix,C_{out}}(t)dt \quad 5\text{-}17$$

$m_{mix,C}(0)$ and $H_{mix,C}(0)$ are initial mass and enthalpy of the multicomponent mixture inside a chamber and subscripts in/out denotes inflow and outflow of mass and enthalpy. For the sake of simplicity the Euler forward differencing numerical algorithm was chosen to solve equations 5-16 and 3-57.

5.4.3.4 Models of Saturated Vapour Pressure (SVP)

Prediction of plume and flow characteristics in pMDI requires regular evaluation of saturated vapour pressure of the multicomponent mixture formulation. This property is included in the calculation using two different models.

5.4.3.4.1 Empirical SVP model

Our empirical model of vapour pressure (equation 5-1) is used in conjunction with the assumption that ethanol is a non-volatile species (vapour phase is HFA only).

5.4.3.4.2 Raoult's law

As an alternative, Raoult's law (Reid et al., 1987) in combination with Dalton's law is also implemented for the purpose of comparison and assessing the validity of each model. Following Raoult's law, the partial vapour pressure of each species is linearly proportional to the mole fraction of species i, in liquid phase and its saturated vapour pressure:

$$p_i = x_i p_{sat,i} \quad 5\text{-}18$$

By summing all species partial pressures, the total vapour pressure of the mixture can be estimated as defined by Dalton's law:

$$p_{mix} = \sum_{i=1}^{N} p_i \quad 5\text{-}19$$

Where N is total number of species in the solution mixture. In this work ethanol is treated as non-evaporating, so HFA is the only species in the vapour phase.

5.4.3.5 Multicomponent aerodynamic atomisation

The LISA atomisation model was linked with the multicomponent internal flow model to predict the droplet size issuing from a pMDI. The equations are technically the ones present in chapter 4, section 4.3.2.1 and 4.3.2.2, but modified to include the effect of ethanol in liquid phase. This is achieved by modification of thermodynamic and transport properties of liquid phase appearing in LISA using the mass weighted mixing rule (as presented by equation 5-6).

In short wave regime equation 5-20 is numerically maximised to evaluate wave number of maximum growth rate, denoted by K_s.

$$\omega_r = -2\bar{v}_{ls}k^2 + \sqrt{4\bar{v}_{ls}^2k^4 + \bar{\Gamma}V_{rel}^2k^2 - \frac{\bar{\sigma}_{ls}k^3}{\bar{\rho}_{ls}}} \qquad 5\text{-}20$$

Where $\bar{v}_{ls} = 1/\bar{\rho}_{ls}$. $\bar{\Gamma}$ is the specific volume ratio between the multicomponent liquid phase and gas phase (i.e. $\bar{v}_{ls}/v_g$), $\bar{v}_{ls}$ is the kinematic viscosity of multicomponent liquid and k (=$2\pi/\lambda$) is the wave number. For the short wave regime, the ligament diameter d_{lig} is calculated using equation 4-7 which is restated here:

$$d_{lig} = \frac{2\pi C_{lig}}{K_s} \qquad 4\text{-}7$$

In the long wave regime, K_s is obtained from:

$$K_s = \frac{\rho_g V_{rel}^2}{2\bar{\sigma}_{ls}} \qquad 5\text{-}21$$

And the ligament diameter is calculated using equation 4-9 which reads as follows:

$$d_{lig} = \sqrt{\frac{8\acute{h}}{K_s}} \qquad 4\text{-}9$$

The final droplet size is calculated by equation 4-10 (restated here) where the Ohnesorge number for multicomponent liquid is expressed by equation 4-11:

$$D_d = 1.88 d_{lig}(1 + 3Oh)^{1/6} \quad \text{4-10}$$

$$Oh = \sqrt{\frac{\bar{v}_{ls}\bar{\mu}_{ls}^2}{\bar{\sigma}_{ls} d_{lig}}} \quad \text{5-22}$$

5.5 Results and discussion

5.5.1 Effect of SVP model representation

In the following set of results, temporal variations of flow parameters inside the pMDI are examined using (i) Raoult's law representation of SVP and (ii) empirical SVP model.

5.5.1.1 Test case

Geometric properties of the actuator and test conditions are summarised in Table 5.5. For both SVP models, mass fraction of ethanol in liquid phase,Y_E, varied from 0% (i.e. pure propellant) to 20%. Values of discharge coefficient was selected based on the work of Clark (1991), as discussed in chapter 3, section 3.7.1.1.

Parameter	Value	Parameter	Value
Vol_{mc}	50 µl	D_{vo}	0.7 mm
Vol_{ec}	50 µl	D_{so}	0.3 mm
$C_{d,vo}$	0.6	$C_{d,so}$	0.7
T_{amb}	295 K	Propellant	HFA134

Table 5.5 Geometric and modelling parameters of the test case

5.5.1.2 Chambers pressure and temperature

The temporal evolution of two-phase two-component flashing flow pressure and temperature, are illustrated in Figure 5.14 to Figure 5.17.

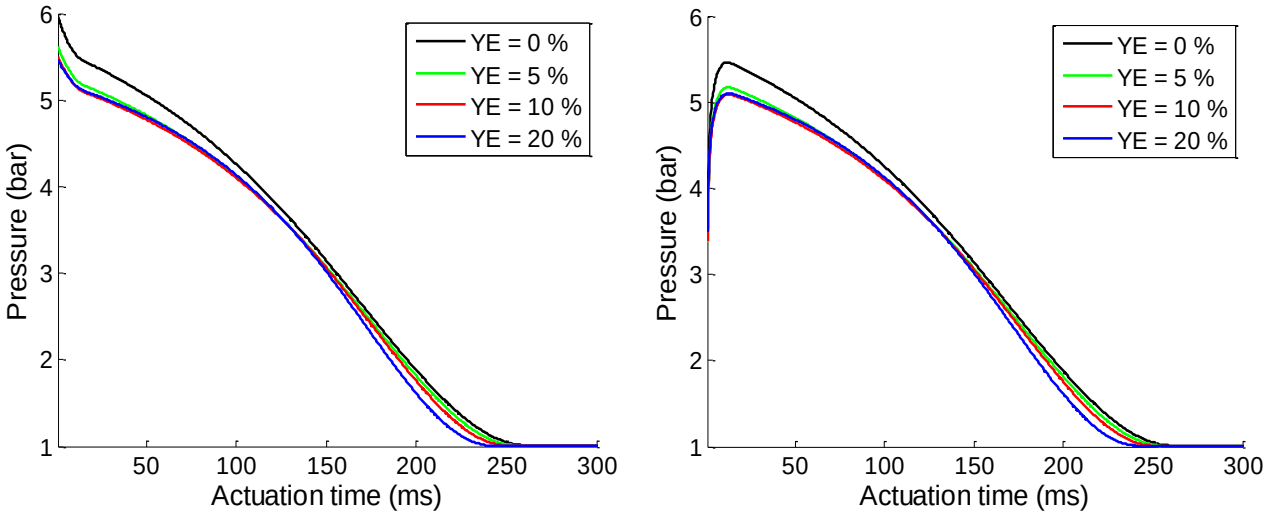

(a) metering chamber **(b) expansion chamber**

Figure 5.14 Temporal evolution of formulation pressure inside pMDI, using empirical SVP model

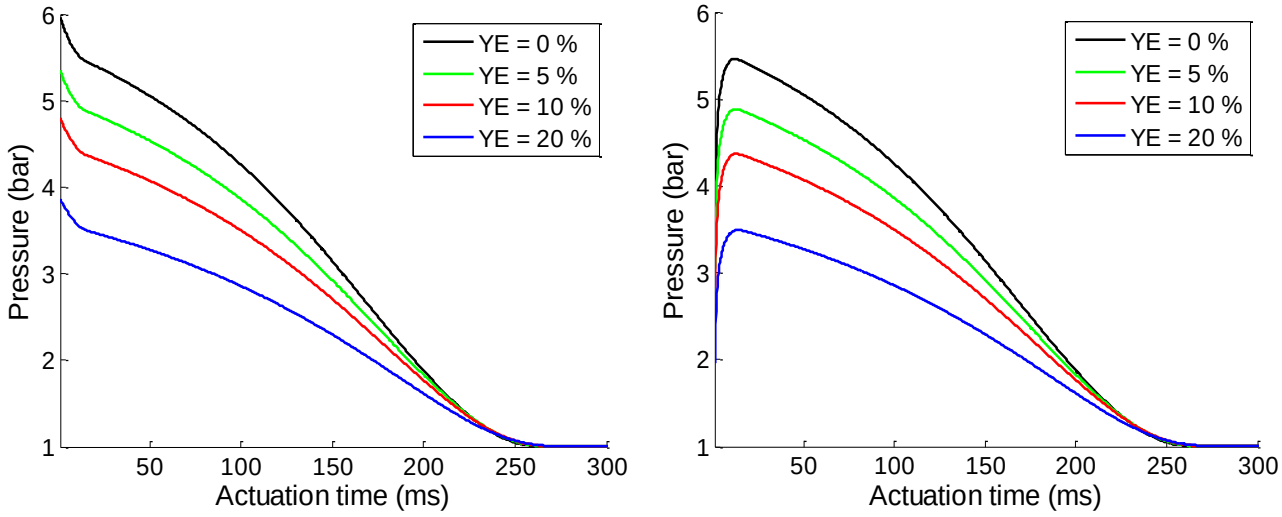

(a) metering chamber **(b) expansion chamber**

Figure 5.15 Temporal evolution of formulation pressure inside pMDI, using Raoult's law SVP model

Figure 5.14 and Figure 5.15 compare the results for pressure change inside the expansion chamber and metering chamber as a function of actuation time for the new empirical SVP expression and Raoult's law. Regardless of the ethanol concentration, pressure-time trends in both chambers are similar to the ones observed for pure propellant (see chapter 3, section 3.7.1.2). Figure 5.14 shows the predicted pressures using empirical SVP model (equation 5-1). Results suggest that the effect of ethanol concentration is small. The largest differences occur as the ethanol content changes from Y_E =0% to Y_E=5%. Figure 5.15 shows the predictions of pressure based on Raoult's law. Here one can observe a strong dependence of predicted pressure on ethanol concentration from Y_E=0% to Y_E=20%. The initial pressure reduces from 6 bar to 3.85 bar in metering chamber as ethanol content rises to 20%. The application of Raoult's law reduces the predicted maximum pressure in the expansion chamber from 5.4 bar to 3.8 bar for these ethanol concentrations.

Temperatures inside the chambers as a function of time are shown in Figure 5.16 and Figure 5.17. The traces show behaviour that corresponds to the trends of the predicted pressure, since the pressure and temperature in the chambers are linked through the assumption of thermodynamic equilibrium. In Figure 5.16 (a-b) the temperature is almost independent of ethanol concentration over the entire actuation duration. Towards the end of the actuation, temperature drops down to its final value. This value is around 251 K for all ethanol content formulations and 247 K for pure HFA134 propellant, corresponding to saturation temperature at atmospheric condition. Figure 5.17 shows that that the temperature profiles based on Raoult's law strongly depends on Y_E. As the actuation time advances, the mixtures with higher ethanol content are predicted to have higher temperature when Raoult's law is used. For the modelled ethanol concentration range of 0% to 20%, final temperature varies from 247K to 260K, respectively.

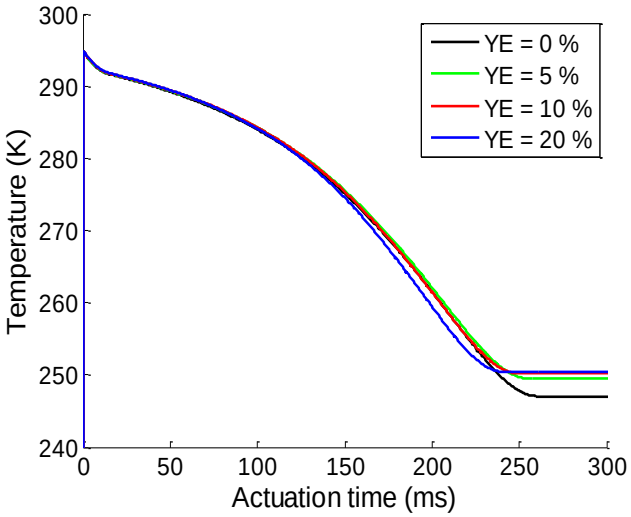

(a) metering chamber

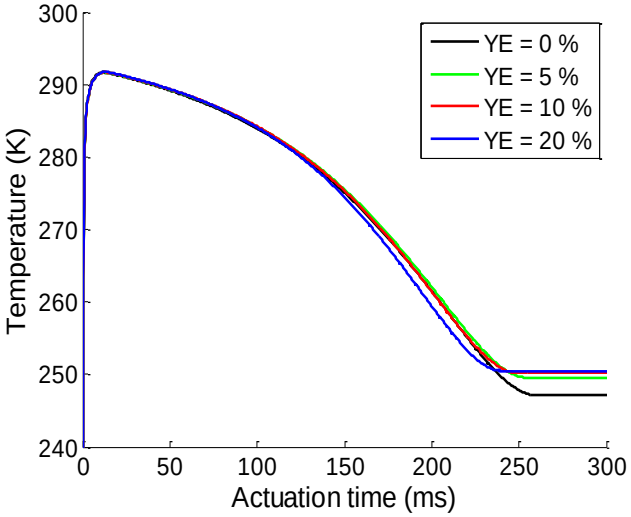

(b) expansion chamber

Figure 5.16 Temporal evolution of formulation temperature inside pMDI, using empirical SVP model

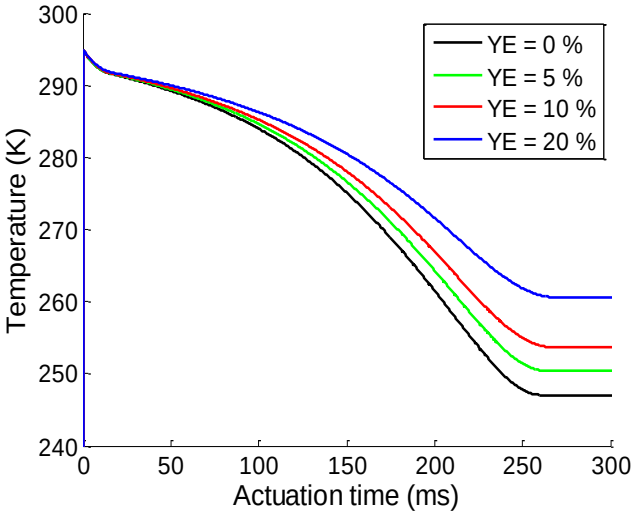

(a) metering chamber

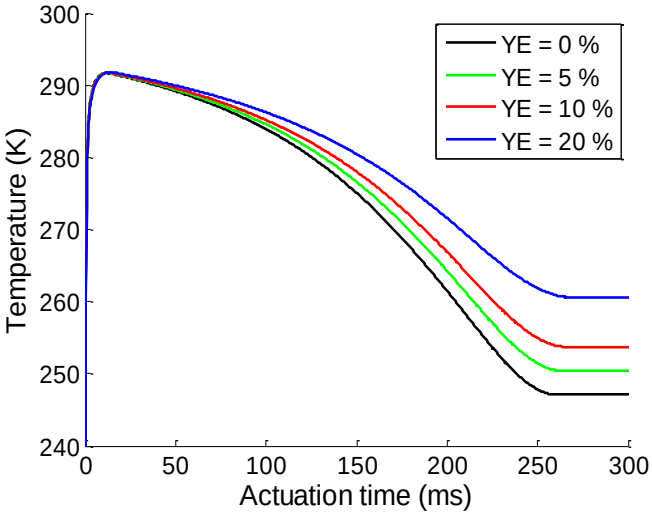

(b) expansion chamber

Figure 5.17 Temporal evolution of formulation temperature inside pMDI, using Raoult's law SVP model

Reasons for the large difference in the predicted final states of the formulation inside the chambers are explored in more detail by examining the SVP values as functions of ethanol mole fraction and temperature in Figure 5.18 (a-b) for empirical SVP model, and Figure 5.19 (a-b) for Raoult's law model. In both figures, the surface colour provides an indication of the SVP values. The black data points on the surfaces are the SVP values calculated by equation 5-1 and delineate the range of temperature that forms the basis of the empirical SVP equation 5-1. The red data points at the left end of the surface are the equation outcomes with slight extrapolations beyond the data range of the original temperature i.e. 247K and 250K. The corresponding temperatures are calculated by the model as the final states for pure HFA134 and mixture formulations, respectively. Four coloured lines (black, green, red and blue) indicate how the p-T conditions of the HFA134/ethanol mixtures with four different initial ethanol concentrations change during an actuation event, inside metering chamber. The colours are those used in the diagrams with pressure-time and temperature-time traces (Figure 5.14 - Figure 5.17) for corresponding initial ethanol mass fraction. The initial and final states are indicated by means of black dashed lines. For visual clarity, a top view of each 3D diagram is provided in Figure 5.18 (b) and Figure 5.19 (b).

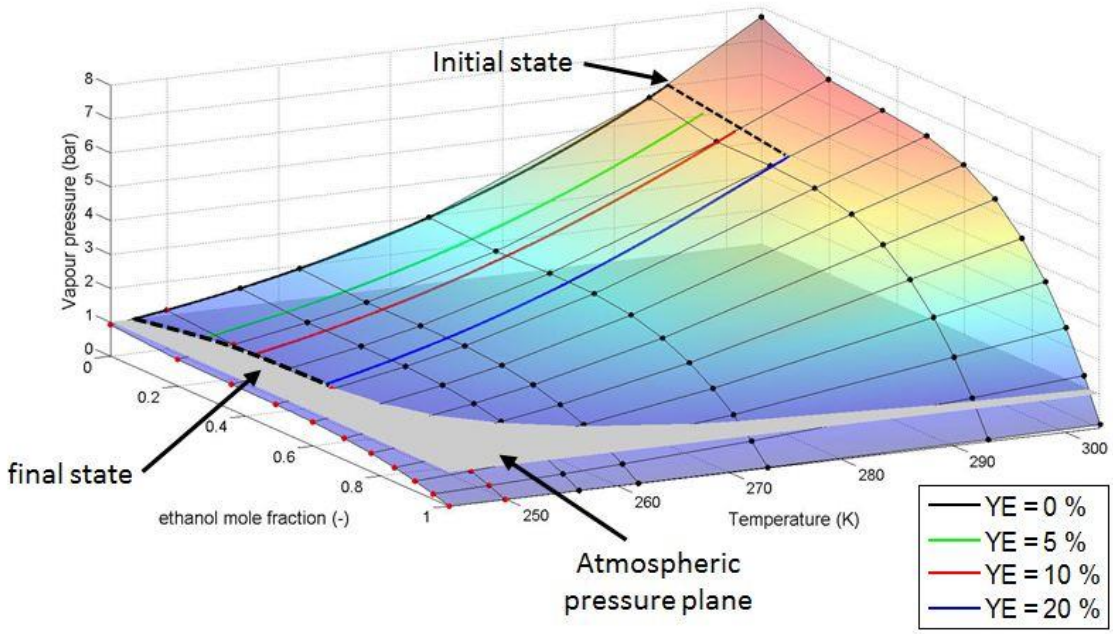

Figure 5.18 (a) Landscape of HFA134/ethanol

empirical SVP values as functions of ethanol mole fraction and temperature

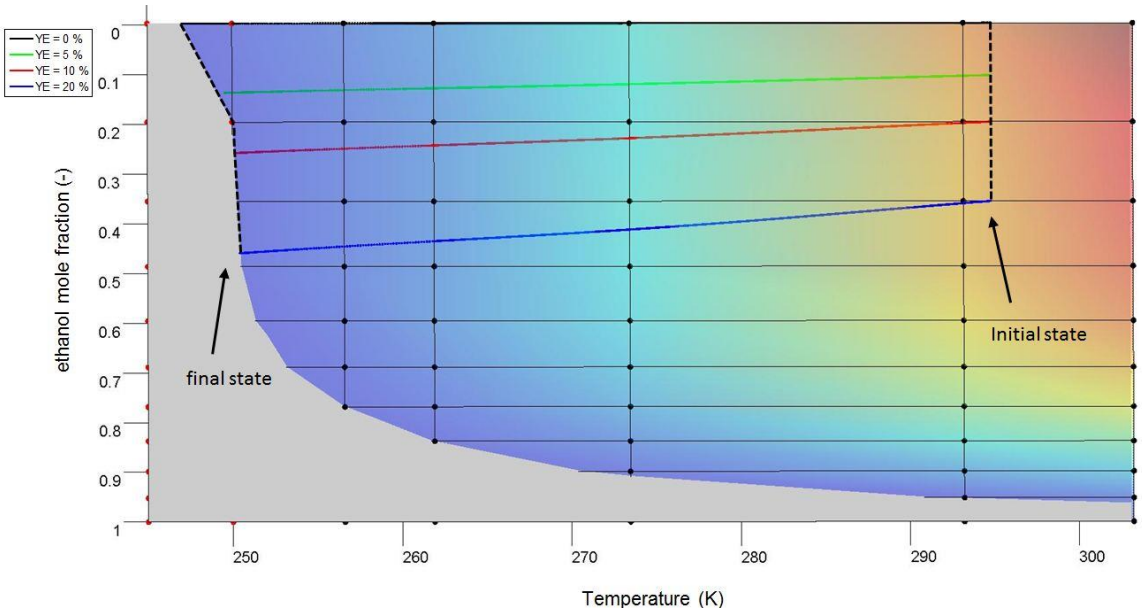

Figure 5.18 (b) Top view of HFA134/ethanol

empirical SVP landscape as functions of ethanol mole fraction and temperature

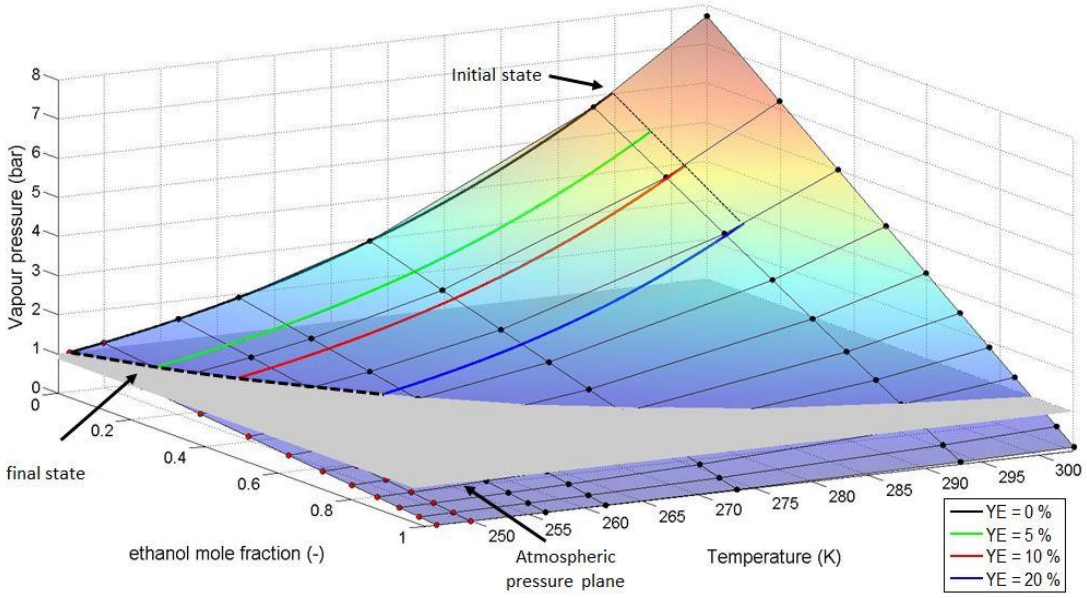

Figure 5.19 (a) Landscape of HFA134/ethanol

Raoult's law SVP values as functions of ethanol mole fraction and temperature

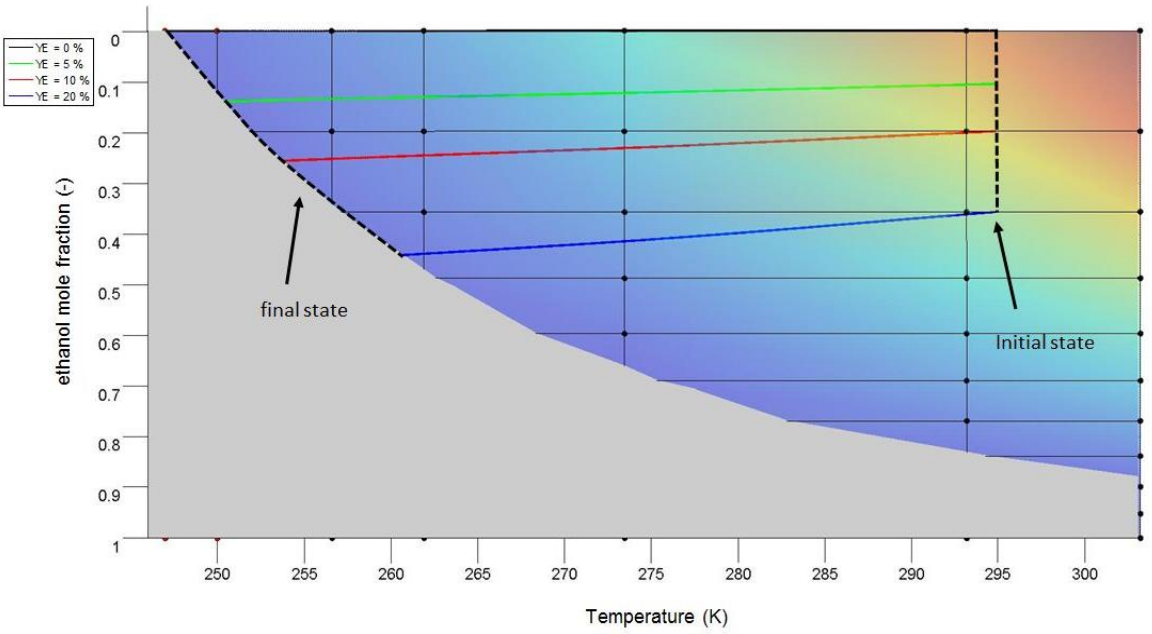

Figure 5.19 (b) Top view of HFA134/ethanol

Raoult's law SVP landscape as functions of ethanol mole fraction and temperature

The SVP and temperature in metering chamber continually decrease until atmospheric pressure condition is reached. For the empirical SVP model, the final temperature is lowest for pure HFA134, whereas, for the remaining ethanol concentrations, the final temperatures are slightly higher and with little differences between them. Formulations with Y_E=10% & Y_E=20% exhibit similar final temperature of 250.5K and the final temperature for Y_E=5% is 249.5 K. According to Figure 5.19 (a-b), Raoult's law predicts final temperatures of 250 K, 253 K and 260 K for Y_E =5%, 10% and 20% formulation, respectively, so the final temperatures for these formulation are predicted to be quite different. These differences depend on the details of the shape of the $p_{mix} - T_{mix} - Y_E$ surface in the vicinity of atmospheric pressure.

5.5.1.3 Spray velocity

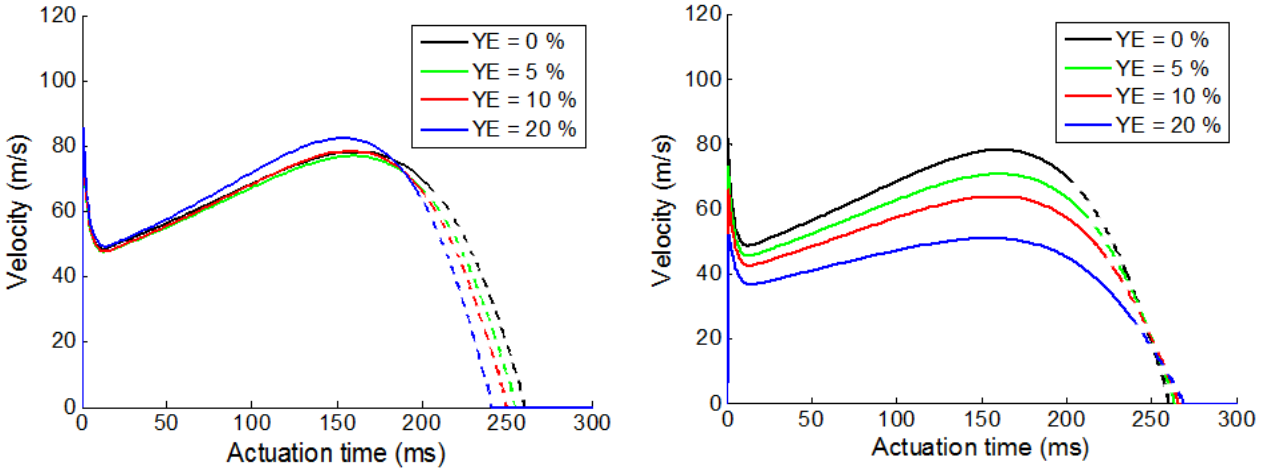

(a) empirical SVP model **(b) Raoult's law**

Figure 5.20 Near-orifice spray velocity as a function of actuation time

Predictions of the near-orifice spray velocity for formulations with different ethanol content using the empirical SVP formula and Raoult's law are shown in Figure 5.20 (a-b), respectively. The region of the curves which are shown with solid lines is the one over which 95% of mixture mass is emitted. It can be observed that all velocity-time traces of Figure 5.20 exhibit similar temporal behaviour. The trend follows the general pattern discussed in chapter 3, section 3.7.1.2 for pure propellants. Figure 5.20 (a) suggests that the predicted velocity is almost independent of ethanol content when our empirical SVP model is used.

This is attributable to the positive deviation of real SVP values from Raoult's law, which is captured by our empirical SVP model. As shown in Figure 5.20 (b), velocity generally reduces with increasing ethanol content when Raoult's law is used to represent SVP. This is due to lower SVP predictions by this model leading to the prediction that less energy would be available for flow acceleration. The differences between predicted velocities for different SVP models are larger for higher concentration of ethanol. Suitability of SVP models for velocity prediction in pMDIs will be discussed in section 5.5.2.4.1, by comparing predictions against PDA data.

5.5.1.4 Droplet size

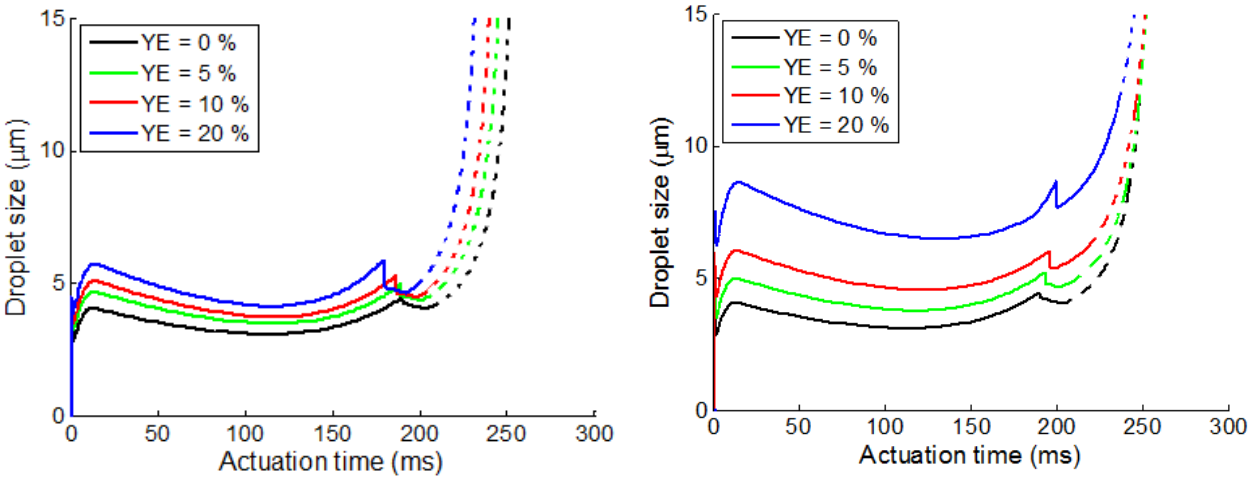

(a) empirical SVP model **(b) Raoult's law**

Figure 5.21 Near-orifice spray droplet size as a function of actuation time,

Predicted droplet size using the multicomponent LISA model is shown in Figure 5.21 (a-b) for the empirical SVP model and Raoult's law. All traces show similar temporal behaviour demonstrating an inverse relation with the corresponding velocity traces. This relationship is due to the flow velocity being the major energy source for droplet fragmentation as pointed out in chapter 4, sections 4.4.1.2 & 4.4.2.3. This trend was also previously observed by Baeckstroem and Nilsson (1988) and Harnor et al. (1993) for CFC formulations, Clark (1991) and Wigley et al., (2002) for HFA formulation and more recently by Myatt et al. (2015 a-b) for HFA/ethanol mixture formulations.

Results show that as the concentration of ethanol increases in the formulation, the predicted droplet size also increases. This correlation is weaker in Figure 5.21 (a) for the empirical SVP model, compared with Figure 5.21 (b) for Raoult's law base SVP model. Additionally, for a fixed ethanol concentration in the formulation, the droplet size predicted by Raoult's law model is always larger than its empirical SVP model counterpart. This trend becomes more apparent as ethanol increases in the mixture and is primarily a result of lower SVP, which in turn diminishes the velocity. As a result, the predicted droplet size becomes larger. Suitability of SVP models for droplet size prediction in the case of pMDI, will be discussed in section 5.5.2.4.2, by comparing predictions against PDA data.

5.5.2 Validation against PDA measurement

In this section the outcome of the multicomponent flow model in terms of spray velocity and droplet size is compared against PDA measurements of mixture formulations of HFA134/ethanol. The set of PDA data used here corresponds to the outcome of a parallel experimentally based project carried out by Ben Myatt. Some analysis related to these PDA measurements can be found in Myatt et al. (2015 a-b) and further details will be reported elsewhere in future.

5.5.2.1 Test case

Geometric properties of the actuator and test conditions are the ones presented in Table 5.5. PDA data collected for a series of 30 spray events at 15 mm away from spray orifice for HFA134 based propellant systems. The mass fraction of ethanol in liquid phase, Y_E, varied from 5% to 20%. PDA data are ensemble averaged over 10 ms time bins.

5.5.2.2 PDA measurements

5.5.2.2.1 Velocity

Plume velocity for different ethanol concentrations is shown in Figure 5.22. The broad temporal trends of velocity and droplet sizes are similar for all formulations, particularly during the first 200 ms of the actuation event.

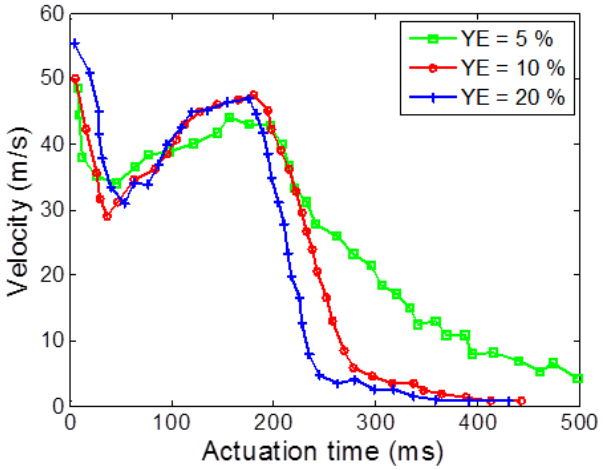

Figure 5.22 Temporal axial velocity of HFA134/ethanol mixtures at 15 mm away from spray nozzle

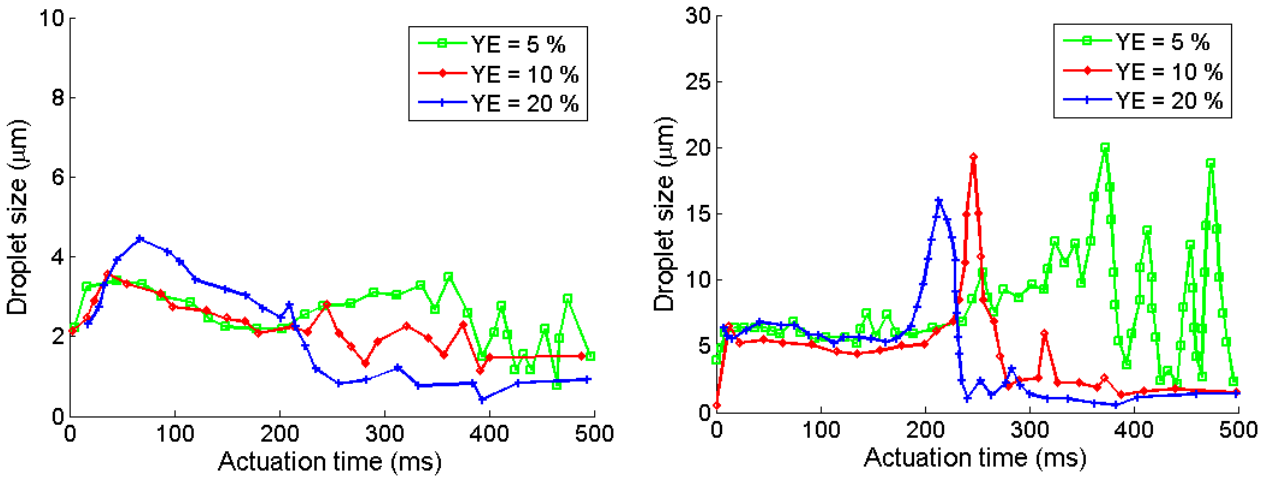

(a) D_{10} **(b) D_{32}**

Figure 5.23 Temporal D32 of HFA134/ethanol mixtures at 15 mm away from spray nozzle

5.5.2.2.2 Droplet size

The measured droplet size is represented by D_{10} and D_{32} in Figure 5.23. Here the broad trend of both metrics shows similarities over 200 ms. The differences between D_{10} values is only considerable when the formulation composition migrates to YE=20%. For D_{32}, these differences are a lot less over the range of considered compositions, up to 200 ms.

5.5.2.3 Near-orifice extrapolation

Similar to the validation activity process in chapter 3 and 4, direct comparison of model predictions against PDA data requires further processing of PDA measurements. This includes extrapolating PDA data back from its measured position (i.e. 15 mm) to a near-orifice region location unaffected by large amounts of mixing between pMDI aerosol and surrounding air, so that the model predictions are likely to be valid. This needs having the knowledge of axial variations of plume characteristics, which were provided by the parallel experimentally based project. “10 mm” is the closest point from spray orifice where velocity values can be measured with reasonable accuracy, as determined by test protocol of parallel experimentally based project. By getting any closer to spray orifice than 10 mm, velocity values may be affected by dense spray effect and related data drop out.

5.5.2.3.1 Velocity

Variation of plume centreline velocity with respect to axial measurement location, for different HFA134 based formulations, is presented in Figure 5.24. Considerable decay in plume velocity over a distance of 100 mm from the spray orifice is observed, as a result of plume-air momentum transfer. As discussed in chapter 3, extrapolation of PDA data to the near-orifice region requires investigating if the plume velocity reasonably follows quasi-steady jet/plume relationships. This relationship is expressed by equation 3-58:

$$\frac{V_{cl}}{V_{ref}} = \frac{C}{(x - x_s)/D_{so}} \qquad 3\text{-}58$$

Composition	C	V_{ref}	x_s	R^2
$Y_E = 5\%$	56.9	57.79	9.38	0.99
$Y_E = 10\%$	56.95	58.52	10.52	0.99
$Y_E = 20\%$	60.19	60.98	11.29	0.99
Average line	57.21	60.43	10.39	0.99

Table 5.6 Constants in equation 3-58 for different ethanol compositions in mixture formulation

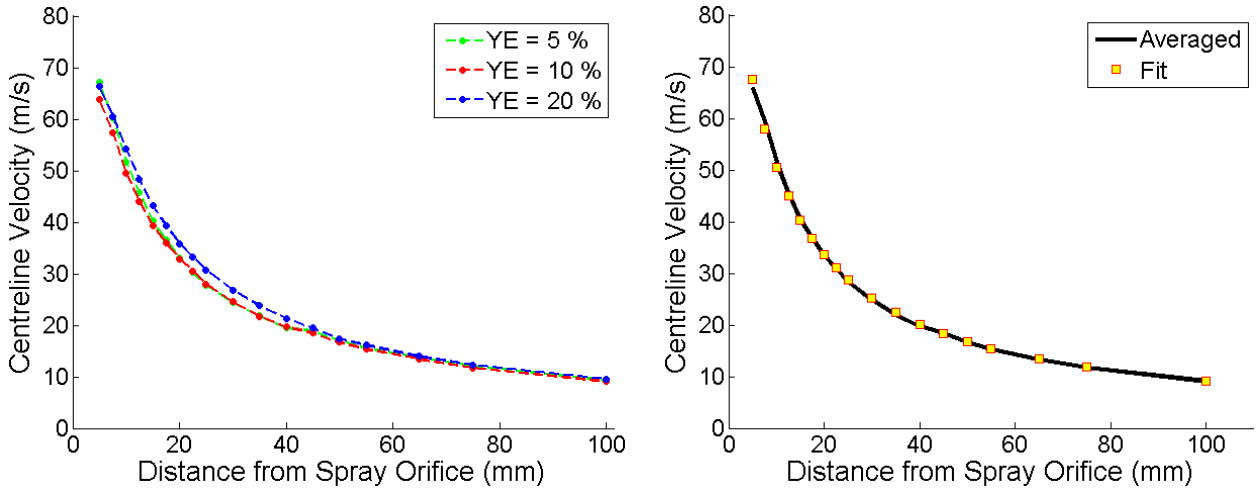

(a) Measured data **(b) Averaged data & fit**

Figure 5.24 Axial variation of plume centreline velocity with respect to formulation composition

According to the constants of the fit for different ethanol composition shown in Table 5.6, inspection of the fitted data suggests that the decay rate of centreline velocity is almost independent of the formulation ethanol composition. By neglecting differences between traces for different ethanol concentrations, we would be able to replace the traces in Figure 5.24 (a) with an average trace as shown with solid line in Figure 5.24 (b). Constants presented in Table 5.6 for average line are used to construct the best fit line. The average

deviation of the data from the best fit is 2.90 % with a maximum deviation of 7.27% at axial position of 65 mm from spray orifice exit.

5.5.2.3.2 Droplet size

Variation of centreline droplet size with respect to measurement location for different formulations, is presented in Figure 5.25. Closest to the spray orifice, the data shows ascending trends: over the first 20 mm for D_{10}, over 40 mm for D_{32}. Detailed analysis of the PDA data within the experimental project showed that these rising trends are due to the effect of PDA data dropout in the dense spray region. Thus, the axial droplet data in regions close to spray orifice are not sufficiently reliable for validation. Additionally analysis of the data showed that there did not appear to be much correlation between velocity and drop size. In this case, extrapolation is not applicable to droplet trends. Hence the raw droplet data will be used as it is for comparison/trend verification.

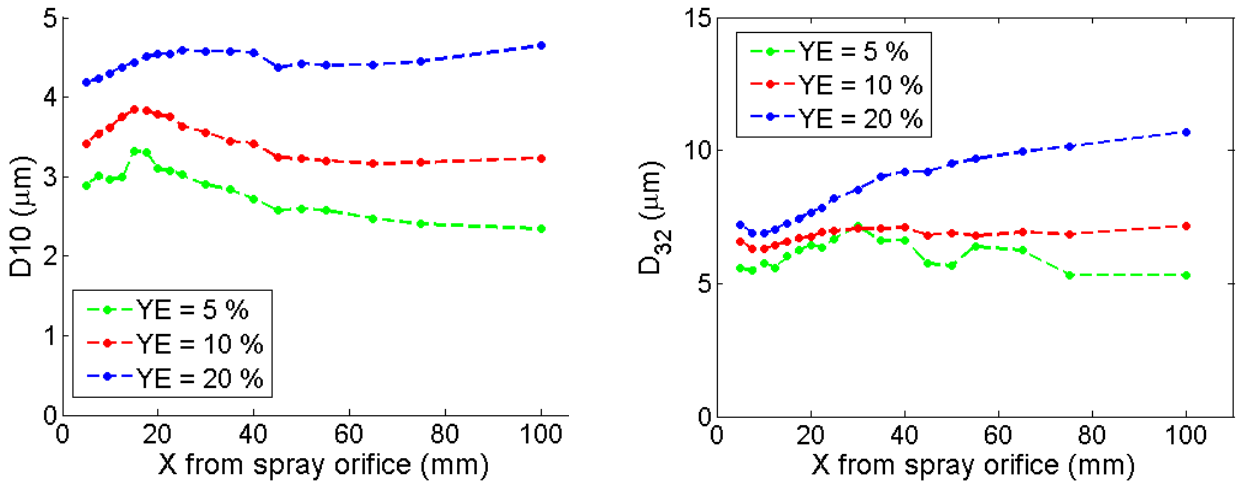

(a) D_{10} **(b) D_{32}**

Figure 5.25 Axial variation of droplet size for different formulation compositions

5.5.2.4 Result validation

5.5.2.4.1 Velocity

A comparison between the predicted near-orifice velocity and PDA measurements is presented in Figure 5.26. The extrapolated traces are shown with dashed lines in the following figures. Figure 5.26 (a-c) shows that velocity trend and the extrema corresponding to different stages of the actuation event are correctly captured by the multicomponent flow model. With reference to the extrapolated velocity, the magnitude of model predictions is also in very good agreement for all formulations with extrapolated PDA over approximately the first 200 ms of the actuation event. This represents approximately 95% of the emitted metering chamber mass. Calculations predict an overall plume duration of around 250 ms for all of the formulations due to adiabatic cooling. The PDA data, on the other hand, shows a progressive decrease of the duration of the final phase velocity decay as the ethanol concentration increases. This stage of plume formation is associated with rather slow evaporation of formulation remnants inside the actuator body emitted in the form intermittent “puffs”. Heat transfer between the formulation and the actuator walls will be involved at this stage, so representation of the final stages of the actuation event was outside the scope of the present work.

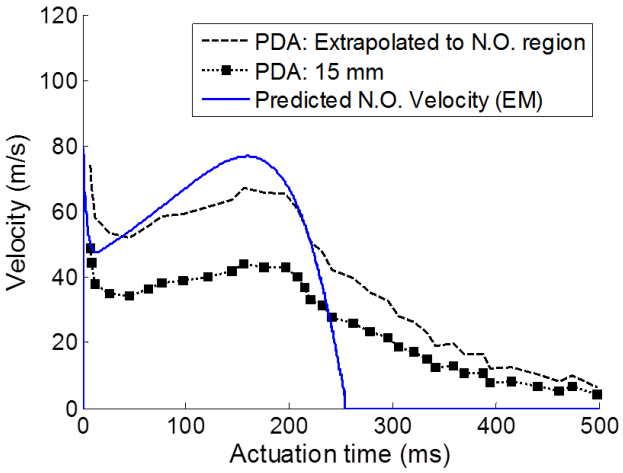

(a) YE=5%

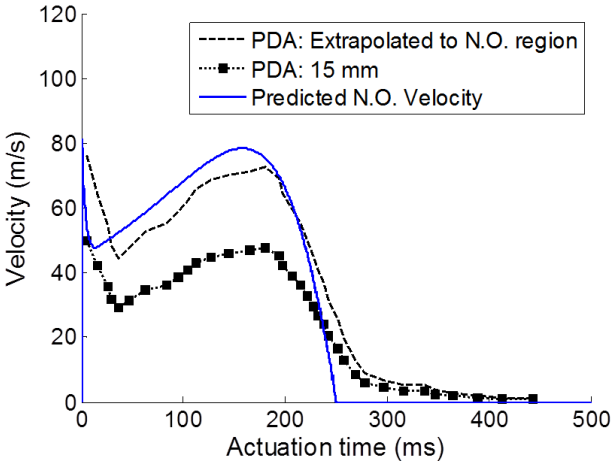

(b) YE=10%

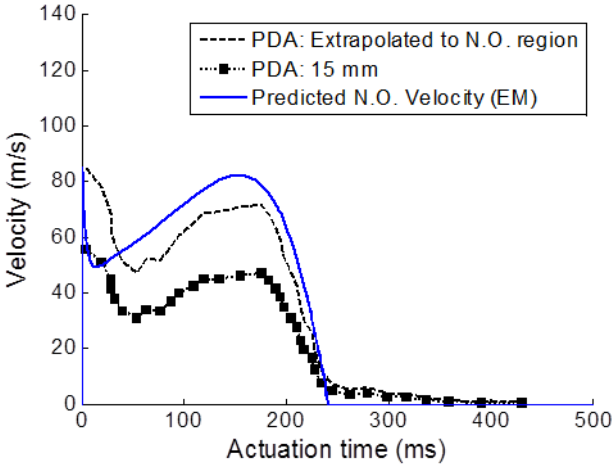

(c) YE=5%

Figure 5.26 Predicted, measured and extrapolated velocities, corresponding to different formulation compositions

Ethanol content	Velocity (m/s)		
Y_E (w/w %)	PDA at 15 mm (Extrapolated to 10 mm)	Predictions (Empirical SVP)	Predictions (Raoult's law SVP)
5	63.99	64.91	60.73
10	63.84	65.73	55.45
20	67.89	68.35	45.45

Table 5.7 Averaged plume velocity for ethanol content formulations, over duration of 95% mass emission

The level of modelling accuracy can be determined by looking at the deviation of predicted velocity from PDA measurements. To obtain a single metric, temporal traces (predicted ones and extrapolated PDA ones) are averaged over the duration which 95% of mass emission takes place. Results of this comparison, which includes velocity predictions using the empirical SVP model and Raoult's law, are shown in Table 5.7. It can be seen that predictions deviation from extrapolated PDA data using empirical SVP model is generally very small. A maximum deviation of 3% occurs at Y_E=10%. On the other hand, Raoult's law based calculations show progressively larger deviation from measured data, as ethanol concentration increases. Moreover, Raoult's law predicts a decrease of the time-averaged plume velocity with increasing ethanol content, whereas the time-averaged measured velocity increases by 6%. This result confirms that our empirical SVP model can significantly improve model predictions.

5.5.2.4.2 Droplet size

The predicted temporal trends of droplet size are compared with measured D_{10} and D_{32} in Figure 5.27. The predicted droplet size - time trend shows good agreement with measured data for all formulation compositions. During the first 200 ms, the predicted droplet size is consistently between the measured values of D_{10} and D_{32}, adding weight to the predictive capability of the atomisation models.

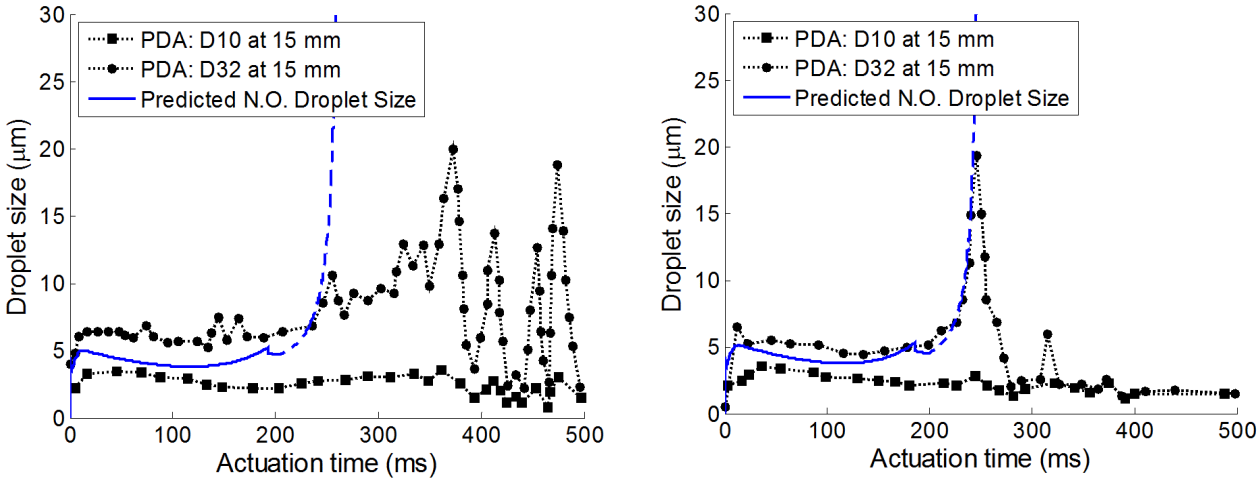

(a) YE=5%

(b) YE=10%

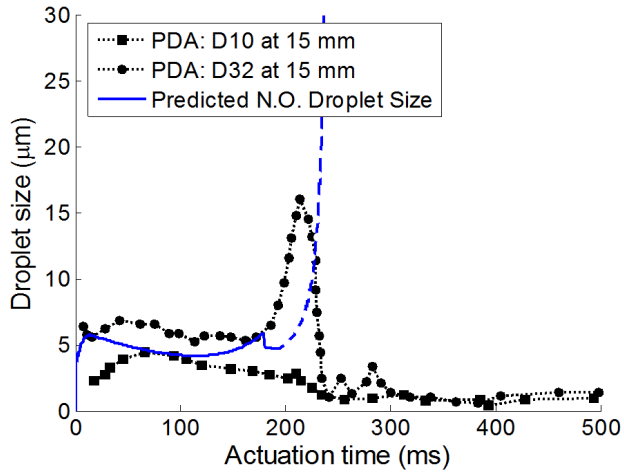

(c) YE=20%

Figure 5.27 Predicted and measured droplet size, corresponding to different formulation compositions

Table 5.8 gives the time-averaged droplet size predicted by empirical SVP, Raoult's law and PDA data over 95% of mass emission duration. The value of D_{10} is best captured by the empirical SVP formula, which is considerably more accurate than those based on Raoult's law. Use of Raoult's law yields a 75% increase in the predicted droplet size as ethanol content increases to 20% w/w. Such an increase is not detectable in the measured data. In line with the velocity predictions, the inaccuracy associated with the use of Raoult's law for droplet size prediction becomes progressively larger as ethanol content of the formulation increases.

Ethanol content	Droplet size (μm)			
Y_E (w/w %)	PDA: D_{10}	PDA: D_{32}	Predictions (Empirical SVP)	Predictions (Raoult's law SVP)
5	2.73	5.91	4.04	4.33
10	2.74	5.02	4.36	5.26
20	3.34	6.15	4.85	7.53

Table 5.8 Averaged spray droplet size for ethanol content formulations, over duration of 95% mass emission

The results show that the atomisation model indicates an increase in ethanol concentration should lead to a small increase in temporal droplet size. This behaviour is also noticeable in the time-averaged measured values of D_{10} and D_{32} in Table 5.8. Considering the fact that velocity is almost identical for all formulations, these predicted changes in droplet size as function of ethanol concentration should, therefore, be attributable to the effects on atomisation due to mixture properties other than its saturated vapour pressure, such as viscosity and surface tension. These factors are shown to be influential on droplet size issued by pMDIs (Smyth, 2003).

5.5.3 Factors influencing droplet size

To demonstrate further the capability of multicomponent atomisation model, the trends of our predictions are compared against available high-quality measured data in the literature (Stein & Myrdal, 2004; Meakin et al. 2000). It should be noted that multiple datasets are presented in the mentioned references, corresponding to range of actuator geometric parameters. For comparison against our model predictions, we only select the data which are obtained from 50 µl metering valve with spray orifice diameter of 0.3 mm. Rest of the actuator parameters can be found in Table 5.5.

5.5.3.1 Method of mean diameter reconstruction

Measurements by Stein & Myrdal (2004) and Meakin et al. (2000) were conducted using APS (aerodynamic particle sizer) and ACI (Anderson cascade impactor), respectively, and the reported metric is mass median aerodynamic diameter (MMAD). Our atomisation model based on the framework by Senecal et al. (1999) predicts the "most representative droplet size"; in chapters 4 and in current chapter, this droplet size metric was previously compared against D_{10} and D_{32}. The procedure of comparison against APS and ACI data is not straightforward and requires two stages of post processing. Firstly, the measured $MMAD_{Res}$ corresponds to the residual droplet size, and must be corrected to find an initial droplet size (at spray orifice exit) for comparison with model predictions. The procedure suggested by Stein & Myrdal (2004) was followed to estimate the initial $MMD_{d,init}$ values of the pMDI aerosol source:

$$MMD_{d,init} = \frac{MMAD_{Res}}{\left(\rho_{d,init} C_{NV}\right)^{\frac{1}{3}} \rho_{Res}^{\frac{1}{6}}} \qquad 5\text{-}23$$

where C_{NV} is the non-volatile concentration. Equation 5-23 is based on mass conservation of the non-volatile components of aerosol droplets as propellant evaporates along the droplet trajectory from the actuator to the measurement location.

Secondly, D_{10} and D_{32} should be calculated based on reconstructed distributions of Stein & Myrdal (2004) and Meakin et al. (2000). From the outcome of equation 5-23 and by assuming lognormal distribution (Finlay, 2001), count median diameter (CMD) can be calculated using equation 5-24 (Finlay 2001):

$$CMD = \frac{MMD}{\exp[3(\ln[GSD])^2]} \qquad 5\text{-}24$$

Where value of GSD is obtained from the literature (Stein & Myrdal, 2004; Meakin et al., 2000), corresponding to the considered data set. Eventually D_{10} and D_{32} can be obtained from the distributions using equations 4-29. This procedure requires assuming the GSDs of initial and residual MMD are identical as implemented by (Stein & Myrdal, 2004).

5.5.3.2 Effect of ethanol content

5.5.3.2.1 Distribution reconstruction

Based on the procedure described in section 5.5.3.1, distributions are reconstructed and shown in Figure 5.28. D_{10} and D_{32} corresponding to these distributions are summarised in Table 5.9 and Table 5.10

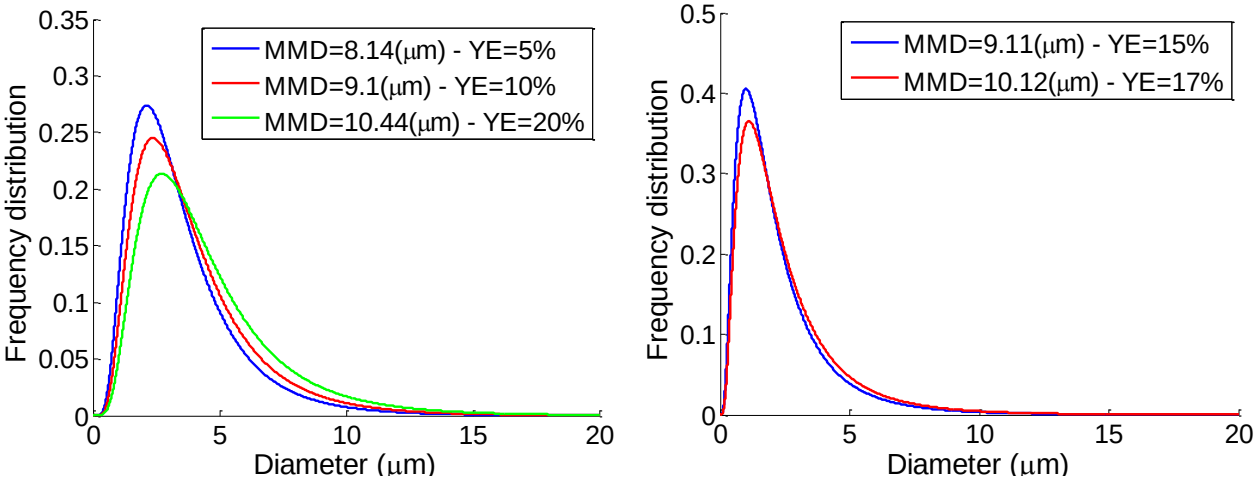

(a) (Stein & Myrdal, 2004) – GSD = 1.8

(b) (Meakin et al., 2000) – GSD = 2.2

Figure 5.28 Reconstructed distributions based on initial MMDs, corresponding to different ethanol composition

YE (w/w%)	Residual MMAD (measured)	Initial MMD (eq. 5-23)	D_{10} (reconstructed)	D_{32} (reconstructed)	Averaged GSD
5	1.92	8.14	3.5	6.57	1.8
10	2.13	9.1	3.91	7.21	
20	2.72	10.44	4.46	8.02	

Table 5.9 Reported and reconstructed droplet size metrics of (Stein & Myrdal, 2004)

YE (w/w%)	Residual MMAD (measured)	Initial MMD (eq. 5-23)	D_{10} (reconstructed)	D_{32} (reconstructed)	Averaged GSD
15	2.8	9.1	2.28	6.13	2.2
17	3.1	10.12	2.53	6.62	

Table 5.10 Reported and reconstructed droplet size metrics of (Meakin et al., 2000)

5.5.3.2.2 Droplet size comparison

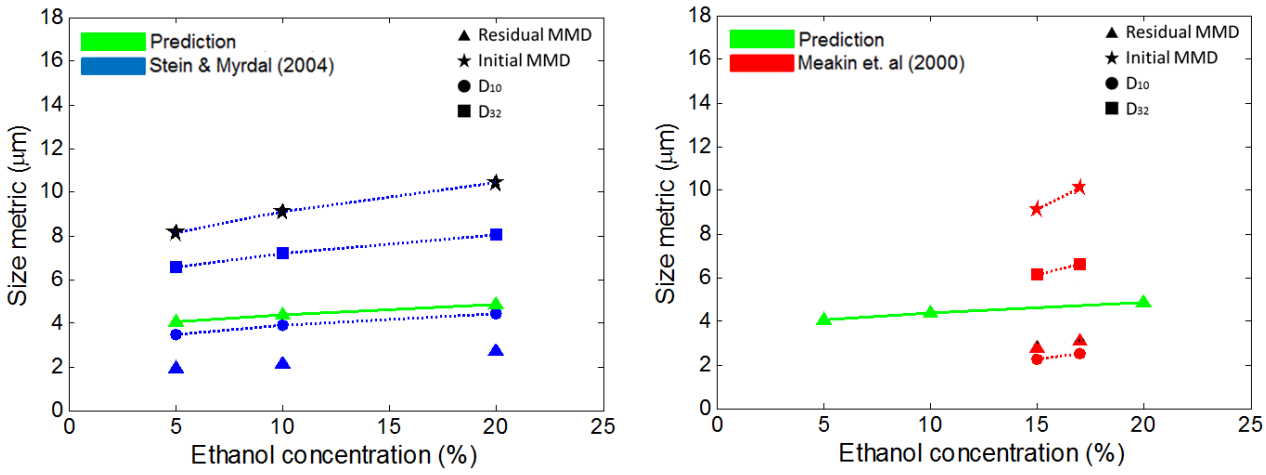

(a) (Stein & Myrdal, 2004) **(b) (Meakin et al., 2000)**

Figure 5.29 Model predictions against experimental measurement for different ethanol composition in HFA134 formulation

Comparison of multicomponent atomisation model against measurements of Stein & Myrdal (2004) and Meakin et al. (2000) is shown in Figure 5.29. Sources of data are specifically coloured where each size metric is distinguished with a symbol, as shown in the figure legend. In the figure it can be seen that the magnitude of the reconstructed D_{10} is considerably below the corresponding initial MMD. This is due to the dependency of this metric to droplet volume, giving rise to its magnitude.

All sets of data demonstrate that as ethanol concentration increases, droplet size increases consistently. This trend is very well captured by the model. It is also observable that the

slops of the reconstructed and measured lines are broadly similar to model prediction suggesting that dependency of droplet size to ethanol content is reasonably represented in the model. At any particular formulation composition, model predictions lay within the range of reconstructed D_{10} and D_{32}. This enhances the validity of model outcome capable of predicting droplet size with in the correct order of magnitude.

Increase in droplet size as ethanol content increase, suggests that the atomisation quality becomes poorer with addition of ethanol in the mixture. For an aerodynamic atomisation mechanism such as LISA the source of atomisation energy is SVP of the formulation. However, as discussed previously, the SVP values of the mixture (especially up to Y_E=20%) are only marginally affected by ethanol content. Therefore, alteration of other fluid properties such as viscosity and surface tension which are effective factors in aerodynamic atomisation could play more significant part as previously acknowledged. This is also pointed out by Smyth (2008) and can now be elucidated from our predictions.

5.5.3.3 Effect of temperature

5.5.3.3.1 Distribution reconstruction

Here we reconstruct distribution from APS measurement of Stein & Myrdal (2004) and Stein & Myrdal (2006), for three distinct ambient temperatures of 20°C, 30°C and 45°C. At each temperature four ethanol concentration of YE=1%, 5%, 10% and 20% are considered. These distributions are illustrated in Figure 5.30. The relevant D_{10} and D_{32} values are approximated from the reported MMD values and are presented in Table 5.11.

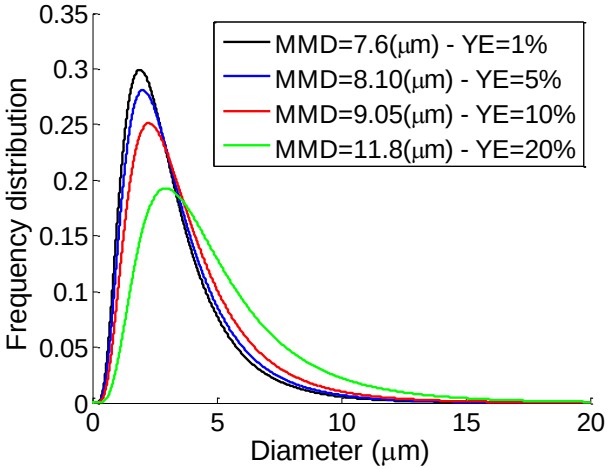

(a) T=20 °C

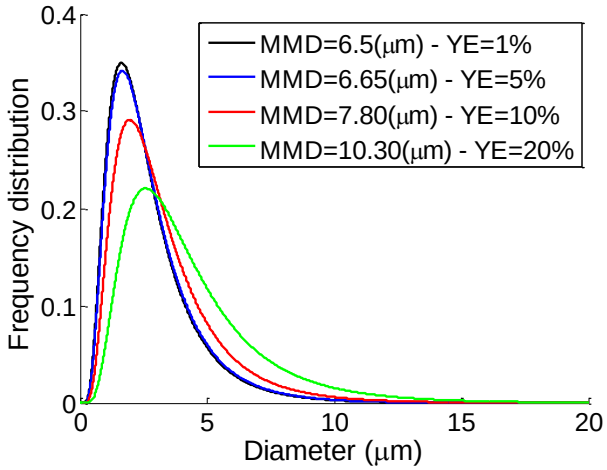

(b) T=35 °C

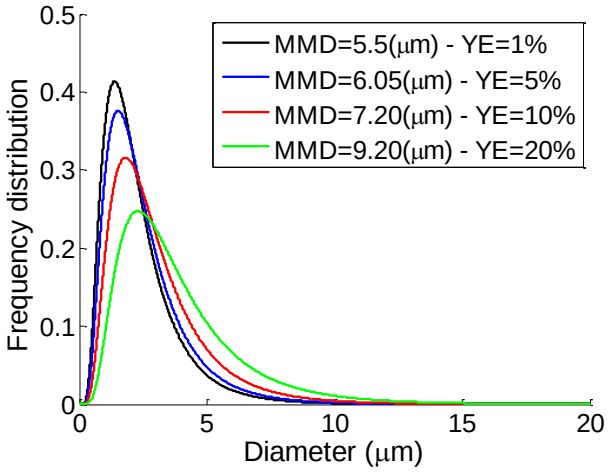

(c) T=45 °C

Figure 5.30 Reconstructed distributions of (Stein & Myrdal, 2004) and (Stein & Myrdal, 2006) based on initial MMDs and average GSD of 1.8, corresponding to different ethanol composition, at different temperatures

		Initial MMD (eq. 5-23)				D_{10} (reconstructed)				D_{32} (reconstructed)				GSD
Temp (◦C)	YE (%)	1	5	10	20	1	5	10	20	1	5	10	20	
20		7.60	8.10	9.05	11.80	3.19	3.40	3.79	4.89	6.15	6.50	7.12	8.69	1.8
30		6.50	6.65	7.80	10.30	2.73	2.80	3.20	4.30	5.34	5.46	6.29	7.88	
45		5.50	6.05	7.20	9.20	2.30	2.50	3.03	3.85	4.57	5.00	5.85	7.20	

Table 5.11 Reported and estimated droplet size metrics of (Stein & Myrdal, 2004) and (Stein & Myrdal, 2006)

5.5.3.3.2 Droplet size comparison

Model predictions are compared against reconstructed D_{10} and D_{32} in Figure 5.31. The increasing trend of droplet size with respect to ethanol concentration increase is evident in each figure. It can also be seen that at any specific ethanol concentration, droplet size (regardless of the size metric) decreases, as temperature rises. This trend is captured with the model. Results at T= 20 °C and T=30 °C show that model predictions are in very good agreement with reconstructed D_{10}. For the case of 45°C it can be seen that model predictions under predicts the reconstructed values. This may be attributable to different reasons. Firstly, it is possible that empirical SVP model is used above its functioning temperature end (i.e. 30 °C). Equation 5-1 may over predict SVP at 45 °C which leads to formation of smaller droplet size. This requires SVP model scrutiny against data at higher temperatures. Secondly, behaviour of mixture surface tension and viscosity may be far from linear mass weighting representation as used in this model, for higher temperature. This means that these properties of the whole mixture may not decrease to considerable extent while temperature increases from 30 °C to 45 °C. However in the absence of any experimental data, this is only at the level of speculation and further works is required for confirmation.

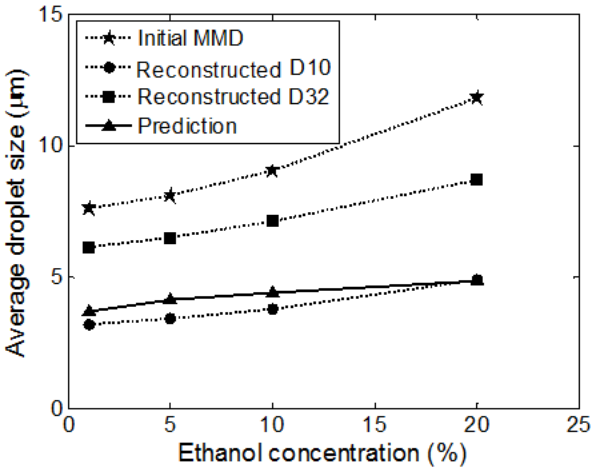

(a) T=20 °C

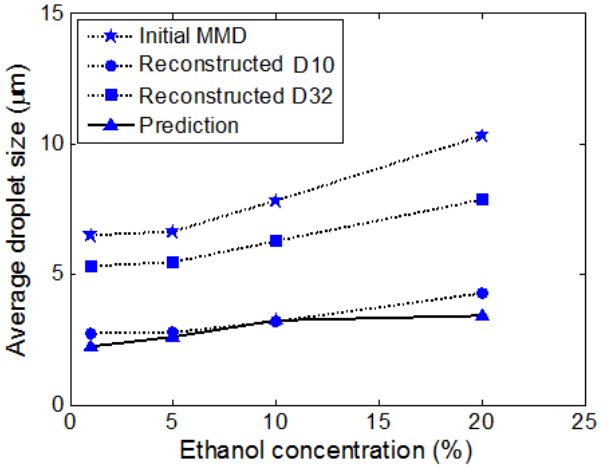

(b) T=35 °C

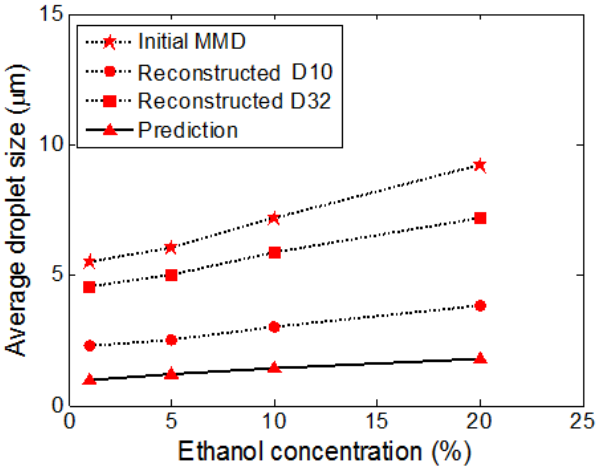

(c) T=45 °C

Figure 5.31 Model prediction against (Stein & Myrdal, 2004) and (Stein & Myrdal, 2006) at different temperatures

In general as the temperature increases, SVP of the mixture also increase. For the current range of investigated temperature, formulation SVP varies from approximately 5.5 bar to 10 bar. This means that the greater the SVP is, the smaller the issued droplets from pMDI becomes. As predicted by our model, this hypothesis is consistent with what has reported earlier (Smyth, 2003; Clark, 1991; Polli et al., 1969).

5.6 Summary and conclusion

This chapter presented a numerical model for the prediction of two-phase flows of flashing HFA/ethanol mixtures through a twin-orifice geometry representative of a pMDI. The homogeneous frozen flow model of internal flow was linked to the multicomponent LISA atomisation model to predict the velocity and droplet size of sprays issuing from the device. Due to the significance of the saturated vapour pressure (SVP) in atomisation and internal flow predictions, this quantity was measured over a wide range of relevant ethanol concentrations and temperatures. The SVP data was presented separately to enhance the current database for the benefits of formulation design and device optimisation purposes by pharmaceutical community as well as future modelling efforts.

Strong deviation from Raoult's law was found in the measured SVP values, clearly questioning the applicability of this law to pMDI formulations. In the present work on multicomponent flashing mixtures, the measured SVP was used in the model by means of a compact mathematical representation.

When using this empirical SVP model, variations of pressure and temperature inside the actuator body did not exhibit strong dependence on ethanol concentration as it increases up to Y_E=20%. Comparative predictions using Raoult's law, however, showed strong dependency of flow variables to increase in ethanol concentration. This provided predictions that can be tested experimentally in future work.

Near-orifice velocity and droplet size of mixture formulations were predicted and validated against our PDA measurements at 15 mm away from spray nozzle. It was observed that the predicted spray velocity during the period that 95% of mass emission takes place (adiabatic regime) was in good agreement with extrapolated PDA data. None of the predicted and measured velocity curves showed a large dependence on ethanol concentration. Comparison of the average predicted velocity against PDA data revealed that Raoult's law based calculation leads to considerable underestimation of the near-orifice plume velocity compared with the empirical SVP model. The temporal patterns and order-of-magnitude droplet size were also predicted very well by our atomisation model. It was also found that droplet size calculation using Raoult's law, over predicts D_{10} values compared with empirical SVP model.

The role of temperature and ethanol concentration was investigated on droplet size by comparing modelling outcomes against available data in literature (Stein & Myrdal, 2006; Stein & Myrdal 2004; Meakin et al. 2000). Predictions of our atomisation model were within the correct order of magnitude for all of the studies and followed the established trends claimed in the literature. Model predictions suggest that increase of ethanol in the formulation leads to increase in the droplet size. It was observed that formulations with higher SVP produce smaller droplets. As predicted by our model, this hypothesis is consistent with what has been reported earlier (Smyth, 2003; Clark, 1991; Polli et al. 1969).

The largely successful outcome of our wide-ranging validation exercise increases confidence in the predictive capability of the models, which have brought together for the first time the capability to predict from first principles the velocity and drop size for pMDI actuators with HFA / ethanol mixtures with ethanol contents up to 20% w/w.

Chapter Six

CFD Simulation of pMDI Injection into Confined Space of USP-IP

6 Chapter Six: CFD Simulation of pMDI Injection into Confined Space of USP-IP

6.1 Introduction

In order to study the transport characteristics and dispersion of the droplets released from a pMDI, a computer based CFD model is constructed. Providing results with reasonable level of validity requires two major considerations. Firstly, the CFD model must be capable of representing all the major physics capturing the interactions between the pMDI aerosol and its surroundings, where applicable, the geometry into which the plume is injected (Finlay, 2001). Significant physics which occurs in the problem are the dispersion of the droplets owing to turbulence diffusion, rapid adiabatic flash evaporation in the near-orifice region and momentum and heat transfer between droplets and surroundings causing slow evaporation of multi-component droplets. Secondly, CFD model must be equipped with accurate and well defined boundary conditions; in particular spray source related boundary conditions (Kleinstreuer et al., 2007).

In the current CFD work, the spray source is technically a kernel of information which includes spray parameters. Depending on the modelled physics, these parameters are normally spray velocity, mass flow rate, temperature, particle size distribution (PSD), etc. One common cause of mismatch between the experiment and CFD outcome is the oversimplification of spray source which is often defined based on case specific experimental outcome or assumed values (Kleinstreuer et al., 2007).

The main aim of the current chapter is to demonstrate the capabilities of the spray source model, which predicts spray velocity, mass flow rate, temperature and instantaneous mean droplet size from first principles. The model involves multicomponent internal flow model as well as atomisation model used as a time-dependent spray boundary condition. Source droplet size is applied in conjunction with a lognormal droplet size distribution with an assumed geometric standard deviation based on typical values reported in the literature. The source is injected at the spray orifice location of a pMDI into USP-IP the construction of the CFD model involves the following stages which will be explained in detail in this chapter:

- Computational geometry construction

- Discretisation of the continuous geometry into computational grids (i.e. mesh generation stage)
- Specification of boundary conditions including the definition of the spray source in CFD
- Relevant solver selection and setting using STAR CCM+ V9.04.001

The chapter concludes by providing the results of the CFD work as well as relevant scientific discussion.

6.2 Conceptual image of models

6.2.1 General considerations

The physical problem involves the injection of a pMDI into a standard USP-IP accompanied by ambient co-flow (USP, 2005). As shown in Figure 6.1, the surroundings of the entire system are at ambient condition, which is indicated by the red dashed border. A vacuum pump pulls a steady flow rate of 30 l/min of ambient air into the inhaler and through the USP-IP. The outlet face of the induction port is attached to the vacuum pump via a pipe.

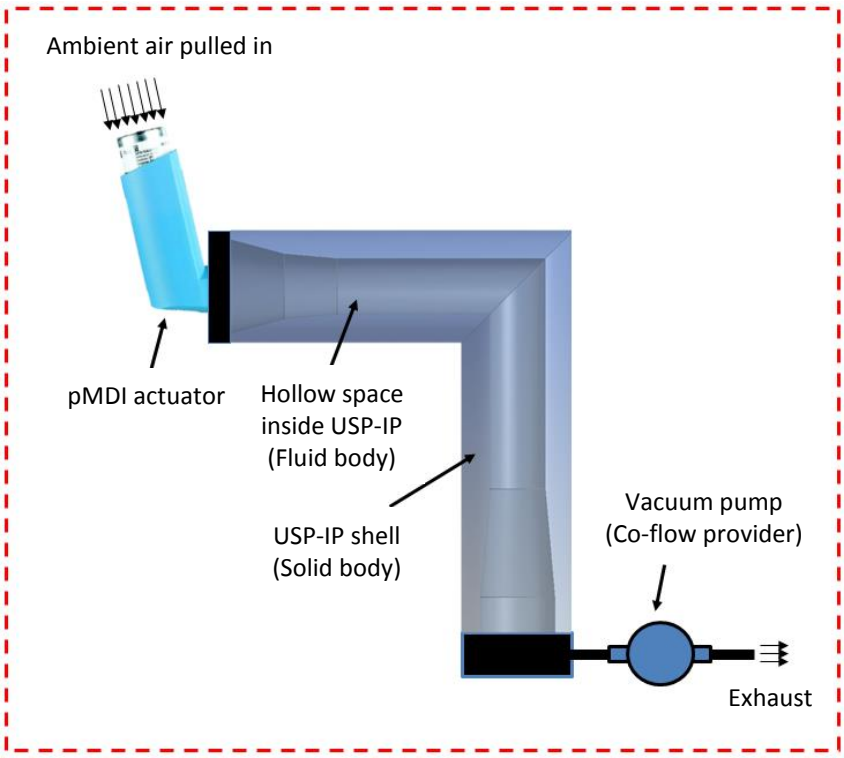

Figure 6.1 Schematic of physical problem (pMDI injection in USP-IP)

The spray plume emerges from the spray orifice of the pMDI actuator with high initial velocity and presence of this substantial velocity at near-orifice region results in turbulence eddies in the flow. These eddies affect the droplet dispersion pattern. The propellant partially evaporates inside the expansion chamber of the pMDI actuator, meaning that the resulting spray contains both liquid and vapour components. The propellant vapour mixes with the ambient air that is drawn through the set-up by the vacuum pump and its local concentration reduces.

Once the droplets are sprayed out, due to the high saturated vapour pressure of the multicomponent droplet, rapid propellant evaporation further decreases the droplet size. The mass of evaporating species is then added to the continuous phase (air) and increases the propellant vapour concentration. Lastly, interaction of the droplet with the boundaries of USP-IP potentially leads to impaction on its walls. Liquid droplets are assumed to deposit on the surface of the wall (i.e. droplet bounce is not considered in these simulations).

6.2.2 Concept of Pseudo Spray Source (PSS)

Due to evaporation of formulation inside the pMDI actuator, the emerging spray consists of liquid (droplets) and propellant vapour phase. Droplets and spray vapour phase (HFA vapour) are introduced by means of a transient aerosol generator so-called “pseudo spray source” (PSS). Our PSS is a virtual truncated conical volume, which is located in near-orifice region and contains collective information of the spray parameters (i.e. liquid/ vapour mass flow rate, velocity, mean droplet size and size distribution, droplet composition, droplet temperature and injection angle). In this virtual space numbers of solid cone point injectors are randomly distributed. Such definition of spray source assists us to:

- realistically represent plume structure in near-orifice region (e.g. conical dispersion of droplets)
- define any desired particle size distribution (PSD)
- achieve robust CFD simulation in terms of numerical stability and convergence

The schematic of the PSS is shown in Figure 6.2 by superimposition of the truncated conical volume sketch, on an arbitrary selected image of a real aerosol injected by a transparent pMDI model into the atmosphere. The image is produced in Thermofluid lab of Loughborough University as a part of parallel experimental project.

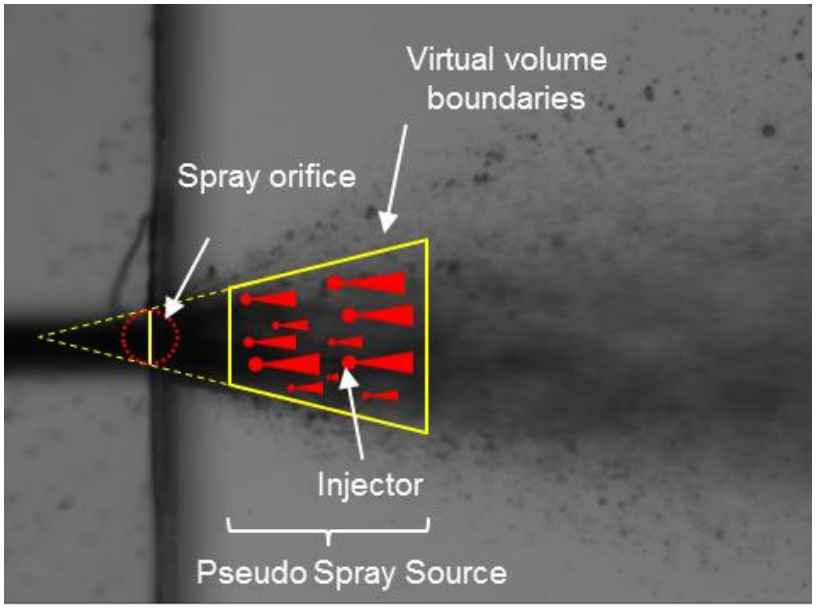

Figure 6.2 Schematic of Pseudo Spray Source (PSS)

The number of injectors is defined to be proportional to the emitted liquid mass flow rate, at any instant of time. Properties of the PSS are computed by the internal flow model of multicomponent mixture as presented and discussed in chapter five, in near-orifice region. In order to account for the transient nature of the plume, the properties of PSS point injectors, as well as spray vapour phase velocity, should change in time. This is accomplished by developing separate JAVA scripts to link the PSS and spray vapour phase to the internal flow model as well as updating source properties as the injection time advances. The values of these parameters will be presented later in section 6.4.2.2.2.

6.3 Theoretical Models

6.3.1 General modelling assumption

The assumptions established to construct the CFD model are summarised as follows:

- Simplified actuator geometry: minor geometric details corresponding to ferrule retaining the metering valve are simplified (see Figure 6.3). This was mainly due to avoid presenting unnecessary small geometric scales, which can cause problems with meshing or numerical instabilities during the computation.
- Adiabatic flow: the effect of heat transfer through the walls of actuator and USP-IP, are neglected.

- No gravity: the effect of gravity force on droplets is ignored. This can be justified by examining the ratio of particle settling velocity ($V_{set} = \rho_d \, g D_d^2 / 18\mu$) to the convective velocity (i.e. at the spray orifice exit). This ratio is calculated to be in the order of 10^{-4} which is too small to influence the particle trajectory.
- Internally homogeneous multicomponent droplets: the species inside the multicomponent droplets are assumed to be distributed uniformly. In the absence of detailed modelling of species distribution in liquid phase, this assumption is the only one available.
- Ethanol is treated as inert species: the ethanol fraction is assumed be non-evaporating; the vapour consists of 100% HFA134. This is justifiable by low saturated vapour pressure of ethanol compared with HFA134.
- Log-normal particle size distribution: it was assumed that at each instant of time, the injected droplets follow log-normal distribution; in practice, inhalation aerosols are routinely interpreted using this distribution with good success (Hichkey & Dunbar, 1997; Finlay, 2001).
- No mechanical secondary atomisation processes: further aerodynamic break-up modes in addition droplet coalescence is assumed to be negligible in the rapidly expanding pMDI spray plumes (Wigley et al. 2002).
- Ideal gas law: the vapour phase is assumed to behave as ideal gas
- Steady air flow: as suggested by the physical test the inhaled air flow is treated as steady flow as would be the case during in-vitro testing of inhalation products (USP, 2005).
- Transient spray flow: considering the time dependent features of the plume emitted from pMDI, the spray phase is modelled using transient formulation.
- Two-way coupled algorithm: due to high mass loading of the spray phase and rapid evaporation of droplets, two-way coupled calculation must be performed to realistically represent the influence of discrete phase on continuous phase.

6.3.2 Governing equations

6.3.2.1 Continuous phase

In the turbulent flow regime, as suggested by Zhang et al. (2004) (see chapter 2, section 2.6), the Reynolds-averaged Navier-Stokes (RANS) equations are used to provide an effective estimation of the flow field. RANS equations of mass and momentum are written as follows in suffix notation (Wilcox, 1994):

$$\frac{\partial \rho}{\partial t} + \frac{\partial \rho V_i}{\partial x_i} = S_{m_i} \qquad 6\text{-}1$$

$$\frac{\partial}{\partial t}(\rho V_i) + \frac{\partial}{\partial x_j}(\rho V_i V_j) = -\frac{\partial p}{\partial x_i} + \frac{\partial}{\partial x_j}\left[\mu\left(\frac{\partial V_i}{\partial x_j} + \frac{\partial V_j}{\partial x_i} - \frac{2}{3}\delta_{ij}\frac{\partial V_k}{\partial x_k}\right)\right] + \frac{\partial}{\partial x_j}\left(-\rho\overline{V_i' V_j'}\right) + S_{M_i} \qquad 6\text{-}2$$

In equations 6-1 and 6-2 V_i is the time averaged velocity component, where attribution of integers 1, 2 and 3 to the index i, describe the x-, y- and z-velocity components, respectively. The time-averaged pressure is denoted by p, while μ and ρ are representing the viscosity and density of the fluid, respectively. Summation is presumed for identical indices and δ_{ij} signifies the Kronecker delta function. Terms S_{m_i} and S_{M_i} in RHS of equations 6-1 and 6-2 accounts for mass and momentum source terms due to interphase interactions. The Reynolds stresses term $\left(-\rho\overline{V_i' V_j'}\right)$ appeared in equation 6-2 is modelled using Boussinesq hypothesis (Hinze, 1975) to link Reynolds stresses to mean velocity gradient as shown in equation 6-3:

$$-\rho\overline{\acute{V}_i \acute{V}_j} = \mu_t\left(\frac{\partial V_i}{\partial x_j} + \frac{\partial V_j}{\partial x_i}\right) - \frac{2}{3}\left(\rho k + \mu_t \frac{\partial V_k}{\partial x_k}\right)\delta_{ij} \qquad 6\text{-}3$$

Where μ_t is the turbulent viscosity and is calculated from equation 6-4 in which C_μ is function of mean strain rate, turbulence kinetic energy,k and turbulence dissipation rate, ε (Shih et al., 1995):

$$\mu_t = \rho C_\mu \frac{k^2}{\varepsilon} \qquad 6\text{-}4$$

Where:

$$C_\mu = \frac{1}{A_0 + A_S \frac{kU^*}{\varepsilon}} \quad \text{6-5}$$

And:

$$U^* \equiv \sqrt{S_{ij}S_{ij}} \quad \text{6-6 (a)}$$

$$A_0 = 4.04 \quad \text{6-6 (b)}$$

$$A_S = \sqrt{6}cos\Phi \quad \text{6-6 (c)}$$

In equation 6-6 (a), S_{ij} is the mean strain rate. The parameter Φ in 6-6 (c) is calculated using equation 6-7 (a-d) (Shih et al., 1995):

$$\Phi = \frac{1}{3}cos^{-1}\left(\sqrt{6}W\right) \quad \text{6-7 (a)}$$

$$W = \frac{S_{ij}S_{ij}S_{ij}}{\tilde{S}^3} \quad \text{6-7 (b)}$$

$$\tilde{S} = \sqrt{S_{ij}S_{ij}} \quad \text{6-7 (c)}$$

$$S_{ij} = \frac{1}{2}\left(\frac{\partial V_j}{\partial x_i} + \frac{\partial V_i}{\partial x_j}\right) \quad \text{6-7 (d)}$$

Turbulence in the continuous phase field is accounted for, by using the realisable $k-\varepsilon$ model which is computationally efficient and widely used in various disciplines. The model is recommended for flows with strong vortices and streamlines curvatures. It is also validated for free flows such as jets as well as flows having complex secondary motions (Kim et al., 1997; Shih et al., 1995). However further work is also required to explore the effect of

various turbulence models on pMDI flow. The transport equations for turbulence kinetic energy k, and turbulence dissipation rate ε, may be written as equations 6-8 and 6-9:

$$\frac{\partial}{\partial t}(\rho k) + \frac{\partial}{\partial x_j}(\rho k V_j) = \frac{\partial}{\partial x_j}\left[\left(\mu + \frac{\mu_t}{\sigma_k}\right)\frac{\partial k}{\partial x_j}\right] + G_k - \rho\varepsilon \quad 6\text{-}8$$

$$\frac{\partial}{\partial t}(\rho \varepsilon) + \frac{\partial}{\partial x_j}(\rho \varepsilon V_j) = \frac{\partial}{\partial x_j}\left[\left(\mu + \frac{\mu_t}{\sigma_\varepsilon}\right)\frac{\partial \varepsilon}{\partial x_j}\right] + \rho C_1 S\varepsilon - \rho C_2 \frac{\varepsilon^2}{k + \sqrt{\nu\varepsilon}} \quad 6\text{-}9$$

$G_k = \mu_t S^2$ is representing the generation of turbulent kinetic energy owing to mean velocity gradient and ν is the kinematic viscosity. The model constants for which the model performs well and has been validated are presented in Table 6.1 (Shih et al., 1995). Constant C_1 reads as equations 6-10 in which S_{ij} is the mean strain rate:

$$C_1 = max\left[0.43\,, \frac{\eta}{\eta + 5}\right] \quad 6\text{-}10\ (a)$$

$$\eta = S\frac{k}{\varepsilon} \quad 6\text{-}10\ (b)$$

$$S = \sqrt{2S_{ij}S_{ij}} \quad 6\text{-}10\ (c)$$

Realisable k-ε Turbulence Model Constant	$C_{1\varepsilon}$	C_2	σ_k	σ_ε
Value	1.44	0.9	1.0	1.2

Table 6.1 Model constants for realizable k-ε turbulence model (Shih et al., 1995)

In order to achieve significant savings in terms of near-wall mesh resolution to resolve turbulence related quantities, "all y^+" wall treatment method is used, where y^+ is non-dimensionalised wall distance given by equation 6-11.

$$y^+ = \frac{yu^*}{\nu} \quad 6\text{-}11$$

In equation 6-11, y is the normal distance from the wall to the near-wall mesh element centroid and u^* is the reference velocity related to wall shear stress (τ_w), as expressed by equation 6-12:

$$u^* = \sqrt{\tau_w/\rho} \quad 6\text{-}12$$

The model gives results similar to the low y^+ treatment as $\lim y^+ \to 0$ and to the high y^+ as $\lim y^+ \to 30$. Details of these wall treatment models can be found in (Versteeg & Malalasekera, 2007). The model is also designed to yield reasonable responses for meshes of intermediate resolution (wall cell centroid falls within the buffer region of the boundary layer i.e. $1 < y^+ < 30$). The method blends turbulence quantities Q_{tur}, such as dissipation rate, calculated by the high or low y^+ approach using an exponential weighing function. The final value for the turbulence quantity is calculated as:

$$Q_{turb} = F_{blend}\, Q_{tur,low\ y^+} + (1 - F_{blend})\, Q_{tur,high\ y^+} \quad 6\text{-}13$$

Where F_{blend} is given as the following:

$$F_{blend} = \exp\left(-\frac{Re_y}{11}\right) \quad 6\text{-}14$$

and Re_y is a wall distance based Reynolds number defined by equation 6-15:

$$Re_y = \sqrt{k}y/\nu \quad 6\text{-}15$$

Where y is the normal distance from the wall to the centroid of the near-wall cell. ν is the kinematic viscosity and k is the turbulence kinetic energy.

The transport equation of HFA vapour phase in the continuous field is governed using the convective-diffusive transport equation in turbulent regime (Bird et al., 2007):

$$\frac{\partial}{\partial t}\left(\rho Y_{g,H}\right)+\frac{\partial\left(\rho V_j Y_{g,H}\right)}{\partial x_j}=-\frac{\partial}{\partial x_j}\left[\left(j_{g,H}+\frac{\mu_t}{Sc_t}\frac{\partial Y_{g,H}}{\partial x_j}\right)\right]+S_{Y,H} \qquad 6\text{-}16$$

where $Y_{g,H}$ is the mass fraction HFA134 vapour and Sc_t represents the turbulent Schmidt number with default value of 0.7. In this relation, $S_{Y,H}$ accounts for the increase in the mass fraction of evaporating species HFA134 within the continuous phase owing to droplet evaporation. $j_{g,H}$ is the diffusion flux of HFA134 vapour which is defined using Fick's law, by equation 6-17:

$$j_{g,HFA}=-\rho D_{g,H}\left(\frac{\partial Y_{g,H}}{\partial x_j}\right) \qquad 6\text{-}17$$

where $D_{g,H}$ is the molecular diffusivity of HFA134.

The energy equation of the system is written as:

$$\frac{\partial(\rho E)}{\partial t}+\frac{\partial}{\partial x_j}\Big(V_j(\rho E+p)\Big)=\frac{\partial}{\partial x_j}\left(k_{eff}\frac{\partial T}{\partial x_j}-\sum_n h_n j_n+\left(\tau_{ij}V_j\right)\right)+S_E \qquad 6\text{-}18$$

Where:

$$k_{eff}=k+\frac{\mu_t c_p}{Pr} \qquad 6\text{-}19\ (a)$$

$$E=h-\frac{p}{\rho}+\frac{V^2}{2} \qquad 6\text{-}19\ (b)$$

$$h=\sum_n Y_n h_n \qquad 6\text{-}19\ (c)$$

$$h_n = \int_{T_{ref}}^{T} c_{p,n} dT \quad \& \quad T_{ref} = 298.15\ K \qquad \text{6-19 (d)}$$

In equation 6-18, T is the field temperature and k_{eff} is the effective thermal conductivity defined by equation 6-19 (a). E is the total energy which is decomposed to equations 6-19 (b-d). h is obtainable from equation 6-19 (c) in which Y_n and h_n are the mass fraction and specific enthalpy of the n^{th} mixture constituent. In this work the continuous phase consists of air and HFA134 vapour phase as mixture constituents. The first three terms on the RHS of equation 6-18, represent energy transfer due to conduction, species diffusion, and viscous dissipation, respectively. S_E represents energy transfer due to interaction with discrete phase. Term τ_{ij} is the deviatoric stress tensor defined as equation 6-20:

$$\tau_{ij} = \mu_{eff}\left(\frac{\partial V_i}{\partial x_j} + \frac{\partial V_j}{\partial x_i}\right) - \frac{2}{3}\mu_{eff}\frac{\partial V_k}{\partial x_k}\delta_{ij} \qquad \text{6-20}$$

In which $\mu_{eff} = \mu + \mu_t$ is the effective viscosity of the flow field.

6.3.2.2 Dispersed phase

In Lagrangian multiphase framework, the droplets equation of motion is expressed by equation 6-21 (Sommerfeld, 1992):

$$m_d \frac{dV_i}{dt} = F_{s,i} \qquad \text{6-21}$$

In which m_d and V_i represent the mass and velocity components of the droplet respectively. $F_{s,i}$ represents the forces acting on i^{th} droplet which is decomposed to equation 6-22:

$$F_{s,i} = F_p + F_D \qquad \text{6-22}$$

F_p is the exerted force on the droplet as a result of local pressure differences in the domain and is calculated using equation 6-23:

$$F_p = Vol_d \nabla p_{static} \qquad \text{6-23}$$

where Vol_d is the droplet volume and ∇ is the gradient field operator $\left(\text{i.e. } \frac{\partial}{\partial x}i + \frac{\partial}{\partial y}j + \frac{\partial}{\partial z}k\right)$. F_D represents the drag force emerging from interaction of droplet with continuous field. This force is calculated using equation 6-24:

$$F_D = \frac{1}{2} C_D \rho A_d |V_{rel}| V_{rel} \qquad 6\text{-}24$$

in which A_d is the projected area of the droplet. $V_{rel} = V_i - V_{d,i}$ which is the relative velocity of the droplet and continuous phase. C_D is the drag coefficient, modelled using Schiller-Naumann (1933) correlation. The correlation is claimed to be suitable for spherical liquid droplets and is shown by equation 6-25:

$$C_D = \begin{cases} \frac{24}{Re_d}(1 + 0.15 Re_d^{0.687}), & Re_d \leq 10^3 \\ 0.44, & Re_d > 10^3 \end{cases} \qquad 6\text{-}25$$

where Re_d is the droplet Reynolds number formulated as follows:

$$Re_d = \frac{\rho |V_{rel}| D_d}{\mu} \qquad 6\text{-}26$$

In which D_d is droplet diameter and $|V_{rel}| = |V_i - V_{d,i}|$.

In order to track the spatial and temporal variations in droplet size, equation 6-27 (Spalding, 1960) is used to govern the rate of mass transfer of the droplet evaporating specie (i.e. HFA134) to the continuous phase:

$$\frac{dm_d}{dt} = -g^* A_s \ln(1 + B) \qquad 6\text{-}27$$

where B is the Spalding transfer number and g^* is the mass transfer conductance ($kg.m^{-2}.s^{-1}$). Spalding number represents the driving force for evaporation, which itself is a function of thermodynamic conditions of the liquid and vapour. Conductance parameter represents geometrical and mechanical effects, such as droplet diameter and velocity. Mathematical representations of these quantities depend on the prevailing evaporation regime. Two distinct regimes are considered namely (i) heat transfer limited evaporation

and (ii) vapour diffusion limited evaporation. The first regime is activated when the saturated vapour pressure at the droplet surface exceeds the surrounding pressure. In this case B is formulated as follows:

$$B = \frac{c_{p,l}(T - T_d)}{h_{lg,d}} \qquad 6\text{-}28$$

Where $c_{p,l}$ is the heat capacity of liquid, T and T_d are flow field and droplet temperatures and eventually h_{lg} is latent heat of the droplet. The conductance parameter is estimated using relation 6-29:

$$g^* = \frac{k}{c_p D_d}(2 + 0.6Re_d^{1/2}Pr^{1/3}) \qquad 6\text{-}29$$

The expression inside the bracket is Ranz-Marshall (1952 a-b) correlation of Nusselt number and Pr is the prandtl number of the continuous phase. For the case where the saturated vapour pressure of the droplet is equal to the surrounding pressure, the mass transfer rate depends on the rate at which vapour can diffuse away from the droplet. For this regime the transfer number estimated by equation 6-30:

$$B = \frac{Y_{g,H}^s - Y_{g,H}^\infty}{1 - Y_{g,H}^s} \qquad 6\text{-}30$$

In this equation superscripts s and ∞ correspond to mass fraction of HFA134 vapour phase at the droplet surface and in the free stream, respectively. The conductance parameter for vapour diffusion limited evaporation regime is defined by equation 6-31:

$$g^* = \frac{\rho D_{g,H}}{D_d}(2 + 0.6Re_d^{1/2}Sc^{1/3}) \qquad 6\text{-}31$$

In equation 6-31, $D_{g,H}$ is the mulecular diffusivity of HFA134 vapour phase. The expression in the bracket is the definition of Sherwood number proposed by Ranz-Marshall (1952 a-b).

The variation of droplet temperature may be tracked using equation 6-32 which is the result of applying heat balance on the droplet:

$$m_d c_p \frac{dT}{dt} = \bar{h} A_d (T_\infty - T_d) + \frac{dm_d}{dt}(h_{lg}) \quad 6\text{-}32$$

where $\bar{h}$ is the heat transfer coefficient which is calculated from the following expression:

$$\bar{h} = \frac{k\left(2 + 0.6 Re_d^{\frac{1}{2}} Pr^{\frac{1}{3}}\right)}{D_d} \quad 6\text{-}33$$

6.3.2.3 Turbulent dispersion

An additional force which influences droplet trajectory as a result of droplet interaction with local eddies of continuous phase is brought into the calculations. This phenomenon is accounted for, by means of the eddy interaction model (EIM) which was also employed by (Gosman, & Ioannides, 1983; Crowe et al., 1996; Loth, 2000; Matida et al., 2000). In this method the droplet experiences an instantaneous fluid velocity component in each eddy, given by equation 6-34:

$$V = \bar{V} + V' \quad 6\text{-}34$$

Where $\bar{V}$ is the mean velocity calculated by RANS and V' is the fluctuating velocity component, unique to each droplet. This fluctuating component is sampled from a Gaussian distribution around the local time-average velocity with a variance which comes from eddy velocity timescale,V_e ,as expressed in equation 6-35:

$$V_e = \frac{l_t}{\tau_t}\sqrt{\frac{2}{3}} \quad 6\text{-}35$$

Where l_t and τ_t are turbulence length scale and turbulence time scale, respectively. The ratio of these two parameters for $k-\varepsilon$ turbulence model is $\sqrt{k}$ (Gosman, & Ioannides, 1983). Once the fluctuating component is generated, it is applied on the droplet over the duration of droplet interaction with the local eddy. This time is termed as eddy interaction time, τ_I, and is expressed as follows:

$$\tau_I = \min(\tau_e, \tau_c) \quad 6\text{-}36$$

Where τ_e is eddy life time and t_c is the duration over which the droplet crosses the eddy. The former is expressed using equation 6-37:

$$\tau_e = \frac{2\mu_t}{\rho V_e^2} \quad 6\text{-}37$$

In this relation μ_t is the turbulent viscosity calculated by equation 6-4. The crossing time of the droplet through the eddy is given by equation 6-38:

$$\tau_c = \begin{cases} \infty & \tau_M \leq \dfrac{l_e}{|V_{rel}|} \\ -\tau_M \ln\left(1 - \dfrac{l_e}{\tau_M |V_{rel}|}\right) & \tau_M > \dfrac{l_e}{|V_{rel}|} \end{cases} \quad 6\text{-}38$$

In this equation, $l_e = V_e \tau_e$ is the eddy length scale and τ_M is the momentum relaxation time scale, given by equation 6-39:

$$\tau_M = \frac{m_d}{0.5 C_D A_d |V_{rel}|} \quad 6\text{-}39$$

6.3.2.4 Two-way coupled calculations

During computation of droplet trajectories, the gains and/or losses of mass, momentum and heat by the droplets are tracked and accumulated, leading to contributions to a source/sink term of the continuous phase equations. This impact is taken into account using a two-way coupled calculation, as any given parcel π, traverses through a control volume. In the case of mass transfer from continuous phase to discrete phase the following equation is obtained:

$$S_m = -\frac{1}{\Delta t} \sum_{\pi} \sum_{\delta t_n} n_\pi \dot{m}_d \delta t_d \quad 6\text{-}40$$

In equation 6-40, $\dot{m}_d$ is the rate of mass transfer from a single particle to the continuous phase. Δt is the calculation time step and δt_d is the local time step of droplet. Eventually, n_π is the number of parcels per cell volume. Similarly, the transferred momentum from the continuous phase to discrete phase is worked out from equation 6-41:

$$S_M = -\frac{1}{\Delta t}\sum_{\pi}\sum_{\delta t_n} n_\pi (F_s + \dot{m}_d V_d)\delta t_d \qquad 6\text{-}41$$

In which F_s is defined by equation 6-22. Finally the total energy transferred to the discrete phase is:

$$S_E = -\frac{1}{\Delta t}\sum_{\pi}\sum_{\delta t_n} n_\pi \left[\bar{h}A_p(T_\infty - T_d) + F_s.V_d + \frac{1}{2}\dot{m}_d V_d^2 + \dot{m}_d h\right]\delta t_d \qquad 6\text{-}42$$

Where $\bar{h}$ is the heat transfer number and h is the droplet enthalpy.

6.4 Model setup and preparation

In this section the path of CFD simulation construct will be presented in details. This starts by defining the combined geometry of pMDI and USP-IP as well as geometry sub-division into computational control volumes (meshing). Subsequently we will specify the boundary conditions for continuous and discrete phase. This sub-section is significant as it includes the details of our novel PSS structure. Afterwards the material properties relevant to both phases are presented. Eventually the selection of appropriate solvers along with the solver parameters (for which the solution is optimally obtainable) is going to be described.

6.4.1 Computational domain

6.4.1.1 Geometry

The computational domain encompasses a standard Bespak pMDI actuator, connected to USP-IP inlet face. The geometries were constructed in Siemens NX v.8.5 CAD packages, as shown in Figure 6.3 (a-d).

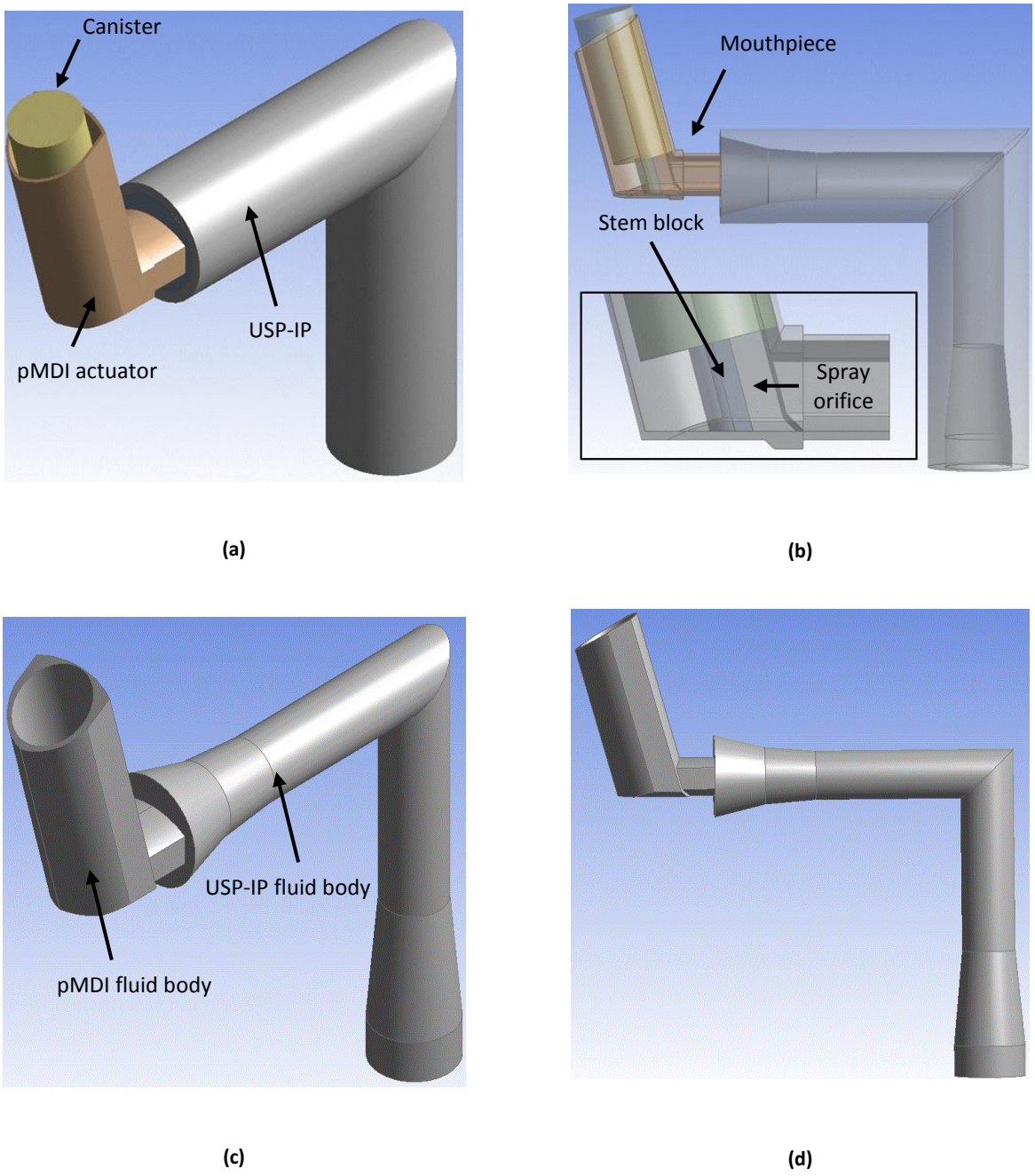

Figure 6.3 Combined geometry of pMDI actuator connected to USP-IP

The geometric complexities of metering valve ferrule and canister necking were approximated by a simple cylinders (see Figure 6.3 (b)) to avoid introducing small geometric scales which are difficult to mesh and may cause numerical instabilities. The flow is assumed to be adiabatic, so the computational domain is limited to the interior fluid body inside the pMDI and USP-IP space. The fluid contained regions are extracted and subsequently merged to form unified fluid continuum as shown in Figure 6.3 (c-d).

6.4.1.2 Mesh

The fluid continuum is subdivided into discretised computational elements using the STAR-CCM+ v.9.04.011 meshing application, as shown in Figure 6.4. As a result, approximately 1,400,000 hexahedral elements are generated. The choice of hexahedral element is supported by previous numerical studies (Longest and Vinchurkar, 2007; Roache, 1997), which show that this meshing strategy minimises numerical diffusion and enhances the convergence rate.

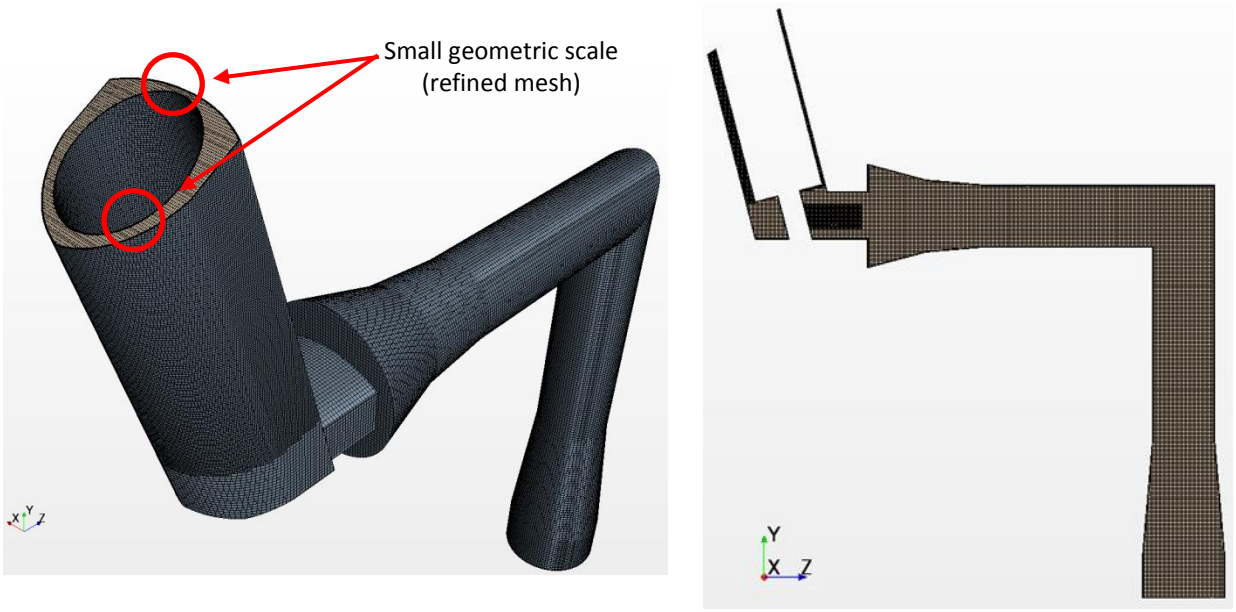

(a) bulk geometry **(b) mid-section plane**

Figure 6.4 Computational mesh rendered on different sections

The element base size is selected as 0.7 mm for the entire domain. The flow pathway becomes narrow in the air inlet region surrounding the canister, particularly at the front side of the canister. In order to adequately resolve the flow scales in this region the element size is further refined to 0.5 mm in this region to allow the narrowest passages (see red circles in Figure 6.4 (a)) to be covered by approximately 10 computational cells.

In order to resolve the spray structure specifically in near-orifice region, the grid resolution has to be at least in the order of spray orifice radius (Abraham, 1997). On the other hand the minimum practically grid resolution is restricted by numerical factors imposed by the Euler-Lagrange formulation. The framework assumes that the local volume fraction of the discrete phase must be sufficiently low around 5% (Sommerfeld, 1992). By decreasing the

near orifice mesh size, this assumption may be violated as a droplet parcel could occupy the entire cell and local void fraction reaches to 1. This eventually results in significant numerical instabilities as observed previously in (Abraham, 1997; Venkatraman & Abraham 1997; Aneja, & Abraham, 1998). The near-orifice grid size was systematically reduced up to the point where solution stability started to become problematic. Trial and error suggest the optimum value of 0.3 mm per element size (see Figure 6.5 (a-b)), which is close to the diameter of the spray orifice and, hence, satisfies the criterion of Abraham (1997). Over an axial distance of 20 mm from the spray orifice, the mesh is gradually coarsened to a base size of 0.7 mm (see Figure 6.5 (a-b)) to optimise the computational resources.

The near wall boundary layer is resolved using the "all y^+" wall treatment model. This enables us to avoid constructing an ultra-fine mesh to resolve the flow scales in boundary layer. Prismatic cells are used to capture flow details in near-wall region. The thickness of the prism layer approximated to be 0.5 mm for a desired y^+value of 5 maximum. This layer is divided into intermediate number of 6 sub-layers with growth factor of 1.5 to produce a smooth near-wall cell transition to the bulk mesh as shown in Figure 6.5 (c).

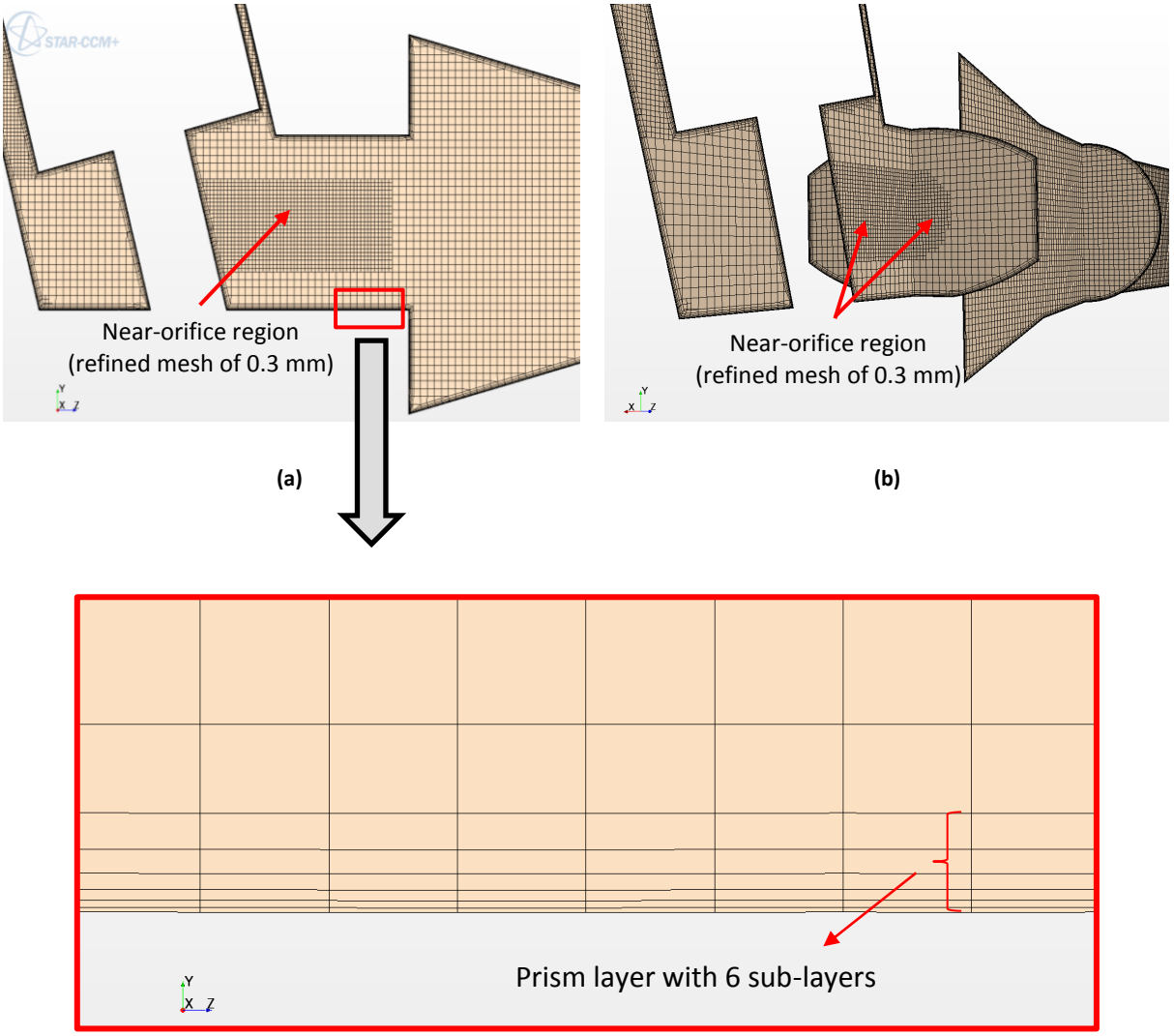

Figure 6.5 Regions of refined mesh: (a-b) near-orifice mesh, (c) near-wall mesh

6.4.2 Boundary conditions

6.4.2.1 Continuous phase

The locations and types of continuous phase boundary conditions are illustrated in Figure 6.6. The values of boundary parameters are summarised in Table 6.2.

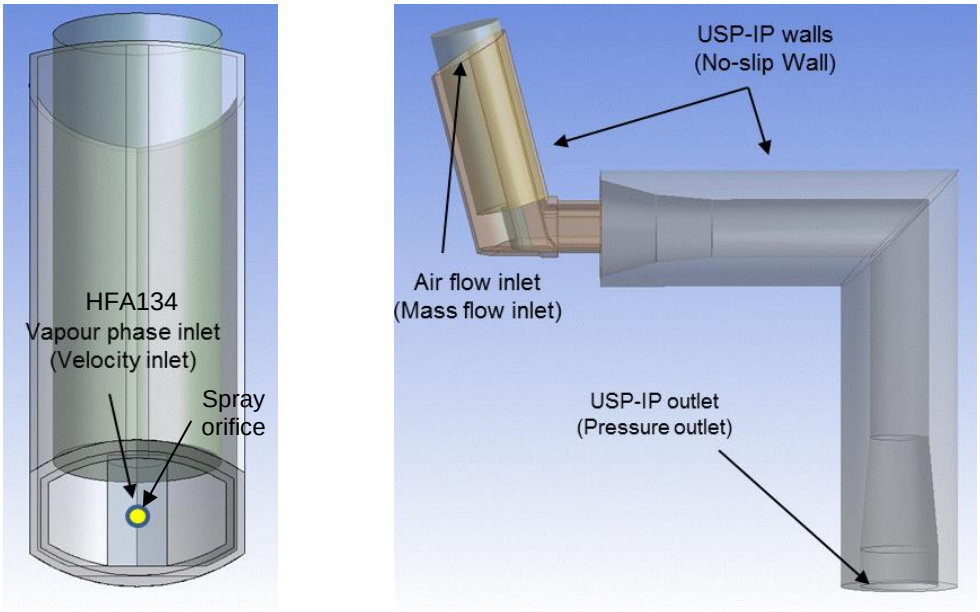

Figure 6.6 Locations and types of continuous phase boundary conditions

Region	Boundary Condition					
	Type (definition method)	Value	Thermal	Species	Turbulence	
					Intensity	Hydraulic diameter
Air flow Inlet	Mass flow inlet (steady)	30 l/min	295 K	Air	5 %	0.018 m
Vapour phase inlet	Velocity inlet (transient-IFM)	Fig 6.9 (b)	250.08 K	HFA134 (gas)	15 %	0.008 m
USP-IP outlet	Pressure outlet (steady)	101325 Pa	295 K	Air	1 %	0.01 m
USP-IP walls	Wall	No-slip	Adiabatic	Impermeable	N/A	N/A
Actuator + Canister Walls	Wall	No-slip	Adiabatic	Impermeable	N/A	N/A

Table 6.2 Types and values of continuous phase boundary conditions

As shown in Figure 6.6 (b), the gap around the canister is the region through which steady air enters into the domain. The corresponding surface is defined as “mass flow inlet” with volumetric flow rate of 30 l/min at 295 K . The outlet face of USP-IP where the suction is applied is defined as “pressure outlet” boundary type and the local flow condition is set to zero gauge pressure. A real difficulty is to reasonably estimate the turbulence parameters and species mass fraction for any possible reverse flow at the outlet. A realistic set of these parameters noticeably minimises the convergence difficulties. In the current study, all backflow-related parameters at the outlet were optimised based on trials to examine solution convergence behaviour.

The yellow circle on the front face of stem block, in Figure 6.6 (a) represents the spray orifice. This region acts as inlet to the computational domain for spray vapour phase (HFA134) and is defined as “velocity inlet”. As described in section 6.2.2, the corresponding velocity boundary values are determined by internal flow model calculations and are updated for current time step, by means of a JAVA script (see Figure 6.9 (c) for velocity values).

The choice of hydraulic diameter (to determine turbulence parameters at boundaries), was made based on the boundary hydraulic diameter. The values of turbulence intensities at each boundary were determined based on (i) crude estimations of possible turbulence level at each region as well as (ii) sets of trial and error for which no numerical instabilities of the solution residuals occurred. Finally, all the walls of the actuator and USP-IP fluid body are set to adiabatic walls with no-slip boundary condition.

6.4.2.2 Discrete phase

6.4.2.2.1 Actuator characteristics

Spray source parameters (e.g. velocity, mass flow rate and droplet size) are linked with the geometric properties of the pMDI actuator as well as utilised formulation. Different combination of actuator characteristics will lead to change in source parameters and event duration. Here we use the actuator characteristics which are summarised in Table 6.3.

Parameter	Value	Parameter	Value
Vol_{mc}	25 µl	D_{vo}	0.7 mm
Vol_{ec}	25 µl	D_{so}	0.3 mm
$C_{d,vo}$	0.6	$C_{d,so}$	0.7
T_{amb}	295 K	Y_E	10 %

Table 6.3 Modelling parameters of the actuator used for PSS construction

6.4.2.2.2 Spray source

Details of the boundary conditions for the point injectors of the PSS are summarised in Table 6.4. Each injector carries a discrete phase mass flow rate, up to 10 µg/s and the number of injectors is determined by the liquid mass flow rate. The selected sample mass flow rate of 10 µg/s per injector, was based on trials with the aim of arriving at a computationally efficient injector number, while spreading the source mass as widely as possible within the truncated cone space of the PSS (see Figure 6.7).

The velocity, composition and temperature of the droplets are identical for all injectors at particular time instant. Since the droplets are at thermodynamic equilibrium, the latter is equal to the saturation temperature of HFA134/ethanol mixture (90:10 w/w%) at atmospheric pressure (101.3 kPa). The velocity and composition boundary values are functions of time and are shown in Figure 6.9 (c) and (d), respectively.

Injector properties	Unit	Definition method	Range (min, max)	Comment
Total mass flow rate	(µg/s)	Internal flow model	(20, 500)	Transient-see Figure 6.9 (a)
Number of injectors	(-)	$\frac{\text{Liquid mass flow rate}}{\text{Sample mass flow rate}}$	(2, 50)	Transient-see Figure 6.9 (b)
Droplet velocity	(m/s)	Internal flow model	(47, 80)	Transient-see Figure 6.9 (c)
Droplet HFA134 mass fraction	(%)	Internal flow model	(86, 90)	Transient-see Figure 6.9 (d)
PSD	µ (µm)	Atomisation model (LISA)	(4, 5.5)	Transient-see Figure 6.9 (e)
	GSD (-)	ACI measurement	2.2	Constant
Cone angle	(deg)	High speed imaging (HSI) observation	(5, 25)	Transient-see appendix B
Droplet temperature	(K)	Internal flow model	250.2	Equilibrium condition

Table 6.4 Boundary conditions and properties of point injectors

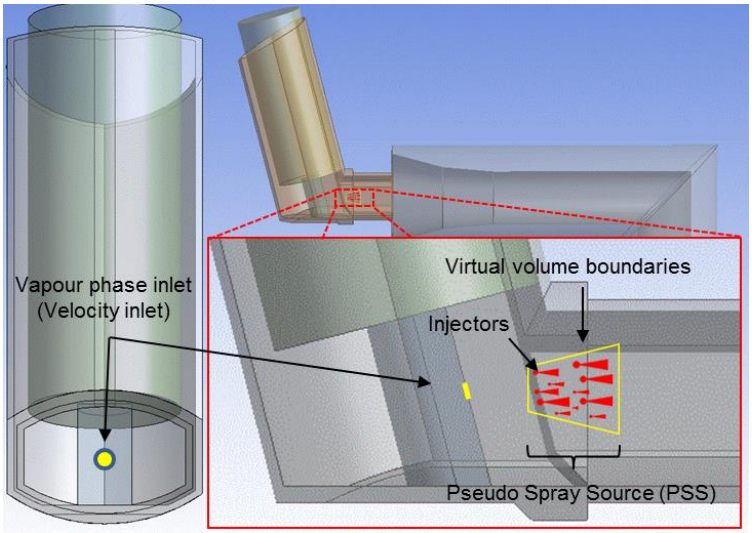

Figure 6.7 Location and conceptual image of discrete phase (PSS)

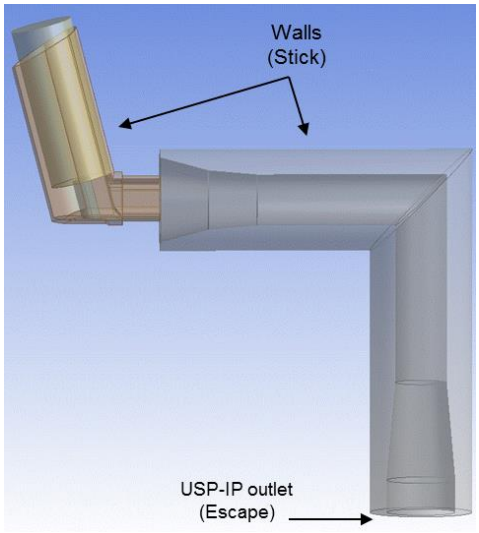

Figure 6.8 Location and type of wall boundary condition

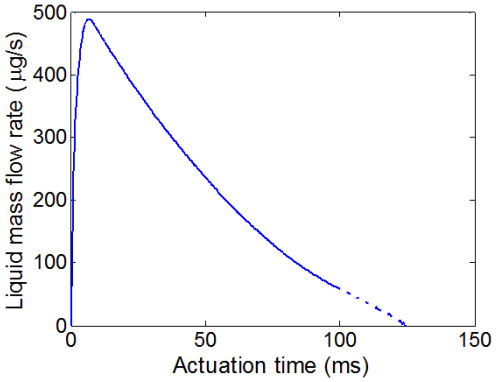

(a) Liquid mass flow rate

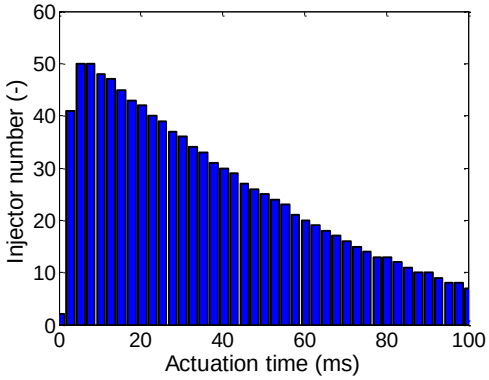

(b) Number of injectors

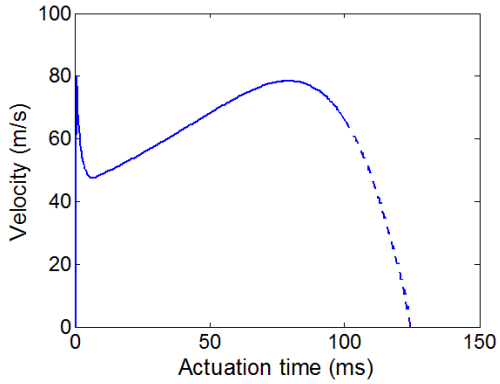

(c) Source velocity (droplet & HFA134 vapour)

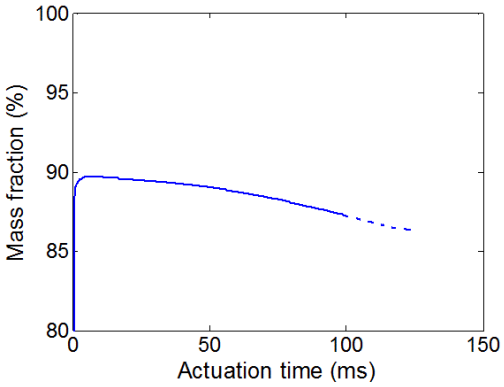

(d) Ethanol mass fraction

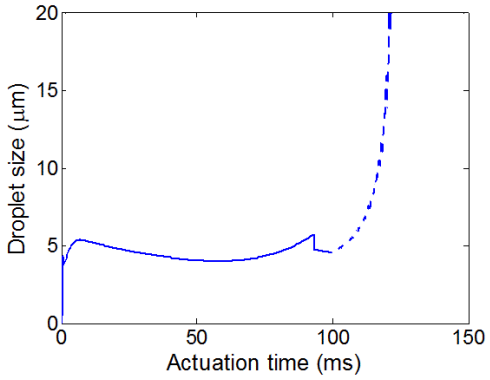

(e) Mean droplet size

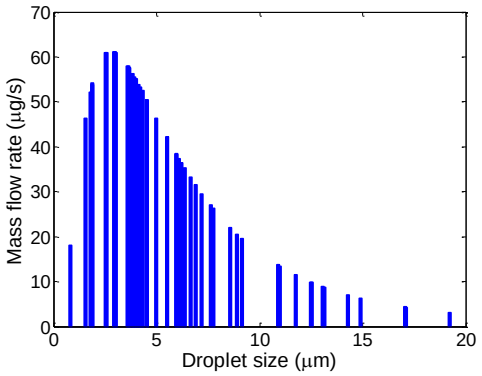

(f) Log-normally distributed mass flow rate over range of diameters

Figure 6.9 Time-dependent pseudo spray source properties

It was assumed that the particle size distribution of the PSS follows a log-normal relationship at each time instant. Thus, the temporal mass flow rate was distributed over an assumed range of 0-20 μm droplet size, using a log-normal relationship. The mean value (μm) of the log-normal function was assumed to be represented by the value produced by the LISA atomisation model calculation, for HFA134/ethanol multicomponent mixture (chapter 5), as shown in Figure 6.9 (e). The geometric standard deviation (GSD) of the distribution was taken as constant. There are currently no data that document the temporal behaviour of this parameter. A GSD value of 2.2 was selected based on ACI measurement for the formulation of interest (Meakin et al., 2000). The distribution is sampled randomly at each time instant of the actuation event. A typical result at 11^{th} ms into a simulated actuation event is shown in Figure 6.9 (f).

6.4.2.2.3 Droplet-wall interaction

Boundary conditions for the discrete phase are defined at walls of the computational domain and for the point injectors constructing the PSS. In order to account for droplets-wall interaction and to estimate particle deposition at the walls, “Stick” boundary was specified. This implies that if a droplet hits a wall its trajectory ends. Any residual evaporating species is flashed to its vapour phase. The outlet face of the USP-IP is defined as “escape” meaning droplets crossing this section will be removed from the calculation. The locations of these boundaries are indicated in Figure 6.8.

6.4.3 Material properties

6.4.3.1 Continuous phase

The material properties, method of definition and the corresponding value for each constituent are summarised in Table 6.5 and Table 6.6. It is worth mentioning that the effects of temperature variations on thermal conductivity are not applied as this quantity do not change appreciably over the temperature region of interest (250 K-295 K). Temperature dependency of dynamic viscosity is also neglected as turbulence viscosity dominates the field viscosity.

Air				
Properties	Unit	Definition	Source	Value
Dynamic viscosity	Pa.s	Constant	STAR-CCM+	1.7250×10^{-5}
Density	kg/m^3	Ideal Gas	N/A	N/A
Molecular weight	Kg/kmol	Constant	STAR-CCM+	28.9664
Specific heat	J/kg.K	Polynomial T	STAR-CCM+	$[9.0952\times10^{2}, 3.2687\times10^{-1}, -1.0270\times10^{-4}]$
Thermal conductivity	W/m.K	Constant	STAR-CCM+	0.0245

Table 6.5 Thermo-physical and transport properties of air

HFA134 vapour				
Properties	Unit	Definition	Source	Value
Dynamic viscosity	Pa.s	Constant	NIST	1.0801×10^{-5}
Density	kg/m^3	Ideal Gas	N/A	N/A
Molecular weight	Kg/kmol	Constant	NIST	102.03
Specific heat	J/kg.K	Polynomial T	NIST	$[3.719\times10^{-2}, -1.557\times10^{1}, 2.371\times10^{3}]$
Thermal conductivity	W/m.K	Constant	NIST	0.012
Diffusion coefficient in air	m^2/s	Linear T	(Finlay, 2001)	$[5.265307\times10^{-8}, -5.725645\times10^{-6}]$

Table 6.6 Thermo-physical and transport properties of HFA134 vapour phase

Hence, the specific heat is defined as a second order polynomial function of temperature. Polynomial coefficients are arranged in descending order, in the corresponding table cell. The rules used to compute weighted averages of thermos-physical properties for vapour multicomponent mixtures are summarised in Table 6.7.

Multicomponent vapour mixture		
Properties	Unit	Definition
Dynamic viscosity	Pa.s	Mass-weighted mixing rule
Molecular diffusivity	(-)	Schmidt Number (= 1.0 as default)
Molecular weight	Kg/kmol	Reciprocal mass-weighted mixing rule
Specific heat	J/kg.K	Mass-weighted mixing rule
Thermal conductivity	W/m.K	Mass-weighted mixing rule

Table 6.7 Thermo-physical and transport properties of multicomponent vapour mixture

6.4.3.2 Discrete phase

Thermo-physical and transport properties of the liquid droplet are summarised in Table 6.8 and Table 6.9. Here the effects of temperature dependency on liquid density are neglected. This is because the liquid phase behaves closely to an incompressible liquid where the variation in density as temperature changes is negligible.

The effect of temperature dependency is considered for liquid specific heat through the use of polynomial function. Mixture properties are defined using mass weighted mixing rules while the multicomponent droplet vapour pressure is represented using equation 5-1, as discussed in chapter 5.

HFA134 liquid				
Properties	Unit	Definition	Source	Value
Critical pressure	Pa	Constant	NIST	4059280
Critical temperature	K	Constant	NIST	374.21
Density	kg/m^3	Constant	NIST	1370
Molecular weight	Kg/kmol	Constant	NIST	102.03
Specific heat	J/kg.K	Polynomial T	NIST	$[2.2694\times10^{-2}, -1.182\times10^{-1}, 2.558\times10^{3}]$

Table 6.8 Thermo-physical properties of HFA134 liquid phase

Ethanol				
Properties	Unit	Definition	Source	Value
Density	kg/m^3	Constant	STAR-CCM+	784.88
Molecular weight	Kg/kmol	Constant	STAR-CCM+	46.0695
Specific heat	J/kg.K	Polynomial T	STAR-CCM+	$[2.676\times10^{3}, -9.451, 2.898\times10^{-2}]$

Table 6.9 Thermo-physical properties of ethanol liquid phase

Multicomponent liquid mixture		
Properties	Unit	Value
Saturated vapour pressure	Pa	Equation 5-1
Density	kg/m^3	Volume-weighted mixing rule
Molecular weight	Kg/kmol	Reciprocal mass-weighted mixing rule
Specific heat	J/kg.K	Mass-weighted mixing rule

Table 6.10 Thermo-physical properties of multicomponent liquid mixture

6.4.4 Solver selection and setting

The commercial CFD code STAR CCM+ V9.04.001 was used to discretise and solve the model equations. The code utilised Semi-Implicit Method for Pressure Linked Equations (SIMPLE) algorithm for pressure-velocity linkage.

Spray phase emergence is accompanied with large mass and momentum exchange with the continuous domain. This introduces high numerical instabilities to the solution, which complicates the path to a converged solution. In this case “best-practice” strategy is to solve flow fields sequentially. For the purpose of improving the convergence rate of a particulate flow problem, the flow field has to be stabilised primarily. Once the flow field is solved it is appropriate to introduce the droplets into the computations.

Table 6.11 summarises the solver parameters for steady air. It should be noted that all equation corresponding to steady air flow are second order accurate in space. The calculations were terminated when the normalised residuals of the equations fall below the values stated in Table 6.12.

Steady air phase			
Model	Solution parameter	Algorithm	Under-relaxation factor
Flow	Pressure	Segregated	0.3
	Velocity		0.7
Energy	Temperature	Segregated - fluid enthalpy	0.5
Turbulence	Turbulence kinetic energy (TKE)	Segregated	0.5
	Turbulence dissipation rate (TDR)		0.5

Table 6.11 Solver parameters of steady air modelling

Steady air phase			
Equation residual	Minimum limit	Equation residual	Minimum limit
Continuity	10^{-3}	X-momentum	10^{-4}
Energy	10^{-4}	Y-momentum	10^{-4}
TKE	10^{-5}	Z-momentum	10^{-4}
TDR	10^{-5}	Species	10^{-4}

Table 6.12 Values of air simulation convergence criteria

Unsteady spray phase			
Model	Solution parameter	Algorithm	Under relaxation factor
Lagrangian multiphase	Particle trajectory	Two-way coupled	0.1
Flow	Pressure	Segregated	0.3
	Velocity		0.5
Energy	Temperature	Segregated - fluid enthalpy	0.3
Species	Local concentration	Segregated	0.5
Turbulence	Turbulence kinetic energy (TKE)	Segregated	0.5
	Turbulence dissipation rate (TDR)		0.5

Table 6.13 Solver parameters of unsteady spray modelling

Table 6.13 shows the solver parameters for the Lagrangian particle tracking model. It should be noted that at this stage equations are discretised both spatially and temporarily. For the unsteady portion of the simulation, discretised equations are second order accurate in time and space. It should be noted that in comparison with steady air modelling, here the CFD model is significantly more under-relaxed. This is necessary to eliminate the potential of numerical instabilities after spray injection.

Under-relaxation values were determined based on trials for which convergence rate was optimised in conjunction with the time step size. The number of iterations per time step was typically around 150. The simulation time step was selected based on discretising the fastest change occurring in source velocity, by 10 time steps. According to Figure 6.9 (c), such rapid change happens during initial transient and it has a time scale around 0.5 ms. Therefore the simulation time step was selected as 50 µs. The number of time steps for a typical actuation of 0.1 sec will be 2000 and around 8000 time steps are needed for droplets to fully exit the USP-IP.

6.5 Results and Discussion

6.5.1 Steady air flow

Distribution of steady air flow is shown in Figure 6.10 and Figure 6.11 in terms of contours of velocity magnitude and flow streamlines. The velocity field is rendered on the symmetry plane of the actuator and USP-IP as well as six arbitrarily selected planes perpendicular to the mean flow path, to comprehensively illustrate the spatial flow distribution. The velocity contours in Figure 6.10 suggest that air flow enters the geometry with mean velocity of around 2.5 m/s. The flow travels through the gaps around the canister up to the region around the stem block where the flow direction sharply changes. Here the flow appears to be skewed towards the bottom surface of the mouthpiece. Next the air appears to move sideways around the stem block as well as upwards, leading to formation of a complex three dimensional flow motion. Such motion can be more easily understood by visualisation of flow streamlines in this region as shown in Figure 6.11 (a). The rapid change in the direction of the flow results in the reduction of flow cross sectional passage, accelerating the flow to around 3.5 m/s at the mouthpiece exit plane.

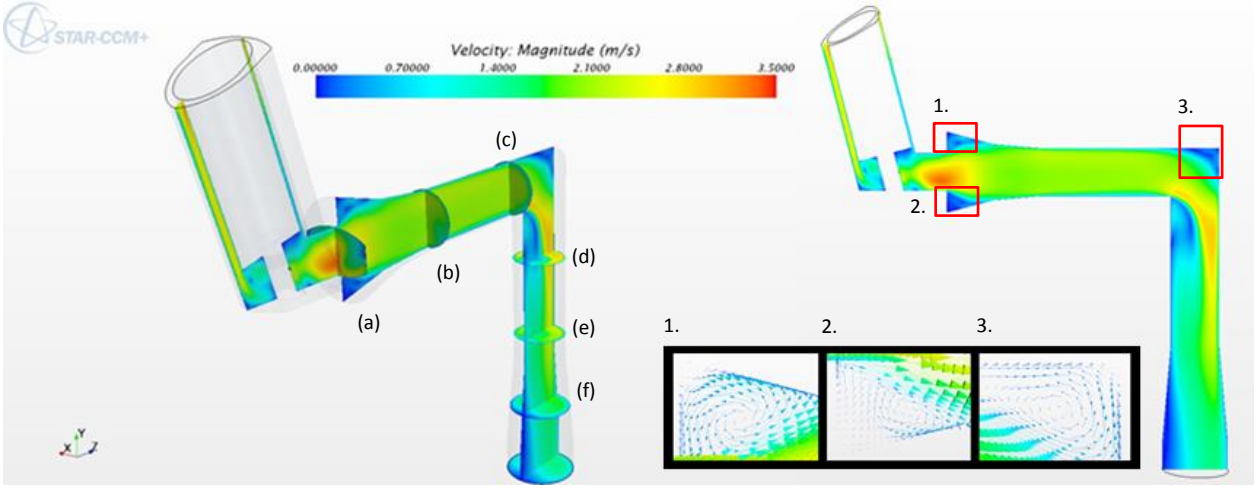

Figure 6.10 Contours of steady air velocity magnitude rendered on mid-section plane

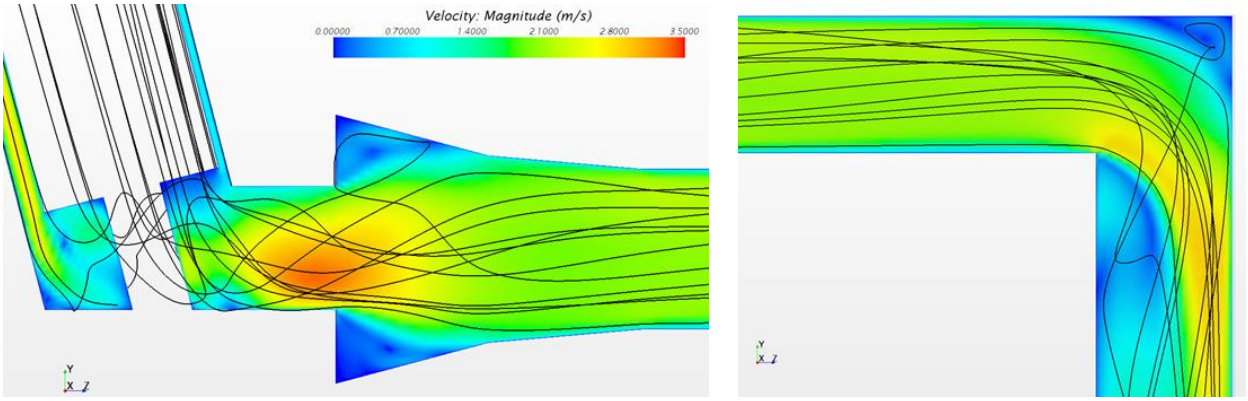

(a) Near-orifice region **(b) 90° bend**

Figure 6.11 Contours of velocity magnitude and streamlines of steady flow in USP-IP

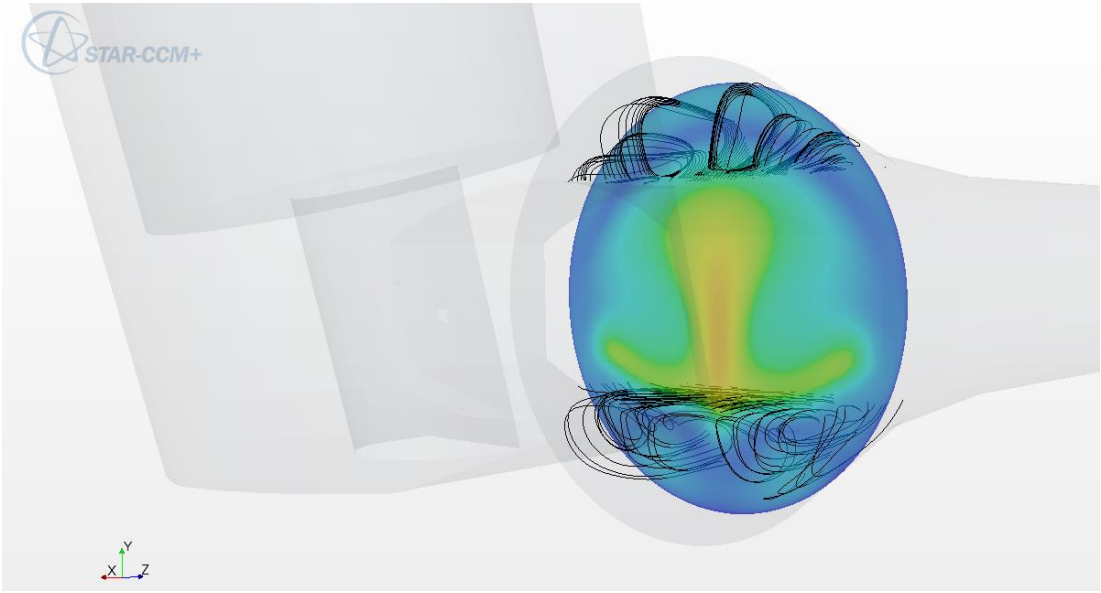

Figure 6.12 Contours of velocity magnitude and outer streamlines of steady flow in USP-IP

Subsequently, the flow enters into the converging section of the USP-IP, where the flow encounters a larger cross-sectional area. This enlargement leads to formation of one toroidal (doughnut shaped) flow structure whose recirculation zone is visible at the top and bottom corners of the USP-IP converged section. This flow pattern is also shown in the form of velocity vector plots in the insets no. 1 and 2 of Figure 6.10. This flow topology in the corners of the USP-IP inlet is three-dimensional and may be better visualised by flow

streamlines in the vicinity of a plane along the central axis of the USP-IP, perpendicular to the one seen in Figure 6.11. Such visualisation is shown in Figure 6.12. It should be noted that for the sake of clarity in visibility, flow streamlines inside the core of the USP-IP are concealed and only the ones at the top and bottom corner of the inlet are visualised. Figure clearly shows flow recirculation adjacent to the walls of USP-IP.

As the flow travels further in the axial direction, flow reattachment occurs and the velocity profile becomes more developed. After the flow reaches the end of USP-IP horizontal section, another rapid change of flow direction occurs, which skews the flow towards the rear wall of the vertical section of the USP-IP. This flow pattern can be seen using flow streamlines, shown in Figure 6.11 (b). Here the flow velocity increases to approximately 3 m/s due to flow separation. This prediction compares favourably with the value of 3.1 m/s from the PIV measurements of Gjellerup and Frederiksen (2007). The flow profile near the top right hand corner of the 90° bend shows an additional recirculation zone. This region is illustrated in more detail using velocity vectors in inset no. 3 in Figure 6.10. The recirculation zone appears to be stretched (almost 1/2 USP-IP inlet diameter in length) along the outer vertical wall which is then reattaches to the main flow stream. The general flow pattern as well as the details of this region of recirculation in a circular duct with a sharp 90° bend was also reported in the work of (Lee et al., 2001; Mossad et al., 2009). Furthermore our predictions shows very good match with the PIV measurement and numerical modelling of Gjellerup and Frederiksen (2007).

The skewed flow profiles near the bottom of the mouthpiece as well as around the outer wall of the USP-IP vertical section region cause the creation of pairs of vortices. As shown in Figure 6.13, these secondary motions can be best visualised in a series of cross-sectional planes perpendicular to the main flow path named alphabetically. The velocity magnitude is indicated by colour coding and velocity vectors illustrate secondary flow motion.

Figure 6.13 (a) shows the air flow profile at the exit of the pMDI mouthpiece just before it enters the USP-IP. The vectors clearly illustrate the pair of vortices with flow moving upwards through the centre of the flow and downwards along the side walls of mouthpiece.

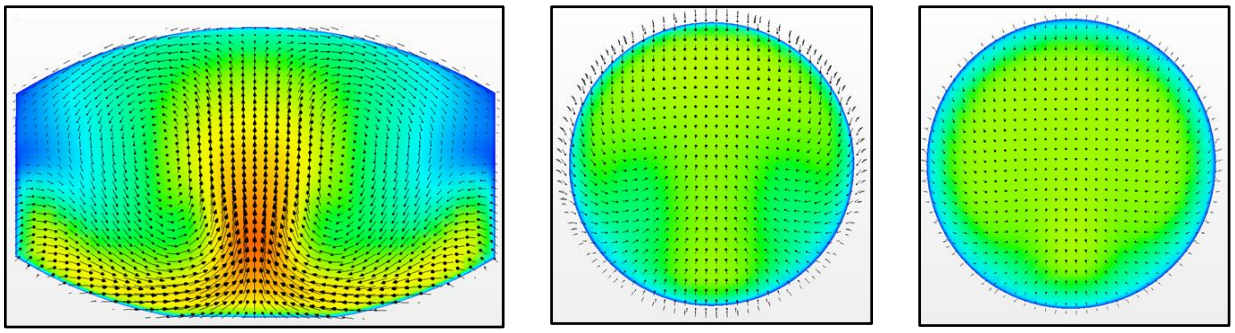

(a) (b) (c)

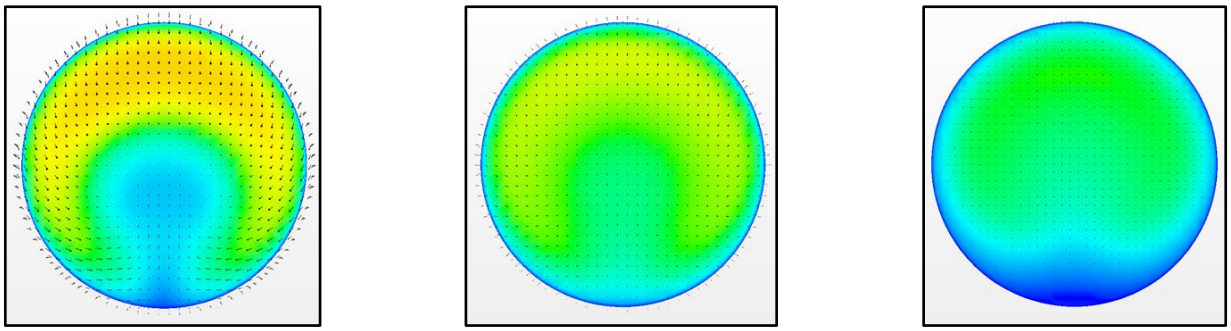

(d) (e) (f)

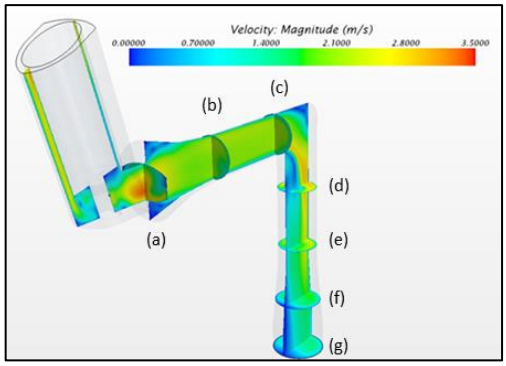

Figure 6.13 Contours of steady air velocity magnitude and streamlines rendered on mid-section planes as well as multiple section plane across flow path

The flow in this region is initiated by the bias of the flow in the annulus between the canister and the actuator walls. The second plane (b) which is situated approximately 4 cm away from plane (a), illustrates the decay of the secondary motions; the average flow direction becomes more aligned with the horizontal axis.

Plane (c) is situated just upstream from the 90^{o} turn. It can be seen that the secondary flow motion has almost completely decayed at this stage. At section plane (d), just below the

sharp 90^{o} bend, flow is skewed towards the wall where strong outward flow is induced by the centrifugal force. In this region, the flow moves from the rear wall to the inner wall of the bend through the core of the flow and returns along the walls of USP-IP leading to formation of the counter-rotating vortices as secondary motion. In the subsequent planes (e) and (f), the arrows are mostly appeared as dots illustrating their downwards orientation. This means that as the flow is getting closer to the outlet of the USP-IP, the secondary motion has decayed and the bulk of the fluid moves vertically downwards. The findings of the current CFD model confirm the previous findings of (Gjellerup, & Frederiksen, 2007; Worth Longest et al., 2007) in terms of flow pattern and velocity magnitude.

6.5.2 Spray phase

6.5.2.1 Plume structure

Temporal evolution of plume location is shown in the time-ordered images of Figure 6.14 where the results correspond to mean-flow-tracking simulation (i.e. no turbulent dispersion of particles). In Figure 6.14 droplets are coloured based on their magnitudes of velocity. The left column exhibits the side view of the plume spatial distribution in which droplets are superimposed on the contour of gas phase velocity, rendered on the symmetry plane of the pMDI actuator and the USP-IP. The right column shows the top view of plume spatial distribution where droplets are superimposed on gas phase velocity rendered on a perpendicular axial plane. Time instant of each snapshot is printed on the image, correspondingly.

Early stages of plume spatial development includes the formation of a shield-like particle embedded configuration at 0.01 s after the actuation. This flow structure appears at the plume tip and is indicated by means of red arrows in Figure 6.14 (a-b). This is due to the plume front edge experiencing most drag force; the droplets at the front are pushed away by the more energetic droplets emerging from the upstream source. This flow pattern have also been observed in the works of (Lee, & Park, 2002; Wu et al., 2006; Kostas et al., 2009).

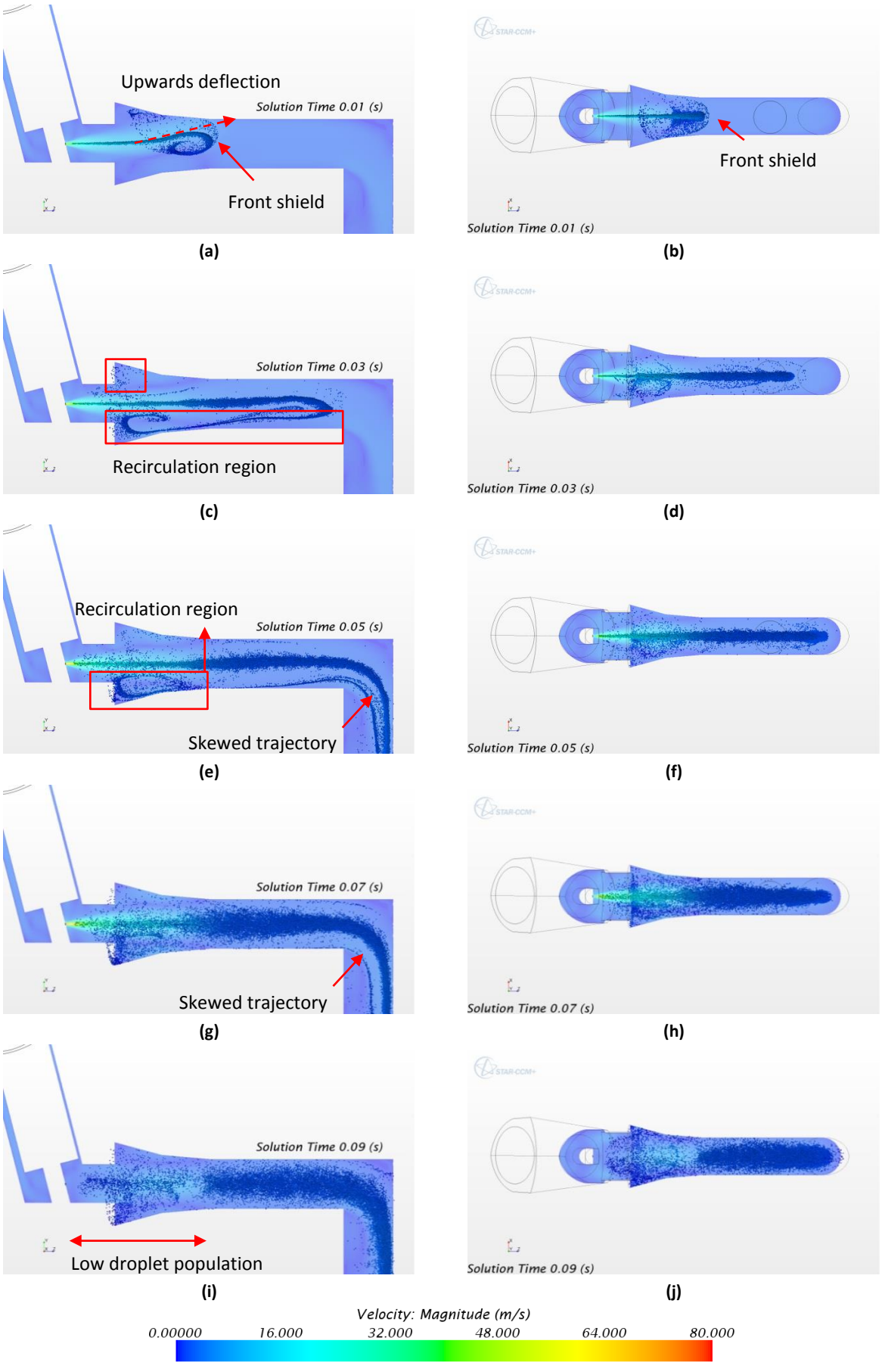

Figure 6.14 Temporal evolution of plume location coloured by droplet velocity magnitude

During the first 0.01 s plume direction appears to be diverted upwards (see Figure 6.14 (a)) where deflection is indicated by red arrow with dashed tail). This is due to influence of air flow mean direction on droplet trajectory. At the initial stages of actuation when the mass loading of the droplets is still small, the spray flow pattern is dictated by the air flow. The results in Figure 6.14 (c) illustrates that this upward plume diversion does not last so long and from 0.03 s onwards, injection axis follows a horizontal line. Now the mass loading of the droplets has become more significant. Consequently, considerable momentum transference occurs from the droplets to the air flow which eventually leads to alignment of air flow streams with the plume nominal injection axis.

Emergence of a fast-moving, high density plume into a comparatively slow moving and low density air flow stream results in the formation of multiple strong recirculation zones. Such regions which can be clearly seen in Figure 6.14 (c) at 0.03 s, and Figure 6.14 (e) at 0.05 s (signified with red rectangle), are generated as a consequence of air entrainment at the plume edges. At 0.03 s the recirculation zone at the bottom of the plume, seems to stretch about 2.5 USP-IP inlet diameters up to the end of USP horizontal section. The droplets at the plume tip are carried by this recirculation zone and travel backwards to the USP-IP inlet forming a swirling string of particles. Identification of such regions is of great importance as they are potential regions to trap small particles and/or disturb their trajectories to impact on neighbouring boundaries. In general, the formation of such regions may contribute to increase the amount of deposition and reduce the overall fine particle fraction. At 0.03 s the plume tip almost reaches the entrance of 90° bend and is inclined to change its direction downwards.

Temporal plume pattern is relatively similar at 0.05 and 0.07 s. At these time points plume has progressed further down the vertical section of the USP-IP. The injection cone angle has become wider at this stage and the population of droplets in the domain has significantly increases. At 0.05 s (Figure 6.14 (e)) it appears that the droplets which were previously swirling in the bottom recirculation zone (bottom rectangle in Figure 6.14 (c)) are now gradually escaping out of this region and travel through the USP-IP vertical section. This is due to gradual disappearance of recirculation regions as the spray source mass flow rate decreases. It can be seen that after 0.07 s the recirculation region has almost vanished and all of the particles in the horizontal section of the USP-IP travel along the mean flow path.

As the droplets travel through the vertical section, the majority of them are pushed towards the outer wall (indicated by arrows in Figure 6.14 (e) and Figure 6.14 (g)). This is due to high inertia of the droplets, as well as the continuous phase forcing the flow outwards through the 90° bend. It is previously observed in Figure 6.11 that the air flow exhibited a skewed pattern towards outer wall. This flow pattern amplifies the bias of the droplet motion towards the outer wall where high droplet deposition is likely.

At 0.09 s (Figure 6.14 (i)) the injection terminates and no more droplets are introduced into the domain. From this point in time onwards, droplet motion is governed by the air flow stream in the entire domain. A region of reduced droplet number concentration can be observed over about 2 USP-IP inlet diameters from the spray orifice, indicating that the plume is being replaced by air in this region and the remainder of the aerosol is advancing towards the vertical section of the USP-IP.

6.5.2.2 Plume velocity

In what follows, the spatial evolution of plume velocity predictions in terms of axial (centreline) and radial velocity distributions, are presented. To assess the validity of CFD practice, model predictions are compared against PDA measurements obtained from the parallel experimentally-based project. The process of data averaging and basis of comparison are also delivered

6.5.2.2.1 Predicted and measured velocity comparison

6.5.2.2.1.1 Method of averaging

The CFD and PDA data corresponds to axial droplet velocities which are averaged over the entire actuation duration (event averaged), at specific axial and radial locations. In the case of centreline velocity comparison, the axial locations are placed at 5, 10, 15, 20, 25, 35, 45, 55 and 75 mm downstream from the spray orifice, along plume nominal axis. These arrangements are shown in Figure 6.15 (a) schematically. PDA data corresponds to average point measurement where the CFD data corresponds to averaged velocity of droplet, passing through a series of tiny cylindrical control volumes, with diameter and height of 0.5 mm. These dimensions are chosen so that reasonably large number of droplets can be presented in a region of space and therefore statistically meaningful averaging can be

performed on CFD data. The average velocity at each axial measurement location is calculated using simple arithmetic averaging expressed by equation 6-43:

$$\bar{V}_{cl} = \frac{\sum_{i=1}^{n} n_i V_i}{\sum_{i=1}^{n} n_i} \qquad 6\text{-}43$$

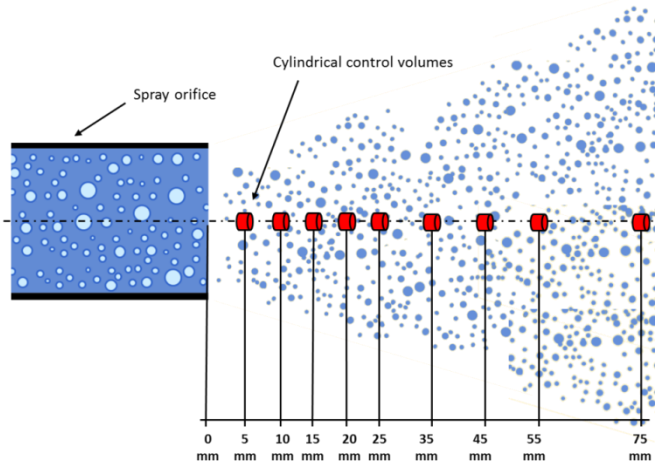

(a) Axial measurement locations arrangement

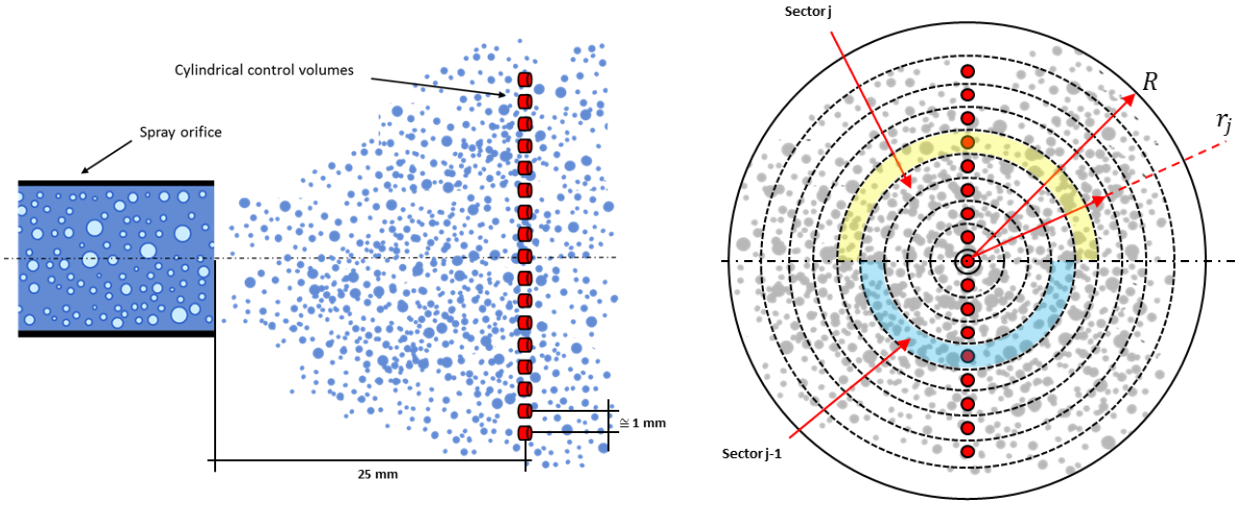

(b.1) Side view **(b.2) Front view**

(b) Radial measurement locations arrangement

Figure 6.15 Schematic of axial and radial measurement locations, along and across the plume

Where subscript cl denotes the centreline. n_i is the number of droplets in each axial location and V_i is individual droplet axial velocity. In the case of radial comparison, 17 equidistant radial measurement locations are placed across the plume. These points are positioned at 25 mm away from spray orifice with approximately 1 mm away from each other as shown in Figure 6.15 (b.1). PDA data is area-weighted to provide approximate representation of planar velocity distribution, using equation 6-44:

$$\bar{V}_r = \frac{\sum_{j=1}^{j_{max}} (2\pi r_j) \Delta r_j \sum_{i=1}^{n} n_{i,j} V_{i,j}}{\pi R^2 \sum_{i=1}^{n} n_{i,j}} \qquad 6\text{-}44$$

In this equation $n_{i,j}$ represents the number of droplets, i, within the measurement point of j. r_j is the radius of the measurement point to the plume centre and R is the absolute spray radius (see Figure 6.15 (b.2) for clarity). For the case of CFD the average velocity corresponds to arithmetic average velocity of droplets presented within the sector j. This region of space is highlighted in Figure 6.15 (b.2) (i.e. no area weighting).

6.5.2.2.1.2 Comparison against PDA

The numerical visualisation of the spray plume in Figure 6.14 illustrates that droplets start their motion with high velocity. The velocity of the droplets rapidly decays by almost 50% over the initial 20 mm of droplet travel. This distance corresponds to the length of the mouthpiece. Such decay is the result of rapid momentum exchange between the droplets and the entrained air. As a result of this interaction, air flow accelerates in the regions close to the spray orifice.

Care must be taken while interpreting the comparison outcome as the PDA results are for a pMDI plume injected into free and stagnant air. On the other hand, in the CFD spray droplets are injected into a confined space (USP-IP geometry) with finite co-flow of air. Thus the flow-surrounding interaction is expected to be different due to (i) different amount of available air for entrainment and (ii) rapid orientation in flow path imposed by USP-IP. However, close to the spray orifice, the effects of the constraining boundaries will be least, so a comparison may still yield useful indications.

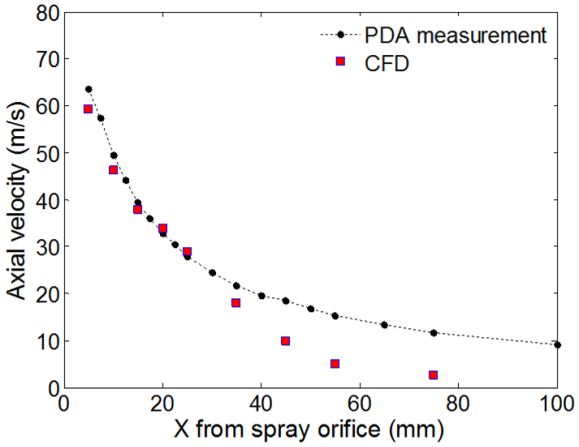

Figure 6.16 Comparison of predicted event-averaged centreline velocities injected into USP-IP, and measured event-averaged centreline velocity injected into free air

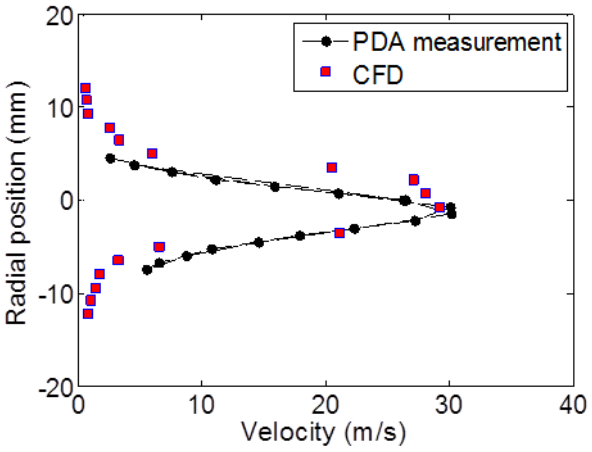

Figure 6.17 Comparison of predicted event-averaged radial velocities injected into USP-IP, and measured event-averaged radial velocity injected into free air, at 25 mm

Figure 6.16 shows the comparison of CFD and PDA plume centreline velocity. At distances up to 25 mm, the predicted centreline velocity agrees well with the ones measured using PDA technique. Further from the spray orifice, the predicted velocity is underestimated and the difference between the predicted and PDA values progressively increases with distance. Close to the spray orifice, the spray source momentum is large enough to dominate the flow pattern and the rate of velocity decay follows the measured values corresponding to injection into free air. After 25 mm, the differences between the axial velocity profiles may be due to the presence of confining solid boundaries in CFD simulation which can alter flow pattern in a significant way (Hill, P. G., 1965). In the case of confined jet, additional air entrainment further downstream results in generation of locally low pressure regions around the plume, which in turn draws the plume vertically, towards the solid walls of the confinement. This will subsequently reduce the stream wise momentum of the jet further, and results in plume to slow down with greater rate compared with the free air injection. Such behaviour is also reported by (Liu et al., 1997) and (Rajaratnam & Humphries, 1984), who observed that axial mean velocity of confined circular turbulent jet, decelerates with greater rates, compare to those of the free jet.

Figure 6.17 shows the predicted and measured radial distribution of plume velocity at 25 mm away from spray source. Figure 6.17 indicates that spatial velocity trend and magnitude are reasonably in line with the measured data, which follow a Gaussian profile. Such profile is a well-known feature of the jet which is captured by CFD. Both data sets

specify that droplet velocity reduces significantly from the core to the edges of the plume due to air entrainment and momentum transfer between the high speed spray plume and the surrounding air at the plume edges. This spatial velocity distribution can be also qualitatively confirmed by observing Figure 6.14 in which droplets around the plume periphery appear to have much less velocity than the ones placed in the plume core.

6.5.2.3 Plume droplet size

In this section the spatial and temporal evolution of plume droplet size are presented. To provide quantitative assessment of the CFD model, the predicted droplet size is also compared against PDA measurement. The comparisons are made on the basis of axial (centreline) variations in droplet size as well as presenting particle size distribution at particular region in space.

6.5.2.3.1 Droplet size spatial evolution in USP-IP

The distribution of plume droplet size in horizontal section of USP-IP is visualised at four selected time instants as shown in Figure 6.18 (a-d). The predictions suggest that as the plume travels further away from the source, droplet diameter reduces. However due to time-dependent changes of the maximum droplet size as well as obscuration of core droplets by outer ones, the trend is not easy to grasp from Figure 6.18.

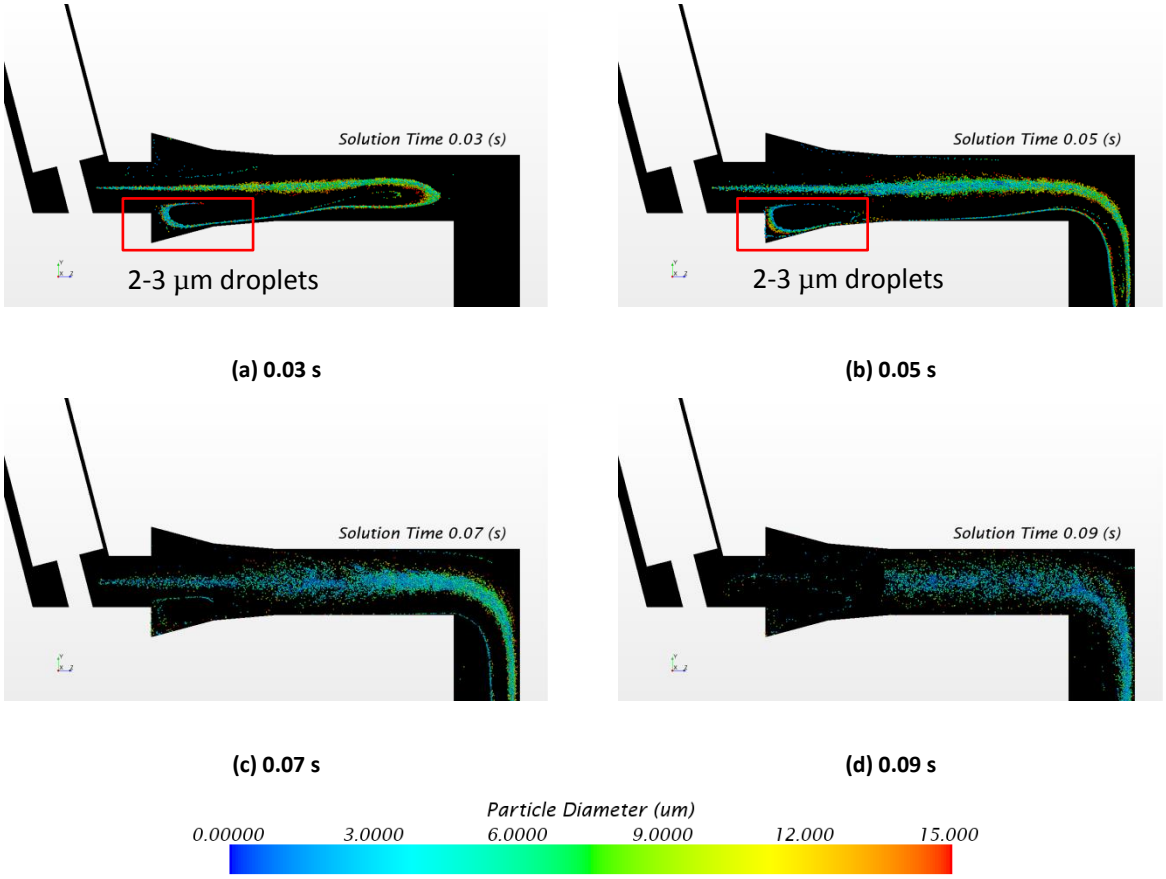

(a) 0.03 s **(b) 0.05 s**

(c) 0.07 s **(d) 0.09 s**

Figure 6.18 Temporal evolution of plume location, coloured by droplet diameter

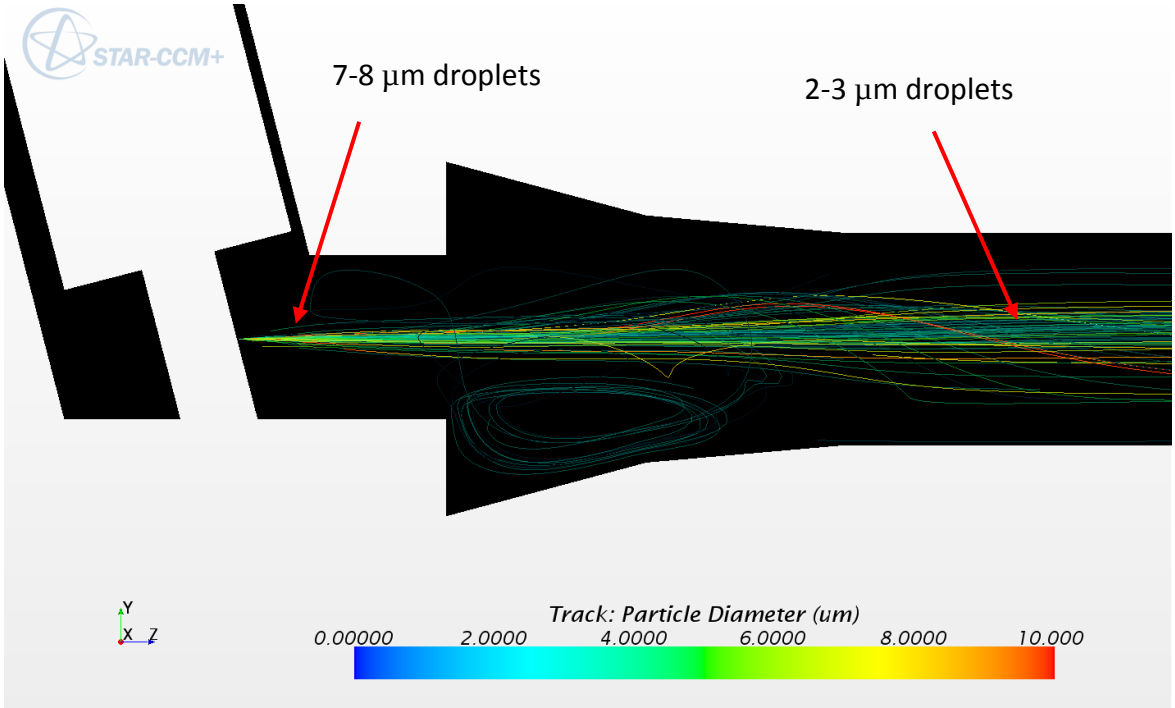

Figure 6.19 Droplet trajectory colour coded by droplet diameter in near-orifice region

The axial size change can be more clearly visualised in regions close to spray source, using droplet tracks that are colour coded by droplet diameter as shown in Figure 6.19. It can be seen that there is a general shift in streamlines colour from yellow/green to blue. This means that within 50 mm from the spray orifice the droplet diameter reduces to 2-3 μm from 7-8 μm.

Droplet size change is caused by rapid evaporation of HFA134 content. The droplets are emitted from the source at saturation temperature at ambient condition (i.e. 250 K), so initially they are in equilibrium with their surroundings. Once the droplets are introduced into the high temperature air field of 295 K, further evaporation takes place due to heat transfer between droplets and air. Initially this evaporation will be rapid, since the saturated vapour pressure of the HFA/ethanol mixtures is almost unaffected by presence of ethanol up to 0.4 mass fraction (see section 5.2.2). As heat is supplied to the droplets they continue to reduce in size. The droplets that are trapped in recirculation zones (see red rectangles in Figure 6.14) have longer residence time, so they can evaporate more. It should be noted that evaporation continues until all HFA134 content depletes and only ethanol remains as droplet material.

From that point onwards, as ethanol is treated as non-evaporating species, only heat transfer takes place until droplets arrive at thermal equilibrium with the mixture of co-flowing air and HFA143 vapour. Evaporation of HFA134 content results in multicomponent droplet to be enriched in ethanol. Temporal and spatial evolution of the ethanol mass fraction of the droplet plume is visualised in Figure 6.20. It can be seen that, within a relatively short distance of 30 - 50 mm, the ethanol fraction reaches to values of 0.8 - 0.9. This can be also taken as complementary indication of axial droplet size change. It is also evident that all HFA134 content of droplets collected in recirculation zone is evaporated and ethanol fraction is very close to 1.

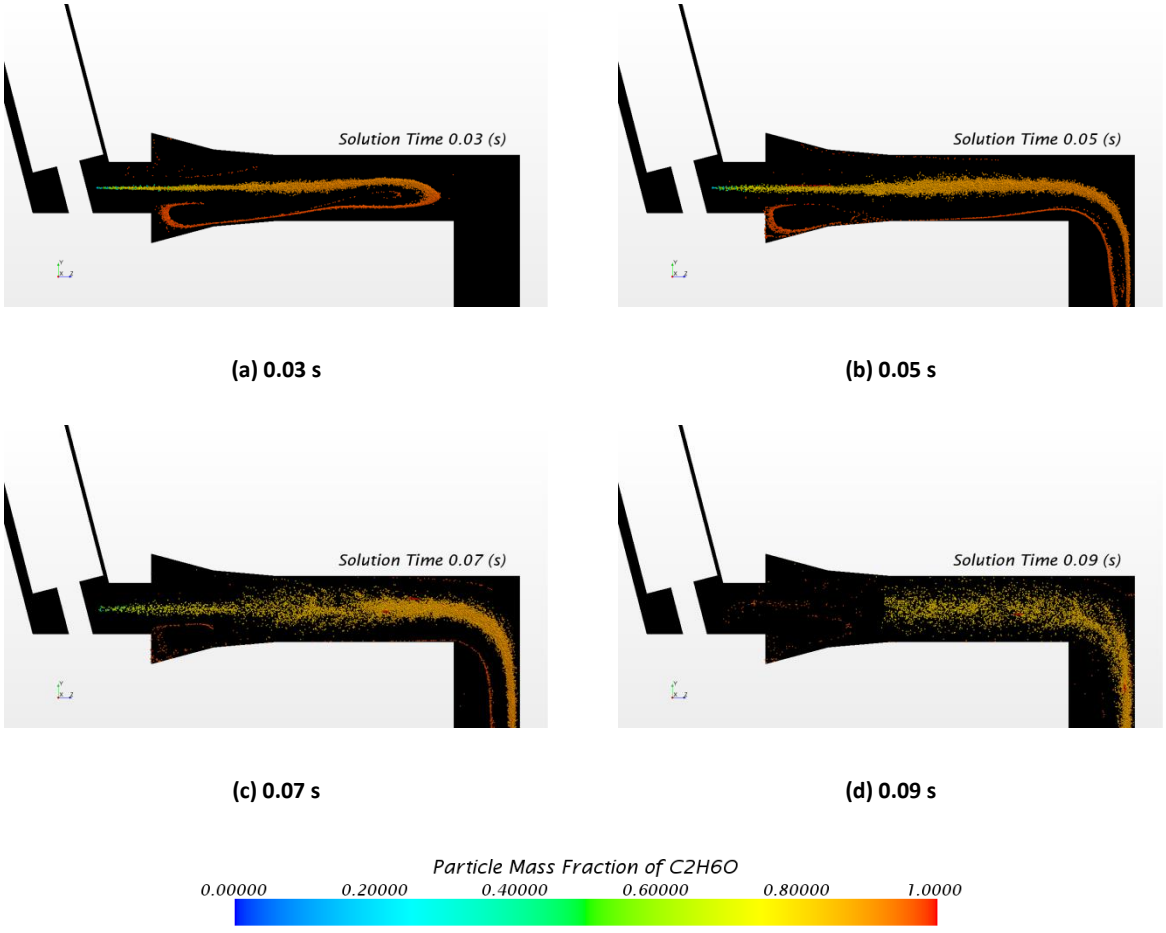

(a) 0.03 s **(b) 0.05 s**

(c) 0.07 s **(d) 0.09 s**

Figure 6.20 Temporal evolution of plume location, coloured by ethanol mass fraction in droplet

6.5.2.3.2 Predicted and measured droplet size comparison

6.5.2.3.2.1 Method of averaging

In the case of centreline droplet size, droplet diameters are event averaged at axial locations shown in Figure 6.15 (a). Droplets are represented using mean diameters of D_{10} and D_{32} (equation 4-29 (a-b)).

In the case of size distribution comparison, predicted and measured droplet size data at radial locations, are used to construct frequency and mass cumulative distribution curves (see Figure 6.15 (b) for radial location arrangements). PDA data is area-weighted to provide approximate representation of planar size distribution using equation 6-45:

$$\chi = \frac{\sum_{j=1}^{j_{max}} (2\pi r_j) \Delta r_j N_{i,j}}{\pi R^2} \qquad 6\text{-}45$$

Where χ is the area average coefficient and $N_{i,j}$ is the number of droplets within a diameter bin range of of d_i and d_{i+1}. CFD data on the other hand corresponds to droplets presented within the sector j, within a diameter bin range of d_i and d_{i+1}.

6.5.2.3.2.2 Comparison against PDA

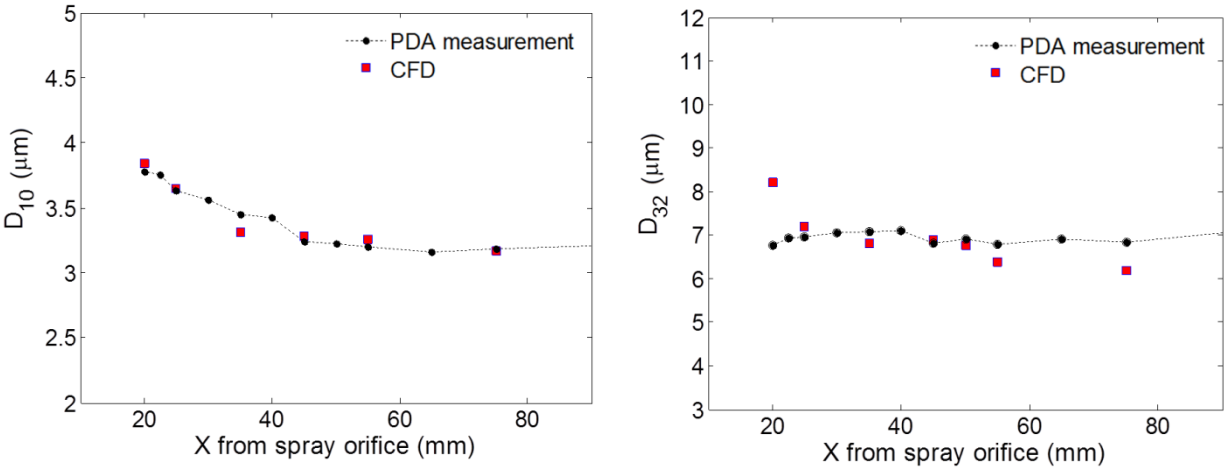

(a) D_{10} **(b) D_{32}**

Figure 6.21 Comparison of predicted event-averaged centreline droplet size injected into USP-IP, and measured event-averaged centreline droplet size injected into free air

Figure 6.21 (a-b) suggest that the magnitude and axial trend of droplet size is very close to the measured values. According to Figure 6.21 (a), droplet size shows a magnitude of 3.8 µm at 20 mm and continually reduces to 3.2 µm at 45 mm away from the spray source. From this point onwards both CFD and PDA data show that the droplet size is almost constant suggesting that evaporation is almost insignificant. At these points ethanol fraction in droplets reaches high values (typically greater than 0.8), which reduces the saturated vapour pressure of the mixture, which, in turn, decreases the evaporation rate. This trend confirms that up to 80 mm droplet travelling distance, the original assumption describing that ethanol acts as non-evaporating species is reasonable. Figure 6.21 (b), indicates that D_{32} has a larger magnitude and exhibits a similar axial trend to D_{10}, because this diameter metric is directly correlated with droplet volume. It can be seen that predicted D_{32} follows the PDA measurement curve closely.

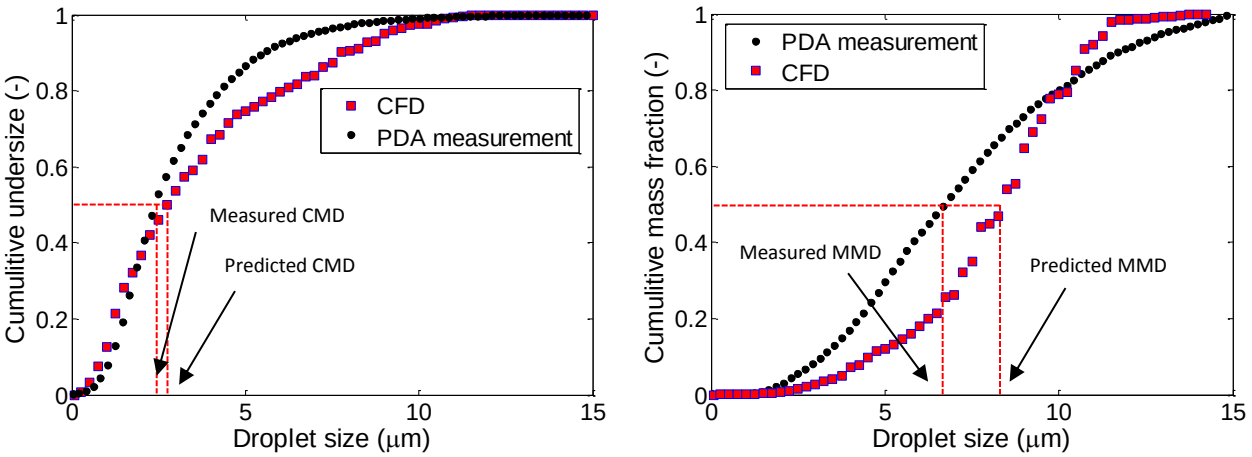

(a) Cumulative undersize **(b) Cumulative mass fraction**

Figure 6.22 Predicted plume particle size distribution compared with area-weighted PDA measurement of particle size at 25 mm vertical plane

The major deviation occurs at the measurement point of 20 mm. Here CFD predicts a value of 8.2 µm where PDA measurement shows a value of 7 µm. Although it is beyond the scope of this work to comment on PDA data, such deviation could potentially happens due to difficulties with the detection by PDA of sufficiently large samples of larger droplets at regions closer to the source when the particle size distribution is wide.

Figure 6.22 shows the comparison between predicted and measured particle size distributions at vertical plane, placed at 25 mm axial distance from the spray orifice. The figure indicated by (a) represents the cumulative frequency distribution where figure indicated by (b) shows cumulative mass distribution. Figure 6.22 (a) shows that both CFD and PDA distribution suggest that almost all of the droplets are below 10 µm, and about 45%-50% of the droplets are below 3 µm. The difference between CFD and PDA is concentrated on the size distribution of droplet fractions between 3-10 µm. PDA curve suggest that 90% of droplets are below 5 µm which results in fraction between 3 µm -5 µm to be around 40%-45%. Since CFD curve suggests that around 75% of the droplets are below 5 µm, then the fraction between 3 µm -5 µm should be around 25%-30%. This then describes that the mass fraction of droplets within the range of 3-5 µm and 5-10 µm is under predicted and over predicted by CFD, respectively. This mismatch between CFD predictions and PDA measurements may be attributable to variety of reasons. Firstly the comparisons are made for two different flows i.e. spray PDA measurement in free air vs.

spray CFD simulation in USP-IP. Therefore the interaction of plume-surrounding may alter the spatial size distribution of plume at particular location. Secondly CFD spray source is constructed based on assumed GSD value of 2.2, which is a typical value determine by ACI (Meakin et al., 2000). However, GSD of the plume in near-orifice regions may be different and is likely to be a function of actuation time. Therefore further work in needed to define GSD values on temporal basis and to link it to governing physics inside the actuator.

Location (mm)	Predicted CMD (GSD=2.2)	Measured CMD	Predicted MMD (GSD=2.2)	Measured MMD
25	2.75	2.39	8.75	6.68
50	2.68	2.18	8.25	6.71
75	2.50	2.08	7.25	6.89

Table 6.14 Predicted and measured count median diameter (CMD) and mass median diameter (MMD)

Predicted and measured values of count mean diameter (CMD) and mass median diameter (MMD) at 25 mm as well as 50 mm and 75mm vertical planes across the plume are summarised in Table 6.14. Table 6.14 shows that the differences between measured CMD and MMD at different locations are subtle. At all planes of measurement, CMD is around 2.2 μm and the MMD is around 6.7 μm indicating the closeness of these diameter metrics to each other. This could indicate that after 25 mm of plume travelling distance in free air, evaporation does not reduce the droplet size further. In other words most significant evaporation process of plume in free air is concluded within the first 25 mm of travelling distance from the spray orifice.

According to the table, at 25 mm vertical plane, CMD is predicted to be around 2.75 μm which is in very good agreement with the measured value of 2.39 μm. As the plume travels further to 50 mm, evaporation model reduces the droplet size and the predicted CMD value is 2.68 μm which is in reasonable agreement with measured CMD value of 2.18 μm. Predicted MMD value at 50 mm is 8.25 μm and is larger than the measured value, due to lower evaporation rate at this plane. At 75 mm predicted and measured CMD/MMD values

show a minimal mismatch of around 15% and 4% respectively. This agreement may suggest that 75 mm travelling distance of plume in USP-IP results in similar evaporation rate and size distribution, as if the plume was travelling 25 mm in free air.

6.5.2.4 Deposition

In this section we report the outcome of preliminary deposition study of the CFD simulation. To be able to obtain information regarding the impacted droplets to the solid boundaries, simulation activities showed that it is required to consider the diffusion of droplets due to turbulence (equations 6-34 to 6-39), inside the domain. This results in droplet-wall impaction which did not seem to be achieved while using mean flow tracking

6.5.2.4.1 Turbulent dispersion and size distribution

It is expected that the inclusion of turbulent diffusion on the faith of the droplets, affects the spatial distribution of the droplets locally. Therefor it is appropriate to visualise droplet size related metrics in the presence of such model. This will help us to gain understandings regarding the key influence of turbulent dispersion of droplet size.

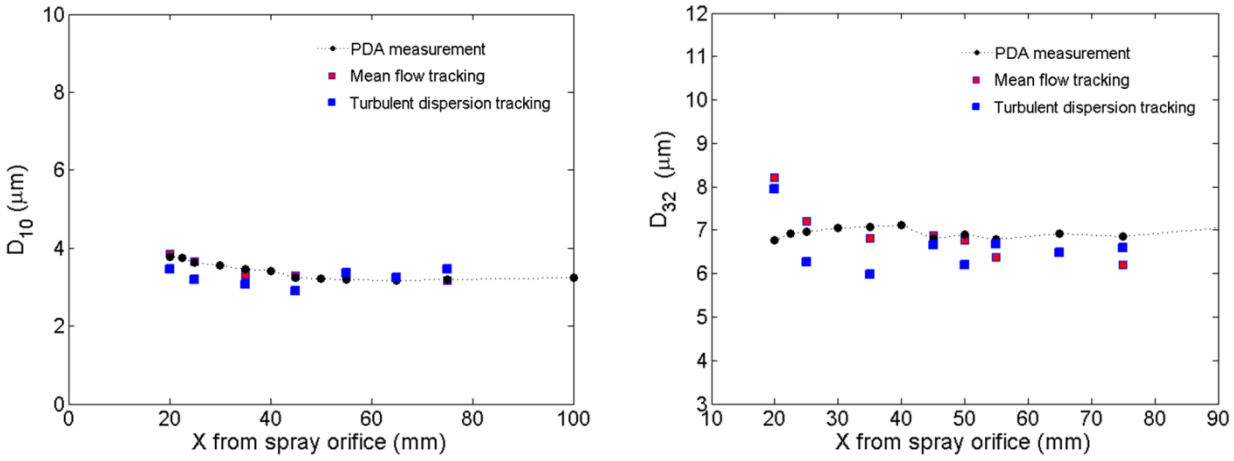

(a) Cumulative undersize **(b) Cumulative mass fraction**

Figure 6.23 Comparison of predicted event-averaged centreline droplet size injected into USP-IP, and measured event-averaged centreline droplet size injected into free air

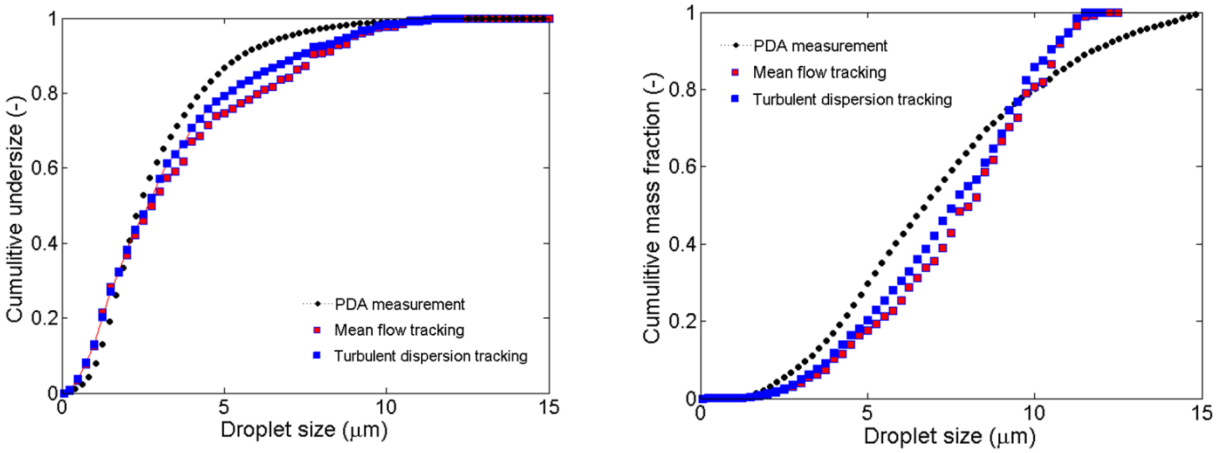

(a) Cumulative undersize **(b) Cumulative mass fraction**

Figure 6.24 Predicted plume particle size distribution compared with area-weighted PDA measurement of particle size at 25 mm vertical plane

Figure 6.23 shows the centreline evolution of D_{10} and D_{32}. The figure includes the CFD predictions, using mean-flow-tracking (MFT) and turbulent-dispersion-tracking (TDT), in addition to PDA measurements. Each set of data is colour coded correspondingly in the figure legend. Both figures suggest that the general trend of PDA data is captured which is broad decrease in droplet size as the plume travels further downstream. It can be seen that the TDT prediction is relatively similar to those predicted using MFM. Results show that the magnitude of the droplet size using TDT is generally lower than MFM which is more clearly evident in the case of D_{32}. This is due to the greater level of droplet-air interaction in the presence of TDT model. In this case droplets temporary trap inside eddies which results in increasing droplets residence time in the domain. This in turn leads to greater evaporation and reduce droplet size further. Similar to predictions of MFM and PDA measurement, here it is seen that droplet size plateaus after around 25 mm, suggesting the depletion of evaporating species.

Figure 6.24 shows size distribution of droplets using MFM, TDT and measured PDA. Results show that both cumulative curves are just slightly affected by the presence of TDT. It can be seen that TDT predicts slightly greater particle fraction below 7 μm. this is also evident in cumulative mass fraction graph, showing an increase in the mass fraction of droplets below 7 μm. such trend is attributable to enhanced evaporation which shifts the cumulative curve towards smaller droplets.

6.5.2.4.2 Turbulent dispersion and droplet trajectory

For the purpose of estimating plume deposition on the boundaries of the geometry, influence of turbulence eddies on droplet trajectories needs to be considered. Such interaction results in highly disturbed particle trajectory specifically for droplets with small size. For illustrative purposes Figure 6.25 exhibit the trajectory of droplets under the influence of turbulent diffusion. Figure 6.25 (a) shows the trajectory of droplets with diameters of below 1 µm inside the geometry of USP-IP. It can be seen that droplets trajectory is highly irregular. The chaotic droplet motion starts in regions close to the spray orifice and can be observed in the far field region when droplet is escaping out of the domain. This is due to the small size of these droplets causes it to have low inertia. Most of the droplet trajectories end in the horizontal section of the USP-IP, indicating that these droplets collide with the wall here.

Figure 6.25 (b) shows the trajectory of droplets with diameter between 1 µm and 5 µm. Here it can also be seen that droplet trajectories are still strongly affected by turbulent fluctuation both close to the spray orifice and far-field region. Many of these droplets impact the horizontal section wall of USP-IP. It can also be seen that some of these droplets impact on the vertical section of the wall as a results of fluctuation in flow field.

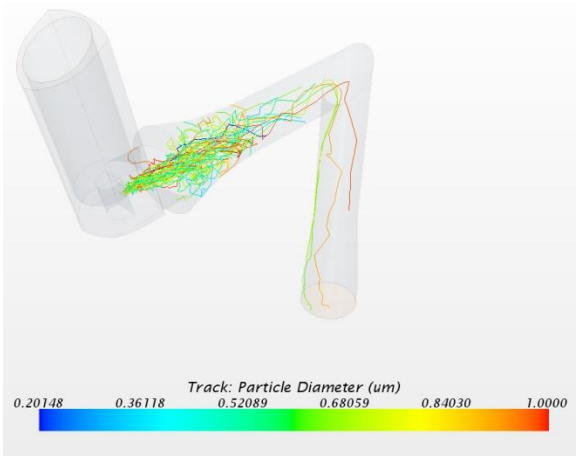

(a) initial diameter: below 1 µm

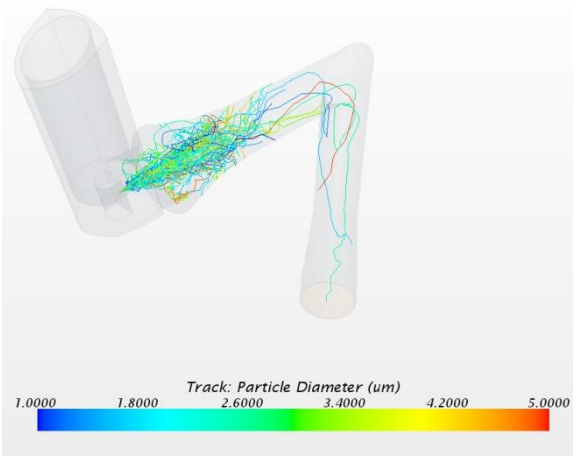

(b) initial diameter: between 1-5 µm

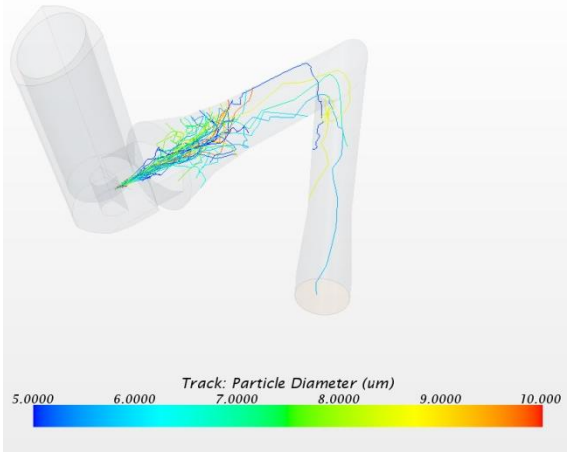

(c) initial diameter: between 5-10 µm

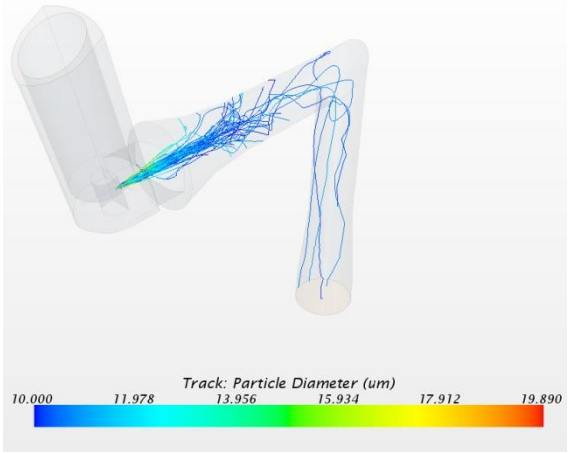

(d) initial diameter: above 10 µm

Figure 6.25 Trajectories of sampled number of particles with initial coloured by variations in droplet diameter

The next group of particles has a diameter between 5 µm to 10 µm. The corresponding droplet trajectories are shown in Figure 6.25 (c). Close to the spray orifice, the trajectories are straight line indicating ballistic trajectories due to higher droplet inertia. Around 50 mm away from the spray orifice, trajectories become unstable. As the droplets are carried further downstream, evaporation will reduce the droplet diameter and, hence, their inertia. Therefore, the droplet trajectories are more strongly affected by turbulence fluctuations. The predictions suggest that droplets in this size range are likely to deposit on both horizontal and vertical sections of USP-IP.

Finally, Figure 6.25 (d) shows the trajectories of droplets above 10 µm, which are almost straight due to high droplet inertia. It can be seen that their trajectories is least affected along the horizontal section of USP-IP. This means that the droplet is able to rip the flow

layer and follow a straight path, being almost irresponsive to local fluctuations. As a consequence few of these droplets impact on the horizontal section.

6.5.2.4.3 Local deposition estimation

Figure 6.26 shows qualitative representation of deposition profile of droplets on the combined geometry of mouthpiece and USP-IP. The figure is decomposed into four droplet size groups which are indicated in the figure caption.

Figure 6.26 (a) shows the deposition profile of sub-micron droplets. In line with the particle trajectory shown in Figure 6.25 (a), it can be seen that significant portion of these droplets are deposited on the mouthpiece and horizontal section of USP-IP. Deposition profile appears to stretch 2 USP-IP inlet diameters along the horizontal section. Figure 6.26 (b) shows the deposition profile of 1-5 µm droplets. It can be seen that the amount of deposition is increased in the mouthpiece region and horizontal section, due to the high population of these droplets. It can be seen that the deposition profile is now stretched over the whole horizontal section as these droplets are travelled further away from the source. It is evident that 1-5 µm droplets build up a deposition profile in the vertical section of USP-IP. This profile is due to the combination of droplet diffusion mechanism and also droplet impaction to the outer wall of the geometry. According to Figure 6.26 (c), it can be seen that the mouthpiece deposition for 5-10 µm range droplets is decreased. This is because larger droplets are capable of flying further away from the source before get trapped inside flow field fluctuations. Droplet deposition in horizontal section is still significant for this size range. According to trajectories of these droplets shown in Figure 6.25 (c), these droplets get deposited on the walls due to combination of diffusion and impaction. Eventually Figure 6.26 (d) shows that no mouthpiece deposition occurs for above 10 µm. It can also be seen that around 1 inlet diameter along the USP-IP, deposition profile is minimal.

As a result of the CFD model, the total amount of deposition is estimated to be 88%. This value is technically the mass of pure ethanol droplet stuck to the wall normalised to the initial ethanol mass inside the metering chamber. The corresponding ACI measurement shows a value of 51% which suggest that CFD model highly over predicts the deposition amount.

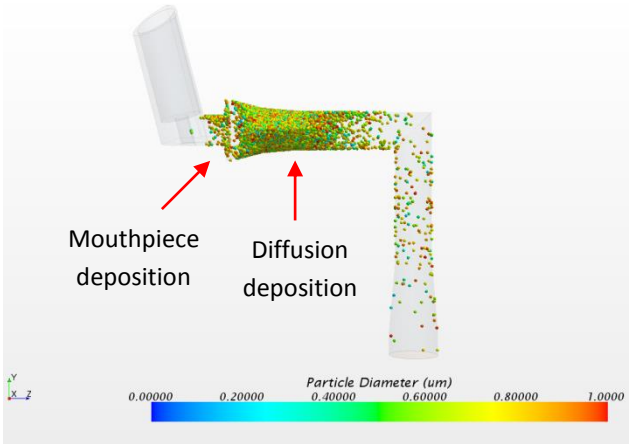

(a) initial diameter: below 1 µm

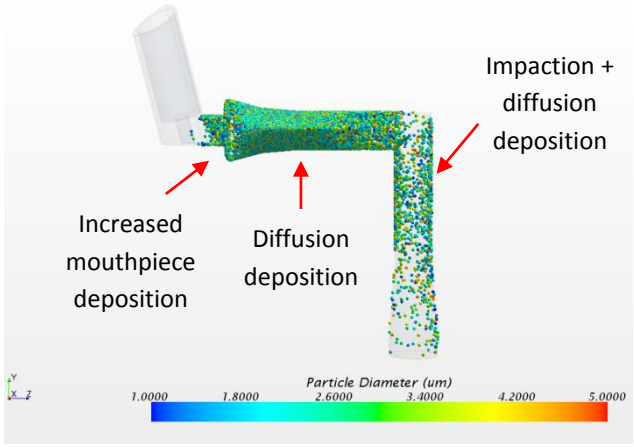

(b) initial diameter: between 1-5 µm

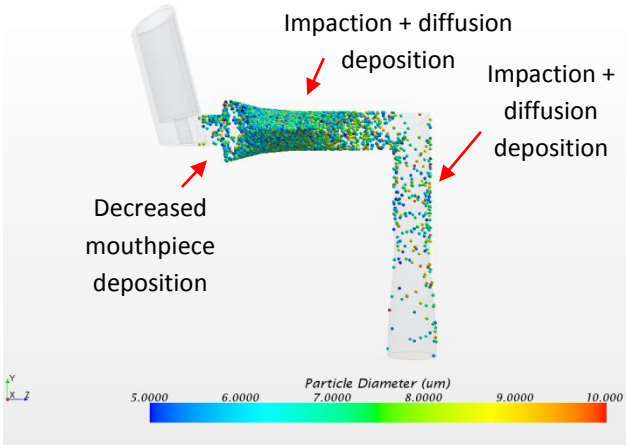

(c) initial diameter: between 5-10 µm

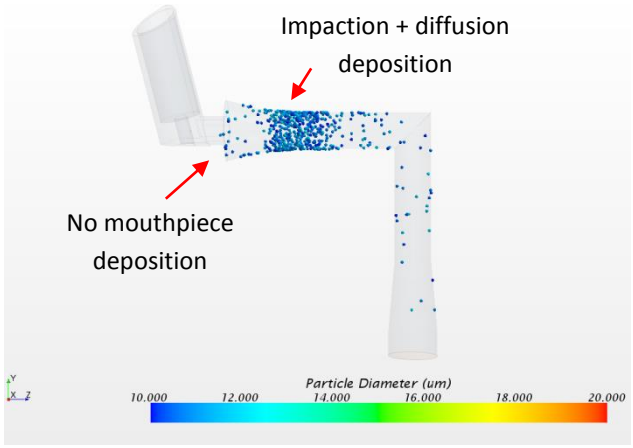

(d) initial diameter: above 10 µm

Figure 6.26 Deposition profile inside mouthpiece and USP-IP geometries coloured by droplet diameter

Such over prediction is also observed in the work of Matida et al., (2006) who assessed alternative turbulence models to predict deposition. The average deposition value of 90% was reported in realistic mouth-throat geometry, whilst using turbulent diffusion model. The over prediction can be attributed to the deficiency of turbulence model. Droplet deposition is dominated by the velocity fluctuation component normal to the geometry wall. This quantity is over predicted as a result of isotropy assumption in turbulent fluctuating component. Hence droplet size in near-wall region will be over predicted.

6.6 Summary and Conclusion

In this chapter a CFD simulation of pMDI injection into combined geometry of pMDI actuator and USP-IP was developed. The model is developed using STAR CCM+ V9.04.001 commercial CFD code. The model is constructed based on a novel approach which defines spray source from first principle. The definition of spray source is improved by linking source properties to fundamental physics governing upstream flow inside the pMDI. The chapter presented the mathematical theory of a pMDI spray injection into a standard USP-IP. The relevant equations describing the continuous phase flow field and discrete phase behaviour are governed. The effect of discrete phase and continuous phase interaction was also considered and hence the equations through which mass, momentum and heat may be transferred between the phases are also provided. The chapter also provided detailed information of CFD model set-up and preparation. These stages include construction and discretisation of computational geometry, defining steady and time dependent boundary conditions, in detail construction of pseudo spray source and tuning the relevant solver parameters.

Spatial distribution and characteristics of the steady air inside the geometry was presented and good agreement was achieved comparing with previous numerical and experimental works (Gjellerup & Frederiksen, 2007). It was observed that the flow is highly complex, three-dimensional and contains multiple regions with secondary motions. Two main regions of skewed flow profile were observed. One region is in the neighbouring of mouthpiece bottom wall and one towards the outer wall of USP-IP. Formation of pairs of Dean like vortices in the layers of fluid parallel to the outlet face was also evident.

Temporal plume structure was presented over the injection duration. Results suggest that at the initial stages of injection, plume is diverted upwards as a consequence of following flow mean path. Emergence of plume into the domain resulted in formation of strong recirculation zones around the plume edges due to entrainment of ambient air.

Investigation of plume centreline velocity revealed rapid axial decay in velocity values. Result indicated that the plume velocity drops by around 50% after only 20 mm travelling distance. Velocity values are compared with PDA measurement of plume centreline velocity injected into free air. Very good agreement is achieved over the first 20 mm of travelling

distance. After this point, predicted velocity values start to deviate and falls below measurements. The deviation is attributable to effect of solid boundaries confining the flow. Radial distribution of plume velocity at 25 mm away from spray orifice is presented and compared with PDA measurement. In line with PDA experiment, radial velocity distribution showed Gaussian profile. Very good match in velocity values is achieved with PDA measurement at 25 mm.

According to the CFD result, axial reduction in droplet size is observed. Centreline plume droplet size is represented using mean diameter metrics of D_{10} and D_{32}. Predicted data is compared with corresponding PDA measurement into free air. Axial trend and magnitude of droplet size matched nicely with the measured values. It was concluded that such good agreement may credit the original assumption treating ethanol as non-evaporating specie, along 80 mm travelling distance.

Predicted MMD values at 25, 50 and 75 mm vertical planes were presented. Results indicate that the predicted MMD values deviated from measured values by 23% and 18% at 25 and 50 mm planes, respectively. However minimal deviation of 4% is observed at 75 mm. This trend is justified by different amount of available air for entrainment which provides the heat source for evaporation. Entrained air for evaporation is less available in the case of injection into USP-IP that free air injection. These results in incomplete evaporation in USP-IP injection compared with free air, at 25 and 50 mm planes. However at 75 mm plane, complete evaporation is obtained and predicted data matches nicely with PDA data.

An attempt was made to predict the deposition of droplets inside the geometry. To do so, droplet trajectory was governed under the influence of flow field velocity fluctuations (i.e. turbulence diffusion model). The overall predicted deposition value was considerably deviated from selected ACI measurement provided by industrial partner. The predicted value is around 90% where the ACI measurement is around 50%. The deviation is believed to be as the turbulence isotropy assumption linked with turbulence diffusion model. Further work is scoped to assess the effect of turbulence model on deposition.

Chapter Seven

Summary, Conclusion and Recommendation for further work

7 Chapter Seven: Summary, Conclusion and recommendation for further work

7.1 Summary

In chapter three, novel 1-D model of flashing propellant flow through twin-orifice system of pMDI was constructed and presented. A range of alternative orifice flow models was implemented to assess their validity for metered pMDI flows: the homogeneous frozen model (HFM), the homogeneous equilibrium model (HEM), the slip equilibrium model (SEM) and a new hybrid-homogeneous flow model (H-HFM). The models predictions are compared against PDA measurements in terms of near-orifice spray velocity. The outcome of this phase of the modelling is used to develop atomisation model of pMDI as well as defining time-dependent boundary conditions for spray source (e.g. velocity, temperature, mixture composition, etc.), for CFD modelling.

In chapter four validated theoretical approaches were developed to predict the droplet size issued from a pMDI from first principle. Two district atomisation models were formulated based on aerodynamic and flashing mechanisms. Aerodynamic atomisation model was developed based on the breakup of flat liquid sheet (LISA) at spray orifice exit. Flashing model is based on growing of bubbles in superheated liquid layer flowing into the spray orifice. Model decides whether growing of the bubbles is sufficient to disrupt the liquid layer. Both models are linked to internal model of propellant flow through which flow characteristic at the point of breakup are predicted. The outcome of this modelling phase is used to define temporal droplet size of the spray source in CFD modelling.

In chapter five, theoretical models to predict flow characteristics of HFA/ethanol multicomponent mixture, inside twin-orifice assembly of pMDI were developed and presented. Semi-empirical equation of HFA/ethanol vapour pressure is developed to capture non-linear behaviour of vapour pressure with respect to ethanol concentration and temperature. Vapour pressure data is also presented to enhance the current data base for the benefits of formulation design and device optimisation purposes by pharmaceutical community. Internal flow and LISA atomisation models are generalised to include the effect of multicomponent formulations on plume characteristics. Modelling outcomes were then validation against PDA measurements of spray velocity and droplet size.

In chapter six, CFD simulation of pMDI injection into confined geometry of USP-IP was delivered. The chapter provides an innovative methodology to conduct CFD simulation of pMDI, based on novel concept of pseudo spray source (PSS). By means of this, definition of spray source is significantly improved by linking source properties to fundamental physics governing upstream flow characteristics and droplet generation process, inside the pMDI actuator. Temporal predictions of internal flow and atomisation models are linked to commercial CFD code, using multiple JAVA scripts to represent spray source. Attempts made to validate modelling outcomes such as droplet size, velocity and size distribution, against available experimental data.

7.2 Conclusions

In what follows, we summarise key conclusions drawn from current research work:

1. With reference to various test cases, HEM consistently over predicts spray velocity as a consequence of complete evaporation assumption. Similarly predicted vapour phase velocity by SEM shows large over prediction of velocity values where the predicted liquid phase velocity is consistently under estimated. H-HFM which explored the potential of bubble growth along the spray nozzle, showed very close predictions to HFM as a result of small evaporation amount. However the model requires improvements as it (i) incorporates nuclei population as an uncertain factor and (ii) computationally expensive. Among the flow models, HFM delivers sound predictions of velocity compared with PDA measurements over the duration of 95% original mass emission. Model capability is linked to no evaporation assumption.
2. Among explored design parameters of the pMDI device, saturated vapour pressure of the propellant system appears to be the most influential factor on spray velocity. This is confirmed by numerically employing alternative propellant systems of HFA134, HFA227 and CFC12 as well as device actuation at 285 K, 295 K and 303 K ambient temperature. These parameters manifest themselves by altering saturated vapour pressure of the system. Ranging the metering chamber volume from 25 µl to 63 µl did not appear to have significant impact on plume velocity but substantially increased spray duration by almost 100%. Increasing of spray orifice diameter by 50% did result in marginal velocity increase of 5%. The magnitude of the acceleration is underestimated compared with experimental data (Clark, 1991) where 50%

increase in spray orifice diameter led to 20% acceleration. Decreasing of spray orifice diameter led to considerable elongation of plume duration.

3. LISA predictions of droplet size is more in line with D_{10} in the case of pMDI sprays, which seem to be different to industrial sprays where LISA outcome is commonly compared with D_{32}. Good consistency is achieved between LISA predictions and PDA measurements in terms of droplet size order of magnitude and temporal trend, over 95% duration of mass emission. Slight mismatch between the predictions and PDA data, wherever observed, was predominantly connected with evaporative related size reduction of measured droplets. This happened in the data set whose measurement location is 15 mm from orifice and above where almost disappeared in the one taken at 2.6 mm.
4. Hybrid atomisation model suggests that the dominant atomisation regime as well as magnitude of formed droplets is a strong function of nuclei populations inside the liquid. This factor itself depends on liquid metastability and geometric arrangement of the device. Based on nuclei population, atomisation mechanism can shift from aerodynamic dominant to multimode, to flashing dominant. When C_b, the nuclei multiplier is unity, hybrid model predictions are very similar to LISA model and dominant atomisation mechanism is aerodynamic. When the C_b increases to 20 a combination of aerodynamic and flashing atomisation mechanisms were observed. In this case both sheet-thinning (KH) and vibrational (TAB) secondary mechanisms were responsible in forming the child droplets from the original blob. By increasing nuclei population by $C_b = 50$ almost constant droplets were achieved as consequence of primitive cubic topological arrangement of nuclei inside the liquid.
5. Using LISA atomisation model, an inverse relationship between droplet size and vapour pressure of propellant is observed. It is also revealed that among the design parameters, propellant system and ambient temperature are the most influential ones on generated droplet size. Minimal effect is observed in final droplet size by ranging spray orifice diameter from 0.2-0.48 mm and by changing expansion chamber volume from 12.5-50 µl.
6. Saturated vapour pressure of HFA/ethanol binary mixture, showed strong positive deviation from Raoult's law over the entire ethanol fraction values. This implies that net repulsive forces between the molecular species take place in HFA/ethanol

mixtures, resulting in larger amounts of HFA entering the vapour phase. This behaviour therefore indicates that Raoult's law is least valid assumption in pMDI formulations.

7. Numerical modelling of multicomponent flashing propellant flow inside pMDI shows that flow temperature, pressure and spray velocity remains almost unchanged as the ethanol is added to the formulation from 5-20 w/w%. Raoult's law based predictions of flow variables on the other hand, exhibit considerable changes in time dependent solution variables by systematic increase in ethanol concentration from 0-20 w/w%.
8. Prediction of spray velocity for multicomponent HFA/ethanol mixtures showed good agreement with measured PDA data, both magnitude wise and trend wise over duration of 95% mass emission. As confirmed by measured data and predicted by numerical model, no significant composition related change is observed in spray velocity for 5-20 w/w% ethanol fractions. However Raoult's law based modelling showed considerable decrease in velocity as ethanol is added to the formulation. Independency of velocity to ethanol concentration is attributable to strong positive deviations of mixture vapour pressure values from Raoult's law.
9. Over 95% of mass emission duration, good match is achieved between predicted mixture droplet size order of magnitude and measured D_{10} and D_{32}. As confirmed by PDA measurements increasing of ethanol in the formulation leads to increase in droplet size but not to a degree when using Raoult's law as vapour pressure model. The level of his increase is more in consistency with our vapour pressure model. Increase in droplet size by ethanol addition is also a consequence of alteration in mixture surface tension and viscosity.
10. Comparison of demonstrative CFD modelling of pMDI injection into USP-IP against PDA measurement of pMDI injection into free air showed that plume centreline velocity rapidly decays by 50% over 25 mm of travelling distance, as a consequence of large momentum exchange between the plume and entrained air. The axial velocity profile follows nicely the ones obtained by PDA up to 25 mm. At this point radial distribution of velocity shows a Gaussian profile which fits well with the ones obtained by PDA. After 25 mm, predicted axial velocity showed negative deviation with reference to PDA measurement. The discrepancy is attributed to onset of wall

effect in CFD simulation. However in regions close to the spray source flow pattern and characteristics are dictated by the spray source.

11. CFD results indicate considerable droplet size decrease of 50%-75% over 50-60 mm of travelling distance. The size reduction is associated with rapid evaporation of HFA134 content of multicomponent droplets. As validated by PDA measurement of D_{10} and D_{32}, centreline plume droplet size appears to remain approximately unchanged after 40-45 mm away from the spray orifice until 80 mm. This suggest that as HFA content evaporates and droplets become enriched in ethanol up to fractions above 0.8 mixture vapour pressure reduces. Vapour pressure reduction leads to significant slowdown in evaporation rate. This may backup the assumption of treating ethanol as non-evaporating specie up to 80 mm.
12. Comparison of predicted droplet size distribution against area-weighted PDA measurement suggest that MMD values is over predicted by 23%, 15% and 4% at 20 mm, 50 and 75 mm planes, respectively. The fact that level discrepancy decreases by distance is a consequence of difference in plume evaporation rate in confined space and free air. In the case of free air injection, the amount of air for evaporation is higher compared with injection into USP-IP case. As a result, rate of plume evaporation is expected to be higher in free air injection compared with USP-IP injection. Least deviation of predicted MMD from measured ones at 75 mm, may indicated that this travelling distance in USP-IP results in similar evaporation rate and size distribution, as if the plume was travelling 25 mm in free air.

7.3 Contribution to original knowledge

Here we list the key contributions of this research work to the existing knowledge:

1. Construction and validation of internal flow model of two-phase flashing propellant flow inside twin-orifice system of pMDI and assessment of various interphase phenomena assumptions.
2. Construction and validation of novel aerodynamic primary atomisation model being capable of predicting droplet size issued from pMDI, from first principle.
3. Construction of novel primary hybrid atomisation model capable of predicting droplet size within the correct order of magnitude, based on multimode atomisation mechanism.

4. Measurement and presentation of compact mathematical formula of saturated vapour pressure values as a function of wide range of ethanol composition and temperature. This item benefits pharmaceutical community for the purpose of formulation design and device optimisation.
5. Construction and validation of internal flow and atomisation models of multicomponent two-phase flashing flow of propellant/ethanol mixture formulation, inside twin-orifice system of pMDI.
6. Introducing novel concept and methodology to improve definition of spray source based on time-dependent variation of upstream flow inside pMDI actuator. This method is implementable for CFD calculation purposes where effect of source is oversimplified, leading to considerable predictions deviation from measurement.

7.4 Recommendations for further work

- Two-phase flow regime inside chambers: current models assumes homogeneous two-phase flow regime inside the chambers and orifice nozzles. However flow visualisations in transparent models of pMDI suggest that flow regime is far from being homogeneous. In the presence of ethanol, recent visualisation study shows dramatic changes in flow regime as a function of ethanol increase (Myatt, 2015 a-b). In ideal case, studies should be conducted to develop theoretical (or semi-empirical) models to predict flow regime as a function of formulation composition and geometry. This has impacts on liquid length scale from which droplets are generated and must be applied correspondingly.
- Droplet formation due to flashing: there are uncertainties associated with current flashing model which requires fundamental understanding of physics governing nucleation and bubble bursting in superheated propellants. Mathematical relations need to be established to determine nuclei population in pMDI compartments, as a function of formulation thermos-physical properties and geometric scales. The outcome of this can also serve as further improvement to H-HFM model to more realistically estimate propellant evaporation. Additionally semi-empirical correlations can be established (using optical diagnostic techniques) to include more accurate representation of the produced droplet size after bubble bursting. This may be

defined as a function of liquid degree of superheat, thermos-physical properties and device geometry.

- Multicomponent formulation representation: current work in the case of mixture formulation, assumes homogeneous distribution of ethanol inside propellant. Such representation cannot be as realistic due to the large density difference between the constituents, which is expected to form rather a stratified mixture. This arrangement requires different approach of representing thermodynamic and transport properties of the mixture in the model. Furthermore, stratified arrangement can potentially result in evaporation inhibition as ethanol layer will be placed on top of HFA and does not let HFA molecules to be added into vapour phase. This will have impact on mass flow emission and retardation of post-nozzle evaporative droplet size change.
- Droplet deposition: although was the current CFD model reasonably successful in terms of predicting axial droplet size and velocity evolution of the spray, deposition was largely over predicted. This is the deficiency in turbulent dispersion model assuming isotropy in fluctuating velocity component, specifically in near-wall region. This requires assessing the effect of alternative turbulence models and droplet-eddy interaction, in presence of our PSS. Additionally, improvements should be applied to reasonably defined droplet-boundary interaction in near-wall regions.

Appendix A: Derivation of Speed of Sound

For a constant area nozzle, by substitution of equation 3-2 in equations 3-44 to 3-46 mass, momentum and energy equations for the system can be rewritten as follows:

$$\frac{dV}{dz} - \frac{V}{\bar{v}}\frac{d\bar{v}}{dz} = 0 \qquad \text{A - 1}$$

$$V\frac{dV}{dz} + \bar{v}\frac{dp}{dz} = 0 \qquad \text{A - 2}$$

$$V\frac{dV}{dz} + \frac{d\bar{h}}{dz} = 0 \qquad \text{A - 3}$$

Next step is to evaluate derivatives of mixture specific volume and mixture enthalpy with respect to distance appeared in equations A - 1, A - 2 and A - 3. As described in section 3.3.2.4.2, any mixture thermodynamic property denoted as $\overline{\Pi}$ follows the mass weighted format of equation A - 4:

$$\overline{\Pi} = x_0\Pi_{g,core} + (1-x_0)\left[(1-y)\Pi_{l,M} + (y-x_{RP})\Pi_{g,sat} + x_{RP}\Pi_{l,sat}\right] \qquad \text{A - 4}$$

Any thermodynamic property such as Π, is a function of local pressure and entropy. In the absence of frictional losses, we assume that the entropy is constant and hence thermodynamic property Π becomes a function of pressure. In light of this information and using chain rule, derivative of equation A - 4 can be written as follows:

$$\frac{d\overline{\Pi}}{dz} = x_0\left.\frac{\partial\Pi_{g,core}}{\partial p}\right|_s\frac{dp}{dz}$$

$$+(1-x_0)\left[(1-y)\left.\frac{\partial\Pi_{l,M}}{\partial p}\right|_s + (y-x_{RP})\left.\frac{\partial\Pi_{g,sat}}{\partial p}\right|_s + x_{RP}\left.\frac{\partial\Pi_{l,sat}}{\partial p}\right|_s\right]\frac{dp}{dz} \qquad \text{A - 5}$$

$$+(1-x_0)\Pi_{lg,sat}\frac{dx_{RP}}{dz} + (1-x_0)(\Pi_{l,sat} - \Pi_{l,M})\frac{dy}{dz}$$

After performing some rearrangements on equation A - 5, equation A - 6 can be achieved:

$$\frac{\partial \overline{\Pi}}{\partial z} = \left(x_0 \left. \frac{\partial \Pi_{g,core}}{\partial p} \right|_s + (1 - x_0) \left[(1 - y) \left. \frac{\partial \Pi_{l,M}}{\partial p} \right|_s + (y - x_{RP}) \left. \frac{\partial \Pi_{g,sat}}{\partial p} \right|_s + x \left. \frac{\partial \Pi_{l,sat}}{\partial p} \right|_s \right] \right) \frac{dp}{dz} \quad \text{A - 6}$$
$$+ (1 - x_0) \Pi_{lg,sat} \frac{dx_{RP}}{dz} + (1 - x_0)(\Pi_{l,sat} - \Pi_{l,M}) \frac{dy}{dz}$$

For simplifying notation, we rewrite equation A - 6 as follows:

$$\frac{\partial \overline{\Pi}}{\partial z} = \psi \frac{dp}{dz} + \varphi \frac{dx_{RP}}{dz} + \xi \frac{dy}{dz} \quad \text{A - 7}$$

Where:

$$\psi = x_0 \left. \frac{\partial \Pi_{g,core}}{\partial p} \right|_s + (1 - x_0) \left[(1 - y) \left. \frac{\partial \Pi_{l,M}}{\partial p} \right|_s + (y - x_{RP}) \left. \frac{\partial \Pi_{g,sat}}{\partial p} \right|_s + x_{RP} \left. \frac{\partial \Pi_{l,sat}}{\partial p} \right|_s \right] \quad \text{A - 8 (a)}$$

$$\varphi = (1 - x_0) \Pi_{lg,sat} \quad \text{A - 8 (b)}$$

$$\xi = (1 - x_0)(\Pi_{l,sat} - \Pi_{l,M}) \quad \text{A - 8 (c)}$$

Substitution of equation A - 8 (a), A -8 (b) and A - 8 (c) into equations A - 1, A - 2 and A - 3 yields:

$$\frac{dV}{dz} - \frac{V}{\bar{v}} \left(\psi_v \frac{dp}{dz} + \varphi_v \frac{dx}{dz} + \xi_v \frac{dy}{dz} \right) = 0 \quad \text{A - 9}$$

$$V \frac{dV}{dz} + \bar{v} \frac{dp}{dz} = 0 \quad \text{A - 10}$$

$$V \frac{dV}{dz} + \psi_h \frac{dp}{dz} + \varphi_h \frac{dx}{dz} + \xi_h \frac{dy}{dz} = 0 \quad \text{A - 11}$$

In these equations subscripts h and v, where encountered, symbol Π in equations A-8 (a-c) should be replaced by enthalpy and specific volume, respectively. In the absence of any frictional losses, evaporation is the only factor dictating pressure drop along spray nozzle. Thus, the equation of vapour production rate has to be included as an auxiliary equation to close the system. Definition of two phase flow quality using initial liquid mass flowing into spray orifice yields:

$$x_{RP} = \frac{m_g}{m_{l,0}} \qquad \text{A - 12}$$

where the mass of vapour is related to bubble diameter described by equation A - 13:

$$m_g = \frac{n_b \pi D_b^3(t)}{6 v_{g,sat}} \qquad \text{A - 13}$$

Progression of bubble diameter in equation A - 14 is a function of time and is calculated using equation 3-35 (a-c). The rate of vapour production then would be:

$$\frac{dx_{RP}}{dt} = \frac{n_b \pi}{6 m_{l,0}} \frac{d}{dt}\left(\frac{D_b^3(t)}{v_{g,sat}}\right) \qquad \text{A - 14}$$

After expanding the time derivative on the right hand side of equation A - 14 we transform time domain into space domain (using $dz = Vdt$) as the flow is assumed to be quasi-steady. Therefore equation A - 15 is obtainable:

$$\frac{dx_{RP}}{dz} = \frac{n_b \pi}{6 m_{l,0}} \left[\left(\frac{3 d D_b}{dz} \frac{D_b^2}{v_{g,sat}}\right) - \left(\frac{D_b^3}{v_{g,sat}^2} \frac{\partial v_{g,sat}}{\partial p}\bigg|_s \frac{dp}{dz}\right)\right] \qquad \text{A - 15}$$

Minor rearrangements lead to the final closure equation:

$$\frac{dx_{RP}}{dz} + \Gamma \frac{dp}{dz} = \Psi \frac{dD_b}{dz} \qquad \text{A - 16}$$

In which:

$$\Gamma = \left(\frac{n_b \pi}{6 m_{l,0}} \frac{D_b^3}{v_{g,sat}^2} \frac{dv_{g,sat}}{dp}\right) \quad and \quad \Psi = \left(\frac{n_b \pi}{2 m_{l,0}} \frac{D_b^2}{v_{g,sat}}\right) \qquad \text{A - 17}$$

The term dD_b/dz on the RHS of equation A - 16, is known from approximate solution to Rayleigh-Plesset equation i.e. equation 3-35 (a-c). Therefore the final system of nonlinear first ordinary differential equations is as follows:

$$\bar{v} \frac{dV}{dz} - V\left(\psi_v \frac{dp}{dz} + \varphi_v \frac{dx_{RP}}{dz} + \xi_v \frac{dy}{dz}\right) = 0 \qquad \text{A - 18}$$

$$V \frac{dV}{dz} + \bar{v} \frac{dp}{dz} = 0 \qquad \text{A - 19}$$

$$V \frac{dV}{dz} + \psi_h \frac{dp}{dz} + \varphi_h \frac{dx_{RP}}{dz} + \xi_h \frac{dy}{dz} = 0 \qquad \text{A - 20}$$

$$\frac{dx_{RP}}{dz} + \Gamma \frac{dp}{dz} = \Psi \frac{dD_b}{dz} \qquad \text{A - 21}$$

The system has general mathematical form of:

$$A \frac{dX}{dz} = B \qquad \text{A - 22}$$

where A is the square matrix of flow scalars, dX/dz is the vector of flow dependent variables and eventually B is the vector of independent terms in flow model. The matrices and corresponding components of A - 22 is shown in A - 23:

$$\begin{bmatrix} \bar{v} & -V\psi_v & -V\varphi_v & -V\xi_v \\ V & \bar{v} & 0 & 0 \\ V & \psi_h & \varphi_h & \xi_h \\ 0 & \Gamma & 1 & 0 \end{bmatrix} \begin{bmatrix} \frac{dV}{dz} \\ \frac{dp}{dz} \\ \frac{dx_{RP}}{dz} \\ \frac{dy}{dz} \end{bmatrix} = \begin{bmatrix} 0 \\ 0 \\ 0 \\ \Psi \frac{dD_b}{dz} \end{bmatrix} \quad \text{A - 23}$$

From mathematical point of view, at the point of choking, flow experiences a step change in pressure which implies that $dp/dz = \infty$. This is essentially a singularity in the flow system of equations. The singular point can be identified by the following criterion:

$$\det(A) = 0 \quad \text{A - 24}$$

This suggests:

$$\begin{vmatrix} \bar{v} & -V\psi_v & -V\varphi_v & -V\xi_v \\ V & \bar{v} & 0 & 0 \\ V & \psi_h & \varphi_h & \xi_h \\ 0 & \Gamma & 1 & 0 \end{vmatrix} = 0 \quad \text{A - 25}$$

Parametric solution of equation A - 25 for V yields the singular point in the system at which $V = a$ (i.e. $M = 1$):

$$a = \bar{v}\sqrt{\frac{-\xi_h}{\xi_h\psi_v - \xi_v\psi_h + \xi_v\bar{v} + \Gamma\xi_v\varphi_h - \Gamma\xi_h\varphi_v}} \qquad \text{A - 26}$$

Where a is the speed of sound of the mixture with four constituents.

Appendix B: Transient Cone Angle

The transient nature of pMDI spray manifests itself in terms of time dependent spray characteristics. Our internal flow model of formulation inside pMDI actuator is capable of producing time dependent spray characteristics such as mass flow rate and velocity. However, the current model does not take into account temporal variations of spray angle. This requires multi-dimensional consideration of flow inside the spay orifice. However in order to include time dependent variations of spray angle in spray source (PSS) construction, we use series of high speed images of spray in near-orifice region. The set of images was developed in Loughborough University Optical Engineering Laboratory laboratory using transparent model of actuator, as a part of parallel experimental project.

The actuator and formulation properties, for which high speed images are produced, are summarised in Table B.1. Selected numbers of snapshots of near-orifice plume are shown in Figure B.1, to describe the method of spray angle calculation. Here we describe the method for Figure B.1 (c) which is identical for the rest of the snapshots.

Parameter	Value	Parameter	Value
Vol_{mc}	50 µl	D_{vo}	0.7 mm
Vol_{ec}	50 µl	D_{so}	0.3 mm
T_{amb}	295 K	Y_E	10 (%)

Table B.1 Parameters of the actuator used in near-orifice spray HSI

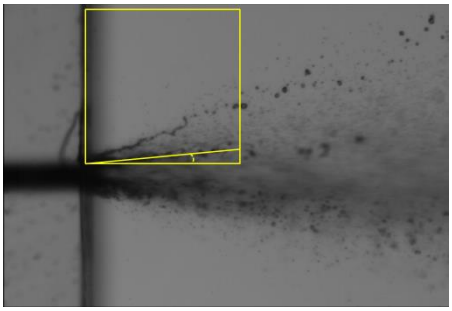

(a) 76 ms – θ=9 deg

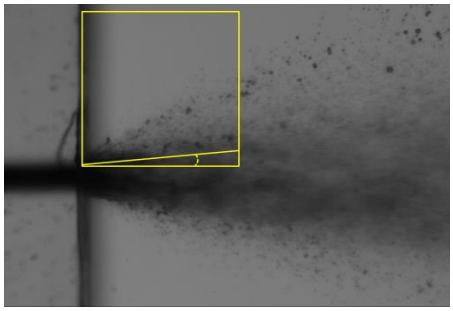

(b) 100 ms – θ=12.7 deg

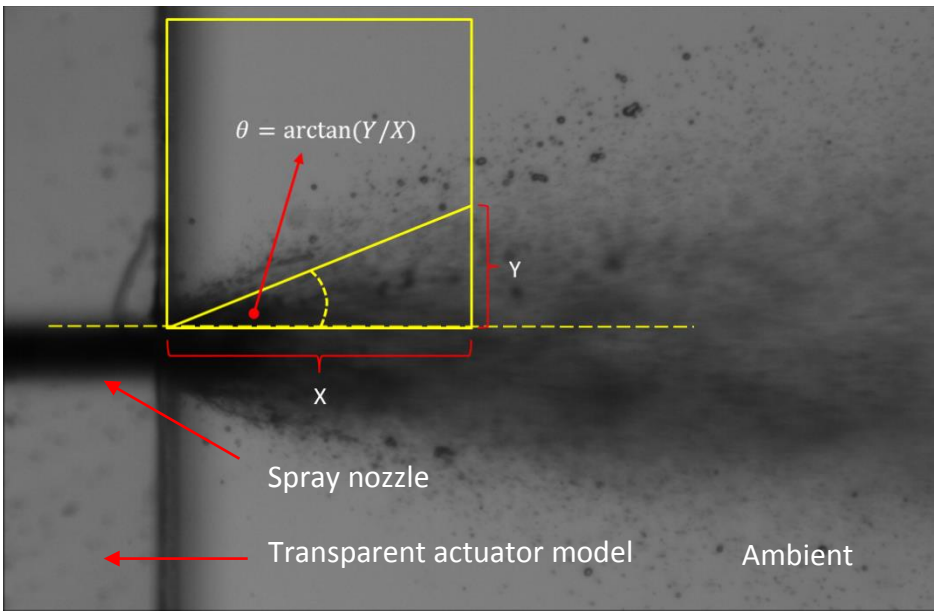

(c) 170 ms – θ=22.03 deg

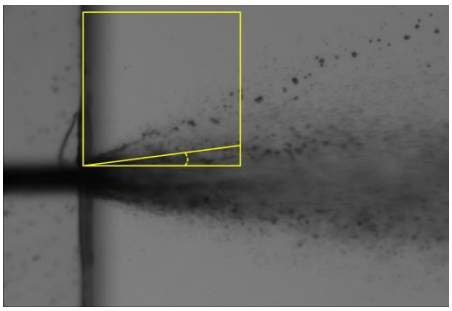

(d) 265 ms – θ=14.2 deg

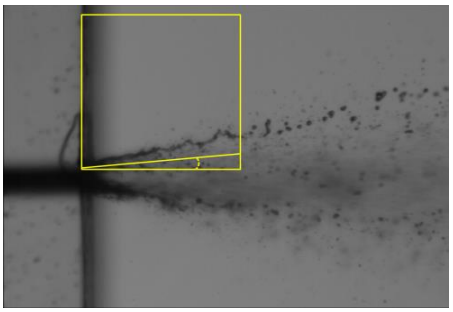

(e) 312 ms – θ=12.03 deg

Figure B.1 Snapshots of pMDI plume in near-orifice region along the actuation event

A square window is placed in near-orifice region, defining the region of interest (see Figure B.1 (c)). Left side of the window is adjusted to coincide with the exit face of the actuator model. The bottom of the window is aligned with the top edge of the spray orifice. These selections provide the reference locations for window placement in the entire series of images. Identification of the spray angle is judged by eye. The edge of the jet, and hence the cone angle, is judged to be located at the boundary of the darker spray region with higher concentration of small droplets. The angle of the spray is calculated by counting the number of pixels corresponding to the horizontal distance X and vertical distance Y indicated in Figure B.1. This process is performed for 16 snapshots of one actuation event. The results of observed cone angles are shown in Figure B.2 using black squares.

Investigations suggest that variations of cone angle can be divided into two main regions. One region is up to 120 ms after the actuation where cone angle shows exponential rise. The other region is after 120 ms where cone angle almost linearly declines until the actuation event concludes. This leads to develop the fit using two separate exponential and linear functions. Nonlinear least squares method using Levenberg-Marquardt algorithm in Matlab was implemented to deduce equation constant which yields equation B-1:

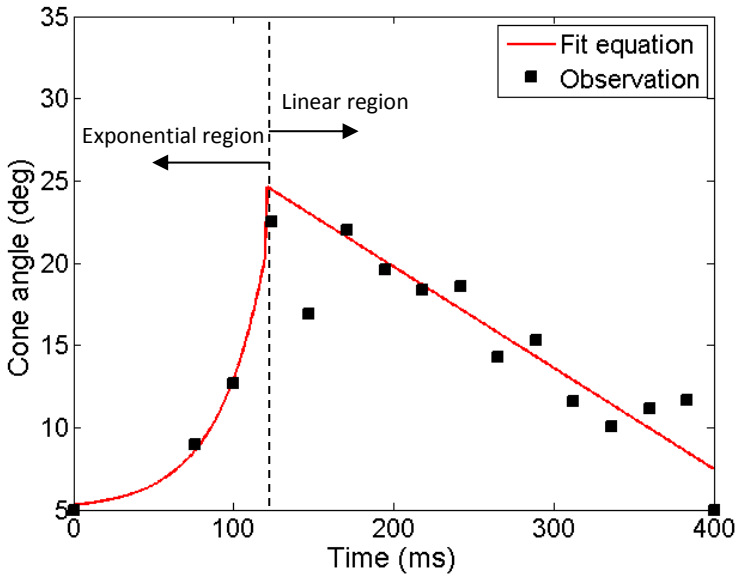

Figure B.2 Observed and fitted values of spray cone angle

$$\theta = 0.2923 \times \exp(0.03309t) + 5 \qquad for \qquad t \leq 120$$

$$\theta = -0.06146t + 32.04 \qquad for \qquad t > 120 \qquad \text{B - 1}$$

Using this equation the R^2 value for exponential and linear regions are 0.99 and 0.82, respectively. It should be noted that this equation is geometry dependent so care must be taken when applying this equation to actuator with other chambers volumes and orifice diameters.

Bibliography

ABRAHAM, J., 1997. What is adequate resolution in the numerical computations of transient jets? *SAE Technical Paper 970051.*

ABRAMOVICH, G., 1976. *Applied gasdynamics.* Moscow Izdatel Nauka.

ANEJA, R., and ABRAHAM, J., 1998. How far does the liquid penetrate in a diesel engine: Computed results vs. measurements? *Combustion Science and Technology,* **138**(1-6), 233-255.

ANON, 2016a. *Chiesi Farmaceutici S.p.A.* [Online]. Chiesi. [viewed 05/02/2016]. Available from: http://www.chiesigroup.com/en/home.

ANON, 2016b. *World Health Organization.* [Online]. World Health Organization. [viewed 08/03/2016] Available from: http://www.who.int/en/.

ANON, 2015. *Asthma Facts a Statistics*. [Online]. Asthma UK. [viewed 09/12/2015]. Available from: https://www.asthma.org.uk/terms/terms-and-conditions/.

ANON, 2011. *Asthma in the US.* [Online]. Centers for Disease Control and Prevention. [viewed 03/05/2011]. Available from: http://www.cdc.gov/vitalsigns/asthma/.

ARAI, T., and HASHIMOTO, H., 1986. Disintegration of a thin liquid sheet in a cocurrent gas stream. *International Journal of Turbo and Jet-Engines,* **3**(4), 301-306.

ARDRON, K., and FURNESS, R., 1976. A study of the critical flow models used in reactor blowdown analysis. *Nuclear Engineering and Design,* **39**(2), 257-266.

ASHGRIZ, N., 2011. *Handbook of atomization and sprays: theory and applications.* New York: Springer Science & Business Media.

ATTOU, A., and SEYNHAEVE, J., 1999. Steady-state critical two-phase flashing flow with possible multiple choking phenomenon: Part 1: physical modelling and numerical procedure. *Journal of Loss Prevention in the Process Industries,* **12**(5), 335-345.

BAECKSTROEM, K., and NILSSON, P., 1988. Measurements of droplet size distributions from metered dose inhalers with different vapour pressures and contents of surfactant. *Journal of Aerosol Science,* **19**(7), 1097-1100.

BERRY, J., HEIMBECHER, S., HART, J.L., and SEQUEIRA, J., 2003. Influence of the metering chamber volume and actuator design on the aerodynamic particle size of a metered dose inhaler. *Drug Development and Industrial Pharmacy,* **29**(8), 865-876.

BIDONE, G., 1829. *Expériences sur la forme et sur la direction des veines et des courans [sic] d'eau lancés par diverses ouvertures.*Paris: Imprimerie royale.

BIRD, R.B., STEWART, W.E., and LIGHTFOOT, E.N., 2007. *Transport phenomena*. Revised 2nd Ed. New York: John Wiley & Sons.

BIRKHOFF, G., MARGULIES, R., and HORNING, W., 1958. Spherical bubble growth. *Physics of Fluids (1958-1988),* **1**(3), 201-204.

BLANDER, M., and KATZ, J.L., 1975. Bubble nucleation in liquids. *AIChE Journal,* **21**(5), 833-848.

BOURÉ, J., FRITTE, A., GIOT, M., and REOCREUX, M., 1976. Highlights of two-phase critical flow: on the links between maximum flow rates, sonic velocities, propagation and transfer phenomena in single and two-phase flows. *International Journal of Multiphase Flow,* **3**(1), 1-22.

BRAMBILLA, G., GANDERTON, D., GARZIA, R., LEWIS, D., MEAKIN, B., and VENTURA, P., 1999. Modulation of aerosol clouds produced by pressurised inhalation aerosols. *International Journal of Pharmaceutics,* **186**(1), 53-61.

BRENNEN, C., 1995. *Cavitation and bubble dynamics.* New York, USA: Oxford University Press.

BRINDLEY, A., 1999. The chlorofluorocarbon to hydrofluoroalkane transition: the effect on pressurized metered dose inhaler suspension stability. *Journal of Allergy and Clinical Immunology,* **104**(6), s221-s226.

BROWN, R., and YORK, J.L., 1962. Sprays formed by flashing liquid jets. *AIChE Journal,* **8**(2), 149-153.

BUSHNELL, D.M., and GOODERUM, P.B., 1968. Atomization of superheated water jets at low ambient pressures. *Journal of Spacecraft and Rockets,* **5**(2), 231-232.

CHOU, W., and FAETH, G., 1998. Temporal properties of secondary drop breakup in the bag breakup regime. *International Journal of Multiphase Flow,* **24**(6), 889-912.

CLARK, A.R., 1995. Medical aerosol inhalers: past, present, and future. *Aerosol Science and Technology,* **22**(4), 374-391.

CLARK, A.R., 1991. *Metered atomisation for respiratory drug delivery*. Thesis (PhD), Loughborough University of Technology, Loughborough, UK.

CROSLAND, B.M., JOHNSON, M.R., and MATIDA, E.A., 2009. Characterization of the spray velocities from a pressurized metered-dose inhaler. *Journal of Aerosol Medicine and Pulmonary Drug Delivery,* **22**(2), 85-98.

CROWE, C., TROUTT, T., and CHUNG, J., 1996. Numerical models for two-phase turbulent flows. *Annual Review of Fluid Mechanics,* **28**(1), 11-43.

DAI, Z., and FAETH, G., 2001. Temporal properties of secondary drop breakup in the multimode breakup regime. *International Journal of Multiphase Flow,* **27**(2), 217-236.

DEHAAN, W., and FINLAY, W., 2004. Predicting extrathoracic deposition from dry powder inhalers. *Journal of Aerosol Science,* **35**(3), 309-331.

DERGARABEDIAN, P., 1960. Observations on bubble growths in various superheated liquids. *Journal of Fluid Mechanics,* **9**(01), 39-48.

DOLOVICH, M.B., and FINK, J.B., 2001. Aerosols and devices. *Respiratory Care Clinics of North America,* **7**(2), 131-174.

DOMBROWSKI, N., and JOHNS, W., 1963. The aerodynamic instability and disintegration of viscous liquid sheets. *Chemical Engineering Science,* **18**(3), 203-214.

DOMNICK, J., and DURST, F., 1995. Measurement of bubble size, velocity and concentration in flashing flow behind a sudden constriction. *International Journal of Multiphase Flow,* **21**(6), 1047-1062.

DUNBAR, C.A., 1996. *An experimental and theoretical investigation of the spray issued from a pressurised metered-dose inhaler*. Thesis (PhD), University of Manchester Institute of Science and Technology.

DUNBAR, C.A., WATKINS, A.P., and MILLER, J.F., 1997. An experimental investigation of the spray issued from a pMDI using laser diagnostic techniques. *Journal of Aerosol Medicine,* **10**(4), 351-368.

DUNBAR, C.A., 1997. Atomization Mechanisms of the Pressurized Merered Dose Inhaler. *Particulate Science and Technology,* **15**(3-4), 253-271.

DUNBAR, C.A., and MILLER, J.F., 1997. Theoretical investigation of the spray from a pressurized metered-dose inhaler. *Atomization and Sprays,* **7**(4),417-436.

DURST, F., MILOIEVIC, D., and SCHÖNUNG, B., 1984. Eulerian and lagrangian predictions of particulate two-phase flows: a numerical study. *Applied Mathematical Modelling,* **8**(2), 101-115.

ELIAS, E., and LELLOUCHE, G., 1994. Two-phase critical flow. *International Journal of Multiphase Flow,* **20**, 91-168.

EL-SHANAWANY, M., and LEFEBVRE, A., 1980. Airblast atomization: effect of linear scale on mean drop size. *Journal of Energy,* **4**(4), 184-189.

ENGINEERING SCIENCES DATA UNIT (ESDU) Data Item 89012., 1989. Two-phase flow pressure losses in pipeline fittings.

FAETH, G., HSIANG, L., and WU, P., 1995. Structure and breakup properties of sprays. *International Journal of Multiphase Flow,* **21**, 99-127.

FEBURIE, V., GIOT, M., GRANGER, S., and SEYNHAEVE, J., 1993. A model for choked flow through cracks with inlet subcooling. *International Journal of Multiphase Flow,* **19**(4), 541-562.

FINLAY, W.H., 2001. *The mechanics of inhaled pharmaceutical aerosols: an introduction.* 6 ed. London: Academic Press.

FLETCHER, G.E., 1975. *Factors affecting the atomisation of saturated liquids*. Thesis (PhD), Loughborough University of Technology, Loughborough, UK.

FORSTER, H.K., and ZUBER, N., 1954. Growth of a vapor bubble in a superheated liquid. *Journal of Applied Physics,* **25**(4), 474-478.

FRASER, R., DOMBROWSKI, N., and ROUTLEY, J., 1963. The atomization of a liquid sheet by an impinging air stream. *Chemical Engineering Science,* **18**(6), 339-353.

FREEDMAN, T., 1957. Medihaler therapy for bronchial asthma; a new type of aerosol therapy. *Postgraduate Medicine,* **20**(6), 667-673.

GABRIO, B.J., STEIN, S.W., and VELASQUEZ, D.J., 1999. A new method to evaluate plume characteristics of hydrofluoroalkane and chlorofluorocarbon metered dose inhalers. *International Journal of Pharmaceutics,* **186**(1), 3-12.

GAD, S.C., 2008. *Pharmaceutical manufacturing handbook: production and processes.* New York: John Wiley & Sons.

GANDERTON, D., LEWIS, D., DAVIES, R., MEAKIN, B., BRAMBILLA, G., and CHURCH, T., 2002. Modulite®: a means of designing the aerosols generated by pressurized metered dose inhalers. *Respiratory Medicine,* **96**, S3-S8.

GAVTASH, B., MYATT, B., O'SHEA, H., MASON, F., LEWIS, D., CHURCH, T., VERSTEEG, H.K., HARGRAVE, G., and BRAMBILLA, G., 2016. Saturated vapour pressure (SVP) measurement of ethanol/HFA binary mixtures. Journal of Aerosol Medicine and Pulmonary Drug Delivery, **29**(3), A12-A12.

GAVTASH, B., VERSTEEG, H.K., HARGRAVE, G.K., LEWIS, D., CHURCH, T., and BRAMBILLA, G., 2014. Linear Instability Sheet Atomisation (LISA) model to predict droplet size issued from a pMDI. In: *Proceedings of the ILASS – Europe 2014, 26th Annual Conference on Liquid Atomization and Spray Systems, Bremen, September 2014.,* pp. 283-285

GHOSE, P., PATRA, J., DATTA, A., and MUKHOPADHYAY, A., 2014. Effect of air flow distribution on soot formation and radiative heat transfer in a model liquid fuel spray combustor firing kerosene. *International Journal of Heat and Mass Transfer,* **74**, 143-155.

GIOT, M., GRANGER, S., PAGES, D., and SEYNHAEVE, J.M., 1994. A model of single and two-phase flow (critical or not) through cracks. *31st meeting of the European two-phase flow group, Piacenza, 6-8 June 1994.* Collection de notes internes de la direction des études et recherches de EDF, (96NB00025), pp. 1-22.

GJELLERUP, C. and FREDERIKSEN, S.O., 2007. *CFD and PIV investigation of the flow inside the USP throat and in a replica of the human upper airways.* Joint Dissertation (MSc), Techical University of Denmark.

GOSMAN, A. D., and LOANNIDES, E., 1983. Aspects of computer simulation of liquid-fuelled combustors. *Journal of Energy,* **7**(6), 482-490.

GUILDENBECHER, D., LÓPEZ-RIVERA, C., and SOJKA, P., 2009. Secondary atomization. *Experiments in Fluids,* **46**(3), 371-402.

GUPTA, A., STEIN, S.W., and MYRDAL, P.B., 2003. Balancing ethanol cosolvent concentration with product performance in 134a-based pressurized metered dose inhalers. *Journal of Aerosol Medicine,* **16**(2), 167-174.

HARDY, P., and MALI, P., 1983. Validation and development of a model describing subcooled critical flow through long tubes. *Revue Énergie Primaire,* **18**(1), 5-23.

HARNOR, K., PERKINS, A., WASTIE, M., WILSON, C., SIMS, E., FEELY, L., and FARR, S., 1993. Effect of vapour pressure on the deposition pattern from solution phase metered dose inhalers. *International Journal of Pharmaceutics,* **95**(1), 111-116.

HARRINGTON, L., VERSTEEG, H.K., EHTEZAZI, T., HORFIELD, M.A., BARRY, P.W. and O'CALLAGHAN, C., 2001. Comparison of the developement of a pharmaceutical aerosel in USP and "biological" throats using computational fluid dynamic. In: *Proceedings of the DDL XII, London, 2001*. Drug Delivery to the Lungs- Aerosol Society, pp. 35-37. ISBN: 0-95297-777-X.

HENRY, R.E., 1970. The two-phase critical discharge of initially saturated or subcooled liquid. *Nuclear Science and Engineering,* **41**(3), 336-342.

HENRY, R.E., 1968. *A STUDY OF ONE-AND TWO-COMPONENT, TWO-PHASE CRITICAL FLOWS AT LOW QUALITIES.*NASA Technical report, Document ID: 19700040046, Acssess Number: 70A16162.

HENRY, R.E., and FAUSKE, H.K., 1971. The two-phase critical flow of one-component mixtures in nozzles, orifices, and short tubes. *Journal of Heat Transfer,* **93**(2), 179-187.

HEWITT, G., 2013. *Annular two-phase flow.* Oxford: Elsevier.

HICKEY, A.J., 1996. *Inhalation aerosols: physical and biological basis for therapy.* Florida: CRC press, Taylor & Francis.

HICKEY, A.T., and DUNBAR, C.A., 1997. A new millenium for inhaler technology. *Pharmaceutical Technology,* **21**(6), 116-125.

HILL, P.G., 1965. Turbulent jets in ducted streams. *Journal of Fluid Mechanics,* **22**(01), 161-186.

HINZE, J., 1975. *Turbulence.* New York: McGraw-Hill.

HOCHRAINER, D., HÖLZ, H., KREHER, C., SCAFFIDI, L., SPALLEK, M., and WACHTEL, H., 2005. Comparison of the aerosol velocity and spray duration of Respimat® Soft Mist™ inhaler and pressurized metered dose inhalers. *Journal of Aerosol Medicine,* **18**(3), 273-282.

HSIANG, L., and FAETH, G.M., 1992. Near-limit drop deformation and secondary breakup. *International Journal of Multiphase Flow,* **18**(5), 635-652.

HUFF, J., 1985. Multiphase flashing flow in pressure relief systems. *Plant/Operations Progress,* **4**(4), 191-199.

HUTCHESON, P.S., CHEW, J.W., THORPE, R.B., and YOUNG, C., 2008. Assessment of models for liquid jet breakup. *ASME Turbo Expo 2008: Power for Land, Sea, and Air,* US, 2008. American Society of Mechanical Engineers, pp. 1517-1529.

HWANG, S., LIU, Z., and REITZ, R.D., 1996. Breakup mechanisms and drag coefficients of high-speed vaporizing liquid drops. *Atomization and Sprays,* **6**(3),353-376.

IVEY, J.W., LEWIS, D., CHURCH, T., FINLAY, W.H., and VEHRING, R., 2014. A correlation equation for the mass median aerodynamic diameter of the aerosol emitted by solution metered dose inhalers. *International Journal of Pharmaceutics,* **465**(1), 18-24.

JEFFERY, P.K., and HAAHTELA, T., 2006. Allergic rhinitis and asthma: inflammation in a one-airway condition. *BMC pulmonary medicine,* **6**(1), S5.

JONES, S., EVANS, G., and GALVIN, K., 1999. Bubble nucleation from gas cavities—a review. *Advances in Colloid and Interface Science,* **80**(1), 27-50.

JOSEPH, D.D., BELANGER, J., and BEAVERS, G., 1999. Breakup of a liquid drop suddenly exposed to a high-speed airstream. *International Journal of Multiphase Flow,* **25**(6), 1263-1303.

JU, D., SHRIMPTON, J., and HEARN, A., 2010. The effect of reduction of propellant mass fraction on the injection profile of metered dose inhalers. *International Journal of Pharmaceutics,* **391**(1), 221-229.

KAWANO, D., ISHII, H., SUZUKI, H., GOTO, Y., ODAKA, M., and SENDA, J., 2006. Numerical study on flash-boiling spray of multicomponent fuel. *Heat Transfer—Asian Research,* **35**(5), 369-385.

KIM, S., CHOUDHURY, D., and PATEL, B., 1997. Computations of complex turbulent flows using the commercial code ANSYS FLUENT. In: *Proceedings of the ICASE/LaRC/AFOSR Symposium on Modeling ComplexTurbulent Flows, Hampton, Virginia 1997. Springer*, pp. 259-276.

KLANG, S.H., FRUCHT-PERY, J., HOFFMAN, A., and BENITA, S., 1994. Physicochemical characterization and acute toxicity evaluation of a positively-charged submicron emulsion vehicle. *Journal of Pharmacy and Pharmacology,* **46**(12), 986-993.

KLEINER, M., and SADOWSKI, G., 2007. Modeling vapor–liquid equilibria of ethanol 1, 1, 1, 2, 3, 3, 3-heptafluoropropane binary mixtures using PC-SAFT. *Fluid Phase Equilibria,* **260**(2), 190-194.

KLEINSTREUER, C., SHI, H., and ZHANG, Z., 2007. Computational analyses of a pressurized metered dose inhaler and a new drug-aerosol targeting methodology. *Journal of Aerosol Medicine,* **20**(3), 294-309.

KOSTAS, J., HONNERY, D., SORIA, J., KASTENGREN, A., LIU, Z., POWELL, C., and WANG, J., 2009. Effect of nozzle transients and compressibility on the penetration of fuel sprays. *Applied Physics Letters,* **95**(2), 024101.

LACKME, C., 1979. Incompleteness of the flashing of a supersaturated liquid and sonic ejection of the produced phases. *International Journal of Multiphase Flow,* **5**(2), 131-141.

LEACH, C., 1999. Effect of formulation parameters on hydrofluoroalkane-beclomethasone dipropionate drug deposition in humans. *Journal of Allergy and Clinical Immunology,* **104**(6), s250-s252.

LEDGARD, J., 2007. *The preparatory manual of explosives.* Lab manual, 3rd ed. Organic Chemist Inventer, Washington.

LEE, C.S., and PARK, S.W., 2002. An experimental and numerical study on fuel atomization characteristics of high-pressure diesel injection sprays. *Fuel,* **81**(18), 2417-2423.

LEE, C.S., and REITZ, R.D., 2001. Effect of liquid properties on the breakup mechanism of high-speed liquid drops. *Atomization and Sprays,* **11**(1), 1-19.

LEE, S.Y.K., WONG, M., and ZOHAR, Y., 2001. Pressure losses in microchannels with bends. *The 14th IEEE International Conference on Micro Electro Mechanical Systems*, Las Vegas, 21-25 January MEMS 2001. IEEE, pp. 491-494.

LEFEBVRE, A.H., 1980. Airblast atomization. *Progress in Energy and Combustion Science,* **6**, 233-261.

LEFEBVRE, A., 1989. *Atomization and sprays.* Florida: CRC press, Taylor & Francis.

LEMMON, E.W., MCLINDEN, M.O., and FRIEND, D.G., "*Thermophysical Properties of Fluid Systems*" in NIST Chemistry WebBook, NIST Standard Reference Database Number 69, Eds. P.J. Linstrom and W.G. Mallard, National Institute of Standards and Technology, Gaithersburg MD, 20899, http://webbook.nist.gov.

LEWIS, D., JOHNSON, S., MEAKIN, B., GANDERTON, D., BRAMBILLA, G., GARZIA, R., and VENTURA, P., 1998. Effects of actuator orifice diameter on beclomethasone dipropionate delivery from a pMDI HFA solution formulation. *RDD VI,* **1**, pp. 363-364.

LEWIS, D., GANDERTON, D., MEAKIN, B., and BRAMBILLA, G., 2004. Theory and practice with solution systems. *RDD IX,* **1,** pp. 109-116.

LEWIS, D., MEAKIN, B., and BRAMBILLA, G., 2006. New actuators versus old: reasons and results for actuator modifications for HFA solution MDIs. *RDD X,* **1**, pp. 101-110.

LEWIS, D., 2007. Metered-dose inhalers: actuators old and new. *Expert Opinion on Drug Delivery*, **4**(3), 235-245. doi: 10.1517/17425247.4.3.235.

LIENHARD, J.H., and DAY, J.B., 1970. The breakup of superheated liquid jets. *Journal of Basic Engineering,* **92**(3), 515-521.

LIU, H., WINOTO, S.H., and SHAH, D.A., 1997. Velocity measurements within confined turbulent jets: Application to cardiovalvular regurgitation. *Annals of Biomedical Engineering,* **25**(6), 939-948.

LIU, Z., and REITZ, R., 1997. An analysis of the distortion and breakup mechanisms of high speed liquid drops. *International Journal of Multiphase Flow,* **23**(4), 631-650.

LONGEST, P.W., and VINCHURKAR, S., 2007. Effects of mesh style and grid convergence on particle deposition in bifurcating airway models with comparisons to experimental data. *Medical Engineering & Physics,* **29**(3), 350-366.

LORENZETTO, G., and LEFEBVRE, A., 1977. Measurements of drop size on a plain-jet airblast atomizer. *AIAA Journal,* **15**(7), 1006-1010.

LOTH, E., 2000. Numerical approaches for motion of dispersed particles, droplets and bubbles. *Progress in Energy and Combustion Science,* **26**(3), 161-223.

LUBETKIN, S., 2003. Why is it much easier to nucleate gas bubbles than theory predicts? *Langmuir,* **19**(7), 2575-2587.

MANEELY, D.J., 1962. *A study of the expansion process of low-quality steam through a de Laval nozzle.* Dissertation (MSc.), University of California, Berkeley.

MARIO, J., MOLINA, M.J., and ROWLAND, F.S., 1974. Stratospheric sink for chlorofluoromethanes: chlorine atom-catalysed destruction of ozone. *Nature,* **249**(28), 810-812.

MARKETOS, S.G., and BALLAS, C.N., 1982. Bronchial asthma in the medical literature of Greek antiquity. *Journal of Asthma,* **19**(4), 263-269.

MASON, F., LEWIS, D., and GAVTASH, B., 2014. Empirical equations for predicting the vapour pressure of HFA 134a or HFA 227ea systems containing ethanol. J*ournal of aerosol medicine and pulmonary drug delivery,* **27**(4) pp. A11-A11.

MATIDA, E.A., FINLAY, W.H., BREUER, M., and LANGE, C.F., 2006. Improving prediction of aerosol deposition in an idealized mouth using large-eddy simulation. *Journal of Aerosol Medicine,* **19**(3), 290-300.

MATIDA, E.A., NISHINO, K., and TORII, K., 2000. Statistical simulation of particle deposition on the wall from turbulent dispersed pipe flow. *International Journal of Heat and Fluid Flow,* **21**(4), 389-402.

MEAKIN, B., LEWIS, D., GANDERTON, D., and BRAMBILLA, G., 2000. Countering challenges posed by mimicry of CFC performance using HFA systems. *RDD VII, Serentec, Raleigh,* pp. 99-107.

MIKIC, B., ROHSENOW, W., and GRIFFITH, P., 1970. On bubble growth rates. *International Journal of Heat and Mass Transfer,* **13**(4), 657-666.

MONTREAL PROTOCOL, 1987. Montreal protocol on substances that deplete the ozone layer. *United Nations (UN), New York, NY, USA, (1987 with subsequent amendments).*

MOODY, F.J., 1965. Maximum flow rate of a single component, two-phase mixture. *Journal of Heat Transfer,* **87**(1), 134-141.

MOSSAD, R., YANG, W., and SCHWARZ, M.P., 2009. Numerical prediction of air flow in sharp 90º elbow. In: *Proceedings of the Seventh International Conference on CFD in the Mineral and Process Industries CSIRO, Meibourne, Australia*, 9-11 december 2009. pp. 11.

MYATT, B., LEWIS, D., CHURCH, T., BRAMBILLA, G., HARGRAVE, G., VERSTEEG, H., LONG, E., and GAVTASH, B., 2015 a. PDA Analysis of HFA/Ethanol pMDI Aerosols: An Improved Test Protocol and New Findings. In: *Proceedings of the ICLASS 2015, 13th Triennial International Conference on Liquid Atomization and Spray Systems, Thailand, August 2015*.

MYATT, B., NEWTON, R., LEWIS, D., CHURCH, T., BRAMBILLA, G., HARGRAVE, G., VERSTEEG, H., GAVTASH, B., and LONG, E., 2015 b. PDA and high speed image analysis of HFA/ethanol pMDI aerosols: new findings. DD*L 26*, *Edinburg, December 2015*. pp. 73-77.

NEUSEN, K.F., 1962. Optimizing of flow parameters for the expansion of very low-quality steam*. Technical report no. UCRL-6152 DOE contract No. W-7405-ENG-48*. California-University, Livermore, Lawrence Radiation Laboratory.

NOAKES, T., 2002. Medical aerosol propellants. *Journal of Fluorine Chemistry,* **118**(1-2), 35-45.

OHNESORGE, W.V., 1936. Formation of drops by nozzles and the breakup of liquid jets. *Z.Angew.Math.Mech,* **16**(4), 355-358.

OLIVEIRA, R.F., TEIXEIRA, S., SILVA, L.F., TEIXEIRA, J.C., and ANTUNES, H., 2010 a. Study of a Pressurized Metered-dose Inhaler Spray Parameters in Fluent™. In: *Proceedings of the World Congress on Engineering*, *London*, *June 30 - July 2, 2010*. WCE 2010 Vol 2.

OLIVEIRA, R.F., TEIXEIRA, S., SILVA, L.F., TEIXEIRA, J.C. and ANTUNES, H., 2010 b. CFD study of the volumetric spacer: a realistic approach, J.C.F. PEREIRA and A. SEQUEIRA, eds. *European Conference on Computational Fluid Dynamics*, *ECCOMAS CFD 2010, June 2010*.

O'ROURKE, P., and AMSDEN, A., 1987. The TAB method for numerical calculation of spray droplet breakup. *SAE Technical Paper 872089.* Los Alamos National Laboratory, Los Alamos, New Mexico.

PARK, B.S., and LEE, S.Y., 1994. An experimental investigation of the flash atomization mechanism. *Atomization and Sprays,* **4**(2), 159-179.

PARK, S.H., KIM, H.J., SUH, H.K., and LEE, C.S., 2009. Atomization and spray characteristics of bioethanol and bioethanol blended gasoline fuel injected through a direct injection gasoline injector. *International Journal of Heat and Fluid Flow,* **30**(6), 1183-1192.

PATTERSON, M.A., and REITZ, R.D., 1999. Modeling spray atomization with the Kelvin-Helmholtz/Rayleigh-Taylor hybrid model. *Atomization and Sprays,* **9**(6), 623-650.

PILCER, G., and AMIGHI, K., 2010. Formulation strategy and use of excipients in pulmonary drug delivery. *International Journal of Pharmaceutics,* **392**(1), 1-19.

PILCH, M., and ERDMAN, C., 1987. Use of breakup time data and velocity history data to predict the maximum size of stable fragments for acceleration-induced breakup of a liquid drop. *International Journal of Multiphase Flow,* **13**(6), 741-757.

PLESSET, M., and PROSPERETTI, A., 1977. Bubble dynamics and cavitation. *Annual Review of Fluid Mechanics,* **9**(1), 145-185.

PLESSET, M., and ZWICK, S., 1952. A nonsteady heat diffusion problem with spherical symmetry. *Journal of Applied Physics,* **23**(1), 95-98.

PLESSET, M., and SADHAL, S., 1984. Void volume growth in superheated liquids. *Am.Soc.Mech.Eng., Heat Transfer Div., Fundam.Phase Change,* **38**, 43-49.

PLESSET, M., and ZWICK, S.A., 1954. The growth of vapor bubbles in superheated liquids. *Journal of Applied Physics,* **25**(4), 493-500.

POLLI, G.P., GRIM, W.M., BACHER, F.A., and YUNKER, M.H., 1969. Influence of formulation on aerosol particle size. *Journal of Pharmaceutical Sciences,* **58**(4), 484-486.

RAJARATNAM, N., and HUMPHRIES, J., 1984. Turbulent non-buoyant surface jets. *Journal of Hydraulic Research,* **22**(2), 103-115.

RANGER, A.A., and NICHOLLS, J., 1969. Aerodynamic shattering of liquid drops. *AIAA Journal,* **7**(2), 285-290.

RANUCCI, J., COOPER, D., and SETHACHUTKUL, K., 1992. Effect of actuator design on metered-dose inhaler plume particles size. *Pharmaceutical Technology,* **16**(3),90-92.

RANZ, M.W., and MARSHALL, W.R., 1952 a. Evaporation from drops, Part I. *Chem En g Progr,* **48** (3), 141-146.

RANZ, M.W., and MARSHALL, W.R., 1952 b. Evaporation from drops, Part II. *Chem.Eng.Prog,* **48**(3), 173-180.

RAYLEIGH, L., 1917. VIII. On the pressure developed in a liquid during the collapse of a spherical cavity. *The London, Edinburgh, and Dublin Philosophical Magazine and Journal of Science,* **34**(200), 94-98.

RAYLEIGH, L., 1878. On the instability of jets. In: *Proceedings of the London mathematical society, London,1878.* **1**(1), pp. 4-13.

RAZZAGHI, M., 1989. Droplet size estimation of two-phase flashing jets. *Nuclear Engineering and Design,* **114**(1), 115-124.

REID, R.C., PRAUSNITZ, J.M. and POLING, B.E., 1987. *The properties of liquids and gases.* New York: McGraw-Hill.

REITZ, R.D., 1990. A photographic study of flash-boiling atomization. *Aerosol Science and Technology,* **12**(3), 561-569.

REITZ, R.D., 1987. Modeling atomization processes in high-pressure vaporizing sprays. *Atomisation Spray Technology,* **3**, 309-337.

REITZ, R.D., 1978. *Atomization and other breakup regimes of a liquid jet*. Thesis (PhD), Princeton University.

RIZK, N., and LEFEBVRE, A., 1984. Spray characteristics of plain-jet airblast atomizers. *Journal of Engineering for Gas Turbines and Power,* **106**(3), 634-638.

RIZK, N., and LEFEBVRE, A., 1980. The influence of liquid film thickness on airblast atomization. *Journal of Engineering for Power,* **102**(3), 706-710.

ROACHE, P.J., 1997. Quantification of uncertainty in computational fluid dynamics. *Annual Review of Fluid Mechanics,* **29**(1), 123-160.

SAZHIN, S.S., FENG, G., and HEIKAL, M.R., 2001. A model for fuel spray penetration. *Fuel,* **80**(15), 2171-2180.

SCHILLER, L., and NAUMANN, A., 1933. Über die grundlegenden Berechnungen bei der Schwerkraftaufbereitung. *Z.Ver.Dtsch.Ing,* **77**(12), 318-320.

SCHMELZER, J.W., 2003. Kinetic and thermodynamic theories of nucleation. *Mater.Phys.Mech,* **6**, 21-33.

SCHMIDT, D.P., NOUAR, I., SENECAL, P., RUTLAND, C., MARTIN, J., REITZ, R., and HOFFMAN, J.A., 1999. Pressure-swirl atomization in the near field. *SAE transactions*, **108**(3), 471-484.

SENDA, J., HOJYO, Y., and FUJIMOTO, H., 1994. Modeling on atomization and vaporization process in flash boiling spray. *JSAE Review,* **15**(4), 291-296.

SENECAL, P., SCHMIDT, D.P., NOUAR, I., RUTLAND, C.J., REITZ, R.D., and CORRADINI, M., 1999. Modeling high-speed viscous liquid sheet atomization. *International Journal of Multiphase Flow,* **25**(6), 1073-1097.

SHAIK, A.Q., 2010. *Numerical modeling of two-phase flashing propellant flow inside the twin-orifice system of pressurized metered dose inhalers.* Thesis (PhD), Loughborough University.

SHEKUNOV, B.Y., CHATTOPADHYAY, P., TONG, H.H., and CHOW, A.H., 2007. Particle size analysis in pharmaceutics: principles, methods and applications. *Pharmaceutical Research,* **24**(2), 203-227.

SHER, E., BAR-KOHANY, T., and RASHKOVAN, A., 2008. Flash-boiling atomization. *Progress in Energy and Combustion Science,* **34**(4), 417-439.

SHER, E., and ELATA, C., 1977. Spray formation from pressure cans by flashing. *Industrial & Engineering Chemistry Process Design and Development,* **16**(2), 237-242.

SHIH, T., LIOU, W., SHABBIR, A., YANG, Z., and ZHU, J., 1995. A new k-epsilon eddy-viscosity model for high Reynolds number turbulent flows: Model development and validation. Computers Fluids, **24**(3), 227-238.

SINGH, B.B., KHORSAN, R., VINJAMURY, S.P., DER-MARTIROSIAN, C., KIZHAKKEVEETTIL, A., and ANDERSON, T.M., 2007. Herbal treatments of asthma: a systematic review. *Journal of Asthma,* **44**(9), 685-698.

SMYTH, H.D.C., 2003. The influence of formulation variables on the performance of alternative propellant-driven metered dose inhalers. *Advanced Drug Delivery Reviews,* **55**(7), 807-828.

SMYTH, H., and HICKEY, A., 2002. Comparative particle size analysis of solution propellant driven metered dose inhalers using cascade impaction and laser diffraction. *RDD VIII,* **2**, pp. 731-734.

SMYTH, H., MEJIA-MILLAN, E., and HICKEY, A., 2002. The effect of ethanol on solvency vapor pressure, and emitted droplet size of solution metered dose inhalers containing HFA 134a. *RDD VIII,* **2,** pp. 735-738.

SOLOMON, A., RUPPRECHT, S., CHEN, L., and FAETH, G., 1985. Flow and atomization in flashing injectors. *Atomisation Spray Technology,* **1**, 53-76.

SOMMERFELD, M., 1992. Modelling of particle-wall collisions in confined gas-particle flows. *International Journal of Multiphase Flow,* **18**(6), 905-926.

SPALDING, D., 1960. A standard formulation of the steady convective mass transfer problem. *International Journal of Heat and Mass Transfer,* **1**(2), 192-207.

SQUIRE, H., 1953. Investigation of the instability of a moving liquid film. *British Journal of Applied Physics,* **4**(6), 167-169.

STAHLHOFEN, W., RUDOLF, G., and JAMES, A., 1989. Intercomparison of experimental regional aerosol deposition data. *Journal of Aerosol Medicine,* **2**(3), 285-308.

STARKMAN, E., NEUSEN, K., MANEELY, D., and SCHROCK, V., 1964. Expansion of a very low quality two-phase fluid through a convergent-divergent nozzle. *Journal of Basic Engineering,* **86**(2), 247-254.

STEFELY, J., DUAN, D., MYRDAL, P., ROSS, D., SCHULTZ, D., and LEACH, C., 2000. Design and utility of a novel class of biocompatible excipients for HFA-based MDIs. *RDD VII,* **1**, pp. 83-90.

STEIN, S.W., and MYRDAL, P.B., 2006. The relative influence of atomization and evaporation on metered dose inhaler drug delivery efficiency. *Aerosol Science and Technology,* **40**(5), 335-347.

STEIN, S.W., and MYRDAL, P.B., 2004. A theoretical and experimental analysis of formulation and device parameters affecting solution MDI size distributions. *Journal of Pharmaceutical Sciences,* **93**(8), 2158-2175.

STEIN, S.W., SHETH, P., HODSON, P.D., and MYRDAL, P.B., 2014. Advances in metered dose inhaler technology: hardware development. *AAPS PharmSciTech,* **15**(2), 326-338.

THIEL, C.G., 1996. From Susie's question to CFC free: an inventor's perspective on forty years of MDI development and regulation. *RDD V,* **1**, pp. 115-123.

TZOU, T., 1998. Density, excess molar volume, and vapor pressure of propellant mixtures in metered-dose inhalers: deviation from ideal mixtures. *RDD VI,* pp. 439-443.

USP. 2005. *"Physical tests and determinations: aerosols, nasal sprays, metered-dose inhalers, and dry powder inhalers."*, United States Pharmacopeia First Supplement, United States Pharmacopeia Convention, Rockville, MD, 3298-3316, vol. 28-NF, General Chapter (601).

VERSTEEG, H.K., and HARGRAVE, G.K., 2006. Fundamentals and resilience of the original MDI actuator design. *RDD X,* **1**, pp. 91-100. ISBN:1-930114-95-8.

VERSTEEG, H.K., HARGRAVE, G., HARRINGTON, L., SHRUBB, I., and HODSON, D., 2000. The use of computational fluid dynamics (CFD) to predict pMDI air flows and aerosol plume formation. *RDD VII,* **1**, 257-264.

VERSTEEG, H.K., and MALALASEKERA, W., 2007. *An introduction to computational fluid dynamics: the finite volume method.* 2nd ed. England: Pearson Education.

VERSTEEG, H., HARGRAVE, G., and KIRBY, M., 2006. Internal flow and near-orifice spray visualisations of a model pharmaceutical pressurised metered dose inhaler. *Journal of Physics: Conference Series* 45, IOP Publishing, 207-217.

VERVAET, C., and BYRON, P.R., 1999. Drug–surfactant–propellant interactions in HFA-formulations. *International Journal of Pharmaceutics,* **186**(1), 13-30.

WALLIS, G.B., 1980. Critical two-phase flow. *International Journal of Multiphase Flow,* **6**(1-2), 97-112.

WEBER, C., 1931. Disintegration of liquid jets. *Z.Angew.Math.Mech,* **11**(2), 136-159.

WHALLEY, P.B., 1987. *Boiling, condensation, and gas-liquid flow.* Oxford: Clarendon Press.

WHITHAM, M.E., and EAGLE, A., 1994. Alternative propellants: proprietary rights, toxicological issues and projected licensing problems. *RDD IV,* **1** , pp. 203-209.

WIENER, M.V., 1958. How to formulate aerosols to obtain the desired spray pattern. *Journal of the Society of Cosmetic Chemists,* **9**, 289-297.

WIGLEY, G., VERSTEEG, H.K., and HODSON, D., ILASS-Europe 2002. Near-orifice PDA measurements and atomisation mechanism of a pharmaceutical pressurised metered dose inhaler. In: *Proceedings of the 18th Annual Conference on Liquid Atomization & Spray Systems*, Zaragoza, Spain, *September, 2002,* pp. 165-170. ISBN: 84-95480-70-0.

WILCOX, D.A., 1994. Simulation of transition with a two-equation turbulence model. *AIAA Journal,* **32**(2), 247-255.

WONG, W., FLETCHER, D.F., TRAINI, D., CHAN, H.K., and YOUNG, P.M., 2012. The use of computational approaches in inhaler development. *Advanced Drug Delivery Reviews,* **64**(4), 312-322.

WORTH LONGEST, P., and HINDLE, M., 2009. Quantitative analysis and design of a spray aerosol inhaler. Part 1: effects of dilution air inlets and flow paths. *Journal of Aerosol Medicine and Pulmonary Drug Delivery,* **22**(3), 271-283.

WORTH LONGEST, P., HINDLE, M., and CHOUDHURI, S.D., 2009. Effects of generation time on spray aerosol transport and deposition in models of the mouth-throat geometry. *Journal of Aerosol Medicine and Pulmonary Drug Delivery,* **22**(2), 67-84.

WORTH LONGEST, P., HINDLE, M., CHOUDHURI, S.D., and BYRON, P.R., 2007. Numerical simulations of capillary aerosol generation: CFD model development and comparisons with experimental data. *Aerosol Science and Technology,* **41**(10), 952-973.

WORTH LONGEST, P., HINDLE, M., DAS CHOUDHURI, S., and XI, J., 2008. Comparison of ambient and spray aerosol deposition in a standard induction port and more realistic mouth–throat geometry. *Journal of Aerosol Science,* **39**(7), 572-591.

WORTH LONGEST, P., and HOLBROOK, L.T., 2012. In-*silico* models of aerosol delivery to the respiratory tract — Development and applications . *Advanced Drug Delivery Reviews,* **64**(4), 296-311.

WU, Z., ZHU, Z. and HUANG, Z., 2006. An experimental study on the spray structure of oxygenated fuel using laser-based visualization and particle image velocimetry. *Fuel,* **85**(10-11), 1458-1464.

YILDIZ, D., VAN BEECK, J., and RIETHMULLER, M., 2002. Global rainbow thermometry applied to a flashing two-phase R134-A jet. *Eleventh International Symposium on Application of Laser Techniques to Fluid Mechanics, Lisbon, July 2002*.

YILDIZ, D., RAMBAUD, P., VAN BEECK, J., and BUCHLIN, J., 2006. Characterization of superheated liquid jet atomisation with phase Doppler anemometer (PDA) and high-speed imaging. In: *Proceedings of the ASME 2006 2nd Joint US-European Fluids Engineering Summer Meeting Collocated With the 14th International Conference on Nuclear Engineering, January 2006*. American Society of Mechanical Engineers, pp. 921-930.

YILDIZ, D., VAN BEECK, J.P., and RIETHMULLER, M.L., 2004. Feasibility Exploration of Laser-based Techniques for Characterization of a Flashing Jet. *Particle & Particle Systems Characterization,* **21**(5), 390-402.

YORK, J., STUBBS, H., and TEK, M., 1953. The mechanism of disintegration of liquid sheets. *Trans.Asme,* **75**(7), 1279-1286.

YUE, B., and WATKINS, D.A., 2005. Mathematical development and numerical analysis of further transport equations for the droplet size moment theory. *Conference on Liquid Atomization & Spray Systems (ILASS-Europe) 2004, Nottingham*. Manchester: University of Manchester. Manchester eScholar ID: uk-ac-man-scw: 2e74.

YULE, A.J., and DUNKLEY, J.J., 1994. *Atomization of melts for powder production and spray deposition.* Oxford: Clarendon Press.

ZEOLI, N., and GU, S., 2006. Numerical modelling of droplet break-up for gas atomisation. *Computational Materials Science,* **38**(2), 282-292.

ZHANG, Y., FINLAY, W. and MATIDA, E., 2004. Particle deposition measurements and numerical simulation in a highly idealized mouth–throat. *Journal of Aerosol Science,* **35**(7), 789-803.

ZHANG, Z., and KLEINSTREUER, C., 2003. Species heat and mass transfer in a human upper airway model. *International Journal of Heat and Mass Transfer,* **46**(25), 4755-4768.